A REDUCED-ORDER CRAWLER CRANE MODEL WITH ACTIVE CONTROL TO ATTENUATE THE TRANSIENT VIBRATIONS

by

Kellen Matthew Finn

Thesis submitted to the Graduate Faculty of the
Virginia Polytechnic Institute and State University
in partial fulfillment of the requirements for the degree of
MASTER OF SCIENCE
in
Mechanical Engineering

APPROVED:

Harry H. Robertshaw, Ph.D., Chairman

Norman S. Eiss, Jr., Ph.D.

Robert G. Leonard, Ph.D.

March 1982

Blacksburg, Virginia

TABLE OF CONTENTS

ACKNOWLEDGMENTS

The advice, insight, and encouragement offered relentlessly by Mr. William N. Patten is deeply appreciated. The author wishes to thank his committee chairman, Professor Harry H. Robertshaw for the advice and cooperation he extended and for his contributions to the control study.

The time and effort devoted by the committee members, Professors Norman S. Eiss and Robert G. Leonard, to understand and polish this work are also appreciated. A special thanks is extended to the computer specialists at User Services for their time-saving assistance, and to the typist Ms. Debbie Wolfe.

LIST OF TABLES

LIST OF FIGURES

LIST OF SYMBOLS

	Description	Units
A	Cross-sectional area of one outer cord of boom structure	m^2
A_p	Cross-sectional area of actuator piston	m^2
A_{WR}	Effective cross-sectional area of wire rope	m^2
C_B	Boom rotational damping coefficient	N·m·sec
C_c	Critical beam damping coefficient	N·m·sec
C_d	Spool valve discharge coefficient	
C_{ep}	Actuator external leakage coefficient	m^3/sec·MPa
C_{ip}	Actuator internal cross-port leakage coefficient	m^3/sec·MPa
C_r	Rotational damping coefficient for soil foundation	N·sec/m
C_{tp}	Actuator total leakage coefficient	m^3/sec.MPa
C_v	Translational damping coefficient for soil foundation	N·sec/m
d_t	Half length of track	m
D_v	Spool valve diameter	m
E	Modulus of elasticity of boom steel	MPa
E_{WR}	Modulus of elasticity of wire rope	MPa
e	Geometric tilting relation	
$\bar{F}$	Beam nodal force vector	N
f	Geometric tilting relation	
f_t	Beam nodal forces of translation	N
f_θ	Beam nodal forces of rotation	N

	Description	Units
G	Shear modulus of soil	MPa
g	Gravity constant	m/sec^2
I	Area moment of inertia of boom cross-section	m^4
I_c	Mass moment of inertia of car body	$N \cdot m \cdot sec^2$
I_T	Mass moment of inertia of tracks	$N \cdot m \cdot sec^2$
I_{xx}	Area moment of inertia of boom cord cross-section	m^4
J	Mass moment of inertia of equivalent boom	$N \cdot m \cdot sec^2$
K	Beam stiffness matrix	
K_B	Boom moment-resisting spring coefficient	$N \cdot m$
K_c	Actuator flow-pressure coefficient	$m^3/sec \cdot MPa$
K_q	Actuator flow gain	$m^3/sec \cdot m$
K_r	Rocking stiffness of soil	$N \cdot m/rad$
K_v	Vertical stiffness of soil	N/m
K_{WR}	Axial stiffness of wire rope	N/m
K_{WRL}	Axial stiffness of load line	N/m
K_{WRP}	Axial stiffness of pendents	N/m
k_{ij}	Beam stiffness coefficient	
L	Simple beam length	m
L_B	Boom link length	m
L_p	Pendent line length	m
L_{p_e}	Pendent line length at equilibrium	m
$L_p(t_o)$	Unstressed pendent line length	m
L_{WR}	Unstressed wire-rope length	m

	Description	Units
m_B	Boom link mass	kg
m_c	Car body mass	kg
m_L	Suspended load mass	kg
m_T	Track mass	kg
$\bar{P}_i$	Position vector	
P_L	Actuator load pressure	MPa
P_s	Actuator supply pressure	MPa
P_i	Crane system i^{th} generalized coordinate	
Q_i	i^{th} generalized force	
Q_L	Actuator load flow	m^3/sec
q_1, q_2	Boom joint displacement	
R_B	Unflexed boom length	m
R_d	Distance from boom butt pin to uppermost point of gantry	m
R_{ev}	Equivalent foundation radius for vertical translation	m
$R_{e\phi}$	Equivalent foundation radius for rotation	m
$\bar{R}_i$	Position vector	
R_o	Boom radius of gyration	m
R_1,R_2,R_3,R_4, R_5,R_8,R_9	Crane component position vectors	m
T	Kinetic energy	N·m
t	Time	sec
U	Beam strain energy	N·m
V	Potential energy	N·m

	Description	Units
V_t	Total actuator chamber volume	m^3
$\bar{v}$	Beam nodal displacement vector	
W	Work	N·m
w_t	Track width	m
X_p	Actuator piston displacement	m
X_v	Spool valve displacement	m
y	Vertical translation of tracks during tilting	m
β	Geometric tilting relation	
β_e	Effective hydraulic fluid bulk modulus	MPa
γ	Beam weight density	N/m^3
η	Geometric tilting relation	
θ_1, θ_2	Local boom joint rotation	rad
ν	Poisson's ratio for the soil	
π	3.1415. . .	
ρ	Soil density	$N\cdot sec^2/m^4$
σ	Hydraulic fluid density	$N\cdot sec^2/m^4$
ϕ_A	Crane configuration constant	rad
ϕ_B	Angle between boom chord and R_d	rad
$\phi_1, \phi_2, \phi_3, \phi_6, \phi_9$	Crane component angular positions	rad
ψ_i	Cubic hermitian polynomial shape function	
ω_n	1^{st} natural frequency of pinned-pinned beam	rad/sec

1. INTRODUCTION

A crawler crane is a self-propelled crane common to many construction sites. The crawler crane has found its greatest utility on the construction site because of its ability to hoist large, heavy loads and to position itself quickly for different tasks. This flexibility is responsible for the crawler crane's popularity and for the large variety of operating conditions it encounters.

The safe operation of a crawler crane relies heavily on the operator's experience. Failure to exercise proper care can result in catastrophic destruction to the machine and its surroundings. Moreover, maximum or rated loads governing the stability of most cranes are established for a level crane on a firm footing in the absence of any dynamic effects. The stability margin preventing a crane from overturning while hoisting a rated load can be as low as 1.18 (1). Most manufactures supply rating charts to help the operator reduce the rated load when his operating conditions vary from the ideal. Tipping or overturning is the most common type of mobile crane-related accident on the jobsite (1).

Normal operating conditions do not produce dynamic loads which can affect the cranes stability. However, rapid acceleration or deceleration of the load caused by an instantaneous release of the load, a sudden application of the brakes during load lowering, or a collision between the load and a stationary structure can produce dynamic forces that will severely affect the crane's response.

For instance, many operators attempt to increase their load lowering speeds by allowing the load to intermittently free-fall. If the load gains too much speed and the operator applies the brakes too forcefully, he can subject the crane to dramatic structural loading. The operator who accidentally induces this dynamic loading finds himself in a very dangerous predicament since the tilting rotation of the crane is so rapid there is no way for him to accurately predict the eventual outcome. Releasing or dropping the load can pose serious threat to the load, the surroundings, the operator, and the crane itself; however, this is the most common procedure. Sometimes releasing the load may recover the crane from certain overturn, but the crane often comes to rest with enough force to damage its major components (1, 2).

Current crane analysis and design techniques are unable to predict the dynamic loads that can cause failures. Mathematicians in the Soviet Union are working on such problems, but crane engineers in the United States feel this sort of loading is of little importance for mobile cranes (1).

The purpose of this thesis is twofold. First, to develop a reduced-order analytical model which accurately describes the dynamic response of a crawler crane. This reduced-order model, simpler than the model developed by Patten (2), is to be used as a tool to further the study of the crane's dynamic characteristics. Because of its simplicity, the model affords the researcher an opportunity to add auxiliary devices to the crane with comparative ease. Secondly, to

adapt a feedback control system and actuator for the crane to attenuate the dynamic response induced by adverse loading. This continuous, real-time controller will absorb energy from the system that might otherwise cause the crane to overturn, or induce large stresses in the crane components.

The model contains the following features, as seen in Fig. 1 (from Patten (2)):

A. An elastic ground model with damping which follows the translation and rotation of the crane car body and track system, as well as allowing the crane tracks to tilt off the soil surface.

B. A flexible boom, allowing:

   1. translation and rotation of the rigid boom elements, and
   2. shortening of the boom length from tip to butt.

C. A pendulating load supported by elastic pendent lines and load lines which act only in tension.

A review of the current literature on crawler crane models and crane controls follows in Chapter 2.

The analytical development of the crane dynamics, in Chapter 3, begins first with a brief review of the method used to obtain the equations of motion. The potential energy and virtual work formed by the elastic deformation of the crane components are developed next.

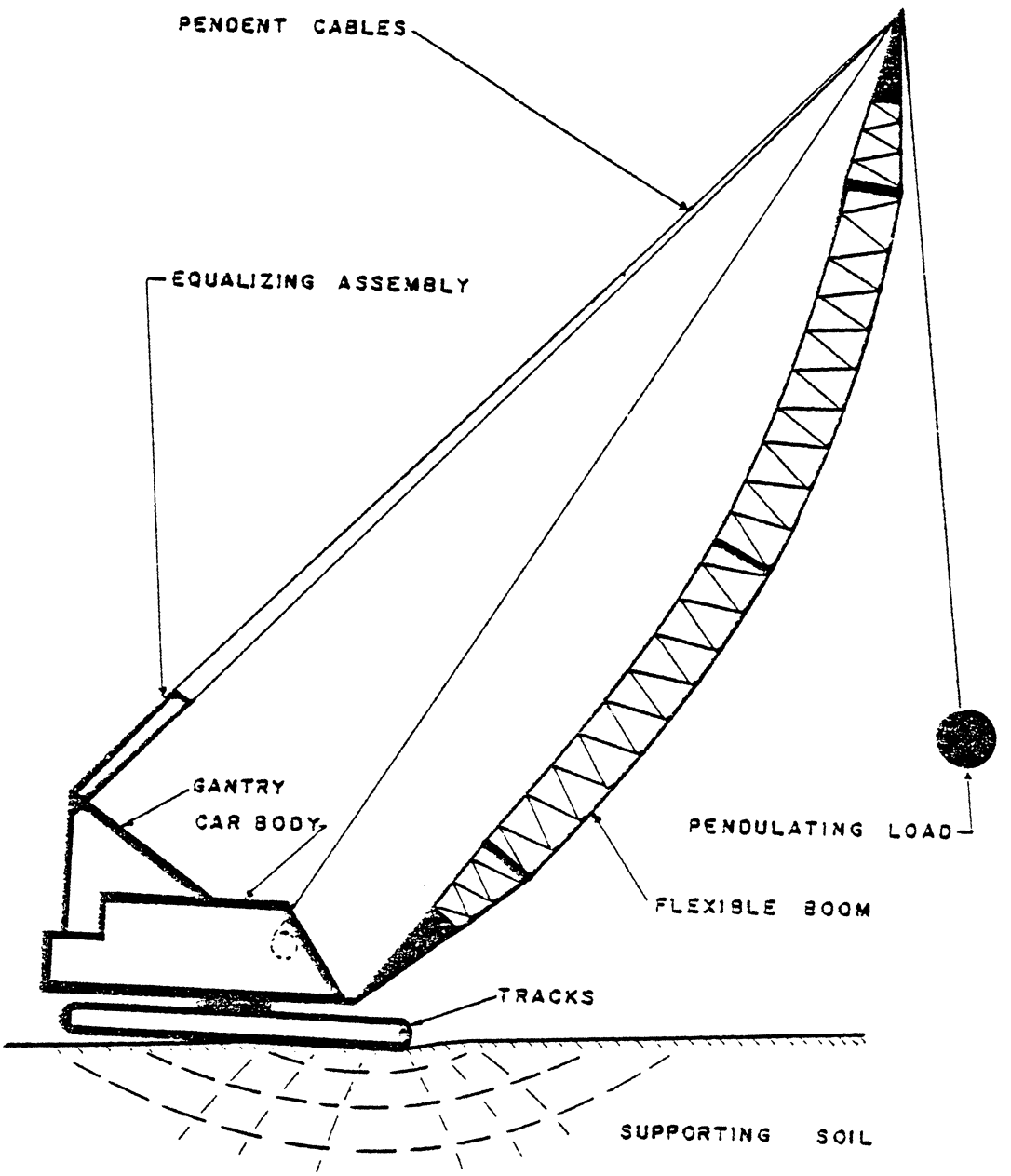

FIG. 1 THE CRAWLER CRANE MODEL (REF. 2)

The total kinetic energy of the system is formulated, as well as the gravitational potential energy. Finally, in Chapter 4, the system differential equations of motion are obtained by applying Lagrange's condition to the total energy of the crane.

The equations of motion of the reduced-order model are numerically integrated for different initial conditions and operating configurations. The time-histories depicting the dynamic characteristics of the model are compared to those from the more detailed Patten model (2) in Chapter 5, to validate the reduced-order system.

In Chapter 6, the dynamics of a hydraulic piston actuator controlled by a spool valve are developed along with the expressions needed to describe the virtual work performed by the nonconservative controlling force. Three feedback compensation techniques to reduce the crane's transient displacements are presented next.

In Chapter 7, the compensated model is subjected to the same initial conditions and operating configurations as those presented in Chapter 5. The controller effectiveness is evaluated by comparing the compensated crane response to the uncompensated response. The thesis concludes with recommendations for future control strategies.

2. LITERATURE SURVEY

A review of current publications developing analytical models of mobile construction cranes is presented in this chapter. The works are divided into two basic groups, those developing models to study the dynamic behavior of construction cranes and those developing models to use in motion control studies. Additional literature used to model crane components is cited in the sections devoted to the model development.

Johnson (3, 4) and Ward and Johnson (5) developed the linearized equations of motion for a two-element crane boom using Newton's method. The boom equations are decoupled using a coordinate transformation, thus neglecting the inertial coupling terms. Johnson chose to disregard the nonlinear pendulation of the load, and elastic backstays, but included nonlinear terms due to large angle rotations.

Saul (6, 7) simulated the motion of a crane boom using a finite-element model. The model is developed to simulate large boom rotations with small local structural deflections and rotations and a random base motion. The equations of motion for the pendulation of a suspended load are derived using Lagrange's equation, and then linearized so that the effects can be superimposed on the structural stiffness matrix of the boom. A Runge-Kutta numerical integration technique is used to solve the linear system equations.

Ito, Senda, and Fujimoto (8, 9) developed an analytical model of the dynamics of a mobile construction crane which they experiment-

ally verified. Specifically, they studied the behavior of vibrations in the elastic load and backstay cables while raising and lowering the load and also while raising and lowering the boom. Their model includes a pendulating load and a one-mode approximation of the boom displacement, for both in-plane bending and out-of-plane bending. The equations of motion were developed with Lagrange's equation assuming small deflection theory, and neglecting crane base motion.

A rather sophisticated crawler crane model has been developed by Patten (2) depicting the transient response of the crane system for in-plane motion. The development includes an elaborate soil model which allows translation and rotation of the crane base, pendulation of the load, rotation of the boom, and nonlinear elastic backstays. The crane boom is modeled as a continuum with three bending modes and rotary inertia. The crane base motion is also modeled to include the effects of tilting. The nonlinear system equations are numerically integrated using the Hamming-Milne predictor-corrector technique.

Two mobile crane models used for motion-control studies are discussed by Smith (10). The cranes are operated aboard cargo ships at sea to off load supplies to lighter vessels. The low-frequency wave motion of the sea overshadows the higher frequency crane system motion; and therefore, dominated the development of the crane-ship models. The crane models developed for this study were made fairly simple to reduce the total number of degrees of freedom for the crane-ship system since the emphasis was placed on load motion control.

The crane model developed by Podgorski (11), for load-motion study, includes rigid boom rotation, a pendulating load, gravitational effects, inertial coupling, and linear-elastic cables. Another crane model developed by Vyzral (12) is simpler than Podgorski's, and neglects crane body motion and nonlinear load pendulation. Both Podgorski and Vyzral linearize the system equations of motion and solve them numerically. Smith (10), in his comparison, utilizes a power spectrum analysis to determine that the in-plane load pendulation and boom rotation of both models are essentially equivalent.

The performance of a rigid crane mounted on a ship deck and modified with load motion compensation devices is presented by Dobeck (13, 14). Dobeck determined that the crane boom tip excursions produced the dominant disturbance in the suspended load. Two simple nonlinear tagline control systems to reduce horizontal pendulation of the load were analyzed. The taglines, modeled as stiff springs with light damping, originate from both sides of the crane body which is fixed in the reference frame of the ship. The nonlinear dynamic equations governing the tagline control force and the hydraulic tagline actuator motors are linearized. A second control system to compensate for the relative vertical motion between the discharging and receiving vessels has also been added using a nonlinear adaptive feedback control law on the load line winch.

Casler, et al., (15) present work paralleling Dobeck's, concerned primarily with controlling the horizontal and heave motion of a load suspended from a crane-ship system on a moderate sea. The suspended load in this system is coupled to the crane-ship motion at the boom

tip. The authors investigate the use of a control system to isolate the boom tip from the crane-base motions, by adjusting the total backstay length. This control is implemented at the boom-hoist winch to adjust the equalizing assembly length, and proves to successfully reduce the horizontal load motion. The power consumed by this boom-topping controller exceeds the established design limits, and is therefore not recommended by the authors.

3. ANALYTICAL DEVELOPMENT OF THE CRANE DYNAMICS

The equations of motion for complex systems with distributed masses, elastic elements, damping elements, and external forces become difficult to express by the direct equilibration of force vectors acting on the masses. The best method to use for this type of problem avoids establishing the vectorial equations of equilibrium, as with d'Alemberts principle, but rather forms the equations of motion from variations of the scalar energy descriptions of the system. This variational method, known as Hamilton's extended principle, states that the variation of the kinetic and potential energy of the system plus the virtual work performed by the nonconservative forces on the system acting through virtual displacements caused by the independent variations, must equal zero during any time interval (16, 17). Hamilton's extended principle may be expressed as,

$$\int_{t_1}^{t_2} \delta(T - V)dt + \int_{t_1}^{t_2} \delta W \, dt = 0 \qquad (3\text{-}2)$$

where:

T = the total kinetic energy of the system,

V = the total potential energy of the system, and

W = the work performed by the nonconservative forces acting on the system.

In order to formulate the equations of motion for a system with multiple degrees of freedom using the variational method, a set of generalized coordinates must be chosen to describe the system's configuration. The set of generalized coordinates for a system with N degrees of freedom are defined as any set of N independent system variables which are not related by any geometric constraints imposed on the system and which completely specify the position of every point within the system (16).

The set of generalized coordinates chosen to describe the crane's motion in a plane is shown in Fig. 2 (after Patten (2)). Each coordinate is depicted in a positive sense of the variation. Descriptions of each of the generalized coordinates follow:

1. R_1: The vertical translation of the tracks measured relative to an arbitrary inertial datum.

2. ϕ_2: The rotation of the tracks measured relative to the plane tangent to the earth's surface.

3. ϕ_6: The rotation of the chord connecting the boom butt to the boom tip, measured relative to the plane tangent to the earth's surface.

4. ϕ_9: The rotation of the load line measured in the plane of motion and perpendicular to the earth's tangent plane.

5. R_9: The length of the load line measured from the boom tip to the center of the load.

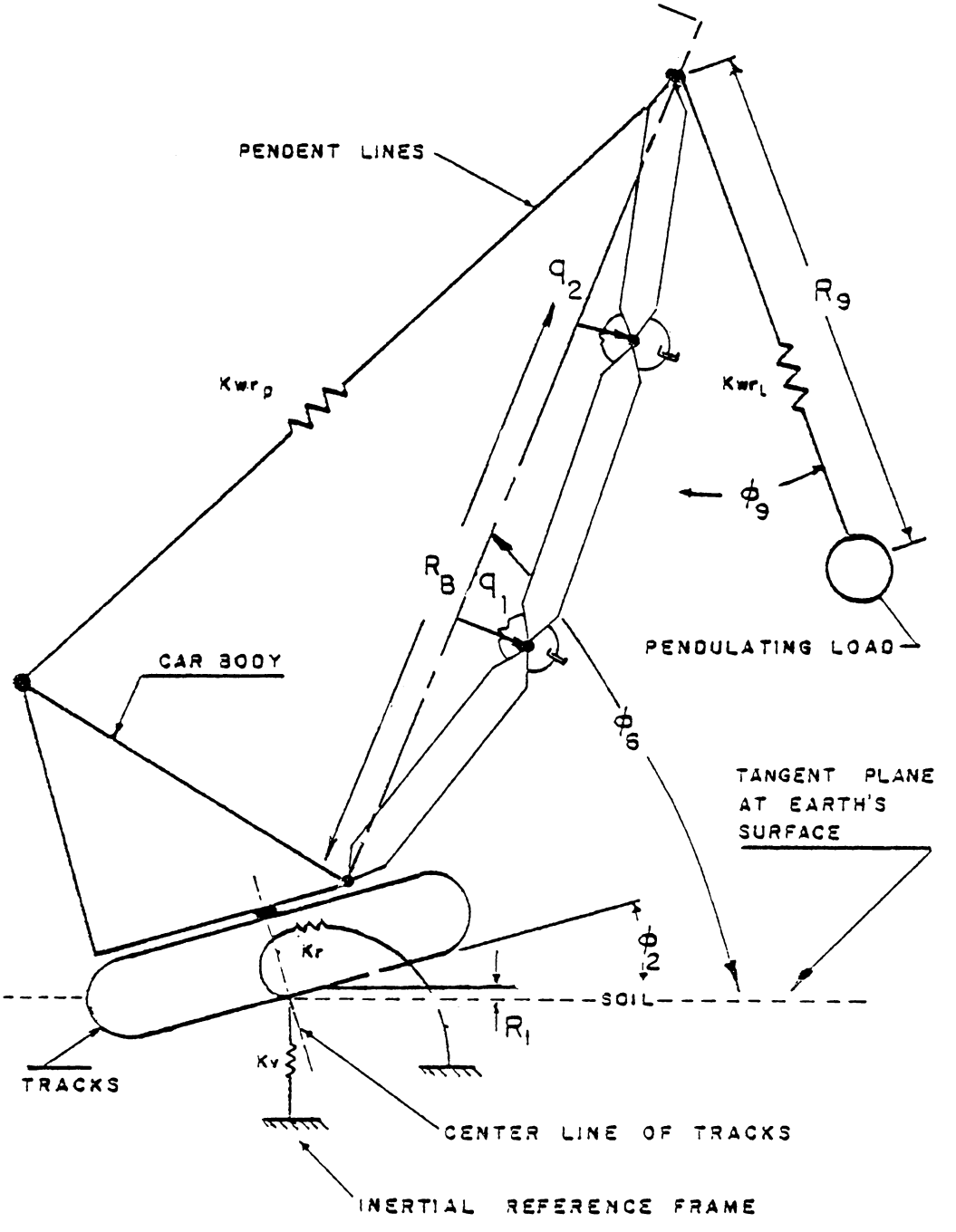

FIG. 2 GENERALIZED COORDINATES

6. q_1: The lower boom joint displacement measured perpendicular to the chord connecting the boom butt to the boom tip.

7. q_2: The upper boom joint displacement measured perpendicular to the chord connecting the boom butt to the boom tip.

The kinetic energy of the crane system can now be expressed in terms of the set of generalized coordinates, p_i, and their time derivates, $\dot{p}_i$, as

$$T = T(p_1, p_2, \ldots, p_N, \dot{p}_1, \dot{p}_2, \ldots, \dot{p}_N). \tag{3-3}$$

Likewise, the system potential energy may be expressed as functions of only the generalized coordinates

$$V = V(p_1, p_2, \ldots, p_N). \tag{3-4}$$

The virtual work performed on the system is expressed as a linear combination of the generalized forcing functions, Q_i, corresponding to each variation

$$\delta W = Q_1\delta p_1 + Q_2\delta p_2' + \ldots + Q_N\delta p_N \tag{3.5}$$

of the generalized coordinate.

Introducing the generalized expressions for the system kinetic energy, potential energy, and virtual work, equations 3-3, 3-4, and 3-5, into Hamilton's extended principle, equation 3-2, performing the required variations, and integrating the velocity dependent terms yields equation 3-6.

$$\int_{t_1}^{t_2} \sum_{i=1}^{\partial} \left[\frac{\partial}{\partial t} \left(\frac{\partial T}{\partial \dot{p}_i} \right) - \frac{\partial T}{\partial p_i} + \frac{\partial V}{\partial p_i} - Q_i \right] \delta p_i \; dt = 0 \qquad (3\text{-}6)$$

Since all variations, δp_i, are independent and arbitrary the terms within the brackets in equation 3-6 must equal zero, or

$$\frac{\partial}{\partial t} \left(\frac{\partial T}{\partial \dot{p}_i} \right) - \frac{\partial T}{\partial p_i} + \frac{\partial V}{\partial p_i} - Q_i = 0 \qquad (3\text{-}7)$$

Equation 3-7 is known as Lagrange's equation for nonconservative, holonomic systems (17). Clearly Hamilton's principle is a necessary and sufficient condition for Lagrange's equations of motion for the crane system.

The generalized expressions for the kinetic and potential energy, and the virtual work of the crane system are developed in the remaining sections of this chapter. The total system energy is them subjected to Lagrange's equation and the resulting differential equations of motion for the crane system are presented in Chapter 4.

3.1 The Potential Energy and Virtual Work of Deformation

The total crane system energy, at any instant, is further subdivided into the potential energy and virtual work due to the local deformation of the flexible crane components, the kinetic energy due to the translational and rotational velocities of the crane component masses, and the gravitational potential energy due to the acceleration

of gravity on the crane component masses. The crane system contains four deformable components, the flexible boom, the pendent cables, load line cables, and the soil foundation. The expressions for the potential energy and the virtual work are developed for each deformable subsystem in terms of the set of generalized coordinates.

3.1.1 The Elastic Boom

The boom structure on a crawler crane is a three-dimensional steel truss, as shown schematically in Fig. 3 (from Patten (2)). This section is devoted to developing the form of the potential energy stored in the boom during deformation, and the virtual work performed by the nonconservative damping forces within the boom.

The equivalent boom model for the reduced-order crane used in this thesis is patterned after a model of a structural element developed by Clough (16). In this model the actual boom, of total length R_B, is discretized in three equal lengths, as seen in Fig. 4. The segments have equal mass, each one-third the total mass of the actual boom. The mass, m_B, is considered to be lumped at the center of each link, L_B. The links are pinned at joints 1 and 2, and are considered completely rigid so that no localized flexure occurs. The joints are elastically restrained by moment-resisting springs, K_B. The damping within the boom is characterized by rotational dashpots, C_B, parallel to the springs at each joint.

The transverse displacements of the boom shorten the boom chord length. The shortening effects have been included since they are

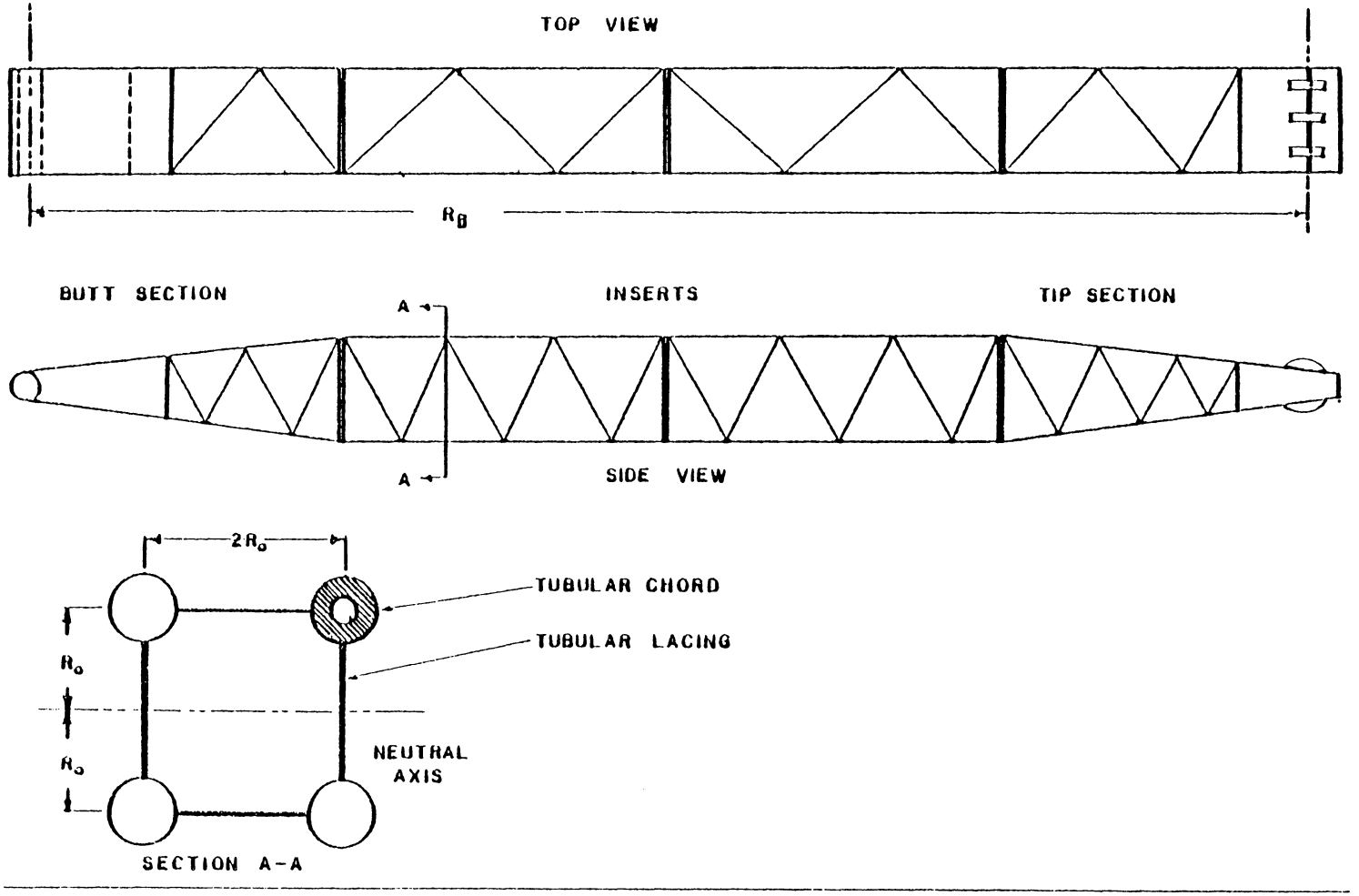

FIG. 3 THE BOOM STRUCTURE (REF. 2)

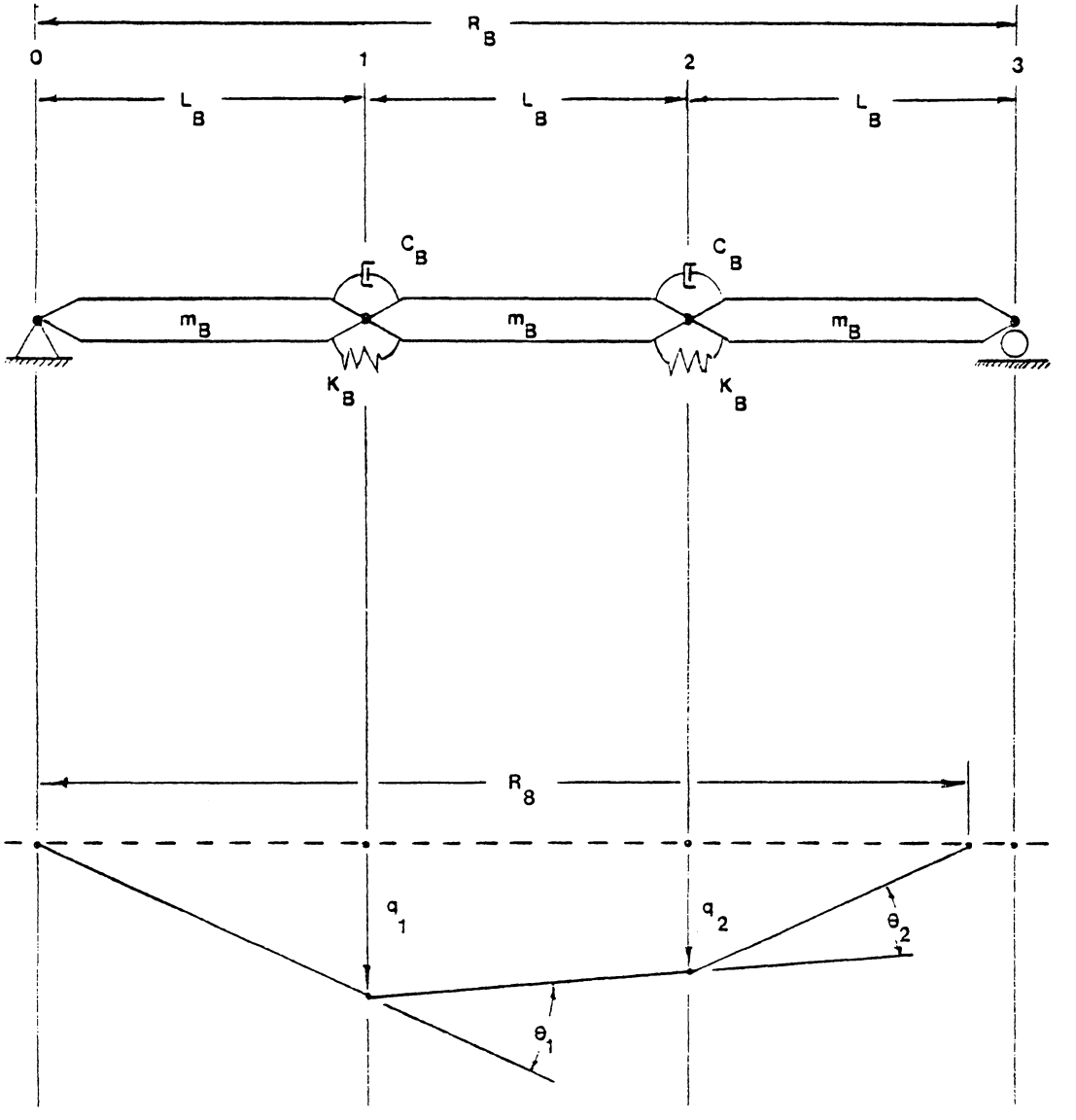

FIG. 4 TWO-DEGREE OF FREEDOM FLEXIBLE BOOM MODEL

considered to significantly affect the pendent line tension. By definition, the boom tip rolls along the boom chord in the plane of motion. This boom model produces a fairly good approximation of the first and second modes of oscillation. The boom description was chosen since Patten (2) showed in his work with a continuum boom model that the first and second modes were dominate in describing the boom's motion.

The equivalent stiffness of the crane boom is developed from a finite-element description of the strain energy within a simple deflected beam. One end of the beam is considered pinned and the other end is allowed to roll freely. The stiffness of the simple beam is used to describe the equivalent stiffness of each of the three links in the crane boom, shown in Fig. 4. The stiffness of the complete boom structure is generated by adding the stiffness coefficients from two adjacent links which correspond to the translation and rotation of each boom joint.

Consider the simple beam element in Fig. 5 as one of the three boom links which is allowed transverse displacements in the plane of motion such that each boundary of the beam, called a node, has two degrees of freedom, vertical translation and rotation. The beam of length, L, has bending stiffness, EI(x), which is a function of its length, x. The deflected shapes resulting from a unit displacement of both translation and rotation at both nodes a and b are shown separately in Fig. 5. The mathematical functions describing the configuration of the beam due to each unit displacement need only satisfy the boundary conditions at the nodes and the internal continuity requirements

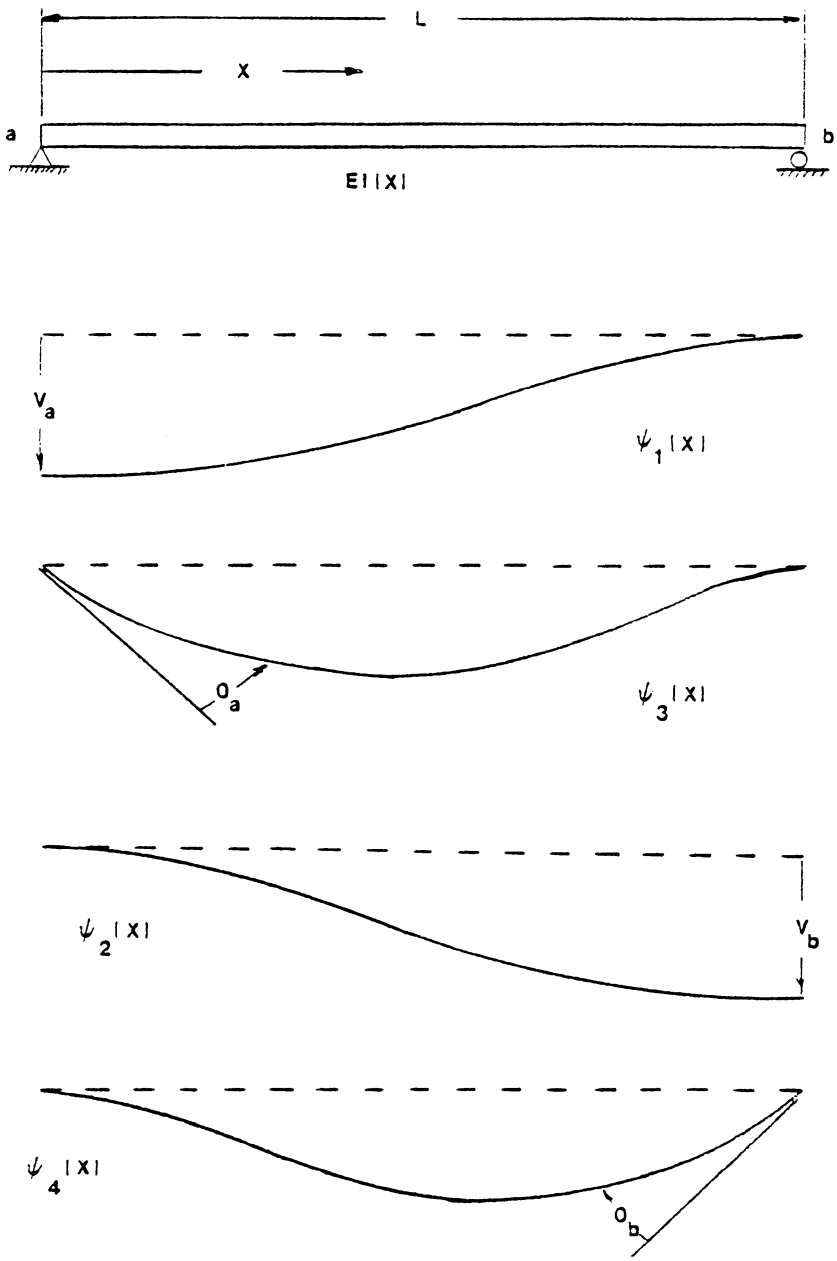

FIG. 5 A SIMPLE BEAM ELEMENT WITH DEFLECTED SHAPES DUE TO NODAL TRANSLATION AND ROTATION DESCRIBED BY CUBIC HERMITIAN POLYNOMIALS

of the beam. Generally, however, the shapes are assumed characteristic of a uniform beam and are described by functions such as the cubic hermitian polynomials given below, as in Clough (16)

$$\psi_1(x) = 1 - 3\left(\frac{x}{L}\right)^2 + 2\left(\frac{x}{L}\right)^3 \qquad (3.1.1\text{-}1)$$

$$\psi_3(x) = x\left(1 - \frac{x}{L}\right)^2 \qquad (3.1.1\text{-}2)$$

$$\psi_2(x) = 3\left(\frac{x}{L}\right)^2 - 2\left(\frac{x}{L}\right)^3 \qquad (3.1.1\text{-}3)$$

and

$$\psi_4(x) = \frac{x^2}{L}\left(\frac{x}{L} - 1\right) \qquad (3.1.1\text{-}4)$$

The strain energy stored in the simple beam element expressed in terms of the nodal displacements is given by

$$U = \frac{1}{2}\bar{v}^T K\bar{v}$$

where:

U = the total strain energy,

$\bar{v}$ = the nodal vector = $\begin{bmatrix} v_a \\ v_b \\ \phi_a \\ \phi_b \end{bmatrix}$,

and

K = stiffness matrix.

Notably, the strain energy in a stable structure, such as the beam element, during any distortion must always be positive, and since the

nodal vector, $\bar{v}$, is chosen arbitrarily to be nonzero, the stiffness matrix, K, is always nonsingular and positive definite, thus it may be inverted. The stiffness matrix is also symmetric as proved by Betti's law in Clough (16). The nodal stiffness coefficient, k_{ij}, is defined as the external force required at node i to cause a unit displacement at node j.

The nodal stiffness coefficient, k_{ij}, can then be determined by equating the work performed by the external forces to the work performed on the internal forces of deformation. The external work, W_{ext}, is

$$W_{ext} = \delta v_i \, k_{ij}, \tag{3.1.1-5}$$

and the internal work, W_{int}, neglecting the effects of shear distortion, is

$$W_{int} = \delta v_i \int_D^L EI(x) \, \ddot{\psi}_i(x) \, \ddot{\psi}_j(x) \, dx \tag{3.1.1-6}$$

where $\ddot{\psi}(x)$ denotes the second derivative of the shape function with respect to x, or

$$\ddot{\psi}(x) = \frac{d}{dx} \left(\frac{d\psi(x)}{dx} \right) \tag{3.1.1-7}$$

Equating equations 3.1.1-5 and 3.1.1-6, the stiffness coefficient, k_{ij}, due to the flexure of the simple beam element becomes

$$k_{ij} = \int_o^L EI(x) \, \ddot{\psi}_i(x) \, \ddot{\psi}_j(x) \, dx \tag{3.1.1-8}$$

Performing the indicated integrations, the nodal force vector, $\bar{F}$, is expressed in terms of the stiffness matrix, K, for the beam element and the nodal displacements, $\bar{v}$, as $\bar{F} = K\bar{v}$, or

$$\bar{F} = \frac{2EI}{L^3}\begin{bmatrix} 6 & -6 & 3L & 3L \\ -6 & 6 & -3L & -3L \\ 3L & -3L & 2L^2 & L^2 \\ 3L & -3L & L^2 & 2L^2 \end{bmatrix} \cdot \begin{bmatrix} v_a \\ v_b \\ \theta_a \\ \theta_b \end{bmatrix} \qquad (3.1.1\text{-}9)$$

The complete stiffness matrix for the crane boom can be constructed from the above description of the simple beam element by superimposing the appropriate stiffness coefficients at each node. Referring to Fig. 4, the nodal displacements of the crane boom are the vertical translations, q_1 and q_2, and the rotations θ_1 and θ_2 at the joints 1 and 2 respectively. Adding the corresponding stiffness coefficients associated with each node, the stiffness matrix, K, for the crane boom is expressed in terms of the nodal forces of translation, f_t, and nodal moments of rotation, f_θ, as

$$\left[\begin{array}{c} f_t \\ \hline f_\theta \end{array}\right] = \frac{2EI}{L_B^3}\left[\begin{array}{cc:cc} 12 & -6 & 0 & 3L_B \\ -6 & 12 & -3L_B & 0 \\ \hdashline 0 & -3L_B & 4L_B^2 & L_B^2 \\ 3L_B & 0 & L_B^2 & 4L_B^2 \end{array}\right] \cdot \left[\begin{array}{c} q_1 \\ q_2 \\ \hline \theta_1 \\ \theta_2 \end{array}\right] \qquad (3.1.1\text{-}10)$$

The rotational stiffness matrix, K_θ, may be obtained by eliminating the translational degrees of freedom from the boom stiffness matrix above using the method of static condensation. Representing

the partioned submatrices of equation 3.1.1-10 with subscripts, t, denoting translation and, θ, denoting rotation, and setting the nodal translation forces equal to zero,

$$\begin{bmatrix} 0 \\ - - \\ f_\theta \end{bmatrix} = \left[\begin{array}{c|c} K_{tt} & K_{t\theta} \\ - - - & - - - - \\ K_{\theta t} & K_{\theta\theta} \end{array}\right] \cdot \begin{bmatrix} v_t \\ - - \\ v_\theta \end{bmatrix} \qquad (3.1.1\text{-}11)$$

where v_t identifies the nodal translations and v_θ identifies the nodal rotations. Reducing equation 3.1.1-11 in terms of the rotational displacements only, yields

$$[f_\theta] = [K_{\theta\theta} - K_{\theta t} K_{tt}^{-1} K_{t\theta}] \cdot [v_\theta] \qquad (3.1.1\text{-}12)$$

Define the rotational stiffness matrix, K_θ, for the crane boom as the terms inside the brackets in equation 3.1.1-12.

Substituting the partioned submatrices in the stiffness matrix of equation 3.1.1-10 into equation 3.1.1-12, the rotational stiffness matrix of the crane boom becomes

$$K_\theta = \frac{3EI}{L_B} \begin{bmatrix} 2 & 1 \\ 1 & 2 \end{bmatrix} \qquad (3.1.1\text{-}13)$$

Note that K_θ is real, positive-definite, and symmetric.

The bending stiffness, EI, of the boom model is found from the description of the crane boom properties, where E is the elastic modulus of steel and I is the area moment of inertia of the boom perpendicular to the axis of bending. The bending resistance of

the crane boom is derived primarily from the four outer boom chords, as seen in the boom cross-section in Fig. 3. The total area moment of inertia of the boom is

$$I = 4AR_o^2 + 4I_{xx} \qquad (3.1.1\text{-}14)$$

where:

A = the material cross-sectional area of a chord,

R_o = the distance from the boom neutral axis to the center of a chord, and

I_{xx} = the area moment of inertia of a chord about its centroidal axis.

Finally, the potential energy, V, in the boom model during elastic deformation is stored entirely in the rotational springs at joints 1 and 2 (see Fig. 4), and is expressed in matrix form in terms of the local angles of deflection, θ_1, and θ_2, at each joint by

$$V = \frac{1}{2} [\theta_1 \quad \theta_2] [K_\theta] \begin{bmatrix} \theta_1 \\ \theta_2 \end{bmatrix} \qquad (3.1.1\text{-}15)$$

Describing the local angles of deflection at each joint in terms of the system generalized coordinates, assuming small angular deflections, gives

$$\theta_1 = \frac{1}{L_B} (2q_1 - q_2) \qquad (3.1.1\text{-}16)$$

and

$$\theta_2 = \frac{1}{L_B} (2q_2 - q_1) \qquad (3.1.1\text{-}17)$$

The coupling terms in equation 3.1.1-15 may also be combined since the rotational stiffness matrix, K_θ, is symmetric by defining

$$K_B = \frac{3EI}{L_B} \tag{3.1.1-18}$$

where K_B is the elastic coefficient of each of the moment-resisting springs in the crane boom. Substituting equations 3.1.1-16, 3.1.1-17, and 3.1.1-18 into equation 3.1.1-15 and performing the necessary matrix algebra, the potential energy stored in the deformed crane boom becomes

$$V = \frac{3K_B}{L_B^2} [q_1^2 + q_2^2 - q_1 q_2] \tag{3.1.1-19}$$

The elastic deformation of the boom also produces virtual work due to the nonconservative forces of damping. An estimate of the critical damping in a pinned-pinned beam undergoing free transverse vibration can be obtained from equation 3.1.1-20

$$C_c = 2 J\omega_n \tag{3.1.1-20}$$

The effective mass moment of inertia, J, is determined by equating the kinetic energy in the vibrating beam and an equivalent second-order rotational system. The mass moment of inertia of the equivalent second-order system is

$$J = \frac{3}{8} m_B R_B^2 \tag{3.1.1-21}$$

The natural frequency of vibration, ω_n of the pinned-pinned beam, also of length, R_B, comes from Harris and Crede (18)

$$\omega_n = \frac{(K\pi)^2}{R_B^2} \sqrt{\frac{EIg}{\gamma A}} \qquad (3.1.1\text{-}22)$$

where:

K = the mode number,

EI = the bending stiffness,

g = the acceleration of gravity,

γ = the weight density, and

A = the cross-sectional area.

This estimate, of course, has the obvious limitation of being only a first-mode approximation of the damping. Combining equations 3.1.1-21 and 3.1.1-22, the damping coefficient, C_B, of each of the two viscous dashpots, assuming 0.7% critical damping in the crane boom becomes

$$C_B = \frac{1}{2}(.007)\, C_c = .007\,(K\pi)^2 \left[\frac{3}{8} R_B^2\right] \sqrt{\frac{EIm_B}{3R_B^3}} \qquad (3.1.1\text{-}23)$$

Recall that the virtual work is expressed as a product of the generalized forces corresponding to each variation and the variation of each generalized coordinate. These generalized forces for damping are proportional to the local angular velocities, $\dot{\theta}_1$, and $\dot{\theta}_2$. The virtual work of damping in the crane boom is then

$$\delta W = -C_B\dot{\theta}_1\delta\theta_1 - C_B\dot{\theta}_2\delta\theta_2 \qquad (3.1.1\text{-}24)$$

where the variations of the local angles of deflection in terms of the generalized coordinates are

$$\delta\theta_1 = \frac{1}{L_B}(2\,\delta q_1 - \delta q_2) \qquad (3.1.1\text{-}25)$$

and

$$\delta\theta_2 = \frac{1}{L_B}(2\,\delta q_2 - \delta q_1) \qquad (3.1.1\text{-}26)$$

Substituting equations 3.1.1-25 and 3.1.1-26, and the time derivatives of equations 3.1.1-16 and 3.1.1-17 into equation 3.1.1-24, the virtual work due to damping in the boom becomes

$$\delta W = \frac{C_B}{L_B^2}[4\dot{q}_2 - 5\dot{q}_1]\delta q_1 + \frac{C_B}{L_B^2}[4\dot{q}_1 - 5\dot{q}_2]\delta q_2 \qquad (3.1.1\text{-}27)$$

3.1.2 The Elastic Cables

The potential energy stored in the elastic cables, both the load line and the pendent line, during tensile deformation is developed in this section. The virtual work resulting from nonconservative damping forces has been neglected, since the contribution of this term to the total system energy is negligible (2). The assumptions governing the elastic cable model are as follows:

1. The cables are treated as massless, conservative springs.
2. The cables only apply force to the crane system when they are in tension.
3. Moments produced by friction in the pulleys at the boom tip are neglected.

In addition, elastic wire-rope cables are helically wound, and have demonstrated nonlinear spring-rates (19); however, the cable model adopted in this thesis uses a constant spring-rate.

The axial force developed in a wire rope can safely be described as a linear function of the stretch when the load is between 20% and 65% of the nominal breaking strength of the wire rope (2). The lumped parameter spring-rate, K_{WR}, is expressed as

$$K_R = \frac{A_{WR} E_{WR}}{L_{WR}} \qquad (3.1.2\text{-}1)$$

where:

A_{WR} = metallic cross-sectional area of the wire rope,

E_{WR} = wire-rope modulus of elasticity, and

L_{WR} = total unstretched length of the wire-rope.

The load line originates on the cable drum at the front of the crane cab and passes over the boom tip to the suspended load. The potential energy stored in the stretched load line due to elastic deformation is

$$V_{WRL} = \frac{1}{2} K_{WRL} (\Delta R_9)^2 \qquad (3.1.2\text{-}2)$$

where:

K_{WRL} = total load line spring-rate, and

ΔR_9 = the stretch of the load line, or

$\Delta R_9 = R_9(t) - R_9(t_o)$

where $R_9(t)$ is the instantaneous load line length, and $R_9(t_o)$ is the unstressed load line length.

The pendent lines support the boom tip, and on a crawler crane span the distance between the equalizing assembly and the tip of the

boom. The pendent line model is considered to span the distance from the uppermost point of the crane cab, called the gantry, to the boom tip, thus replacing the equalizing assembly with an equivalent length of pendent line. Figure 6 depicts the pendent line length described in terms of the system generalized coordinates, where L_p is the time-varying length of the pendent line and R_8 is the time-varying boom chord length. The potential energy stored in the stretched pendent line is given by

$$V_{WRP} = \frac{1}{2} K_{WRP} (\Delta L_p)^2 \qquad (3.1.2\text{-}3)$$

where:

K_{WRP} = equivalent pendent line spring-rate, and

$\Delta L_p = L_p(t) - L_p(t_o)$.

This concludes the development of the potential energy stored in the elastic cables; the virtual work produced by damping forces has been neglected.

3.1.3 The Elastic Foundation

The lumped-parameter ground model developed in this section characterizes the elastic and dissipative properties of the soil supporting the crawler crane. The ground model follows the translation and rotation of the crane car body and track system, and also allows the crane tracks to tilt off the soil surface. The potential energy and the virtual work of deformation are formulated for both crane translation and rotation in this section. Geometric constraints

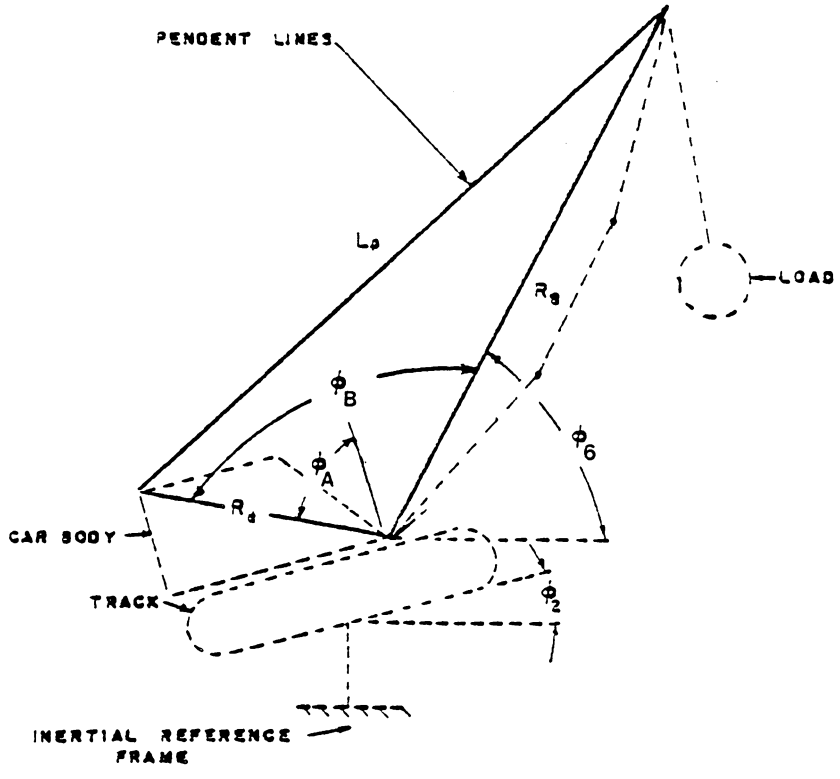

$$L_p = \sqrt{R_s^2 + R_d^2 - 2R_s R_d \cos(\phi_B)}$$

$$R_s = R_B - \frac{1}{L_B}\left| q_1^2 + q_2^2 - q_1 q_2 \right|$$

$$\phi_B = \phi_A + \frac{\pi}{2} - \left\{ \phi_6 - \phi_2 \right\}$$

FIG. 6 PENDENT GEOMETRY

characterizing the tilting condition are introduced to properly adjust the ground model response when a portion of the tracks leaves the soil surface.

Two basic methods have been used to simulate the dynamic properties of a soil foundation. The first, known as the Winkler elastic subgrade method, replaces the soil foundation with a set of independent springs. The second method employs elastic half-space theory to describe the soil properties. A lumped-parameter ground model utilizing elastic half-space theory is used in this thesis, since this model more accurately predicts the energy dissipating qualities of actual soil studies (20).

The ground model is idealized as an infinitely stiff massless plate on the soil, as shown in Fig. 7 (from Patten (2)), with a total surface area equal to that of the crane tracks. The static and dynamic loads applied by the crane act through the centroid of the ground model. An elastic spring, K_V, coupled in parallel with a viscous damper, C_V, characterize the translational properties of the soil foundation. Likewise, the elastic element, K_R, and the viscous damper, C_R, characterize the soil's resistance to crane rotation. The assumptions governing the development of the ground model are as follows:

1. The vertical translation and rotation of the ground model occur independently; and therefore, the horizontal motion induced by their coupling terms is neglected.
2. The soil surface may only be compressed.
3. Ground motion occurs symmetrically about the plane of

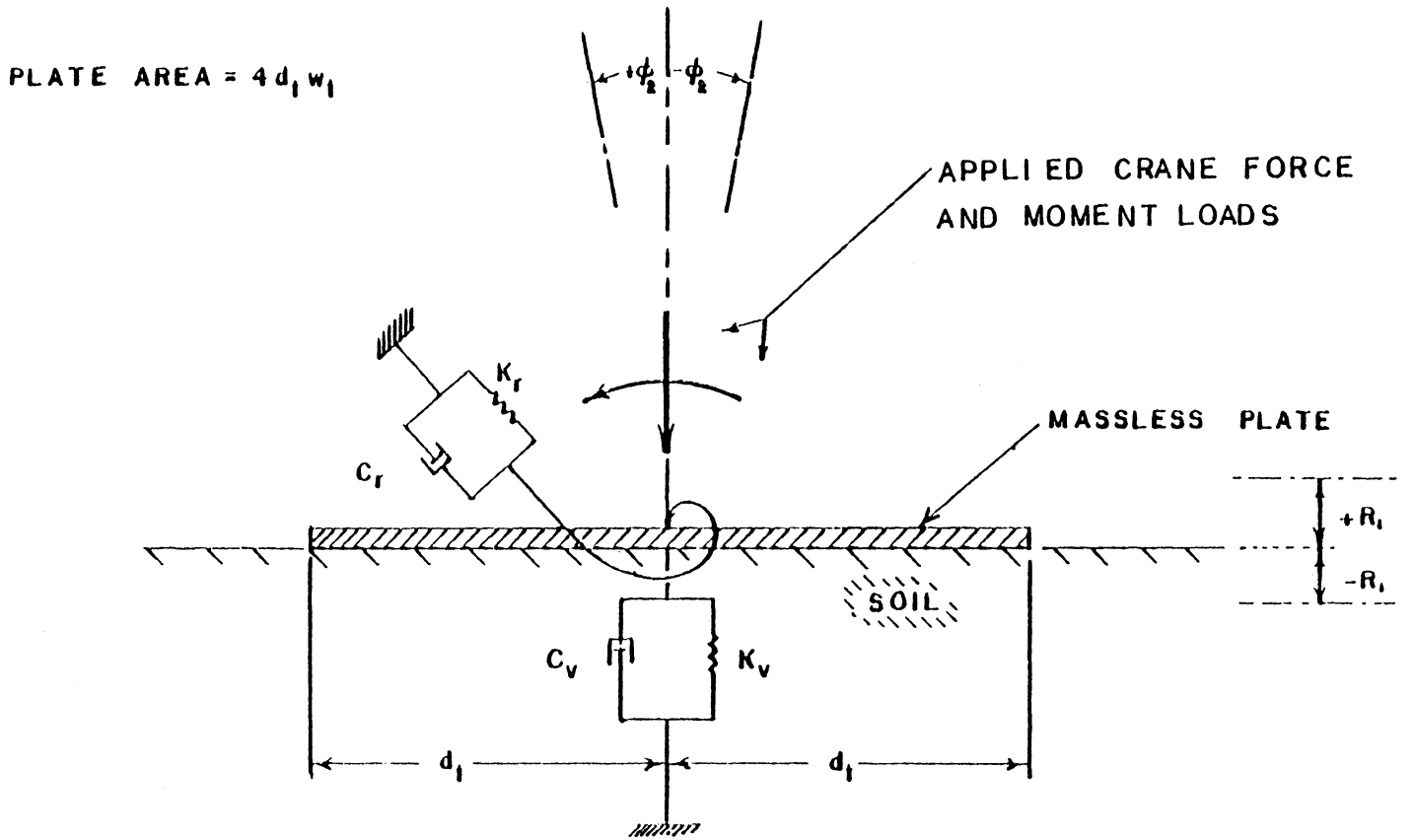

FIG. 7 LUMPED PARAMETER MODEL OF FOUNDATION SYSTEM (REF. 2)

rotation.

The potential energy stored in the soil foundation during a compressive translation is

$$V_v = \frac{1}{2} K_v R_1^2 \qquad (3.1.3\text{-}1)$$

where:

$$K_v = \frac{4 \cdot G \cdot R_{ev}}{1 - \nu} \quad \text{(Lysmer, 20)} \qquad (3.1.3\text{-}2)$$

and

G = shear modulus of soil,

ν = Poisson's ratio for the soil, and

R_{ev} = the equivalent radius for vertical translation.

Similarly, the potential energy stored in the soil foundation due to crane rotation is

$$V_r = \frac{1}{2} K_r \phi_2^2 \qquad (3.1.3\text{-}3)$$

where:

$$K_r = \frac{2.52 \cdot G \cdot (R_{e\phi})^3}{1 - \nu} \quad \text{(Parmelee, 21)} \qquad (3.1.3\text{-}4)$$

and

$R_{e\phi}$ = the equivalent radius for rotation.

During the dynamic simulation the crane is allowed to tilt up off the soil surface, pivoting on the tracks either in front of or to the rear of the ground model centroid. The tilting condition reduces the effective surface area of the crane tracks that contact

the supporting soil, and also produces an eccentric application of the restraining soil reactions. The ground model, incorporating the tilting condition used in this simulation is developed more fully by Patten (2). His analysis shows that the response of a crane is dramatically affected when the crane tracks partially leave the soil surface.

The geometric relations used to describe the tilting condition by Patten (2) are

$$\eta = |\phi_2| \tag{3.1.3-5}$$

$$f = \frac{R_1}{|\sin \phi_2|} \tag{3.1.3-6}$$

$$\beta = \frac{1}{2}\left(1 + \frac{1}{d_t}\right) \tag{3.1.3-7}$$

$$e = \frac{-1}{\eta} \cdot \phi_2 \cdot d_t \, (1 - \beta) \tag{3.1.3-8}$$

with the following limits

$$-1 \leq \frac{f}{d_t} \leq +1 \tag{3.1.3-9}$$

and

$$0 \leq \beta \leq 1 \tag{3.1.3-10}$$

The effective radius values in equations 3.1.3-2 and 3.1.3-4 come from Richart (20). These values modified with the tilting condition to reflect the reduced contact area become

$$R_{ev} = \left(\frac{4}{\pi} \cdot \beta \cdot d_t \cdot w_t \right)^{0.5} \qquad (3.1.3\text{-}10)$$

and

$$R_{e\phi} = \left(\frac{16}{3 \cdot \pi} \cdot (\beta \cdot d_t)^3 \cdot w_t \right)^{0.25} \qquad (3.1.3\text{-}11)$$

where:

d_t = the half-length of the crane tracks,

w_t = width of a single track, when the ratio, d_t/w_t lies within the range,

$$0.1 < \frac{d_t}{w_t} < 4.0 \qquad (3.1.3\text{-}12)$$

The vertical translation of the crane car body is also modified during tilting to reflect the eccentric application of the restraining soil reaction relative to the original ground model centroid. The modified vertical translation, y, and its velocity, $\dot{y}$, in terms of the generalized coordinates and the tilting parameters become

$$y = \frac{1}{2} \cdot \eta(d_t - f) + R_1 \qquad (3.1.3\text{-}13)$$

and

$$\dot{y} = \dot{R}_1 + e \cdot \dot{\phi}_2 \qquad (3.1.3\text{-}14)$$

The virtual work performed by the nonconservative forces of damping in the ground model is largely responsible for dissipating much of the energy away from the vibrating crane. The virtual work associated with vertical translation of the crane is expressed as

$$\delta W = -C_v \dot{R}_1 \delta R_1 \qquad (3.1.3\text{-}15)$$

where:

$$C_v = \frac{3.4 \cdot R_{ev}^2 (\rho G)^{0.5}}{1 - \nu} \quad \text{(Lysmer, 20)} \qquad (3.1.3\text{-}16)$$

and ρ is the specific weight of the soil. The virtual work performed by rotation of the crane is similarly

$$\delta W = -C_R \dot{\phi}_2 \delta \phi_2 \qquad (3.1.3\text{-}17)$$

where:

$$C_R = \frac{0.136 \cdot R_{e\phi}^4 (\rho G)^{0.5}}{1.13 - \nu} \quad \text{(Parmelee, 21)} \qquad (3.1.3\text{-}18)$$

This concludes the development of the potential energy and virtual work of deformation of the crane system.

3.2 The Kinetic Energy

The kinetic energy of the crawler crane system is the sum of the kinetic energy of the individual crane components. It represents the crane system's potential to perform work due to the motion of the component mass centers and the motion about the mass centers. The crane components which possess enough mass and motion to develop significant kinetic energy include: 1) the tracks, 2) the car body, 3) the suspended load, and 4) the crane boom. The soil foundation and elastic cables are treated as massless components in this

simulation, and therefore have no kinetic energy. The kinetic energy of each crane component is formulated separately, and is based on a vector description, in terms of the system generalized coordinates, of the motion of the component relative to the inertial reference frame.

A general expression for the kinetic energy of a rigid body is formulated by Langhaar (22). Let the vector, $\bar{R}_e$, expressed in terms of the system generalized coordinates $(p_1, p_2, \ldots, p_N)$, describe the position of the body's center of mass relative to an inertial reference. The position of an element in the body is described relative to the body's mass-center by vector, $\bar{R}_i$. Then the location of an element in the inertial reference frame is completely specified by the vector, $\bar{P}_i$, where

$$\bar{P}_i = \bar{R}_e + \bar{R}_i \tag{3.2-1}$$

The total time derivative of the position vector, $\bar{P}_i$, describes the velocity of the element, and is expressed as

$$\dot{\bar{P}}_i = \sum_{r=1}^{N} \frac{\delta \bar{R}_e}{\delta P_r} \dot{P}_r + \dot{\bar{R}}_i \tag{3.2-2}$$

The kinetic energy of each element in the homogeneous rigid body is

$$T_i = \frac{1}{2} \Delta m_i \, \dot{\bar{P}}_i \cdot \dot{\bar{P}}_i \tag{3.2-3}$$

where Δm_i is the differential mass of the element. The total kinetic energy of the rigid body becomes

$$T = \frac{1}{2} \int (\dot{\bar{P}} \cdot \dot{\bar{P}})\, dm \tag{3.2-4}$$

A vector description of the position of the crane components, in terms of the system generalized coordinates and body-fixed vectors, is given in Figs. 8 and 9 (from Patten (2)). The position vector of each crane component measured relative to the inertial reference follows:

a. Tracks:

$$\bar{P}_T = \bar{R}_{e_T} + \bar{R}_{i_T} = (\bar{R}_1 + \bar{R}_2) + R_{i_T} \tag{3.2-5}$$

b. Car Body:

$$\bar{P}_c = \bar{R}_{e_c} + \bar{R}_{i_c} = (\bar{R}_1 + \bar{R}_3 + \bar{R}_4) + R_{i_c} \tag{3.2-6}$$

c. Suspended Load:

$$\bar{P}_L = \bar{R}_{e_L} + \bar{R}_{i_L} = (\bar{R}_1 + \bar{R}_3 + \bar{R}_5 + \bar{R}_8 + \bar{R}_9) \tag{3.2-7}$$

The vector description of the i^{th} joint in the three-link boom is given in Fig. 9. The motion of a single boom link is described as the average motion of the end joints since the links are rigid. The vector description of each joint becomes

1. Joint 0:

$$\bar{P}_{i_0} = \bar{R}_1 + \bar{R}_3 + \bar{R}_5 \tag{3.2-8}$$

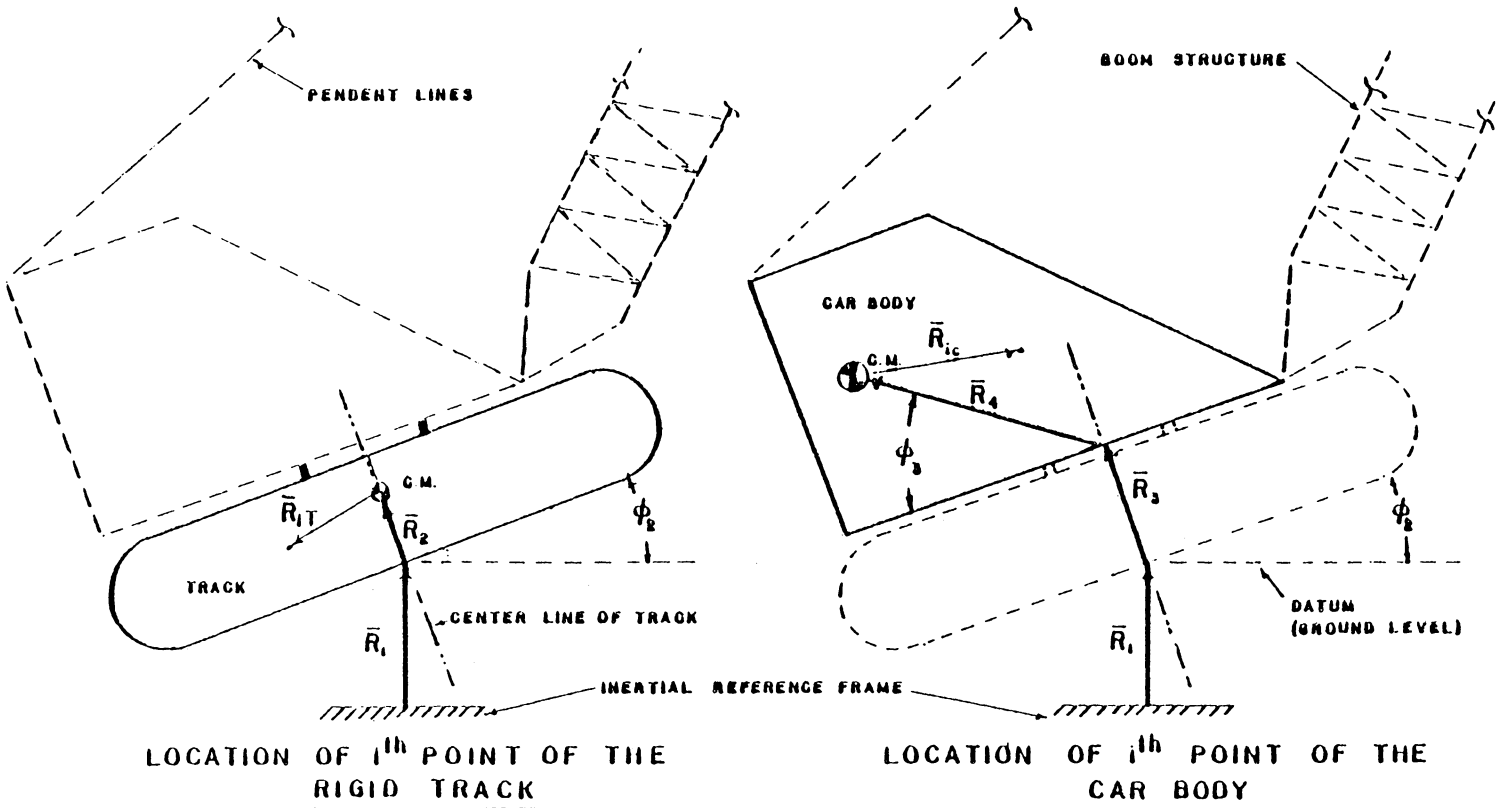

FIG. 8 POSITION COORDINATES OF AN ARBITRARY POINT IN THE RIGID TRACK SYSTEM AND THE RIGID CAR-BODY (REF. 2)

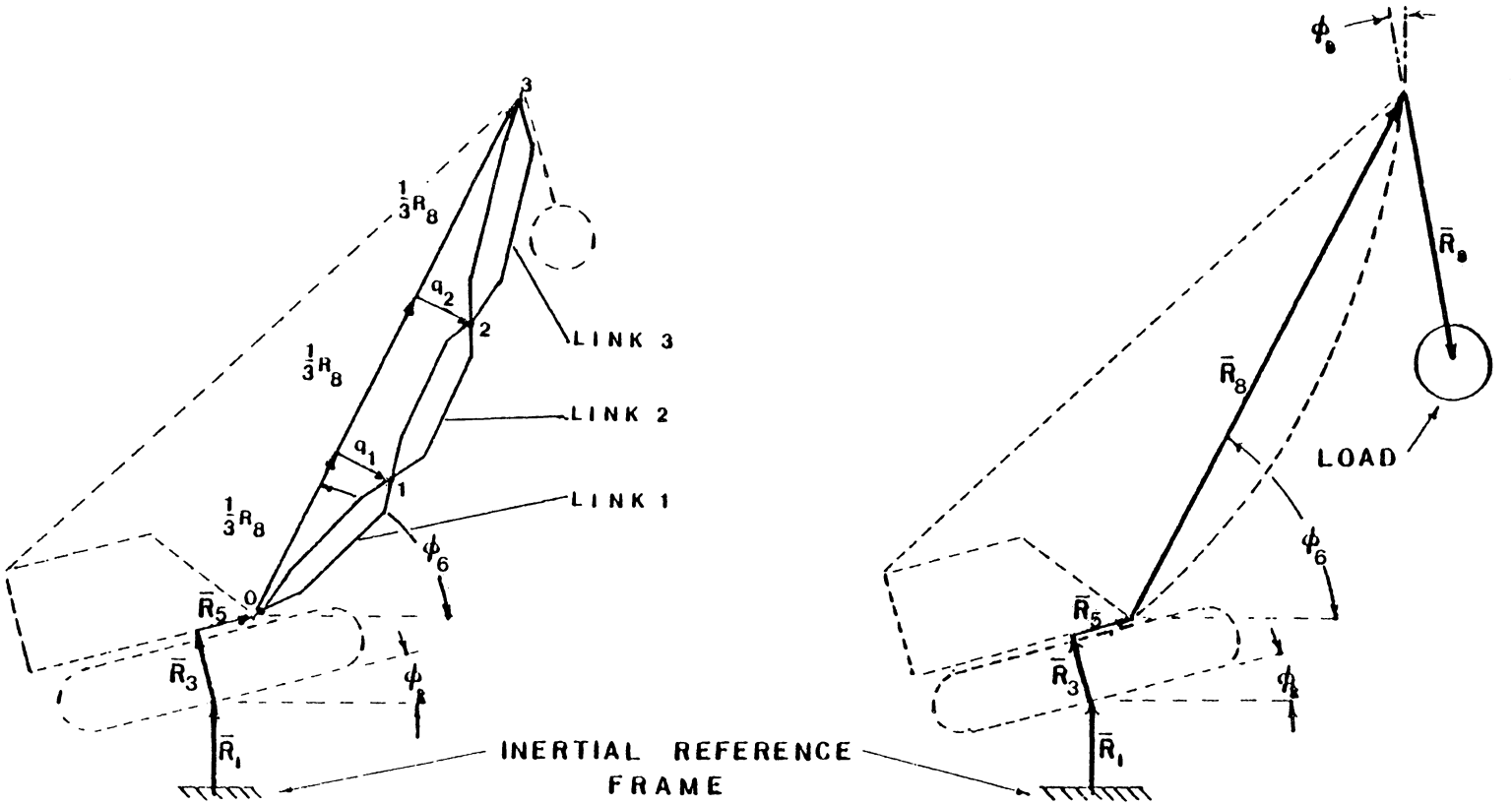

LOCATION OF I^{th} POINT OF BOOM NEUTRAL AXIS

LOCATION OF PENDULATING LOAD

FIG. 9 POSITION COORDINATES OF THE PENDULATING LOAD AND AN ARBITRARY POINT ON THE BOOM NEUTRAL AXIS (REF. 2)

2. Joint 1:

$$\bar{P}_{i_1} = \bar{R}_1 + \bar{R}_3 + \bar{R}_5 + \frac{1}{3}\bar{R}_8 + \bar{q}_1 \qquad (3.2\text{-}9)$$

3. Joint 2:

$$\bar{P}_{i_2} = \bar{R}_1 + \bar{R}_3 + \bar{R}_5 + \frac{2}{3}\bar{R}_8 + \bar{q}_2 \qquad (3.2\text{-}10)$$

4. Joint 3:

$$\bar{P}_{i_3} = \bar{R}_1 + \bar{R}_3 + \bar{R}_5 + \bar{R}_8 \qquad (3.2\text{-}11)$$

The position vector for each of the three links is

d. Boom Link 1:

$$\bar{P}_{B_1} = \frac{1}{2}(\bar{P}_{i_0} + \bar{P}_{i_1}) \qquad (3.2\text{-}12)$$

e. Boom Link 2:

$$\bar{P}_{B_2} = \frac{1}{2}(\bar{P}_{i_1} + \bar{P}_{i_2}) \qquad (3.2\text{-}13)$$

f. Boom Link 3:

$$\bar{P}_{B_3} = \frac{1}{2}(\bar{P}_{i_2} + \bar{P}_{i_3}) \qquad (3.2\text{-}14)$$

The kinetic energy of each crane component is formed by substituting the time derivative of the position vector (Eqs. 3.2-5 through 3.2-7 and Eqs. 3.2-12 through 3.2-14) into the general expression of the kinetic energy in equation 3.2-4. Performing the

indicated vector operations generates the scalar kinetic energy expressions for the crane components given in Figs. 10 and 11.

3.3 The Gravitational Potential Energy

The gravitational potential energy of the crawler crane is the portion of the total crane system energy which is derived from the conservative external forces acting on the system. In this development, the force of gravity is the only conservative external force. The gravitational potential energy of the crane components is, in general,

$$V_i = m_i \bar{g} \cdot \bar{P}_i - V_{o_i}$$

where V_{o_i} is the initial value of the component's gravitational potential energy. The initial value, of course, does not vary with time, and therefore, vanishes when the variations of the generalized coordinates are performed in Lagrange's equations.

Referring to the position vector descriptions of the crane components established in Chapter 3.2 the expressions for the gravitational potential energy of each component is given as follows:

a. Tracks:

$$V_T = m_T \bar{g} \cdot \bar{P}_T - V_{o_T} \tag{3.3-1}$$

b. Car Body:

$$V_c = m_c \bar{g} \cdot \bar{P}_c - V_{o_c} \tag{3.3-2}$$

$$T_T = \frac{1}{2} m_T \dot{R}_1^2 - m_T R_2 \sin\phi_2 \dot{R}_1 \dot{\phi}_2 + \frac{1}{2} m_T R_2^2 \dot{\phi}_2^2 + \frac{1}{2} I_T \dot{\phi}_2^2$$

$$T_c = \frac{1}{2} m_c \dot{R}_1^2 - m_c R_3 \sin\phi_2 \dot{R}_1 \dot{\phi}_2 - m_c R_4 \cos(\phi_2 - \phi_3) \dot{R}_1 \dot{\phi}_2$$

$$+ \frac{1}{2} m_c (R_3^2 + R_4^2) \dot{\phi}_2^2 + m_c R_3 R_4 \sin(\phi_3) \dot{\phi}_2^2 + \frac{1}{2} I_c \dot{\phi}_2^2$$

$$T_L = \frac{1}{2} m_L \dot{R}_1^2 + \frac{1}{2} m_L \dot{R}_8^2 + \frac{1}{2} m_L \dot{R}_9^2 + m_L \sin\phi_6 \dot{R}_1 \dot{R}_8 - m_L \cos\phi_9 \dot{R}_1 \dot{R}_9$$

$$- m_L \sin(\phi_6 - \phi_9) \dot{R}_8 \dot{R}_9 - m_L R_3 \sin\phi_2 \dot{R}_1 \dot{\phi}_2 + m_L R_5 \cos\phi_2 \dot{R}_1 \dot{\phi}_2$$

$$+ m_L R_8 \cos\phi_6 \dot{R}_1 \dot{\phi}_6 + m_L R_9 \sin\phi_9 \dot{R}_1 \dot{\phi}_9 - m_L R_3 \cos(\phi_6 - \phi_2) \dot{R}_8 \dot{\phi}_2$$

$$+ m_L R_5 \sin(\phi_6 - \phi_2) \dot{R}_8 \dot{\phi}_2 + m_L R_9 \cos(\phi_6 - \phi_9) \dot{R}_8 \dot{\phi}_9$$

$$+ m_L R_3 \sin(\phi_2 - \phi_9) \dot{R}_9 \dot{\phi}_2 - m_L R_5 \cos(\phi_2 - \phi_9) \dot{R}_9 \dot{\phi}_2$$

$$- m_L R_8 \cos(\phi_6 - \phi_9) \dot{R}_9 \dot{\phi}_6 + \frac{1}{2} m_L (R_3^2 + R_5^2) \dot{\phi}_2^2 + \frac{1}{2} m_L R_8^2 \dot{\phi}_6^2$$

$$+ \frac{1}{2} m_L R_9^2 \dot{\phi}_9^2 + m_L R_3 R_8 \sin(\phi_6 - \phi_2) \dot{\phi}_2 \dot{\phi}_6 - m_L R_3 R_9 \cos(\phi_2 - \phi_9) \dot{\phi}_2 \dot{\phi}_9$$

$$+ m_L R_5 R_8 \cos(\phi_6 - \phi_2) \dot{\phi}_2 \dot{\phi}_6 - m_L R_5 R_9 \sin(\phi_2 - \phi_9) \dot{\phi}_2 \dot{\phi}_9$$

$$- m_L R_8 R_9 \sin(\phi_6 - \phi_9) \dot{\phi}_6 \dot{\phi}_9$$

(Continued on FIG. 11)

FIG. 10 The System Kinetic Energy

$$
\begin{aligned}
T_B = {} & \frac{3}{2} m_B \dot{R}_1^2 + \frac{35}{72} m_B \dot{R}_8^2 + \frac{1}{4} m_B \dot{q}_1^2 + \frac{1}{4} m_B \dot{q}_2^2 + \frac{1}{4} m_B \dot{q}_1 \dot{q}_2 \\
& + \frac{3}{2} m_B \sin(\phi_6) \dot{R}_1 \dot{R}_8 - m_B \cos(\phi_6) \dot{R}_1 \dot{q}_1 - m_B \cos(\phi_6) \dot{R}_1 \dot{q}_2 \\
& - 3 m_B R_3 \sin(\phi_2) \dot{R}_1 \dot{\phi}_2 + 3 m_B R_5 \cos(\phi_2) \dot{R}_1 \dot{\phi}_2 + \frac{3}{2} m_B R_8 \cos(\phi_6) \dot{R}_1 \dot{\phi}_6 \\
& + m_B q_1 \sin(\phi_6) \dot{R}_1 \dot{\phi}_6 + m_B q_2 \sin(\phi_6) \dot{R}_1 \dot{\phi}_6 - \frac{3}{2} m_B R_3 \cos(\phi_6 - \phi_2) \dot{R}_8 \dot{\phi}_2 \\
& + \frac{3}{2} m_B R_5 \sin(\phi_6 - \phi_2) \dot{R}_8 \dot{\phi}_2 + m_B (\frac{1}{3} q_1 + \frac{2}{3} q_2) \dot{R}_8 \dot{\phi}_6 \\
& - m_B R_3 \sin(\phi_6 - \phi_2) \dot{q}_1 \dot{\phi}_2 - m_B R_5 \cos(\phi_6 - \phi 2) \dot{q}_1 \dot{\phi}_2 - m_B (\frac{1}{3} R_8) \dot{q}_1 \dot{\phi}_6 \\
& - m_B R_3 \sin(\phi_6 - \phi_2) \dot{q}_2 \dot{\phi}_2 - m_B R_5 \cos(\phi_6 - \phi_2) \dot{q}_2 \dot{\phi}_2 - m_B (\frac{2}{3} R_8) \dot{q}_2 \dot{\phi}_6 \\
& + m_B (\frac{3}{2} R_3^2 + \frac{3}{2} R_5^2) \dot{\phi}_2^2 + m_B (\frac{35}{72} R_8^2 + \frac{1}{4} q_1^2 + \frac{1}{4} q_1 q_2 + \frac{1}{4} q_2^2) \dot{\phi}_6^2 \\
& + \frac{3}{2} m_B R_3 R_8 \sin(\phi_6 - \phi_2) \dot{\phi}_2 \dot{\phi}_6 - m_B R_3 q_1 \cos(\phi_6 - \phi_2) \dot{\phi}_2 \dot{\phi}_6 \\
& - m_B R_3 q_2 \cos(\phi_6 - \phi_2) \dot{\phi}_2 \dot{\phi}_6 + \frac{3}{2} m_B R_5 R_8 \cos(\phi_6 - \phi_2) \dot{\phi}_2 \dot{\phi}_6 \\
& + m_B R_5 q_1 \sin(\phi_6 - \phi_2) \dot{\phi}_2 \dot{\phi}_6 + m_B R_5 q_2 \sin(\phi_6 - \phi_2) \dot{\phi}_2 \dot{\phi}_6
\end{aligned}
$$

FIG. 11 The System Kinetic Energy

c. Suspended Load:

$$V_L = m_L \bar{g} \cdot \bar{P}_L - V_{o_L} \tag{3.3-3}$$

d. Crane Boom:

$$V_B = m_B[(\bar{g} \cdot \bar{P}_{B_1} - V_{o_1}) + (\bar{g} \cdot \bar{P}_{B_2} - V_{o_2}) + (\bar{g} \cdot \bar{P}_{B_3} - V_{o_3})] \tag{3.3-4}$$

where V_{o_1}, V_{o_2}, and V_{o_3} refer to the initial value of the potential energy of links 1 through 3, respectively.

The scalar expressions for the gravitational potential energy of the crane components results when the vector dot products are performed in equations 3.3-1 through 3.3-4. These expressions appear in Fig. 12.

$$V_T = m_T g[R_1 + R_2\cos\phi_2]$$

$$V_c = m_c g[R_1 + R_3\cos\phi_2 - R_4\sin(\phi_2 - \phi_3)]$$

$$V_L = m_L g[R_1 + R_3\cos\phi_2 + R_5\sin\phi_2 + R_8\sin\phi_6 - R_9\cos\phi_9]$$

$$V_B = m_B g[3R_1 + 3R_3\cos\phi_2 + 3R_5\sin\phi_2 + R_6\sin\phi_6 + R_7\sin\phi_6 + \frac{1}{2} R_8\sin\phi_6 - q_1\cos\phi_6 - q_2\cos\phi_6]$$

FIG. 12 The Gravitational Potential Energy

4. EQUATIONS OF MOTION AND NUMERICAL METHODS

The equations of motion for the crawler crane, formed by applying Lagrange's equation to the crane system energy developed in Chapter 3, are presented for each generalized coordinate in this chapter. This system of nonlinear differential equations is numerically integrated to simulate the response of the crane system to various conditions. The numerical techniques employed to generate the dynamic response of the crane from the system differential equations of motion are also discussed in this chapter.

The Lagrange equations of motion for the crane system resulting from Hamilton's extended principle are of the form

$$\frac{\partial}{\partial t}\left(\frac{\partial T}{\partial \dot{q}_i}\right) - \frac{\partial T}{\partial q_i} + \frac{\partial V}{\partial q_i} - Q_i = 0 \qquad (4\text{-}1)$$

The partial differentiation required to form the Lagrange equations for the crane is possible since the crane system's kinetic energy, potential energy and virtual work were expressed in terms of the system generalized coordinates in Chapter 3. The Lagrange equations of motion for each generalized coordinate of the crane appear in Figs. 13 through 24.

The crane system equations of motion, although nonlinear, coupled, differential equations, are more conveniently solved when written in the familiar matrix form for dynamical systems as

$$[M(p_i,t)]_{NxN}[\ddot{p}_i]_{Nx1} = [F(\dot{p}_i,p_i,t)]_{Nx1} \qquad (4\text{-}2)$$

where [M] is the time-varying mass matrix, $[\ddot{p}_i]$ is the acceleration vector containing the second time derivatives of the system generalized

$$\frac{\partial}{\partial t}\left(\frac{\partial T}{\partial \dot{R}_1}\right) - \frac{\partial T}{\partial R_1} + \frac{\partial V}{\partial R_1} - Q_{R_1} = 0$$

$$+ [m_T + m_c + m_L + 3m_B]\ddot{R}_1 + [m_L\sin(\phi_6) + \frac{3}{2} m_B\sin(\phi_6)]\ddot{R}_8$$

$$- m_L\cos(\phi_9)\ddot{R}_9 - m_B\cos(\phi_6)\ddot{q}_1 - m_B\cos(\phi_6)\ddot{q}_2 + [-m_T R_2\sin(\phi_2)]\ddot{\phi}_2$$

$$+ [-m_c R_3\sin(\phi_2) - m_c R_4\cos(\phi_2 - \phi_3) - m_L R_3\sin(\phi_2) + m_L R_5\cos(\phi_2)]\ddot{\phi}_2$$

$$+ [-3m_B R_3\sin(\phi_2) + 3m_B R_5\cos(\phi_2)]\ddot{\phi}_2 + [m_L R_8\cos(\phi_6)]\ddot{\phi}_6$$

$$+ [\frac{3}{2} m_B R_8\cos(\phi_6) + m_B q_1\sin(\phi_6) + m_B q_2\sin(\phi_6)]\ddot{\phi}_6$$

$$+ m_L R_9\sin(\phi_9)\ddot{\phi}_9 + [-m_T R_2\cos(\phi_2) - m_c R_3\cos(\phi_2) + m_c R_4\sin(\phi_2 - \phi_3)]\dot{\phi}_2^2$$

$$+ [-m_L R_3\cos(\phi_2) - m_L R_5\sin(\phi_2) + 3m_B R_3\cos(\phi_2) - 3m_B R_5\sin(\phi_2)]\dot{\phi}_2^2$$

$$+ [-m_L R_8\sin(\phi_6) - \frac{3}{2} m_B R_8\sin(\phi_6) + m_B q_1\cos(\phi_6) + m_B q_2\cos(\phi_6)]\dot{\phi}_6^2$$

$$+ m_L R_9\cos(\phi_9)\dot{\phi}_9^2 + 3m_B\cos(\phi_6)\dot{R}_8\dot{\phi}_6 + 2m_L\sin(\phi_9)\dot{R}_9\dot{\phi}_9$$

$$+ 2m_B\sin(\phi_6)\dot{q}_1\dot{\phi}_6 + 2m_B\sin(\phi_6)\dot{q}_2\dot{\phi}_6 + m_L\cos(\phi_6)\dot{R}_8\dot{\phi}_6$$

$$+ g[m_T + m_c + m_L + 3m_B] + K_v R_1 + C_v\dot{R}_1$$

FIG. 13 Equation of Motion for Coordinate R_1

$$\frac{\partial}{\partial t}\left(\frac{\partial T}{\partial \dot{R}_9}\right) - \frac{\partial T}{\partial R_9} + \frac{\partial V}{\partial R_9} - Q_{R_9} = 0$$

$$+ [-m_L\cos(\phi_9)]\ddot{R}_1 + [-m_L\sin(\phi_6 - \phi_9)]\ddot{R}_8 + m_L\ddot{R}_9$$

$$+ [m_L R_3\sin(\phi_2 - \phi_9) - m_L R_5\cos(\phi_2 - \phi_9)]\ddot{\phi}_2$$

$$+ [-m_L R_8\cos(\phi_6 - \phi_9)]\ddot{\phi}_6 + [m_L R_3\cos(\phi_2 - \phi_9)]\dot{\phi}_2^2$$

$$+ [m_L R_5\sin(\phi_2 - \phi_9)]\dot{\phi}_2^2 + [m_L R_8\sin(\phi_6 - \phi_9)]\dot{\phi}_6^2 - m_L R_9\dot{\phi}_9^2$$

$$+ [-2m_L\cos(\phi_6 - \phi_9)]\dot{R}_8\dot{\phi}_6$$

$$- g[m_L\cos(\phi_9)] + K_{wrL}(\Delta R_9)$$

FIG. 14 Equation of Motion for Coordinate R_9

$$\frac{\partial}{\partial t}\left(\frac{\partial T}{\partial \dot{q}_1}\right) - \frac{\partial T}{\partial q_1} + \frac{\partial V}{\partial q_1} - Q_{q_1} = 0$$

$$+ \left[-\frac{2}{L_B} m_L q_1 \sin(\phi_6) + \frac{1}{L_B} m_L q_2 \sin(\phi_6) + \frac{3}{2}\frac{1}{L_B} m_B q_2 \sin(\phi_6)\right]\ddot{R}_1$$

$$+ \left[-\frac{3}{L_B} m_B q_1 \sin(\phi_6) - m_B \cos(\phi_6)\right]\ddot{R}_1 + \left[-\frac{2}{L_B} m_L q_1 + \frac{1}{L_B} m_L q_2\right]\ddot{R}_8$$

$$+ \left[-\frac{35}{18}\frac{1}{L_B} m_B q_1 + \frac{35}{36}\frac{1}{L_B} m_B q_2\right]\ddot{R}_8 + \left[\frac{2}{L_B} m_L q_1 \sin(\phi_6 - \phi_9)\right]\ddot{R}_9$$

$$+ \left[-\frac{1}{L_B} m_L q_2 \sin(\phi_6 - \phi_9)\right]\ddot{R}_9 + \frac{1}{2} m_B \ddot{q}_1 + \frac{1}{4} m_B \ddot{q}_2$$

$$+ \left[\frac{2}{L_B} m_L R_3 q_1 \cos(\phi_6 - \phi_2) - \frac{1}{L_B} m_L R_3 q_2 \cos(\phi_6 - \phi_2)\right.$$

$$\left. - \frac{2}{L_B} m_L R_5 q_1 \sin(\phi_6 - \phi_2)\right]\ddot{\phi}_2 + \left[\frac{1}{L_B} m_L R_5 q_2 \sin(\phi_6 - \phi_2)\right.$$

$$\left. + \frac{3}{L_B} m_B R_3 q_1 \cos(\phi_6 - \phi_2) - \frac{3}{2}\frac{1}{L_B} m_B R_3 q_2 \cos(\phi_6 - \phi_2)\right]\ddot{\phi}_2$$

$$+ \left[-\frac{3}{L_B} m_B R_5 q_1 \sin(\phi_6 - \phi_2) + \frac{3}{2}\frac{1}{L_B} m_B R_5 q_2 \sin(\phi_6 - \phi_2)\right.$$

$$\left. - m_B R_3 \sin(\phi_6 - \phi_2)\right]\ddot{\phi}_2 + \left[-m_B R_5 \cos(\phi_6 - \phi_2)\right]\ddot{\phi}_2$$

$$+ \left[-\frac{1}{L_B} m_B q_1 q_2 - \frac{2}{3}\frac{1}{L_B} m_B q_1^2 + \frac{2}{3}\frac{1}{L_B} m_B q_2^2 - \frac{1}{3} m_B R_8\right]\ddot{\phi}_6$$

$$+ \left[-\frac{2}{L_B} m_L R_9 q_1 \cos(\phi_6 - \phi_9) + \frac{1}{L_B} m_L R_9 q_2 \cos(\phi_6 - \phi_9)\right]\ddot{\phi}_9$$

$$+ \left[\frac{2}{L_B} m_L R_3 q_1 \sin(\phi_6 - \phi_2) - \frac{1}{L_B} m_L R_3 q_2 \sin(\phi_6 - \phi_2)\right.$$

(Continued on FIG. 16)

FIG. 15 Equation of Motion for Coordinate q_1

$$+ \frac{2}{L_B} m_L R_5 q_1 \cos(\phi_6 - \phi_2)]\dot{\phi}_2^2 + [- \frac{1}{L_B} m_L R_5 q_2 \cos(\phi_6 - \phi_2)$$

$$+ \frac{3}{L_B} m_B R_3 q_1 \sin(\phi_6 - \phi_2) - \frac{3}{2} \frac{1}{L_B} m_B R_3 q_2 \sin(\phi_6 - \phi_2)]\dot{\phi}_2^2$$

$$+ [\frac{3}{L_B} m_B R_5 q_1 \cos(\phi_6 - \phi_2) - \frac{3}{2} \frac{1}{L_B} m_B R_5 q_2 \cos(\phi_6 - \phi_2)$$

$$+ m_B R_3 \cos(\phi_6 - \phi_2)]\dot{\phi}_2^2 + [-m_B R_5 \sin(\phi_6 - \phi_2)]\dot{\phi}_2^2$$

$$+ [\frac{2}{L_B} m_L R_8 q_1 - \frac{1}{L_B} m_L R_8 q_2]\dot{\phi}_6^2 + [\frac{35}{18} \frac{1}{L_B} m_B R_8 q_1 - \frac{35}{36} \frac{1}{L_B} m_B R_8 q_2$$

$$- \frac{1}{2} m_B q_1 - \frac{1}{4} m_B q_2]\dot{\phi}_6^2 + [- \frac{2}{L_B} m_L R_9 q_1 \sin(\phi_6 - \phi_9)$$

$$+ \frac{1}{L_B} m_L R_9 q_2 \sin(\phi_6 - \phi_9)]\dot{\phi}_9^2 - \frac{2}{3} m_B \dot{R}_8 \dot{\phi}_6 + [- \frac{4}{L_B} m_L q_1 \cos(\phi_6 - \phi_9)$$

$$+ \frac{2}{L_B} m_L q_2 \cos(\phi_6 - \phi_9)]\dot{R}_9 \dot{\phi}_9 + [- \frac{8}{3} \frac{1}{L_B} m_B q_1 + \frac{2}{3} \frac{1}{L_B} m_B q_2]\dot{q}_1 \dot{\phi}_6$$

$$+ [- \frac{8}{3} \frac{1}{L_B} m_B q_1 + \frac{4}{3} \frac{1}{L_B} m_B q_2]\dot{q}_2 \dot{\phi}_6$$

$$- g[m_B \cos(\phi_6) + \frac{3}{L_B} m_B q_1 \sin(\phi_6) + \frac{2}{L_B} m_L q_1 \sin(\phi_6)]$$

$$+ g[\frac{3}{2} \frac{1}{L_B} m_B q_2 \sin(\phi_6) + \frac{1}{L_B} m_L q_2 \sin(\phi_6)] + \frac{6}{L_B^2} K_B q_1 - \frac{3}{L_B^2} K_B q_2$$

$$+ K_{\omega rp} \frac{(\Delta L_p)}{L_p} [R_8 - R_d \cos\phi_B][\frac{1}{L_B} (q_2 - 2q_1)]$$

$$+ \frac{5}{L_B^2} C_B \dot{q}_1 - \frac{4}{L_B^2} C_B \dot{q}_2$$

FIG. 16 Equation of Motion for Coordinate q_1

$$\frac{\partial}{\partial t}\left(\frac{\partial T}{\partial \dot{q}_2}\right) - \frac{\partial T}{\partial q_2} + \frac{\partial V}{\partial q_2} - Q_{q_2} = 0$$

$$+ \left[\frac{1}{L_B} m_L q_1 \sin(\phi_6) - \frac{2}{L_B} m_L q_2 \sin(\phi_6) + \frac{3}{2}\frac{1}{L_B} m_B q_1 \sin(\phi_6)\right]\ddot{R}_1$$

$$+ \left[-\frac{3}{L_B} m_B q_2 \sin(\phi_6) - m_B \cos(\phi_6)\right]\ddot{R}_1 + \left[\frac{1}{L_B} m_L q_1 - \frac{2}{L_B} m_L q_2\right]\ddot{R}_8$$

$$+ \left[\frac{35}{36}\frac{1}{L_B} m_B q_1 - \frac{35}{18}\frac{1}{L_B} m_B q_2\right]\ddot{R}_8 + \left[-\frac{1}{L_B} m_L q_1 \sin(\phi_6 - \phi_9)\right]\ddot{R}_9$$

$$+ \left[\frac{2}{L_B} m_L q_2 \sin(\phi_6 - \phi_9)\right]\ddot{R}_9 + \frac{1}{4} m_B \ddot{q}_1 + \frac{1}{2} m_B \ddot{q}_2$$

$$+ \left[-\frac{1}{L_B} m_L R_3 q_1 \cos(\phi_6 - \phi_2) + \frac{2}{L_B} m_L R_3 q_2 \cos(\phi_6 - \phi_2)\right.$$

$$\left. + \frac{1}{L_B} m_L R_5 q_1 \sin(\phi_6 - \phi_2)\right]\ddot{\phi}_2 + \left[-\frac{2}{L_B} m_L R_5 q_2 \sin(\phi_6 - \phi_2)\right.$$

$$\left. - \frac{3}{2}\frac{1}{L_B} m_B R_3 q_1 \cos(\phi_6 - \phi_2) + \frac{3}{L_B} m_B R_3 q_2 \cos(\phi_6 - \phi_2)\right]\ddot{\phi}_2$$

$$+ \left[\frac{3}{2}\frac{1}{L_B} m_B R_5 q_1 \sin(\phi_6 - \phi_2) - \frac{3}{L_B} m_B R_5 q_2 \sin(\phi_6 - \phi_2) - m_B R_3 \sin(\phi_6 - \phi_2)\right]\ddot{\phi}_2$$

$$+ \left[-m_B R_5 \cos(\phi_6 - \phi_2)\right]\ddot{\phi}_2 + \left[\frac{1}{3}\frac{1}{L_B} m_B q_1^2 - \frac{4}{3}\frac{1}{L_B} m_B q_2^2 - \frac{2}{3} m_B R_8\right]\ddot{\phi}_6$$

$$+ \left[\frac{1}{L_B} m_L R_9 q_1 \cos(\phi_6 - \phi_9) - \frac{2}{L_B} m_L R_9 q_2 \cos(\phi_6 - \phi_9)\right]\ddot{\phi}_9$$

$$+ \left[-\frac{1}{L_B} m_L R_3 q_1 \sin(\phi_6 - \phi_2) + \frac{2}{L_B} m_L R_3 q_2 \sin(\phi_6 - \phi_2)\right.$$

$$\left. - \frac{1}{L_B} m_L R_5 q_1 \cos(\phi_6 - \phi_2)\right]\dot{\phi}_2^2 + \left[\frac{2}{L_B} m_L R_5 q_2 \cos(\phi_6 - \phi_2)\right.$$

(Continued on FIG. 18)

FIG. 17 Equation of Motion for Coordinate q_2

$$- \frac{3}{2}\frac{1}{L_B} m_B R_3 q_1 \sin(\phi_6 - \phi_2) + \frac{3}{L_B} m_B R_3 q_2 \sin(\phi_6 - \phi_2)]\dot{\phi}_2^2$$

$$+ [- \frac{3}{2}\frac{1}{L_B} m_B R_5 q_1 \cos(\phi_6 - \phi_2) + \frac{3}{L_B} m_B R_5 q_2 \cos(\phi_6 - \phi_2)$$

$$+ m_B R_3 \cos(\phi_6 - \phi_2)]\dot{\phi}_2^2 + [-m_B R_5 \sin(\phi_6 - \phi_2)]\dot{\phi}_2^2 + [- \frac{1}{L_B} m_L R_8 q_1$$

$$+ \frac{2}{L_B} m_L R_8 q_2]\dot{\phi}_6^2 + [- \frac{35}{36}\frac{1}{L_B} m_B R_8 q_1 + \frac{35}{18}\frac{1}{L_B} m_B R_8 q_2 - \frac{1}{4} m_B q_1 - \frac{1}{2} m_B q_2]\dot{\phi}_6^2$$

$$+ [\frac{1}{L_B} m_L R_9 q_1 \sin(\phi_6 - \phi_9) - \frac{2}{L_B} m_L R_9 q_2 \sin(\phi_6 - \phi_9)]\dot{\phi}_9^2 - \frac{2}{3} m_B \dot{R}_8 \dot{\phi}_6$$

$$+ [\frac{2}{L_B} m_L q_1 \cos(\phi_6 - \phi_9) - \frac{4}{L_B} m_L q_2 \cos(\phi_6 - \phi_9)]\dot{R}_9 \dot{\phi}_9 + [\frac{2}{3}\frac{1}{L_B} m_B q_1$$

$$- \frac{4}{3}\frac{1}{L_B} m_B q_2]\dot{q}_1 \dot{\phi}_6 + [\frac{4}{3}\frac{1}{L_B} m_B q_1 - \frac{8}{3}\frac{1}{L_B} m_B q_2]\dot{q}_2 \dot{\phi}_6$$

$$- g[m_B \cos(\phi_6) + \frac{3}{L_B} m_B q_2 \sin(\phi_6) + \frac{2}{L_B} m_L q_2 \sin(\phi_6)]$$

$$+ g[\frac{3}{2}\frac{1}{L_B} m_B q_1 \sin(\phi_6) + \frac{1}{L_B} m_L q_1 \sin(\phi_6)] + \frac{6}{L_B^2} K_B q_2 - \frac{3}{L_B^2} K_B q_1$$

$$+ K_{wrp} \frac{(\Delta L_p)}{L_p} [R_8 - R_d \cos\phi_B][\frac{1}{L_B}(q_1 - 2q_2)]$$

$$+ \frac{5}{L_B^2} C_B \dot{q}_2 - \frac{4}{L_B^2} C_B \dot{q}_1$$

FIG. 18 Equation of Motion for Coordinate q_2

$$\frac{\partial}{\partial t}\left(\frac{\partial T}{\partial \dot{\phi}_2}\right) - \frac{\partial T}{\partial \phi_2} + \frac{\partial V}{\partial \phi_2} - Q_{\phi_2} = 0$$

$$+ [-m_T R_2 \sin(\phi_2) - m_c R_3 \sin(\phi_2) - m_c R_4 \cos(\phi_2 - \phi_3) - m_L R_3 \sin(\phi_2)]\ddot{R}_1$$

$$+ [m_L R_5 \cos(\phi_2) - 3m_B R_3 \sin(\phi_2) + 3m_B R_5 \cos(\phi_2)]\ddot{R}_1$$

$$+ [-m_L R_3 \cos(\phi_6 - \phi_2) + m_L R_5 \sin(\phi_6 - \phi_2) - \tfrac{3}{2} m_B R_3 \cos(\phi_6 - \phi_2)]\ddot{R}_8$$

$$+ [\tfrac{3}{2} m_B R_5 \sin(\phi_6 - \phi_2)]\ddot{R}_8 + [m_L R_3 \sin(\phi_2 - \phi_9) - m_L R_5 \cos(\phi_2 - \phi_9)]\ddot{R}_9$$

$$+ [-m_B R_3 \sin(\phi_6 - \phi_2) - m_B R_5 \cos(\phi_6 - \phi_2)]\ddot{q}_1 + [-m_B R_3 \sin(\phi_6 - \phi_2)]\ddot{q}_2$$

$$+ [-m_B R_5 \cos(\phi_6 - \phi_2)]\ddot{q}_2 + [m_T R_2^2 + I_T + m_c(R_3^2 + R_4^2)]\ddot{\phi}_2$$

$$+ [2m_c R_3 R_6 \sin(\phi_3) + I_c + m_L(R_3^2 + R_5^2) + m_B(3R_3^2 + 3R_5^2)]\ddot{\phi}_2$$

$$+ [m_L R_3 R_8 \sin(\phi_6 - \phi_2) + m_L R_5 R_8 \cos(\phi_6 - \phi_2) + \tfrac{3}{2} m_B R_3 R_8 \sin(\phi_6 - \phi_2)]\ddot{\phi}_6$$

$$+ [-m_B R_3 q_1 \cos(\phi_6 - \phi_2) - m_B R_3 q_2 \cos(\phi_6 - \phi_2) + \tfrac{3}{2} m_B R_5 R_8 \cos(\phi_6 - \phi_2)]\ddot{\phi}_6$$

$$+ [m_B R_5 q_1 \sin(\phi_6 - \phi_2) + m_B R_5 q_2 \sin(\phi_6 - \phi_2)]\ddot{\phi}_6$$

$$+ [-m_L R_3 R_9 \cos(\phi_2 - \phi_9) - m_L R_s R_9 \sin(\phi_2 - \phi_9)]\ddot{\phi}_9$$

$$+ [m_L R_3 R_8 \cos(\phi_6 - \phi_2) - m_L R_5 R_8 \sin(\phi_6 - \phi_2) + \tfrac{3}{2} m_B R_3 R_8 \cos(\phi_6 - \phi_2)]\dot{\phi}_6^2$$

(Continued on FIG. 20)

FIG. 19 Equation of Motion for Coordinate ϕ_2

$$+ [m_B R_3 q_1 \sin(\phi_6 - \phi_2) + m_B R_3 q_2 \sin(\phi_6 - \phi_2) - \frac{3}{2} m_B R_5 R_8 \sin(\phi_6 - \phi_2)]\dot{\phi}_6^2$$

$$+ [m_B R_5 q_1 \cos(\phi_6 - \phi_2) + m_B R_5 q_2 \cos(\phi_6 - \phi_2)]\dot{\phi}_6^2$$

$$+ [-m_L R_3 R_9 \sin(\phi_2 - \phi_9) + m_L R_5 R_9 \cos(\phi_2 - \phi_9)]\dot{\phi}_9^2$$

$$+ [2m_L R_3 \sin(\phi_6 - \phi_2) + 2m_L R_5 \cos(\phi_6 - \phi_2) + 3m_B R_3 \sin(\phi_6 - \phi_2)]\dot{R}_8\dot{\phi}_6$$

$$+ [3m_B R_5 \cos(\phi_6 - \phi_2)]\dot{R}_8\dot{\phi}_6 + [-2m_B R_3 \cos(\phi_6 - \phi_2) + 2m_B R_5 \sin(\phi_6 - \phi_2)]\dot{q}_1\dot{\phi}_6$$

$$+ [-2m_B R_3 \cos(\phi_6 - \phi_2) + 2m_B R_5 \sin(\phi_6 - \phi_2)]\dot{q}_2\dot{\phi}_6$$

$$+ [-2m_L R_3 \cos(\phi_2 - \phi_9) - 2m_L R_5 \sin(\phi_2 - \phi_9)\dot{R}_9\dot{\phi}_9$$

$$+ g[m_L R_5 \cos(\phi_2) + 3m_B R_5 \cos(\phi_2)] - g[3m_B R_3 \sin(\phi_2)]$$

$$- g[m_T R_2 \sin(\phi_2) + m_c R_3 \sin(\phi_2) + m_c R_4 \cos(\phi_2 - \phi_3) + m_c R_3 \sin(\phi_2)]$$

$$+ K_{wrp}(\Delta L_p)[\frac{1}{L_p} R_8 R_4 \sin\phi_B] + K_r\phi_2 + C_r\dot{\phi}_2$$

FIG. 20 Equation of Motion for Coordinate ϕ_2

$$\frac{\partial}{\partial t}\left(\frac{\partial T}{\partial \dot{\phi}_6}\right) - \frac{\partial T}{\partial \phi_6} + \frac{\partial V}{\partial \phi_6} - Q_{\phi_6} = 0$$

$$+ [m_L R_8 \cos(\phi_6) + \tfrac{3}{2} m_B R_8 \cos(\phi_6) + m_B q_1 \sin(\phi_6) + m_B q_2 \sin(\phi_6)]\ddot{R}_1$$

$$+ [\tfrac{1}{3} m_B q_1 + \tfrac{2}{3} m_B q_2] R_8 + [-m_L R_8 \cos(\phi_6 - \phi_9)]\ddot{R}_9$$

$$+ [-\tfrac{1}{3} m_B R_8]\ddot{q}_1 + [-\tfrac{2}{3} m_B R_8]\ddot{q}_2 + [m_L R_3 R_8 \sin(\phi_6 - \phi_2)]\ddot{\phi}_2$$

$$+ [m_L R_5 R_8 \cos(\phi_6 - \phi_2) + \tfrac{3}{2} m_B R_3 R_8 \sin(\phi_6 - \phi_2) - m_B R_3 q_1 \cos(\phi_6 - \phi_2)]\ddot{\phi}_2$$

$$+ [-m_B R_3 q_2 \cos(\phi_6 - \phi_2) + \tfrac{3}{2} m_B R_5 R_8 \cos(\phi_6 - \phi_2) + m_B R_5 q_1 \sin(\phi_6 - \phi_2)]\ddot{\phi}_2$$

$$+ [m_B R_5 q_2 \sin(\phi_6 - \phi_2)]\ddot{\phi}_2 + [m_L R_8^2 + \tfrac{35}{36} m_B R_8^2 + \tfrac{1}{2} m_B q_1^2 + \tfrac{1}{2} m_B q_1 q_2$$

$$+ \tfrac{1}{2} m_B q_2^2]\ddot{\phi}_6 + [-m_L R_8 R_9 \sin(\phi_6 - \phi_9)]\ddot{\phi}_9 + [-m_L R_3 R_8 \cos(\phi_6 - \phi_2)$$

$$+ m_L R_5 R_8 \sin(\phi_6 - \phi_2)]\dot{\phi}_2^2 + [-\tfrac{3}{2} m_B R_3 R_8 \cos(\phi_6 - \phi_2) - m_B R_3 q_1 \sin(\phi_6 - \phi_2)$$

$$- m_B R_3 q_2 \sin(\phi_6 - \phi_2)]\dot{\phi}_2^2 + [\tfrac{3}{2} m_B R_5 R_8 \sin(\phi_6 - \phi_2) - m_B R_5 q_1 \cos(\phi_6 - \phi_2)$$

$$-m_B R_5 q_2 \cos(\phi_6 - \phi_2)]\dot{\phi}_2^2 + [m_L R_8 R_9 \cos(\phi_6 - \phi_9)]\dot{\phi}_9^2$$

$$+ [2m_L R_8 + \tfrac{35}{18} m_B R_8]\dot{R}_8\dot{\phi}_6 + [-2m_L R_8 \sin(\phi_6 - \phi_9)]\dot{R}_9\dot{\phi}_9$$

$$+ [m_B q_1 + \tfrac{1}{2} m_B q_2]\dot{q}_1\dot{\phi}_6 + [\tfrac{1}{2} m_B q_1 + m_B q_2]\dot{q}_2\dot{\phi}_6$$

(Continued on FIG. 22)

FIG. 21 Equation of Motion for Coordinate ϕ_6

$$+ g[m_L R_8 \cos(\phi_6) + \frac{3}{2} m_B R_8 \cos(\phi_6) + m_B q_1 \sin(\phi_6) + m_B q_2 \sin(\phi_6)]$$

$$- K_{wrp}(\Delta L_p) \left[\frac{1}{L_p} R_8 R_d \sin\phi_B \right]$$

FIG. 22 Equation of Motion for Coordinate ϕ_6

$$\frac{\partial}{\partial t}\left(\frac{\partial T}{\partial \dot{\phi}_9}\right) - \frac{\partial T}{\partial \phi_9} + \frac{\partial V}{\partial \phi_9} - Q_{\phi_9} = 0$$

$$+ [m_L R_9 \sin(\phi_9)]\ddot{R}_1 + [m_L R_9 \cos(\phi_6 - \phi_9)]\ddot{R}_8$$

$$+ [-m_L R_3 R_9 \cos(\phi_2 - \phi_9) - m_L R_5 R_9 \sin(\phi_2 - \phi_9)]\ddot{\phi}_2$$

$$+ [-m_L R_8 R_9 \sin(\phi_6 - \phi_9)]\ddot{\phi}_6 + m_L R_9^2 \ddot{\phi}_9$$

$$+ [m_L R_3 R_9 \sin(\phi_2 - \phi_9) - m_L R_5 R_9 \cos(\phi_2 - \phi_9)]\dot{\phi}_2^2$$

$$+ [-m_L R_8 R_9 \cos(\phi_6 - \phi_9)]\dot{\phi}_6^2 + [-2m_L R_9 \sin(\phi_6 - \phi_9)]\dot{R}_8\dot{\phi}_6$$

$$+ [2m_L R_9]\dot{R}_9\dot{\phi}_9$$

$$+ g[m_L R_9 \sin(\phi_9)]$$

FIG. 23 Equation of Motion for Coordinate ϕ_9

coordinates, and [F] is the system forcing function. The equations of motion are numerically integrated to simulate the response of the crane system under various configurations and subject to a particular set of initial conditions.

The static equilibrium values of the generalized coordinates, which describe the crane's initial static deflections, or its deviation from the set of prescribed initial conditions before the simulation begins, are needed to initialize the integration algorithm. All crane accelerations and velocities at equilibrium equal zero; therefore, the crane system equations of motion in equation 4-2 reduce to

$$[F(p_1,p_2,\ldots,p_N)] = 0 \qquad (4\text{-}3)$$

The roots of equation 4-3 are the static equilibrium values of the generalized coordinates. The algorithm used to find the roots of this nonlinear function utilizes Brown's method and was obtained under copyright agreements from the International Mathematics and Statistics Library. Brown's method (23) combines the slower, yet stable, bracketing abilities of the Regula-Falsi technique with the rapid convergence characteristics of the Newton-Raphson approach to find the roots of a nonlinear function.

Once the equilibrium values have been calculated, they are used to initialize the integration algorithm. A new acceleration vector $[\ddot{p}]$ is calculated each time step in the simulation. The acceleration vector is evaluated by substituting the current known values of the generalized coordinates and their time derivatives into the [F] and [M] matrices in equation 4-2. The numerical values effectively reduce the crane system equations of motion to a set of coupled, linear equations in terms of

the accelerations

$$[M]\ [\ddot{p}] = [F] \tag{4-4}$$

Choosing a method to solve equation 4-4 for the acceleration vector requires careful consideration of the crane system. The masses of the crane components are large and roughly similar; and the nonlinear coupling between the crane components is strong. This produces ill-conditioning (23) in the mass matrix, [M], or a condition where the elements on the diagonal of [M] are not the dominant terms in their respective rows. Most methods used to solve linear matrix equations of the variety of equation 4-4 when ill-conditioning exists result in unacceptably large error. Johnson (23) recommends the Gauss elimination method for ill-conditioned systems. Then the acceleration vector in equation 4-4 is determined using the Gauss elimination method with full row and column pivoting. This method tridiagonalizes the mass matrix, [M], and then backsolves to determine the new acceleration vector.

The acceleration vector is integrated numerically to find the new system velocities and displacements. Many numerical integration routines are available. A fourth-order variable-step Runge-Kutta technique was chosen, at some expense of computation time, because of the method's convergence, stability, accuracy, and ease of implementation (23). The Runge-Kutta method is less efficient than some other integration techniques because the function (Eq. 4-4) is evaluated a minimum of four times for each integration step.

Double precision calculation is used in this simulation to reduce the errors which occur in the successive critical matrix operations and integrations. Time-history plots of the simulation results are

generated to help analyze the crawler crane's dynamic characteristics. The inherent coupling which exists in the crane system is not obvious in the time-history plots, so a finite fast Fourier transform of the coordinate responses is performed.

The fast Fourier transform (23) is merely an efficient procedure of computing the amplitude and phase-angle coefficients in the least-squares polynomial used to approximate the Fourier series describing the coordinate responses. The algorithm used in this analysis to perform the fast Fourier transform was obtained from the International Mathematics and Statistics Library under copyright agreements. A windowing technique, used to eliminate the discontinuities at the beginning and the end of the raw simulation results, was obtained from Patten (2) and incorporated in the fast Fourier transform analysis. This concludes the discussion of the numerical techniques used in this simulation.

5. CRANE DYNAMIC RESPONSE

The results of the numerical solution of the crane system equations of motion are presented in this chapter for three sets of crane configurations and initial conditions. The simulations are intended to verify that the response of the reduced-order crane model developed in this thesis is representative of the response of a crawler crane by comparing its responses to those of a higher-order crane model developed by Patten (2). The simulations also serve as the basis for a later comparison between the response of an uncompensated crane, given in this chapter, and the controlled response of a compensated crane given in Chapter 7.

A list of the simulation constants used to specify the crane properties, configuration, and initial conditions is given in Table 1. Each simulation case depicts the transient response of a crane due to the sudden application of the cable drum brake during load-lowering. The initial velocity of the suspended load, in each case, corresponds to the velocity the load would experience due to an unrestrained vertical drop. The initial velocity of the load in Case A corresponds to a vertical drop of 7.6 cm, while the load in both Cases B and C is allowed to experience a 30.5 cm vertical drop. Case A represents a conservative crane configuration with a short boom and a stiff soil foundation. Case B depicts essentially the same crane as Case A, but operating with a steeper boom angle and a softer soil foundation. Case C is an extreme crane configuration with a long boom operating

Table 1

Simulation Constants for Cases A through C

	Case A	Case B	Case C
R_B	45.7 m	45.7 m	91.4 m
G	82.7 MPa	62.0 MPa	41.4 MPa
$\phi_6(t_o)$	60°	70°	70°
D_{wrp}	6.04 cm	4.76 cm	4.76 cm
$R_9(t_o)$	12.2 m	12.2 m	12.2 m
R_o	1.22 m	1.22 m	1.22 m
m_L	1.36×10^4 kg	1.36×10^4 kg	1.36×10^4 kg
m_B	4.73×10^3 kg	4.73×10^3 kg	9.46×10^3 kg
m_T	6.13×10^4 kg	6.13×10^4 kg	6.13×10^4 kg
m_c	8.76×10^4 kg	8.76×10^4 kg	8.76×10^4 kg
K_v	1.19×10^7 N/m	1.19×10^7 N/m	1.19×10^7 N/m
K_r	1.92×10^{13} N/m	1.92×10^{13} N/m	1.92×10^{13} N/m
K_{WRP}	1.59×10^7 N/m	3.49×10^5 N/m	6.57×10^4 N/m
K_{WRL}	3.83×10^6 N/m	3.83×10^6 N/m	3.83×10^6 N/m
K_B	1.31×10^9 N·m	1.31×10^9 N·m	6.53×10^8 N·m
R_d	10.67 m	10.67 m	10.67 m
R_2	0.762 m	0.762 m	0.762 m
R_3	1.78 m	1.78 m	1.78 m
R_4	4.32 m	4.32 m	4.32 m
R_5	1.27 m	1.27 m	1.27 m
d_t	4.11 m	4.11 m	4.11 m

Table 1 (continued)

	Case A	Case B	Case C
w_t	1.22 m	1.22 m	1.22 m
ϕ_3	2.86°	2.86 °	2.86°
ϕ_A	40.1°	40.1°	40.1°
I_c	3.39×10^5 N·m·sec^2	3.39×10^5 N·m·sec^2	3.39×10^5 N·m·sec^2
I_T	3.95×10^5 N·m·sec^2	3.95×10^5 N·m·sec^2	3.95×10^5 N·m·sec^2

at a steep angle on even softer supporting soil.

The discussion of each case begins with a short description of the important simulation constants and the intended purpose of the simulation. A brief analysis of the simulation results follows each description. The transient response of the crane system is displayed next in plots of the velocity and displacement of each of the generalized coordinates. The time-dependent values of the load and pendent line tensions and the boom chord length are also presented. Selected results from the fast Fourier transform analysis of the coordinate amplitude responses are offered when the frequency contents are enlightening. The frequency plots conclude each case study.

Case A

The simulation constants chosen for Case A represent a conservative crane configuration. The case depicts a relatively stiff crane with a short 45.7 m boom at 60^{o} with a half depth of 1.22 m. The shear modulus of the soil is 82.7 MPa.

The simulation results for the reduced-order crane model developed in this thesis are presented along with the results from the simulation of a higher-order crane model developed by Patten (2) for the same crane configuration and initial conditions. The response of a coordinate predicted by both models is plotted on a single figure. This case is primarily offered to verify that the response of the reduced-order model is similar to the Patten model.

Case A presents the transient response of the crane system, due to a 7.6 cm vertical drop of the load, as predicted by two

different crane models, the reduced-order crane model and the more complex Patten crane model.

When comparing the responses of the two models it is important to notice that the response records of the same generalized coordinate predict similar crane characteristics rather than to expect both models to produce equivalent displacements. The general shape of the time-histories and the frequency components which describe their shape determine similar response characteristics more than do equivalent displacements. The crane properties which determine the frequency content and the amplitude of the displacements for either crane model would eventually need to be modified after field tests on a crane for a model to accurately predict the response of a real crawler crane.

Observing the real-time response records of coincident generalized coordinates, given in Figs. 24 through 28, from both models it is evident that the response characteristics are generally similar. The vertical translation of the tracks, coordinate R_1 in Fig. 25, from both models experiences its peak shortly after the initial shock of the dropped load. The rotational and translational coordinates of the tracks are strongly coupled, so likewise both models predict peak track rotation due to the initial shock of the dropped load. Figures 26 and 27 present the rotation of the boom chord and the pendulating load from both models, coordinates ϕ_6 and ϕ_9. Notice the low frequency component which is especially prominent in coordinate ϕ_9 from both models. The oscillation of the suspended

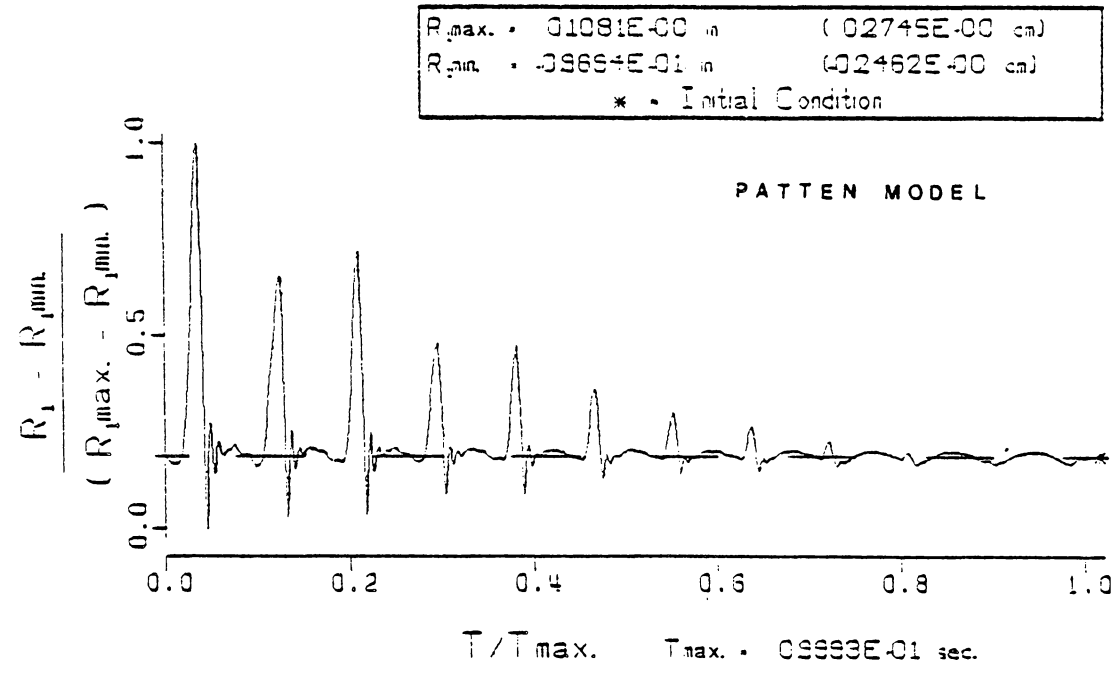

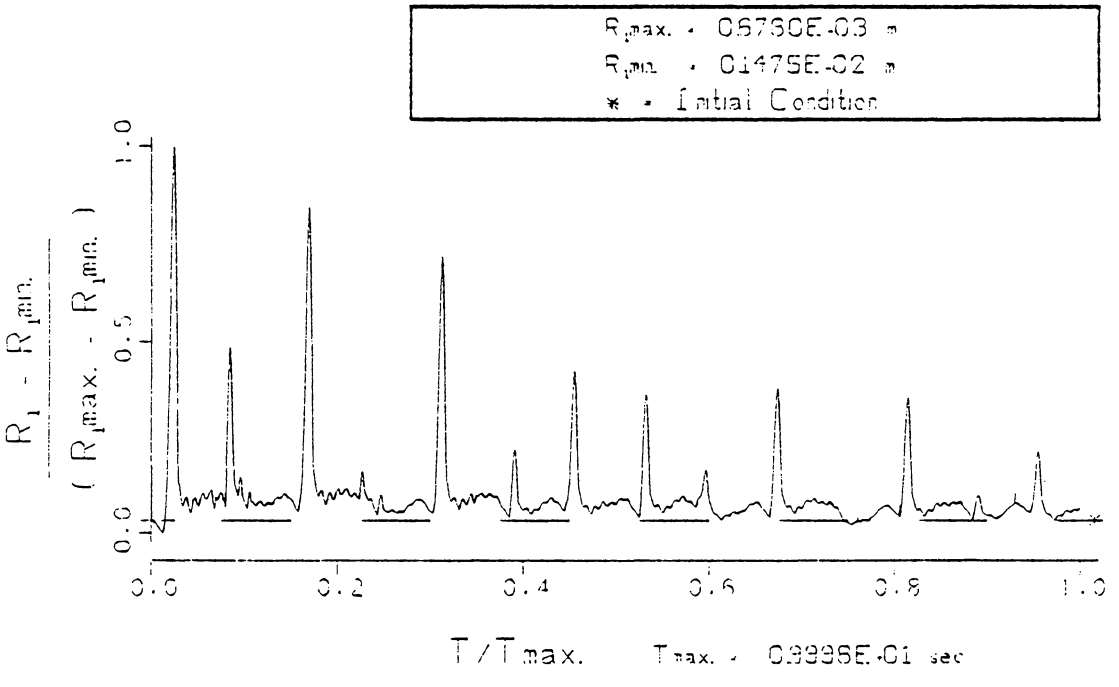

FIG. 24 VERTICAL RESPONSE OF THE TRACKS. (R_1) FOR CONDITIONS OF CASE A WHEN THE CABLE DRUM BRAKE IS APPLIED DURING LOAD-LOWERING.

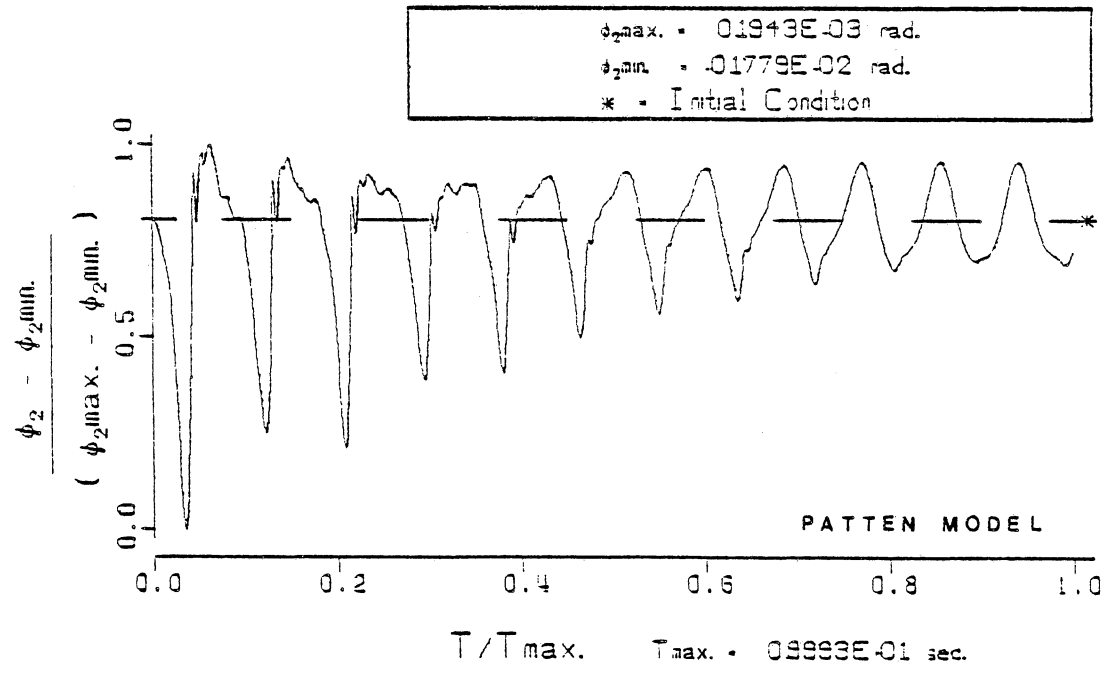

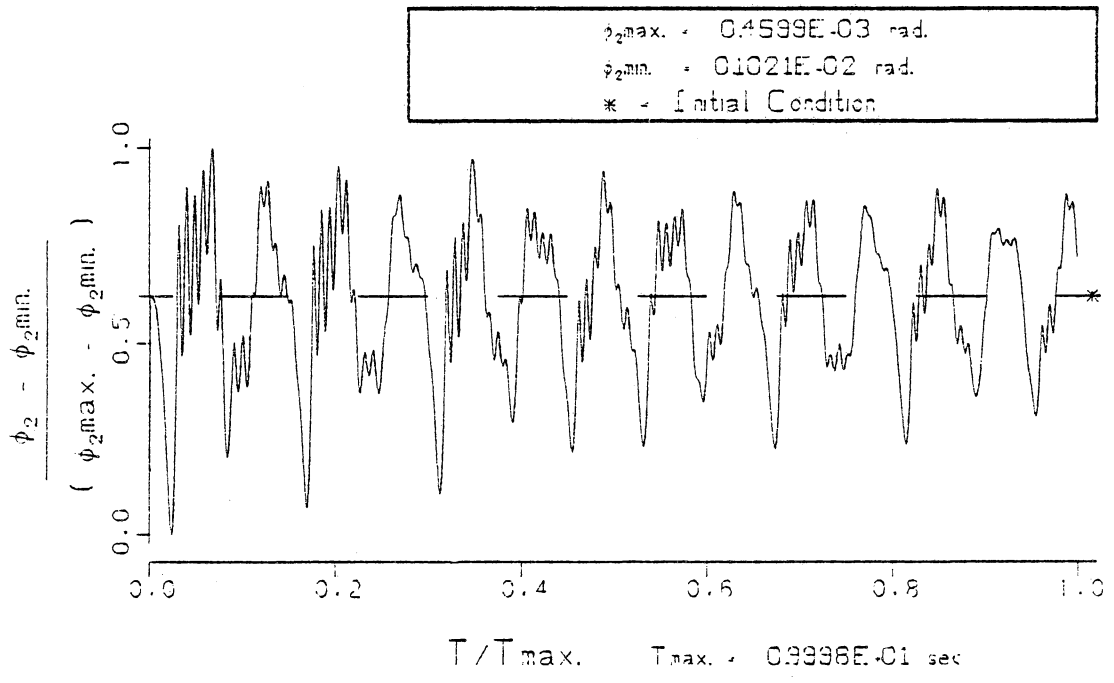

FIG. 25 ROTATIONAL RESPONSE OF THE TRACKS. (ϕ_2) FOR CONDITIONS OF CASE A WHEN THE CABLE DRUM BRAKE IS APPLIED DURING LOAD-LOWERING

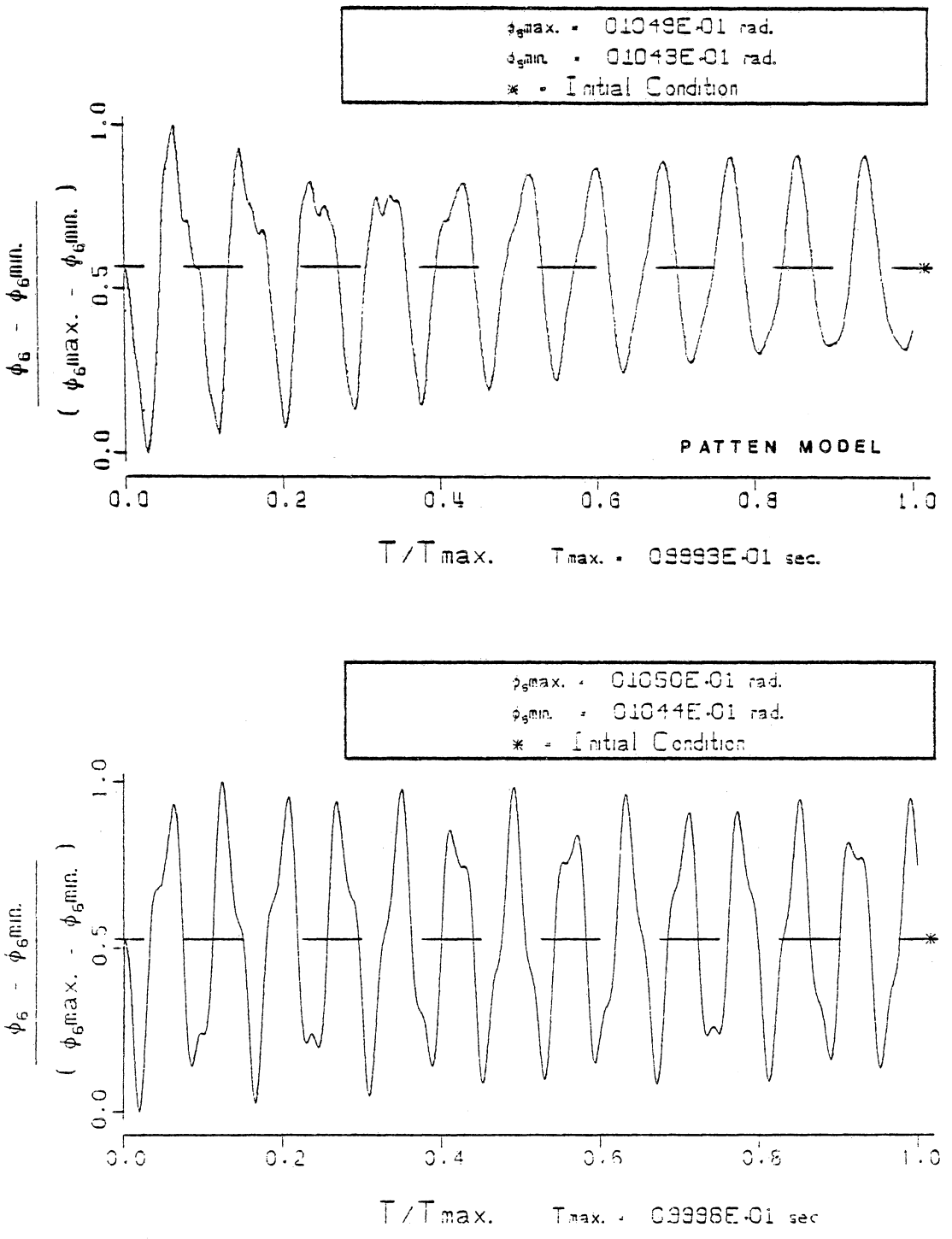

FIG. 26 ROTATIONAL RESPONSE OF THE BOOM CORD. (ϕ_5) FOR CONDITIONS OF CASE A WHEN THE CABLE DRUM BRAKE IS APPLIED DURING LOAD-LOWERING

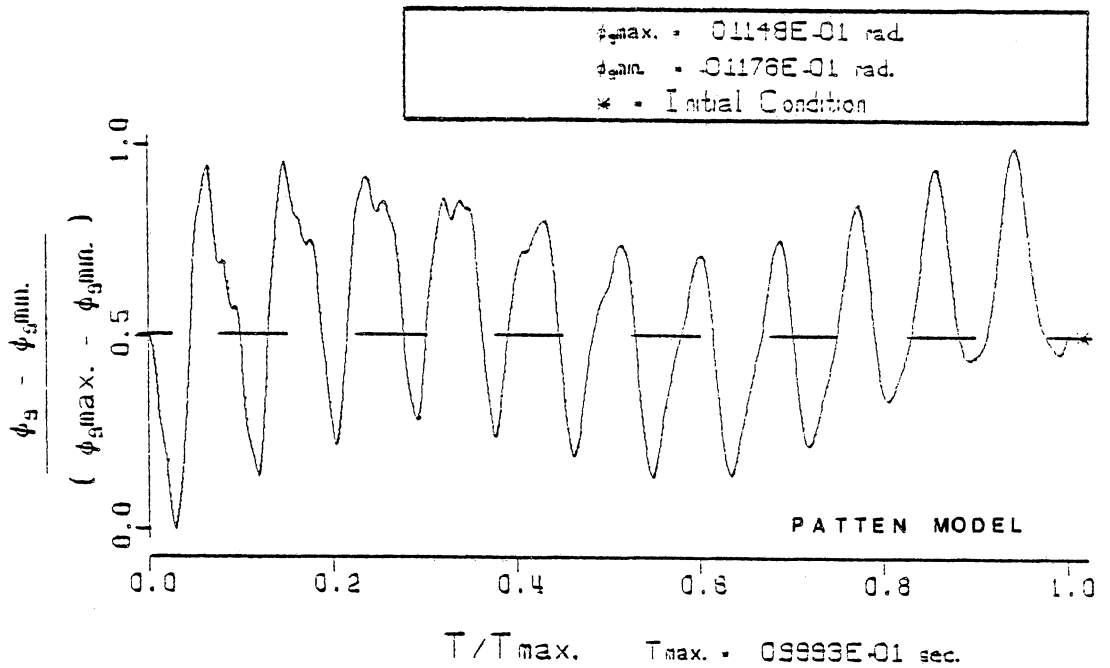

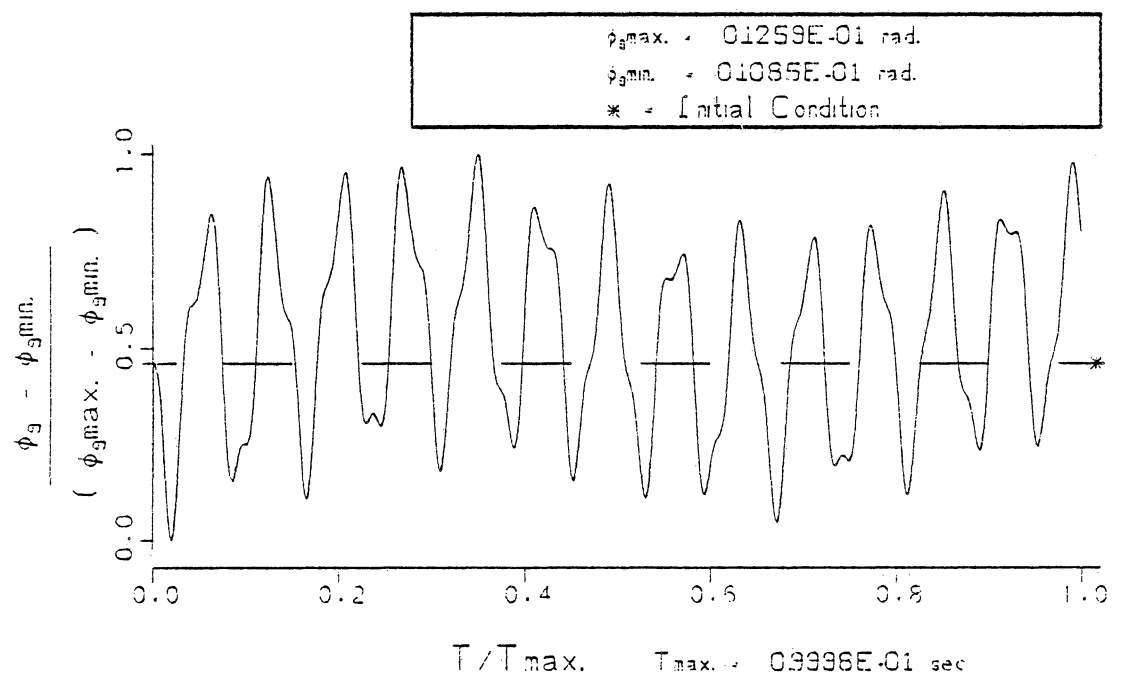

FIG.27 PENDULATION OF THE LOAD. (ϕ_g)
FOR CONDITIONS OF CASE A WHEN THE CABLE
DRUM BRAKE IS APPLIED DURING LOAD-LOWERING

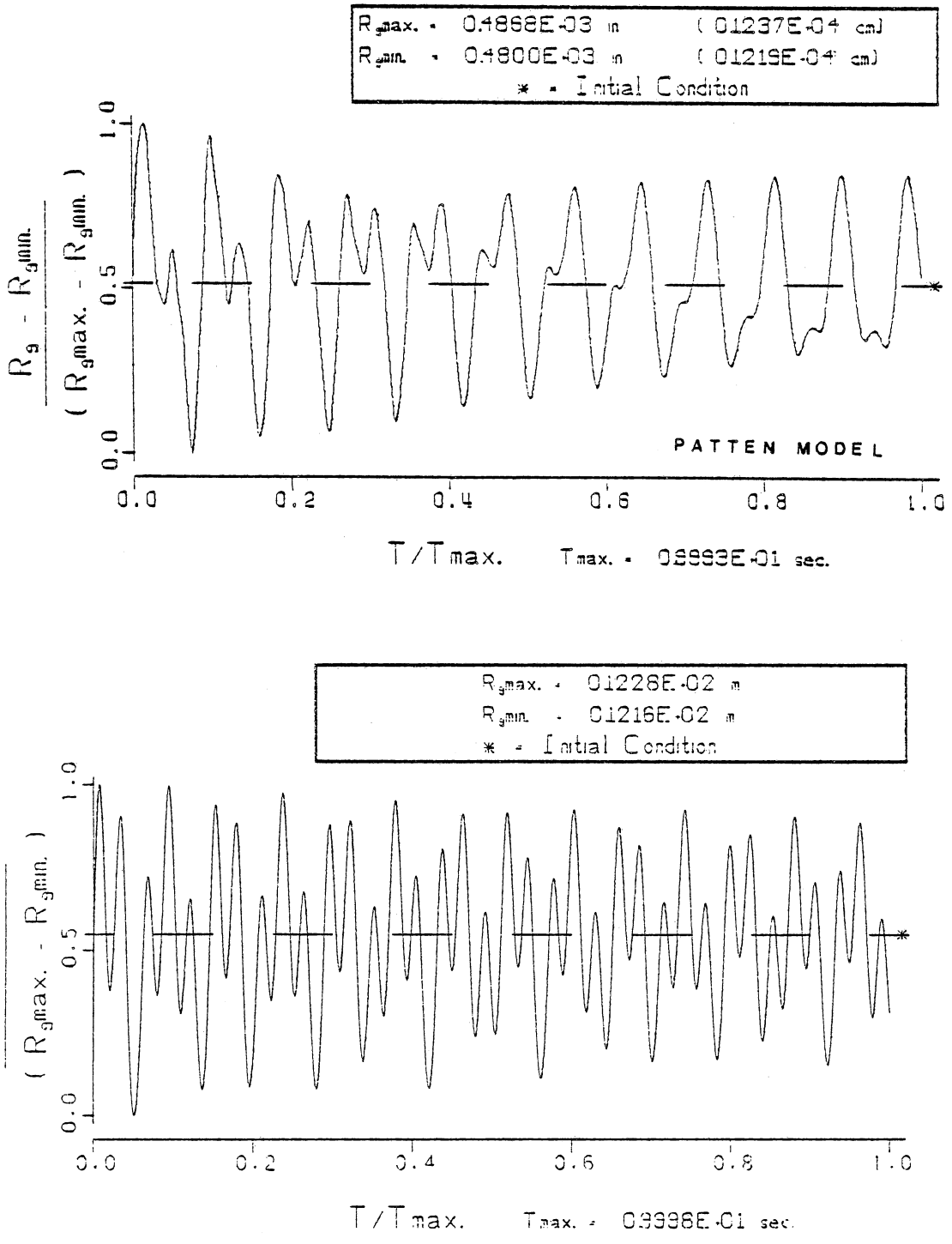

FIG. 28 STRETCH OF THE LOAD LINE CABLE. (R_g) FOR CONDITIONS OF CASE A WHEN THE CABLE DRUM BRAKE IS APPLIED DURING LOAD-LOWERING

load, given in Fig. 28, is strongly coupled to the boom motion, which has been characterized differently in each of the models.

The amplitudes of the coordinate responses from the Patten model damp out more significantly during the 10 seconds of simulation time than the amplitudes of the coordinate responses from the reduced-order model. The reduced-order model has predicted the response of a stiffer crane than the Patten model; this is largely due to the reduced flexibility of the boom. The boom deflections are smaller in the reduced-order model, so the boom chord shortens less, as seen in Fig. 29 from the reduced-order model and Fig. 30 from the Patten (2) model. The stiffer boom in the reduced-order model also causes the pendent lines and the load lines to become slack during the simulation, as seen in Fig. 29. The boom characterization obviously has a strong effect on the crane system response.

The similarities between the two models become even more apparent if the differences in the responses are investigated. The frequency content of each coordinate response from the fast Fourier transform analysis, given in Figs. 31 through 36, reinforces the similarities in the model responses, and also brings out the differences. The vertical drop of the suspended load is used to excite the vibratory motion of both crane models. Two frequencies dominate the oscillation of each suspended load, coordinate R_9, as seen in Fig. 35. The higher frequency of the load oscillation, 18 Hz for the reduced-order model and 11 Hz for the Patten model, is the dominate frequency in the boom vibration. Coordinate q_1 from the

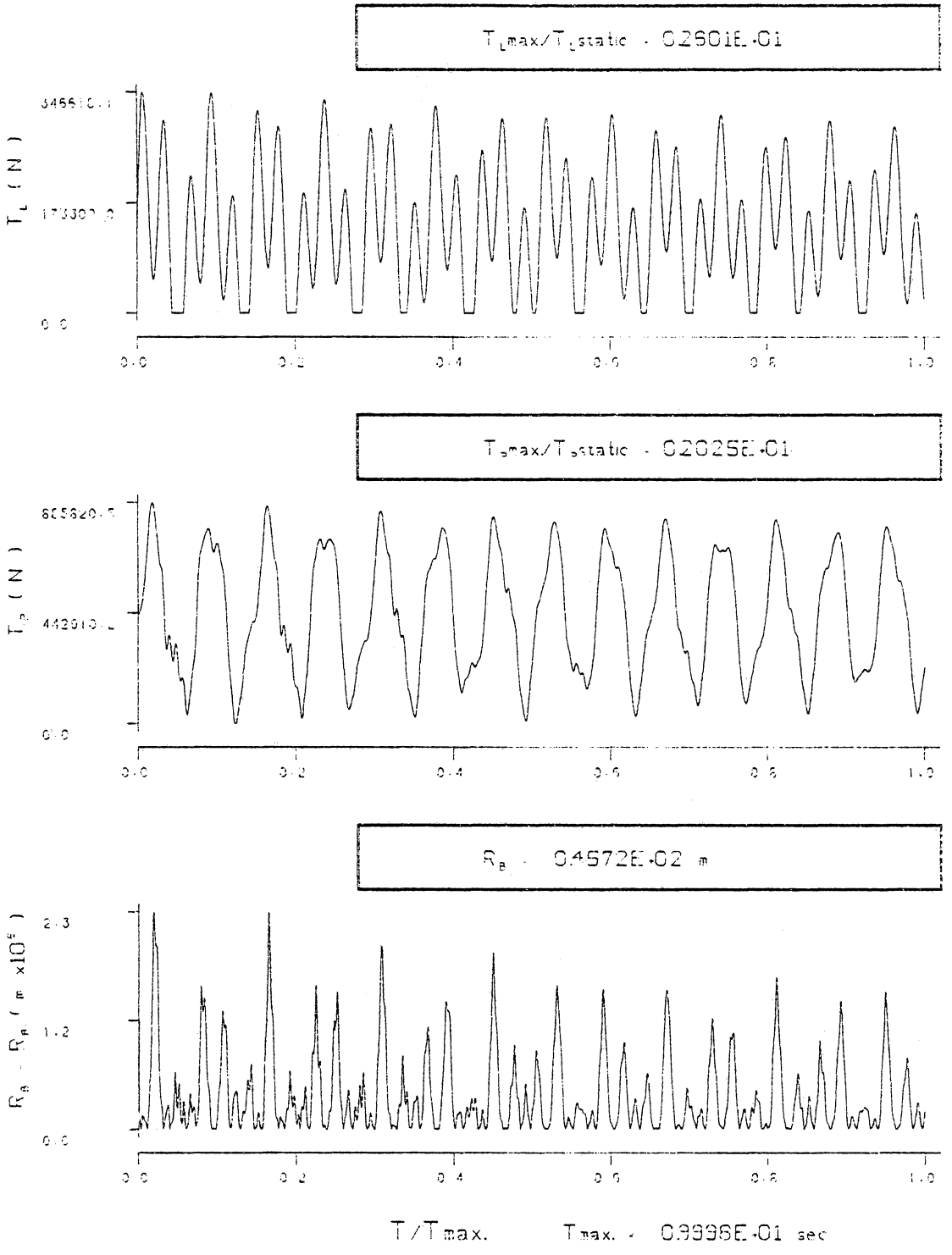

FIG.29 THE TIME DEPENDENT BOOM CORD LENGTH, (R_B) AND THE TENSION IN THE PENDENT AND LOAD LINE ASSEMBLIES, (T_B AND T_L) FOR THE CONDITIONS OF CASE A (UNCOMPENSATED)

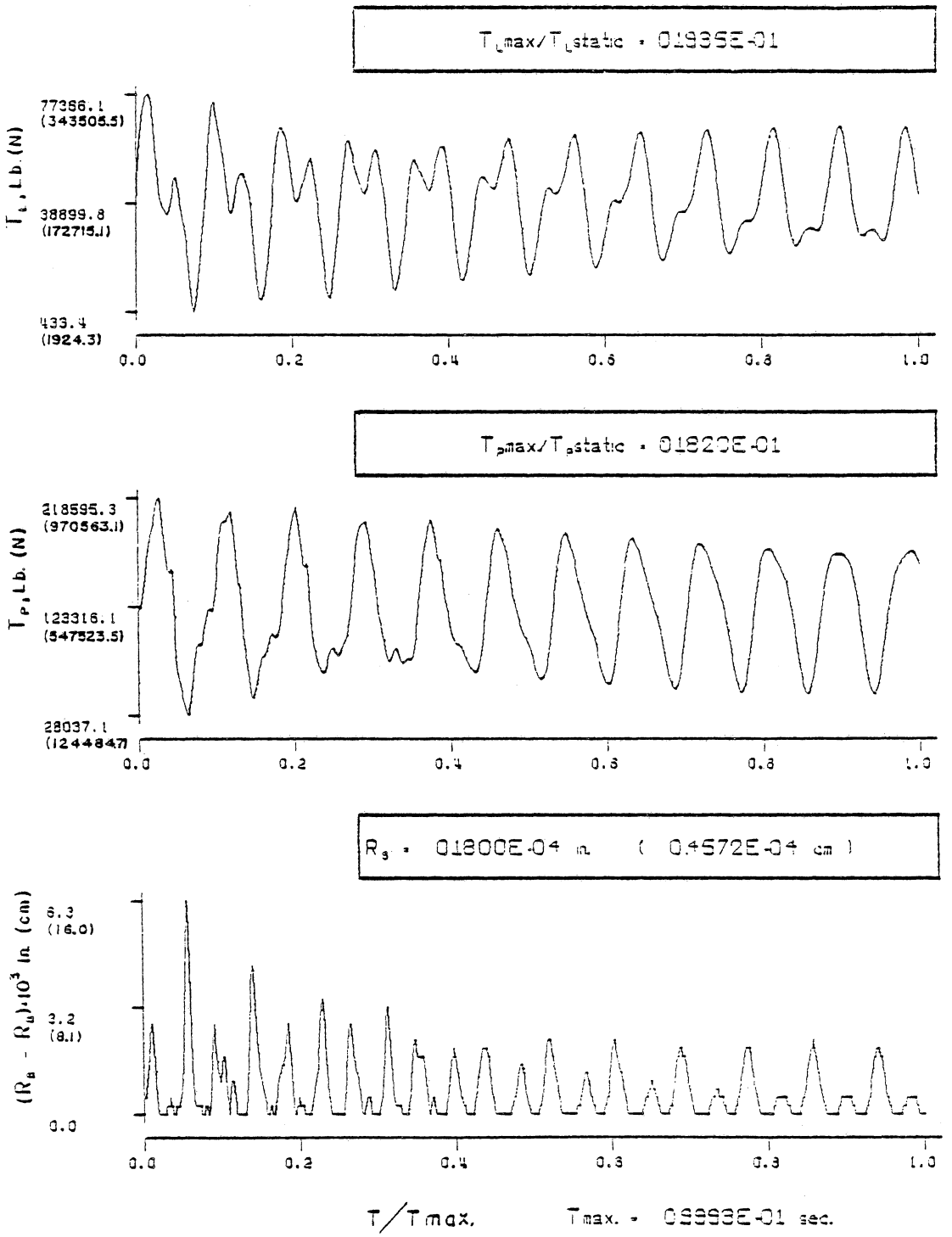

FIG. 30 THE TIME DEPENDENT BOOM CHORD LENGTH, (R_s) AND THE TENSION IN THE PENDENT AND LOAD LINE ASSEMBLIES, (T_s AND T_t), FOR CASE A (PATTEN MODEL)

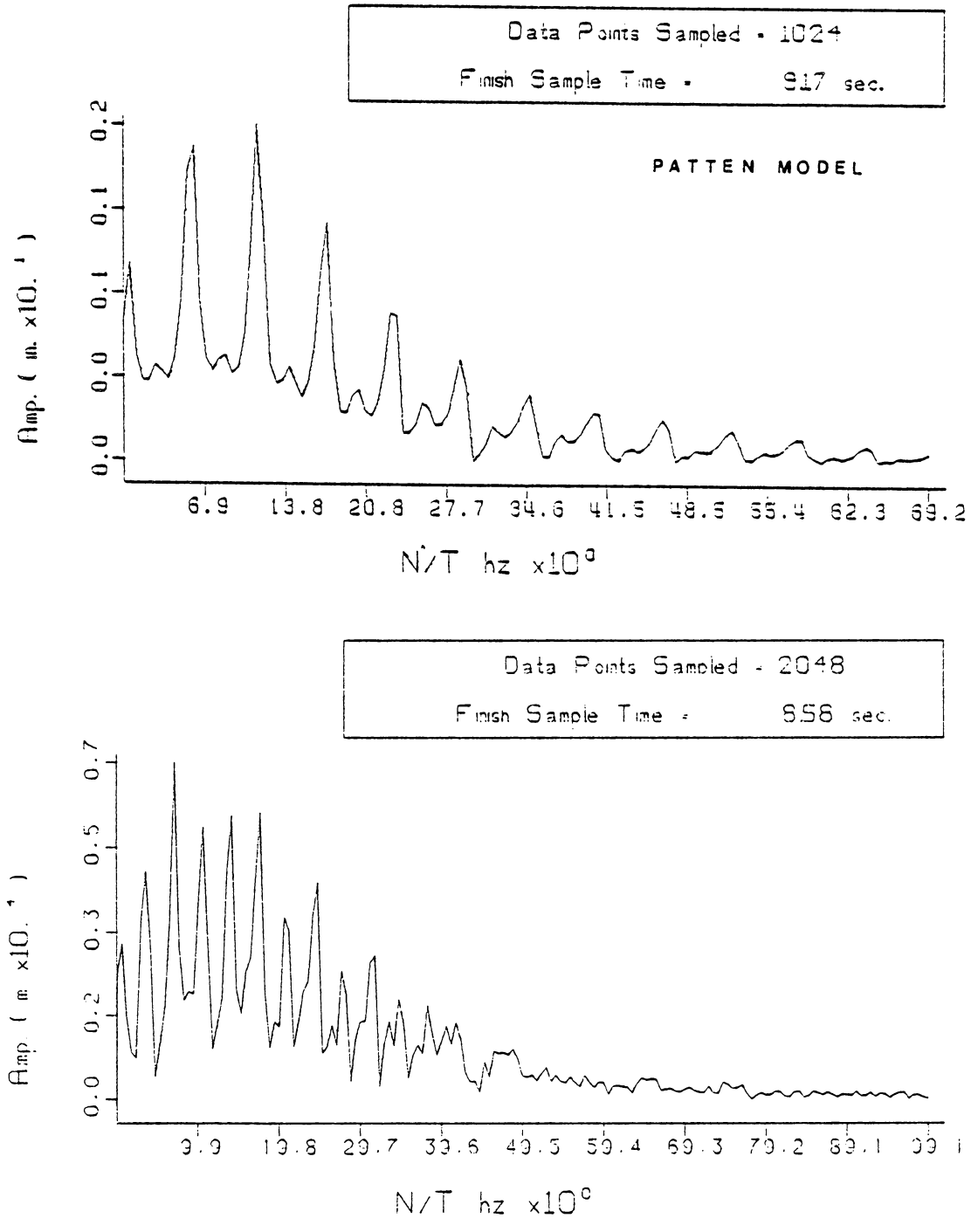

FIG. 31 FREQUENCY ANALYSIS OF COORDINATE R_1 FOR THE CONDITIONS OF CASE A WHILE BRAKING AT LOAD LOWERING

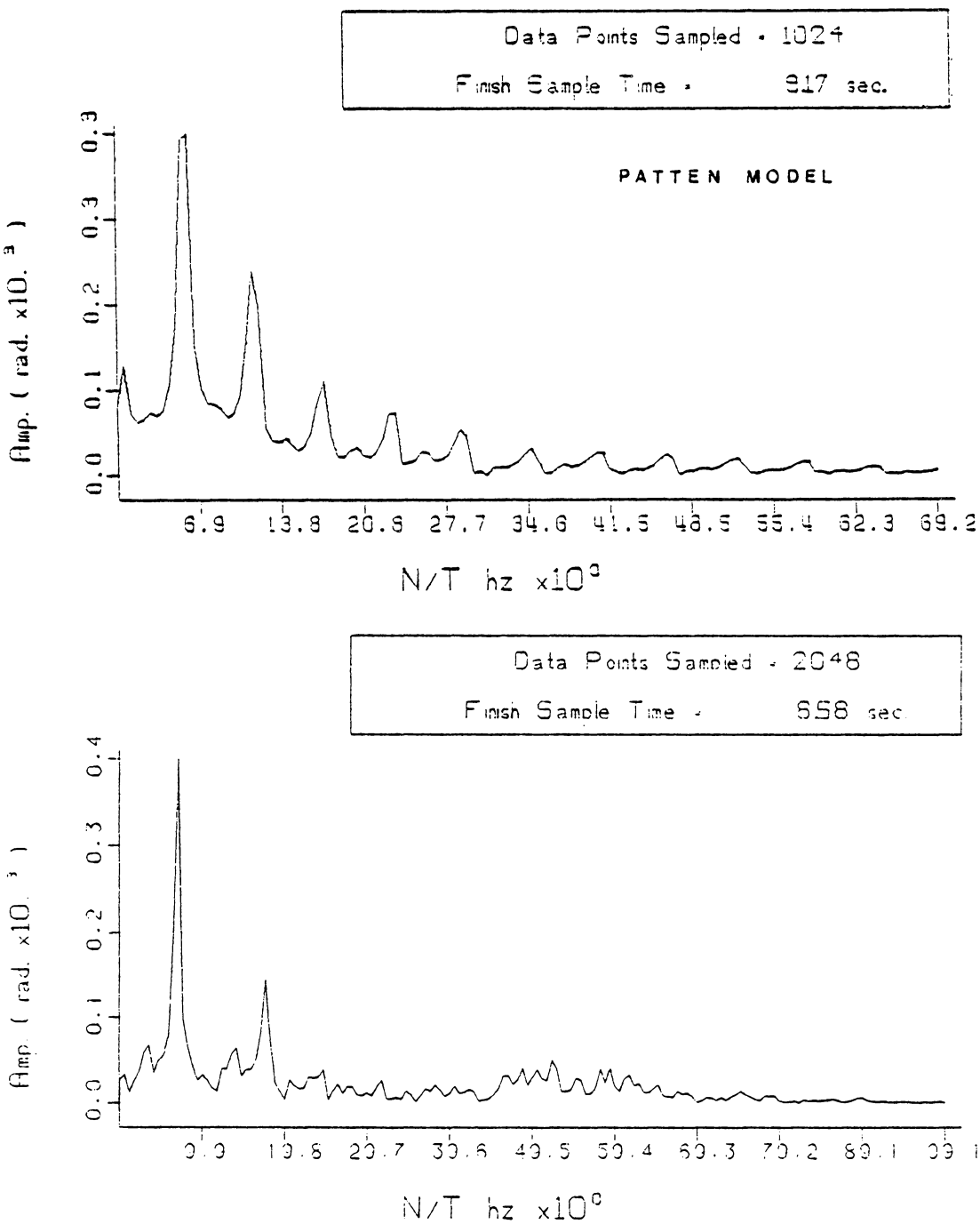

FIG. 32 FREQUENCY ANALYSIS OF COORDINATE φ_2 FOR THE CONDITIONS OF CASE A WHILE BRAKING AT LOAD LOWERING

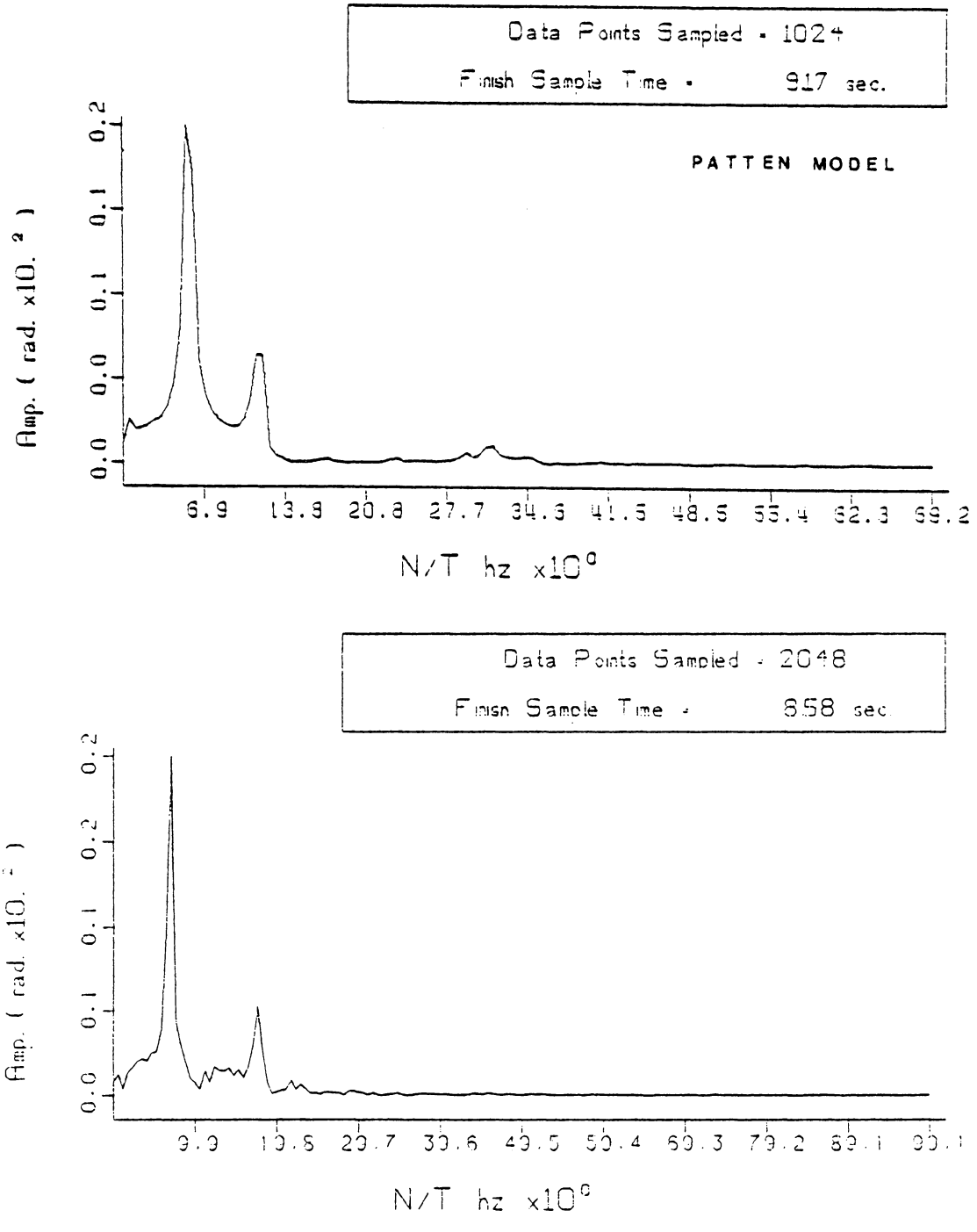

FIG. 33 FREQUENCY ANALYSIS OF COORDINATE ρ_s FOR THE CONDITIONS OF CASE A WHILE BRAKING AT LOAD LOWERING

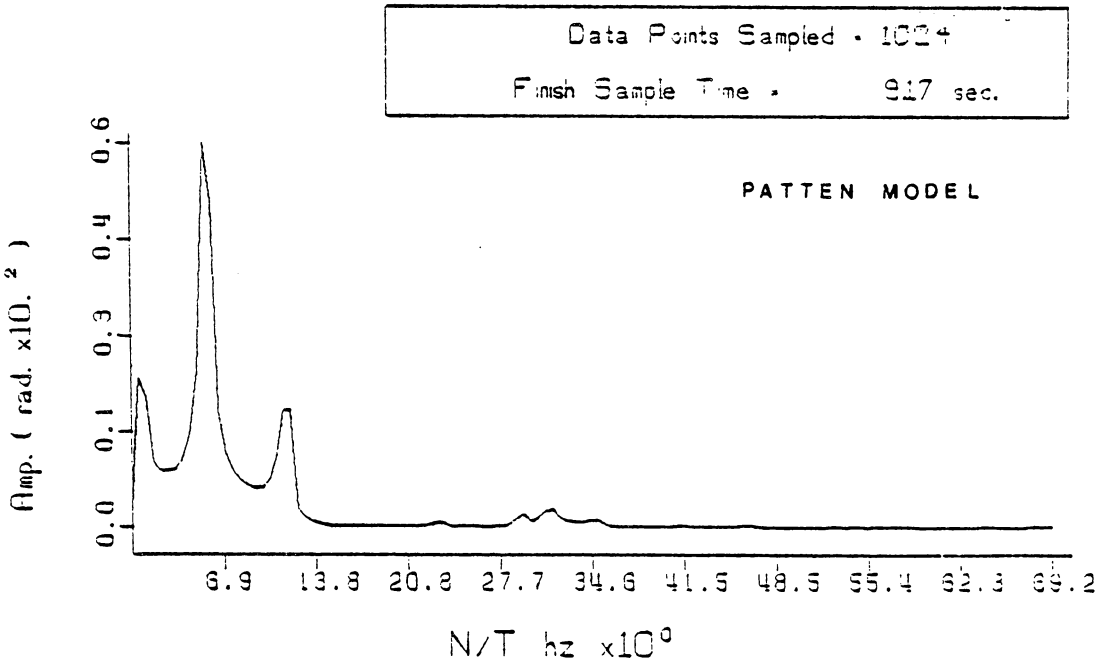

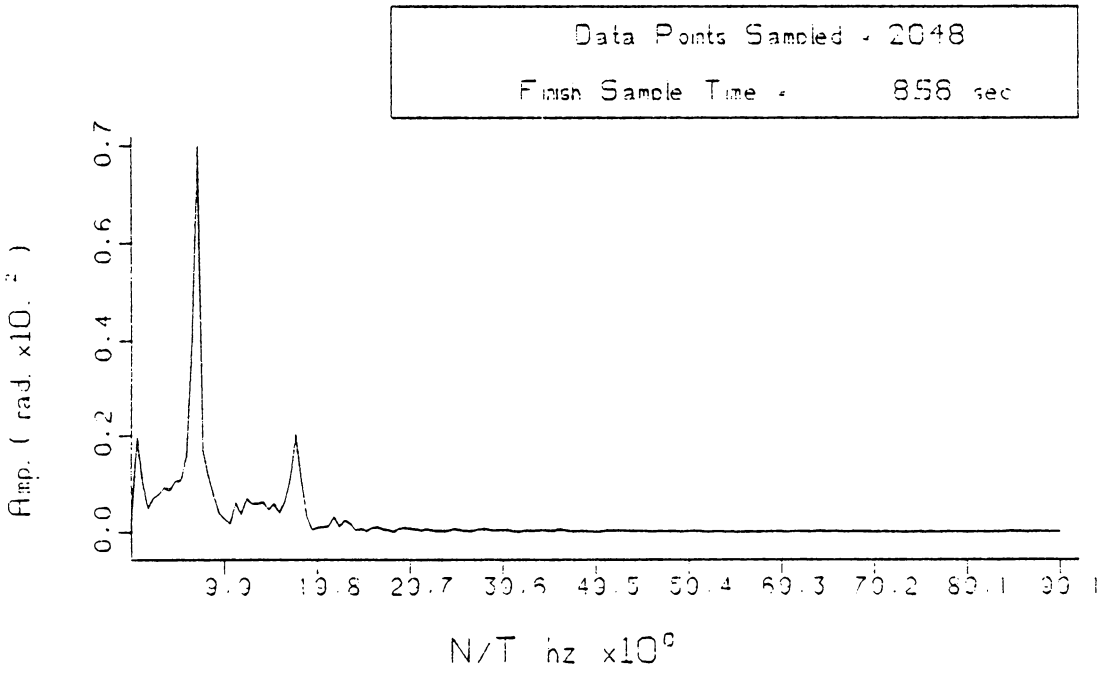

FIG. 34 FREQUENCY ANALYSIS OF COORDINATE φ_3 FOR THE CONDITIONS OF CASE A WHILE BRAKING AT LOAD LOWERING

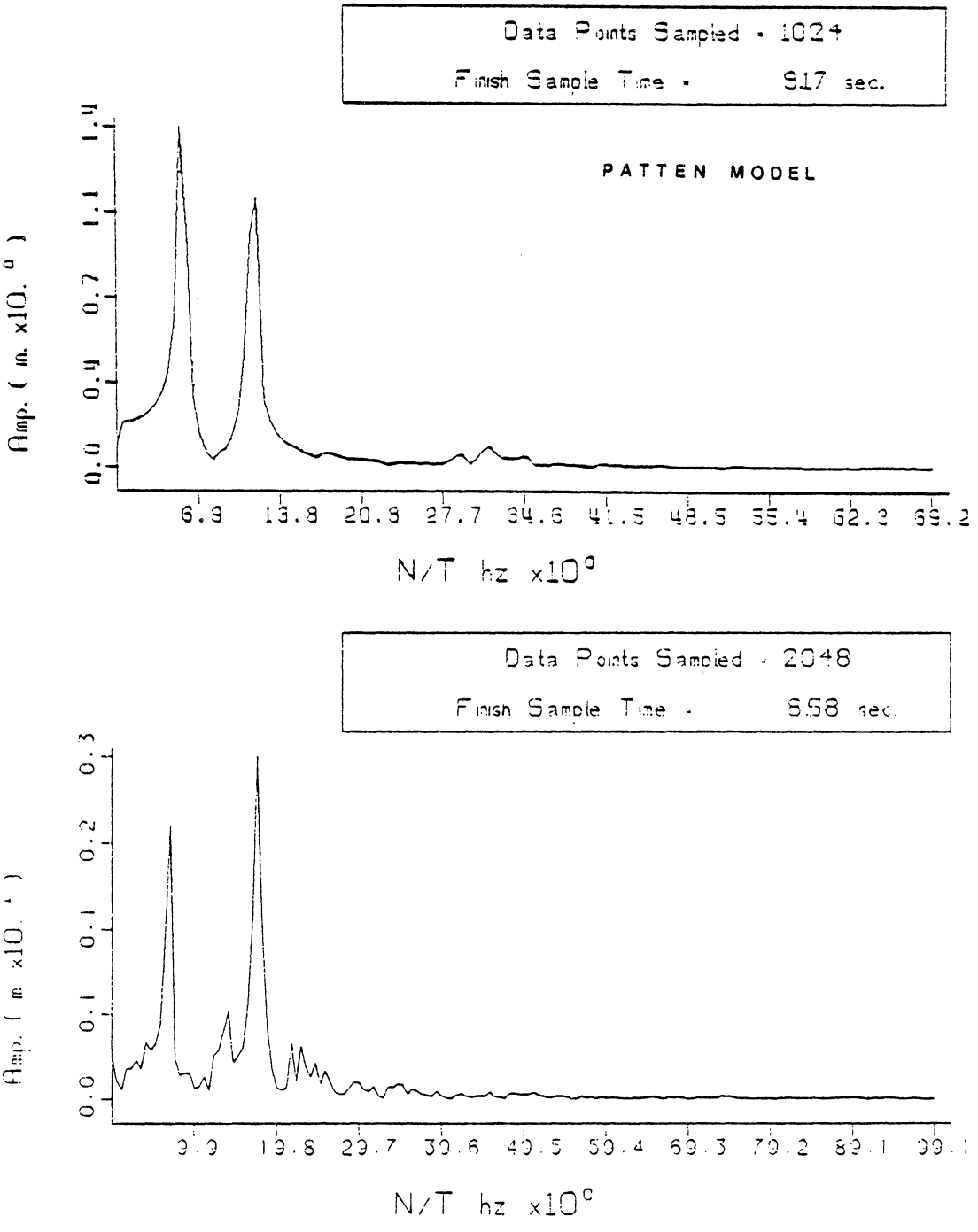

FIG. 35 FREQUENCY ANALYSIS OF COORDINATE R_s FOR THE CONDITIONS OF CASE A WHILE BRAKING AT LOAD LOWERING

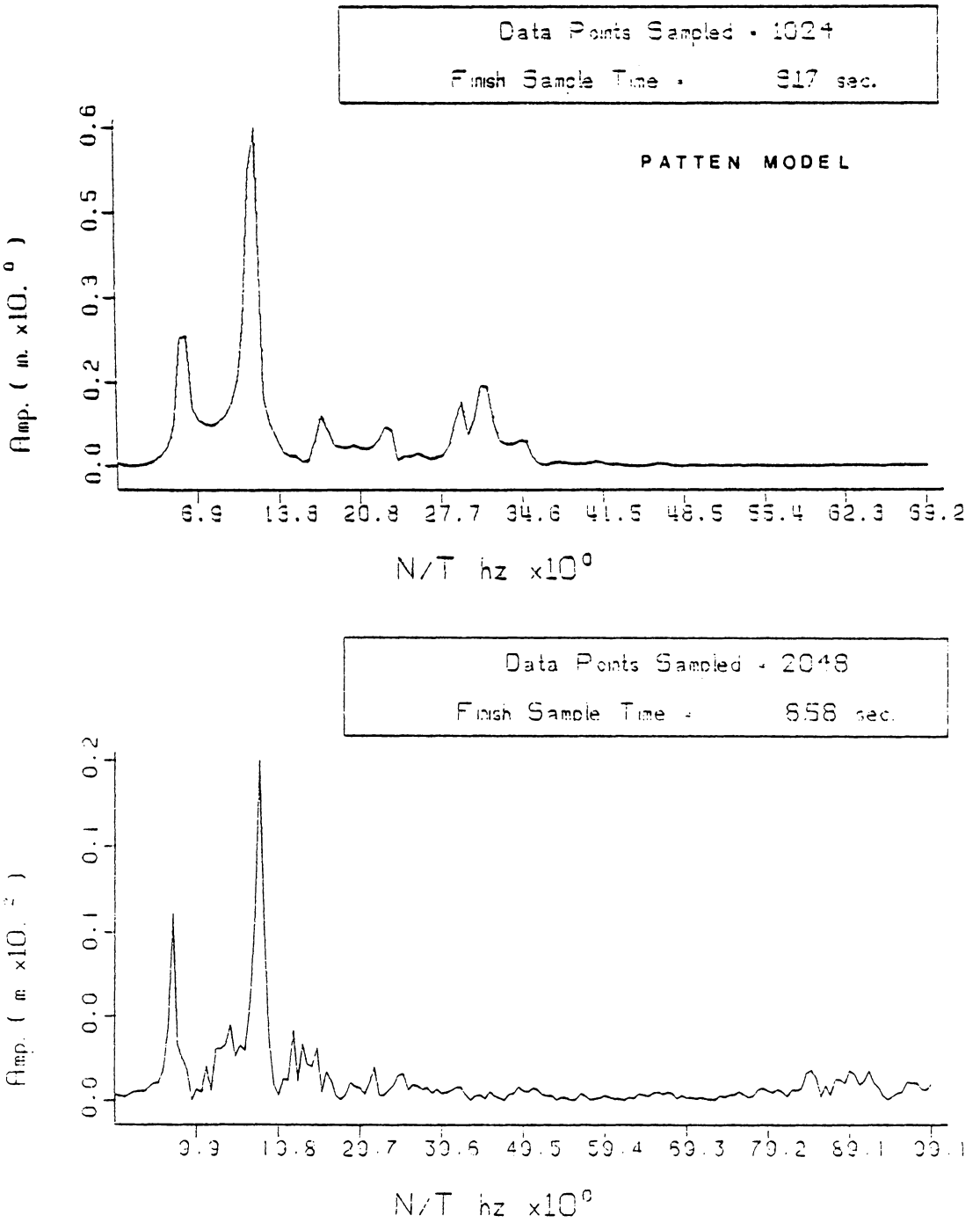

FIG. 36 FREQUENCY ANALYSIS OF COORDINATE q_1 FOR THE CONDITIONS OF CASE A WHILE BRAKING AT LOAD LOWERING

reduced-order model and the first mode, p_1, from the Patten model are compared, as seen in Fig. 36. The lower frequency in the load oscillation, 7 Hz for the reduced-order model and 5.5 Hz for the Patten model, is the largest frequency component in the track rotation, ϕ_2 in Fig. 32, in the boom chord rotation, ϕ_6 in Fig. 33, and in the pendulation of the load, ϕ_9 in Fig. 34, for both models.

The basic difference in the response of the two crane models lies in the frequency content of the oscillation of the suspended load, Fig. 35, which drives the motion of the crane system. First, the two dominate frequencies of load oscillation in the reduced-order model, 7 Hz and 18 Hz are substantially faster than the frequencies of load oscillation in the Patten model, 5.5 Hz and 11 Hz. Second, the higher frequency of load oscillation in the reduced-order model dominates the load motion; this frequency corresponds to the frequency which dominates the structural vibratory motion of the boom. The lower frequency of load oscillation in the Patten model dominates the load motion; and this frequency dominates the remaining crane rotations, coordinates ϕ_2, ϕ_6 and ϕ_9. The load oscillation, then, is coupled more strongly with the higher frequency boom vibration in the reduced-order model, than with the lower frequency crane rotations as in the Patten model.

Returning to the time histories of the generalized coordinates the similarity between the response of the reduced-order crane model and the Patten crane model becomes more apparent with the understanding that the frequency content of the reduced-order model is dominated by

faster frequencies than the Patten model.

Case B

Case B depicts the transient response of essentially the same crane used in Case A, but subject to a different set of initial conditions and crane configuration. The reduction in the diameter of the wire rope in the pendent lines from 6.04 cm in Case A to 4.76 cm in Case B represents the only property change in the crane itself. The remaining changes in the simulation constants used in Case B constitute changes in the crane's operating conditions. The shear modulus of the soil is reduced from 82.7 MPa in Case A to 62.0 MPa in Case B. The boom is operated at an angle of 70^{o} to the earth's tangent plane in Case B, instead of 60^{o} as in Case A. Lastly, the initial velocity of the load in Case B is twice that of Case A.

This case is chosen to study the effect of the larger perturbation and the soft supporting soil on the system's vibration. The specified boom angle is also at the upper operating limit recommended by the manufacturer for a 45.7 m boom.

The time histories of the generalized coordinate displacements in Case B, given in Figs. 37 through 43, look very different from those in Case A, and show that the response of the crane system is uniquely related to the operating conditions. The ground coordinates, R_1 and ϕ_2 in Figs. 37 and 38, experience the most dramatic change. The largest rotation of the tracks, ϕ_2 in Fig. 25, in Case A occurs at 0.2 sec as does the largest vertical translation of the tracks,

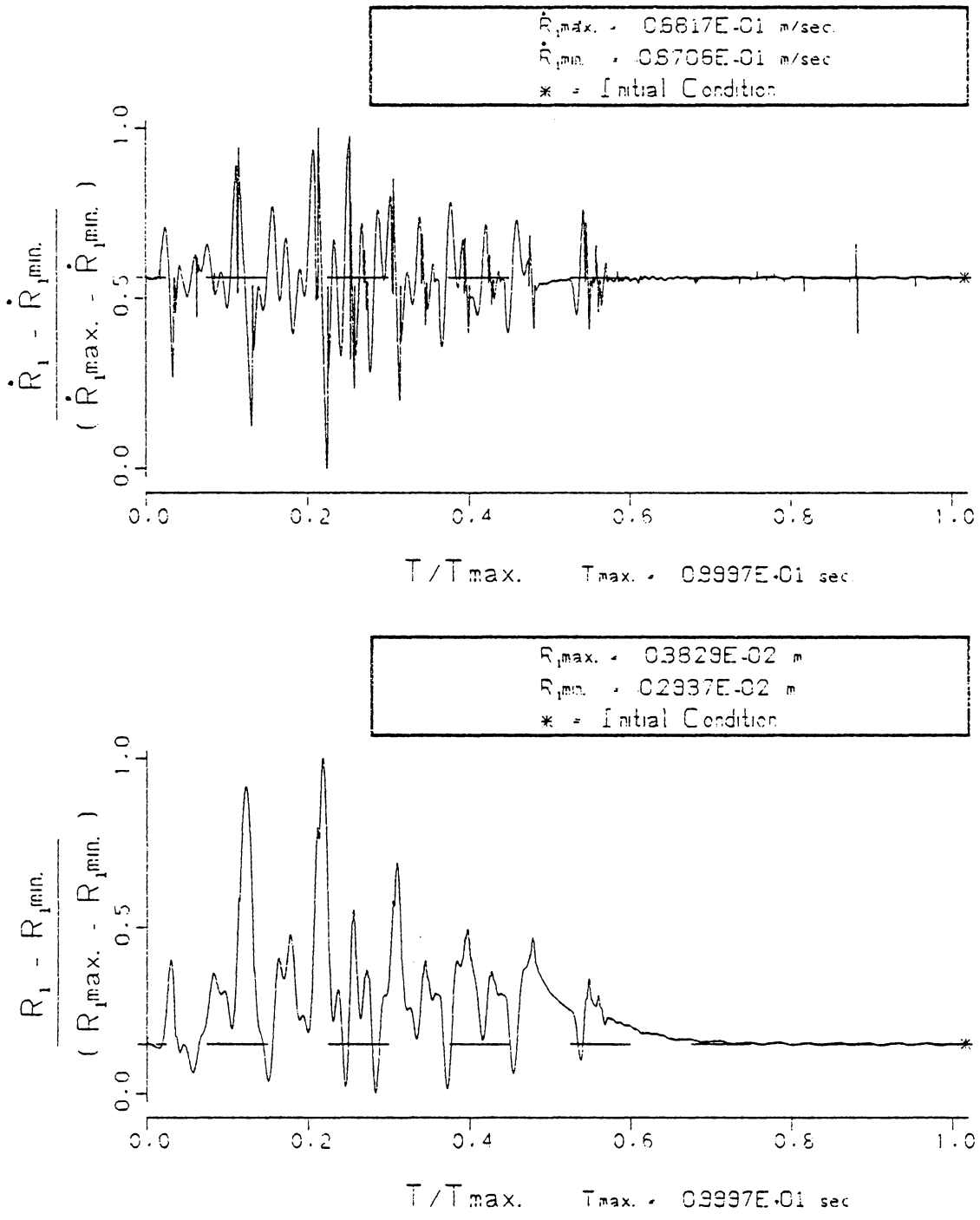

FIG. 37 VERTICAL RESPONSE OF THE TRACKS. (R_1 , $\dot{R}_1$) FOR CONDITIONS OF CASE 6 WHEN THE CABLE DRUM BRAKE IS APPLIED DURING LOAD-LOWERING. (UNCOMPENSATED CRANE)

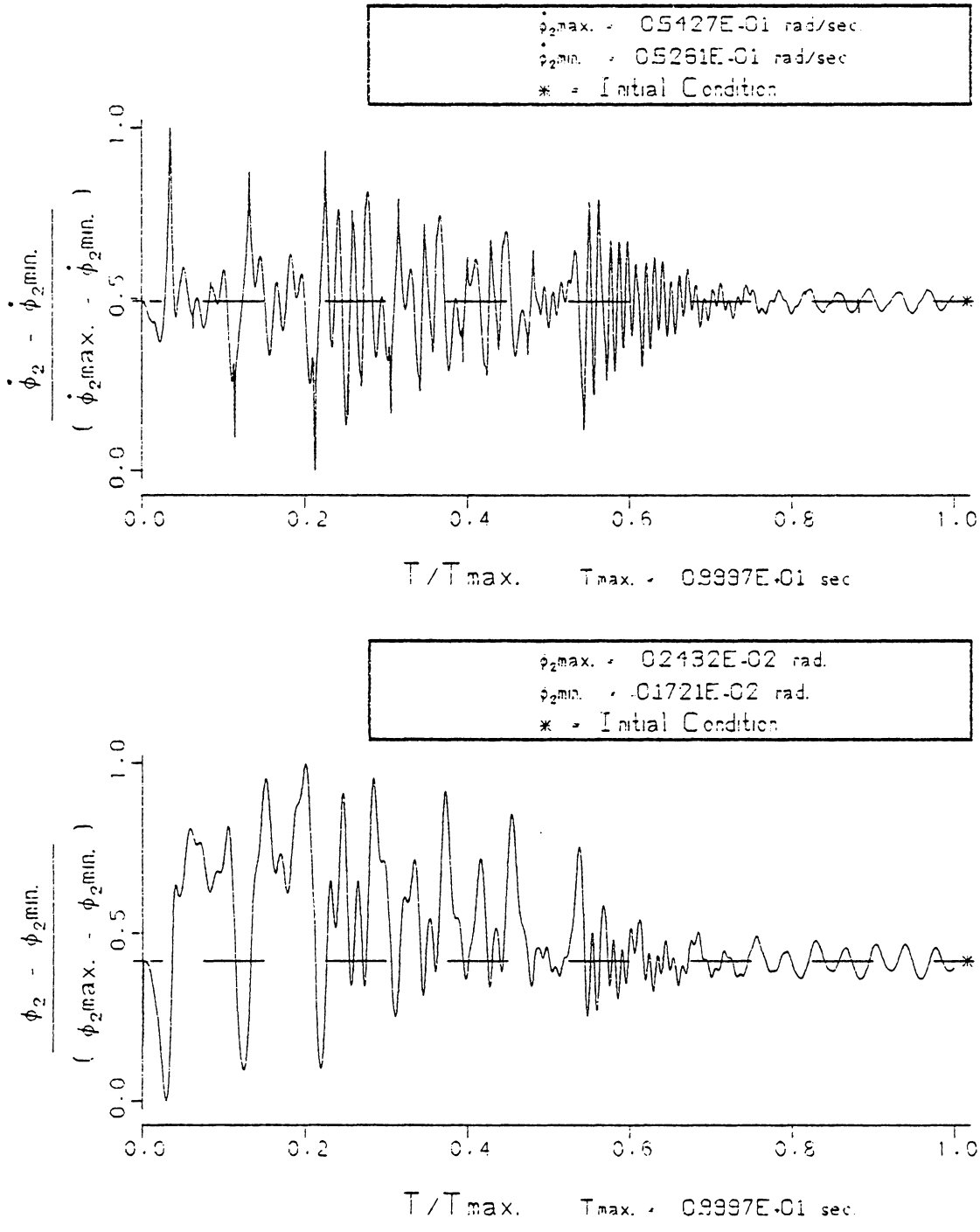

FIG. 38 ROTATIONAL RESPONSE OF THE TRACKS. (ϕ_2 , $\dot{\phi}_2$) FOR CONDITIONS OF CASE B WHEN THE CABLE DRUM BRAKE IS APPLIED DURING LOAD-LOWERING. (UNCOMPENSATED CRANE)

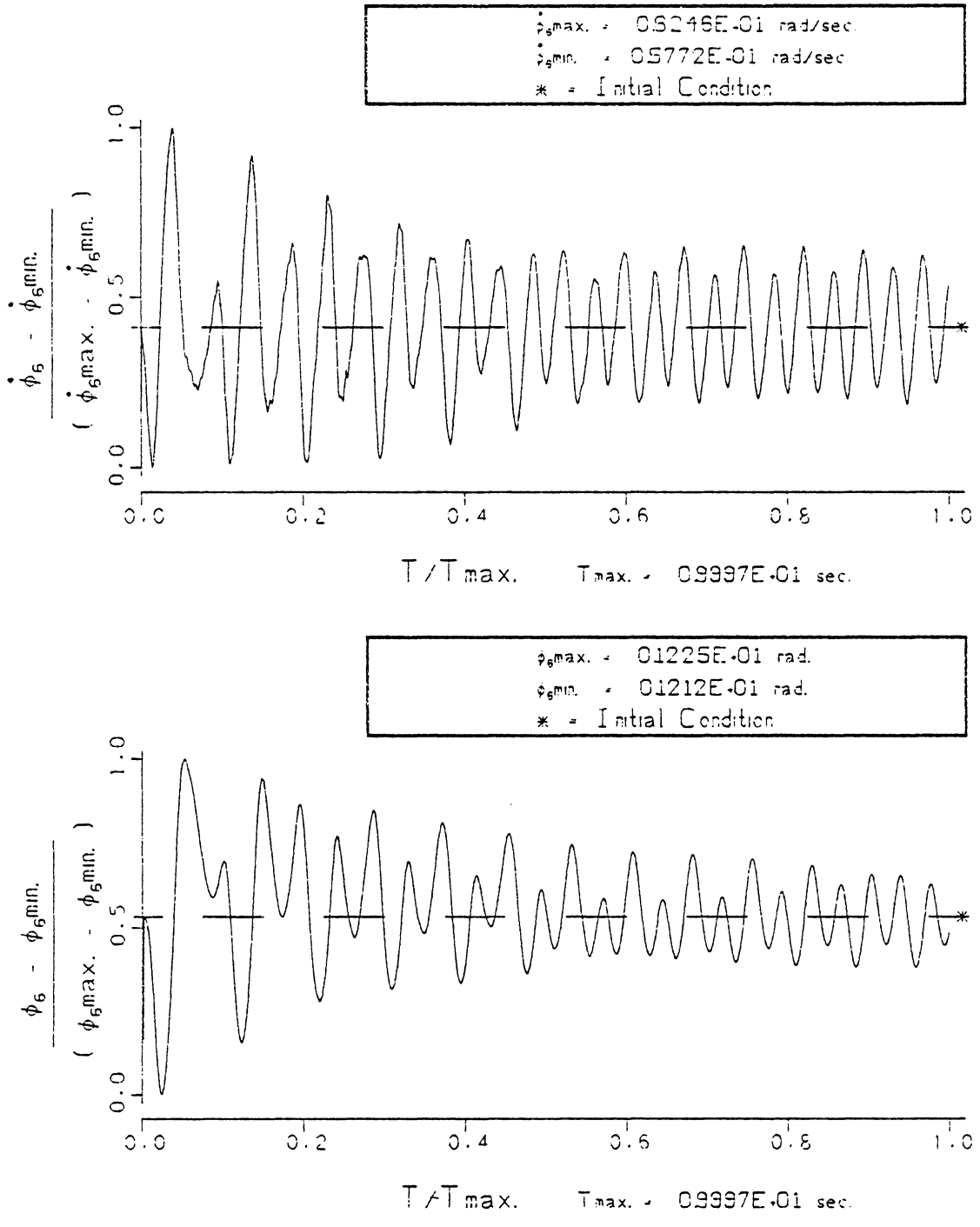

FIG. 39 ROTATIONAL RESPONSE OF THE BOOM CORD. (ϕ_6 , $\dot{\phi}_6$) FOR CONDITIONS OF CASE 5 WHEN THE CABLE DRUM BRAKE IS APPLIED DURING LOAD-LOWERING. (UNCOMPENSATED CRANE)

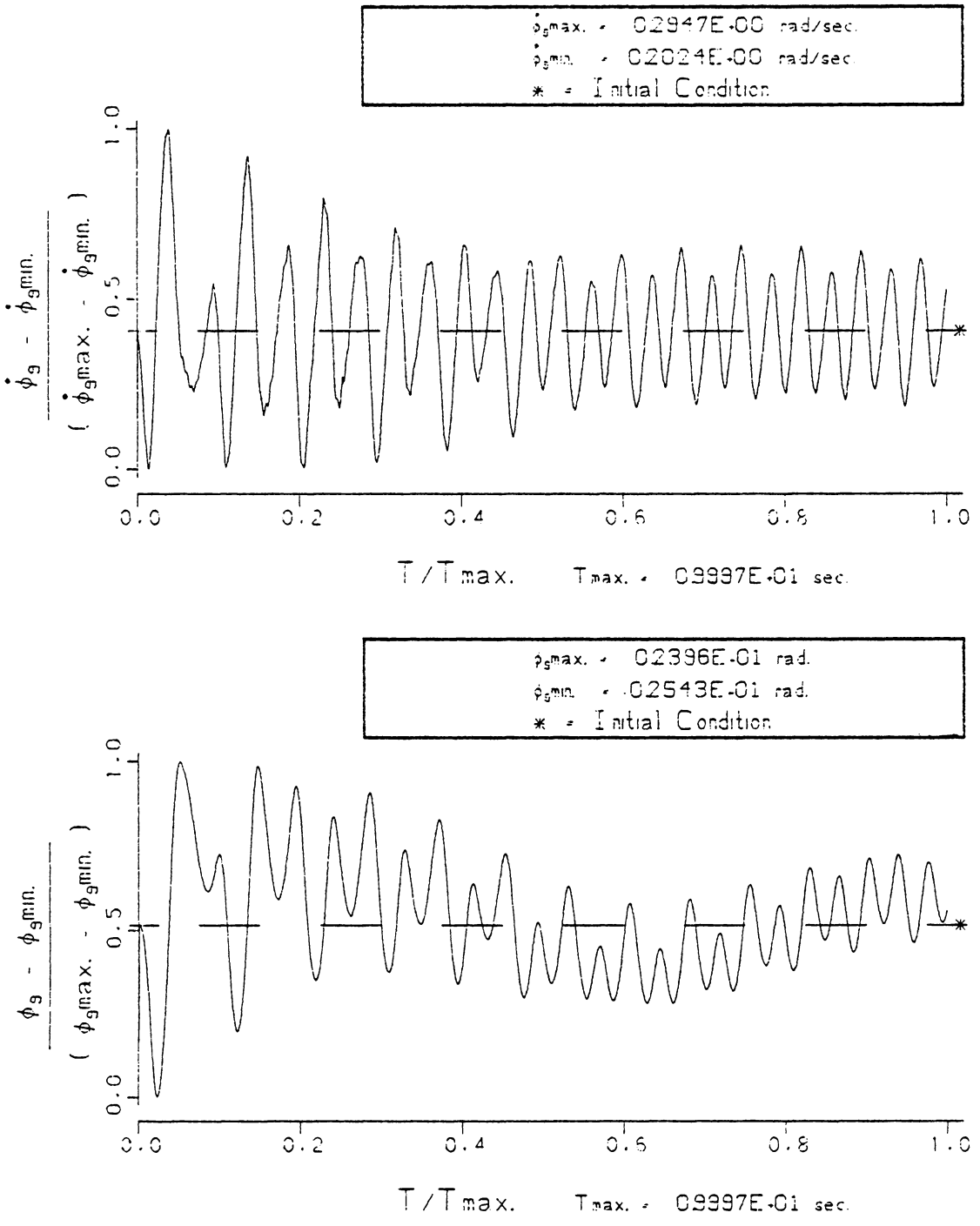

FIG. 40 PENDULATION OF THE LOAD. (ϕ_g $\dot{\phi}_g$)
FOR CONDITIONS OF CASE B WHEN THE CABLE
DRUM BRAKE IS APPLIED DURING LOAD-LOWERING.
(UNCOMPENSATED CRANE)

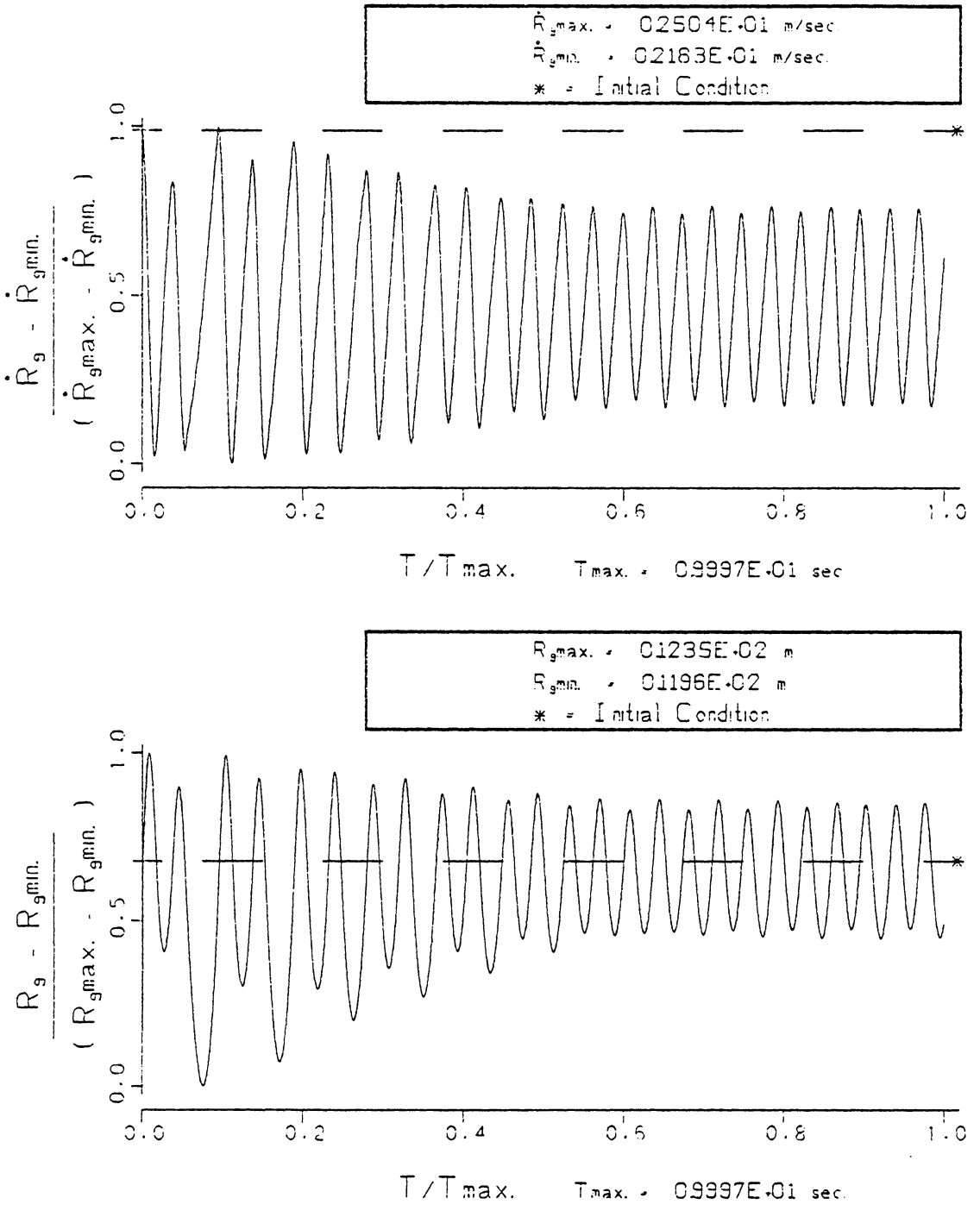

FIG. 41 STRETCH OF THE LOAD LINE CABLE. (R_g , $\dot{R}_g$) FOR CONDITIONS OF CASE 5 WHEN THE CABLE DRUM BRAKE IS APPLIED DURING LOAD-LOWERING. (UNCOMPENSATED CRANE)

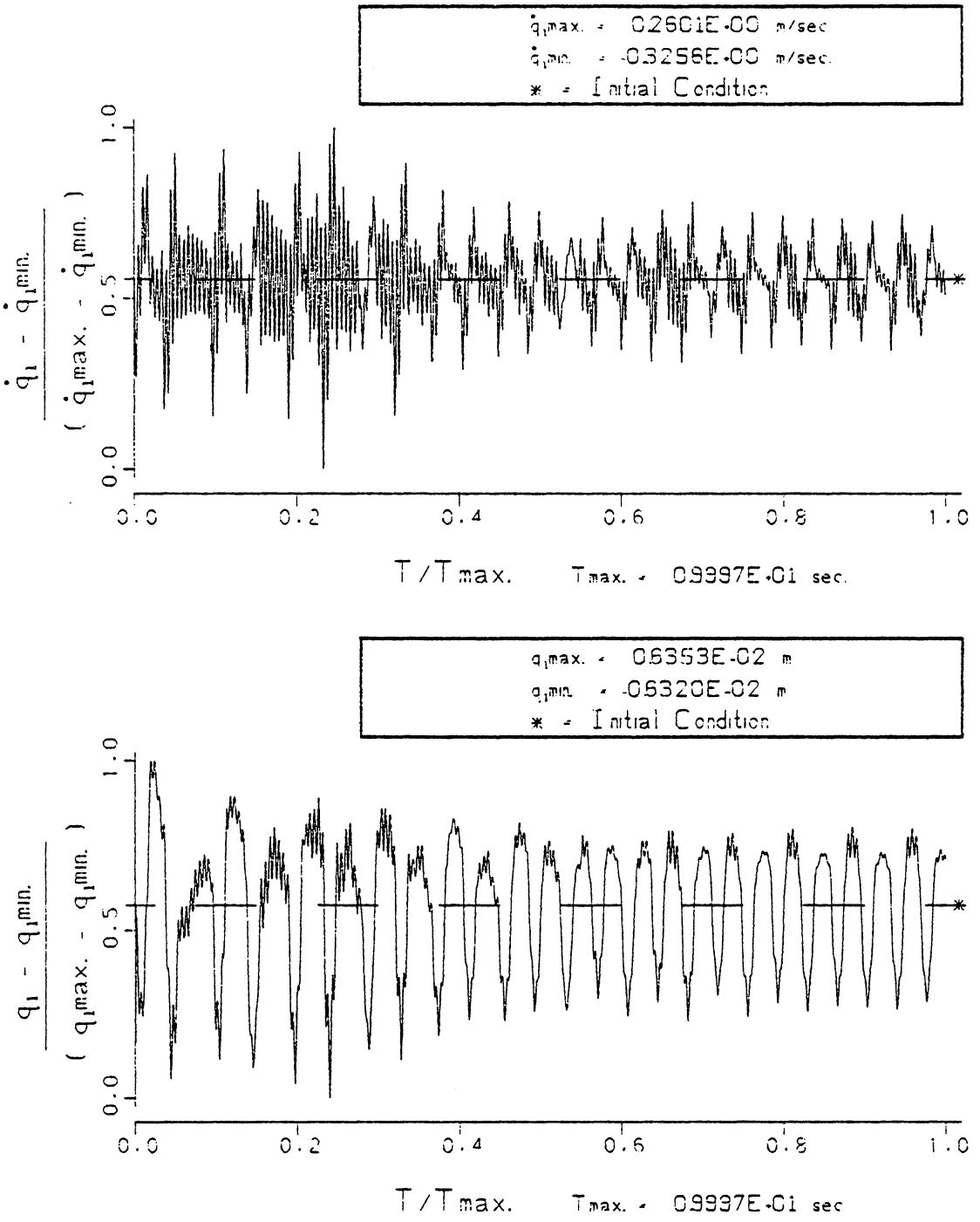

FIG. 42 LOWER BOOM JOINT RESPONSE. (q_1 , $\dot{q}_1$) FOR CONDITIONS OF CASE 5 WHEN THE CABLE DRUM BRAKE IS APPLIED DURING LOAD-LOWERING. (UNCOMPENSATED CRANE)

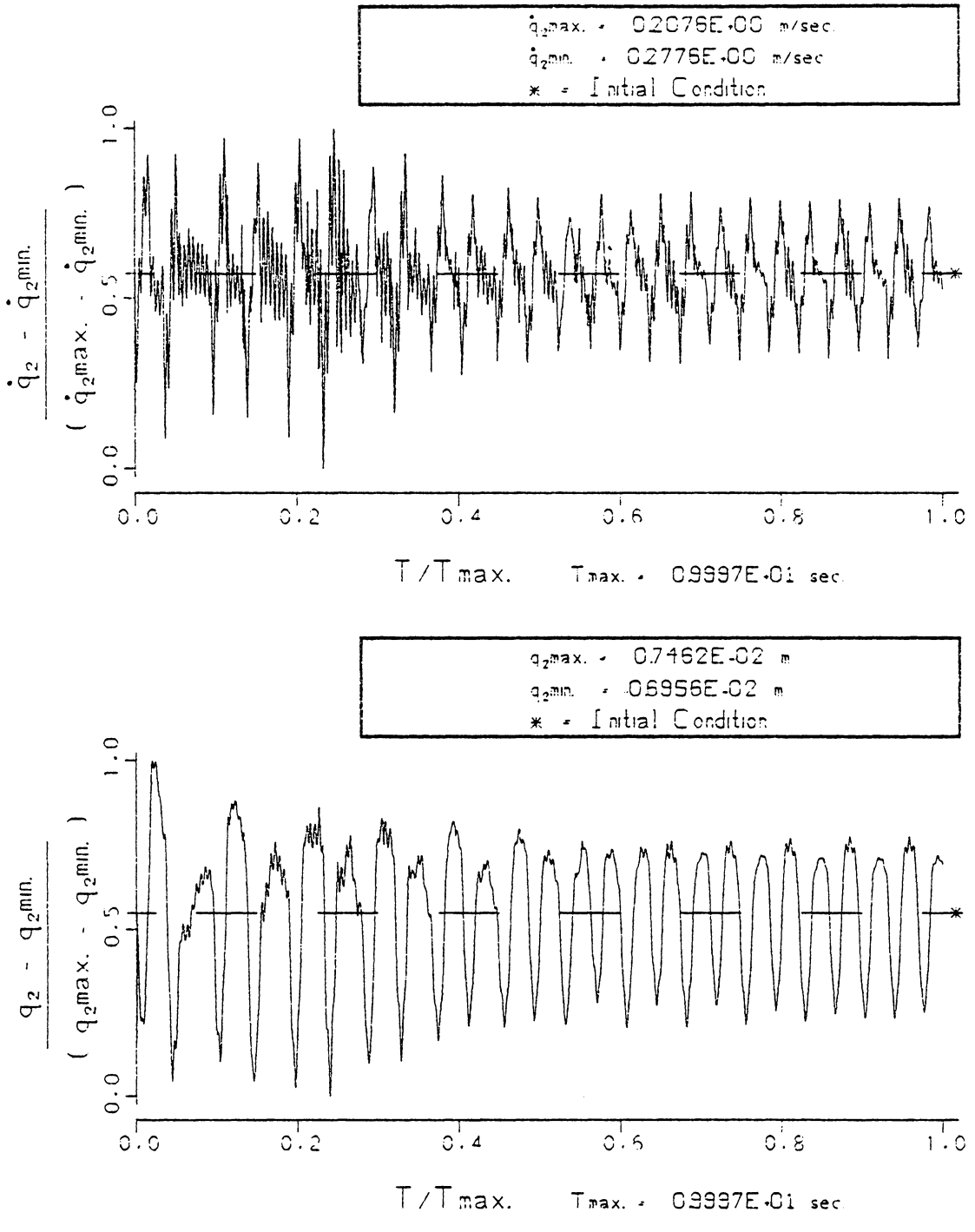

FIG. 43 UPPER BOOM JOINT RESPONSE. (q_2 , $\dot{q}_2$) FOR CONDITIONS OF CASE B WHEN THE CABLE DRUM BRAKE IS APPLIED DURING LOAD-LOWERING. (UNCOMPENSATED CRANE)

R_1 in Fig. 24. This response is clearly a result of the sudden application of the cable drum brakes. The largest rotation of the tracks in Case B, as seen in Fig. 38, occurs at 2.0 sec and the largest vertical translation at 2.2 sec from Fig. 37. The motion of the ground coordinates grow to a maximum at this point, and then begin to damp out and return to equilibrium. The load oscillation, coordinate R_9 in Fig. 41, at the point of maximum ground motion has already damped out significantly. The ground response is clearly the result of a secondary shock caused by the nonlinear coupling in the system. This coupling is again apparent in Fig. 38; the potential and kinetic energy of the crane system influenced by the rotational response of the tracks is at a minimum at 5.0 seconds because ϕ_2 and $\dot{\phi}_2$ are at a minimum. The system energy at this point has not been dissipated, only transferred, because the energy returns to the track rotation at 5.5 seconds where ϕ_2 and $\dot{\phi}_2$ grow to a relative maximum again. The energy transfer in the crane system which produces this ground motion reinforces the need for the model's complexity.

Reducing the shear modulus of the soil from 82.7 MPa in Case A to 62.0 MPa in Case B has increased the dominate frequency characterizing the ground motion from 7.0 Hz in Figs. 31 and 32 to 11.5 Hz in Figs. 44 and 45. The lower soil modulus also produces more system damping as evidenced in each of the coordinate time histories.

The time histories of coordinates ϕ_6 and ϕ_9, as seen in Figs. 39 and 40, are again similar because the boom chord rotation and the load pendulation are strongly coupled. A curious system frequency

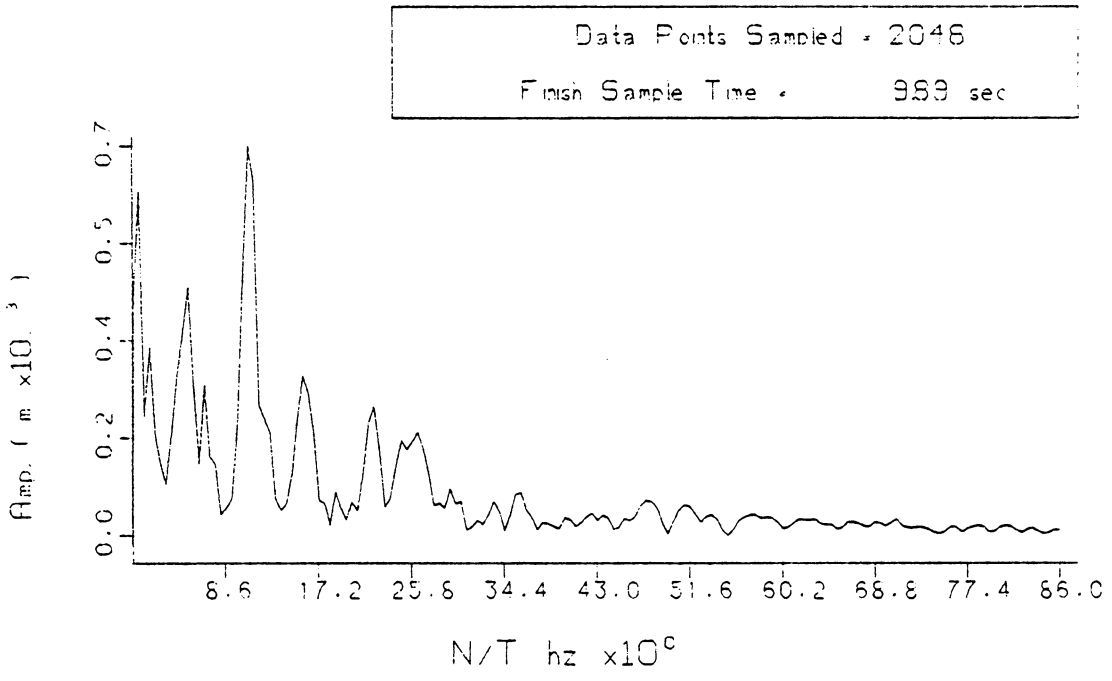

FIG. 44 FREQUENCY ANALYSIS OF COORDINATE R_1 FOR THE CONDITIONS OF CASE 5 WHILE BRAKING AT LOAD LOWERING (UNCOMPENSATED)

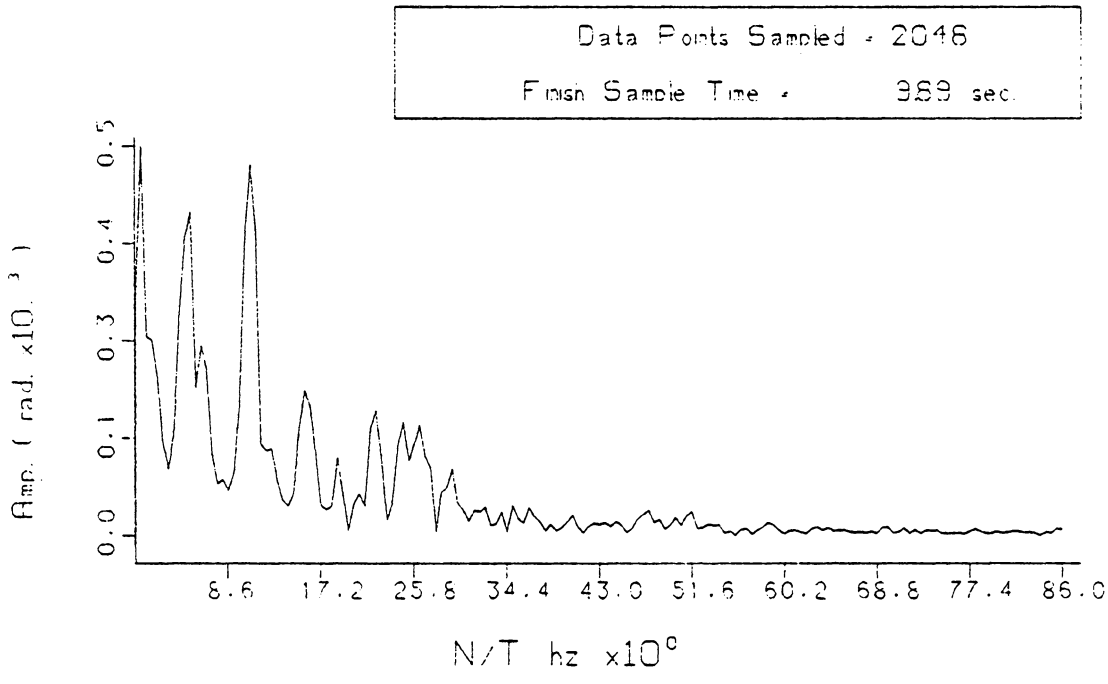

FIG. 45 FREQUENCY ANALYSIS OF COORDINATE ϕ_2 FOR THE CONDITIONS OF CASE 5 WHILE BRAKING AT LOAD LOWERING. (UNCOMPENSATED)

which is lower than all other component frequencies dominates the pendulation of the load in Case B as seen in Fig. 46. This lower system frequency is present in the frequency content of coordinate ϕ_9 in Case A (see Fig. 34), but with one-third the magnitude of Case B.

Coordinates q_1 and q_2, shown in Figs. 42 and 43, characterize the boom response. The boom displacements, q_1 and q_2, and velocities, $\dot{q}_1$ and $\dot{q}_2$, experience a pronounced beat phenomenon at 5.8 sec when both the potential and kinetic energy of the boom are at a minimum. This energy transfer which represents about 5% of the total system energy reinforces the need to include a flexible boom model.

The plot of the pendent line tension given in Fig. 47 portrays the effects of the two significant changes in the simulation constants of Case B. Referring to Figs. 29 and 47, the steeper boom chord angle in Case B causes the pendent lines to go slack for longer periods, and the softer soil foundation damps out the fluctuations in the pendent line tension more quickly.

The crane response presented in this simulation will serve as the uncompensated standard for the control study in Chapter 7.

Case C

The simulation constants chosen for Case C represent an extreme crane configuration. The ground shear modulus, 41.4 MPa, is half that used in Case A. The 91.4 m boom, twice that of Case A, operates at a 70° angle. The remaining parameters are identical to those used in Case B.

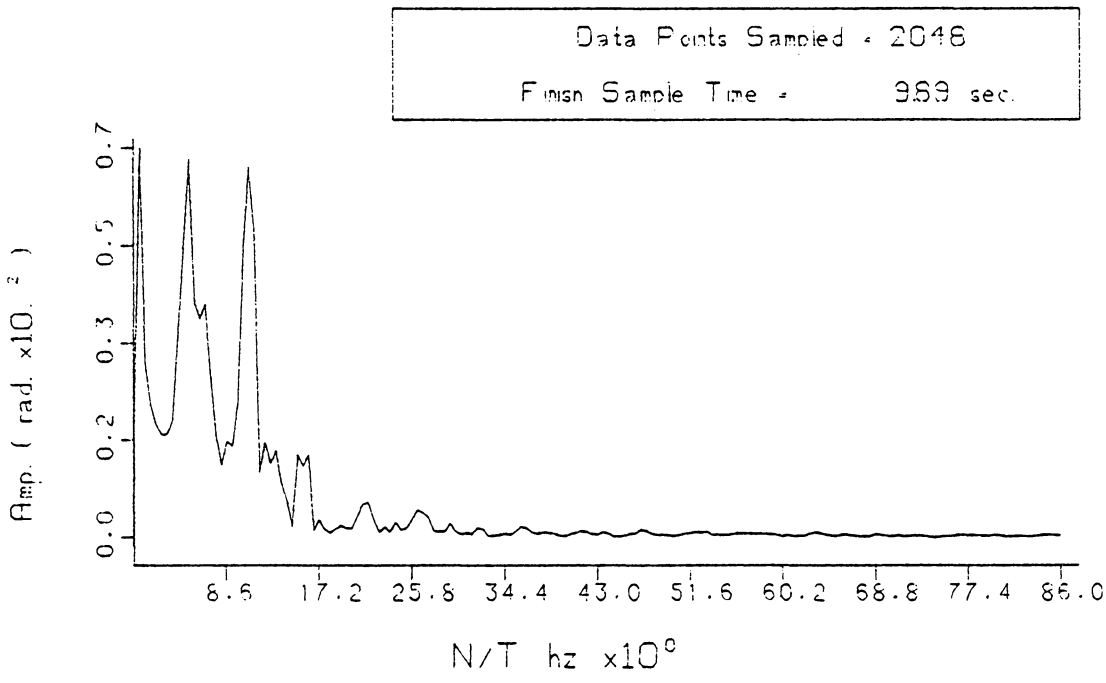

FIG. 46 FREQUENCY ANALYSIS OF COORDINATE ϕ_s FOR THE CONDITIONS OF CASE B WHILE BRAKING AT LOAD LOWERING. (UNCOMPENSATED)

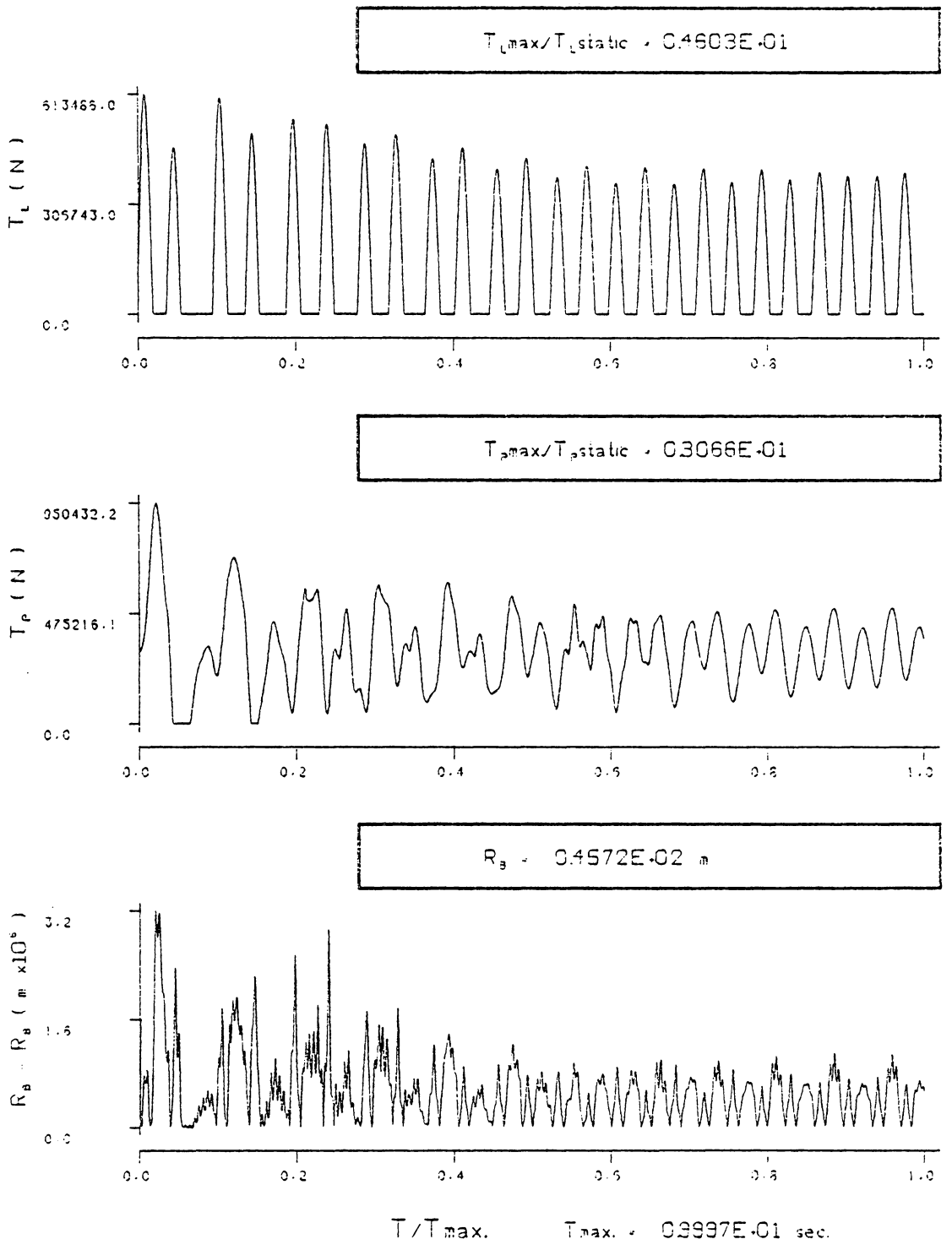

FIG. 47 THE TIME DEPENDENT BOOM CORD LENGTH. (R_B) AND THE TENSION IN THE PENDENT AND LOAD LINE ASSEMBLIES. (T_p AND T_L) FOR THE CONDITIONS OF CASE B (UNCOMPENSATED)

The response of the crane system in this case is expected to be more dramatic, and therefore offers a control system the potential for greater compensation. Plots of the generalized coordinate displacements and velocities are presented.

The time histories of the generalized coordinates in Case C are presented in Figs. 48 through 54. The softer soil foundation produces some interesting crane system responses. The coupling between the ground coordinates R_1 and ϕ_2 is extremely prominent in this case; the response records given in Figs. 48 and 49 are almost identical as are their frequency contents given in Figs. 55 and 56. This strong coupling is responsible for the beat phenomenon which exists in coordinates R_1 and ϕ_2.

The ground motion in this case, as in others, is characterized by multiple frequencies, but the lowest frequency in this case, 2.0 Hz from Figs. 55 and 56, dominates the ground motion. Ironically, the ground motion in Case A, corresponding to an 82.7 MPa soil modulus, is characterized by a dominate frequency of 7.0 Hz in Fig. 31, and the ground motion in Case B, corresponding to a soil modulus of 62.0 MPa, is characterized by a dominate frequency of 11.5 Hz in Fig. 44. The slower ground response is apparent in the time histories of coordinates R_1 and ϕ_2 in Figs. 48 and 49. The maximum rotation and vertical translation of the tracks does not occur until 1.0 sec after the vertical drop of the load. Notice, in Fig. 48, that the crane tracks are displaced above the initial condition for the entire 10 seconds of simulation.

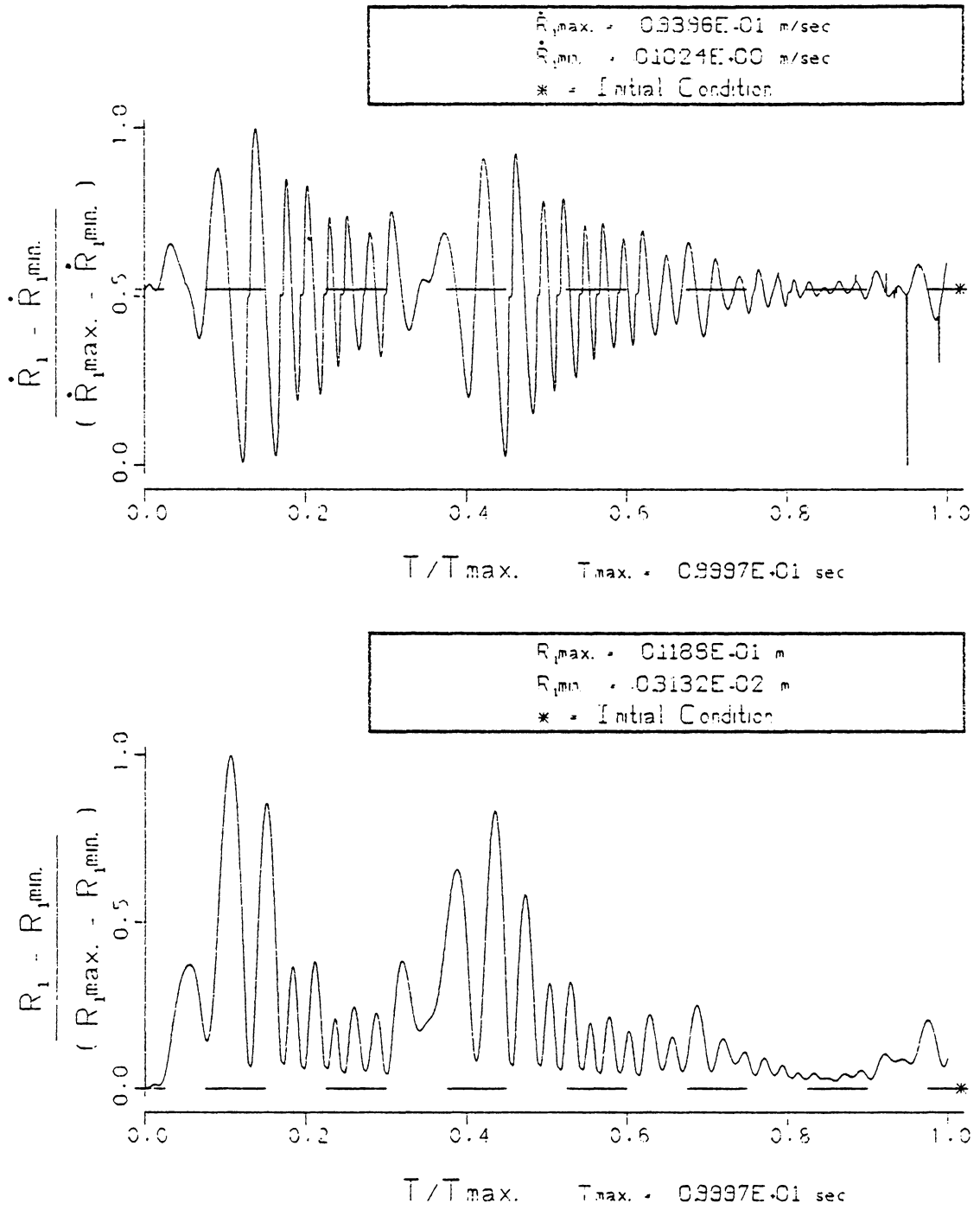

FIG. 48 VERTICAL RESPONSE OF THE TRACKS. (R_1 , $\dot{R}_1$) FOR CONDITIONS OF CASE C WHEN THE CABLE DRUM BRAKE IS APPLIED DURING LOAD-LOWERING. (UNCOMPENSATED CRANE)

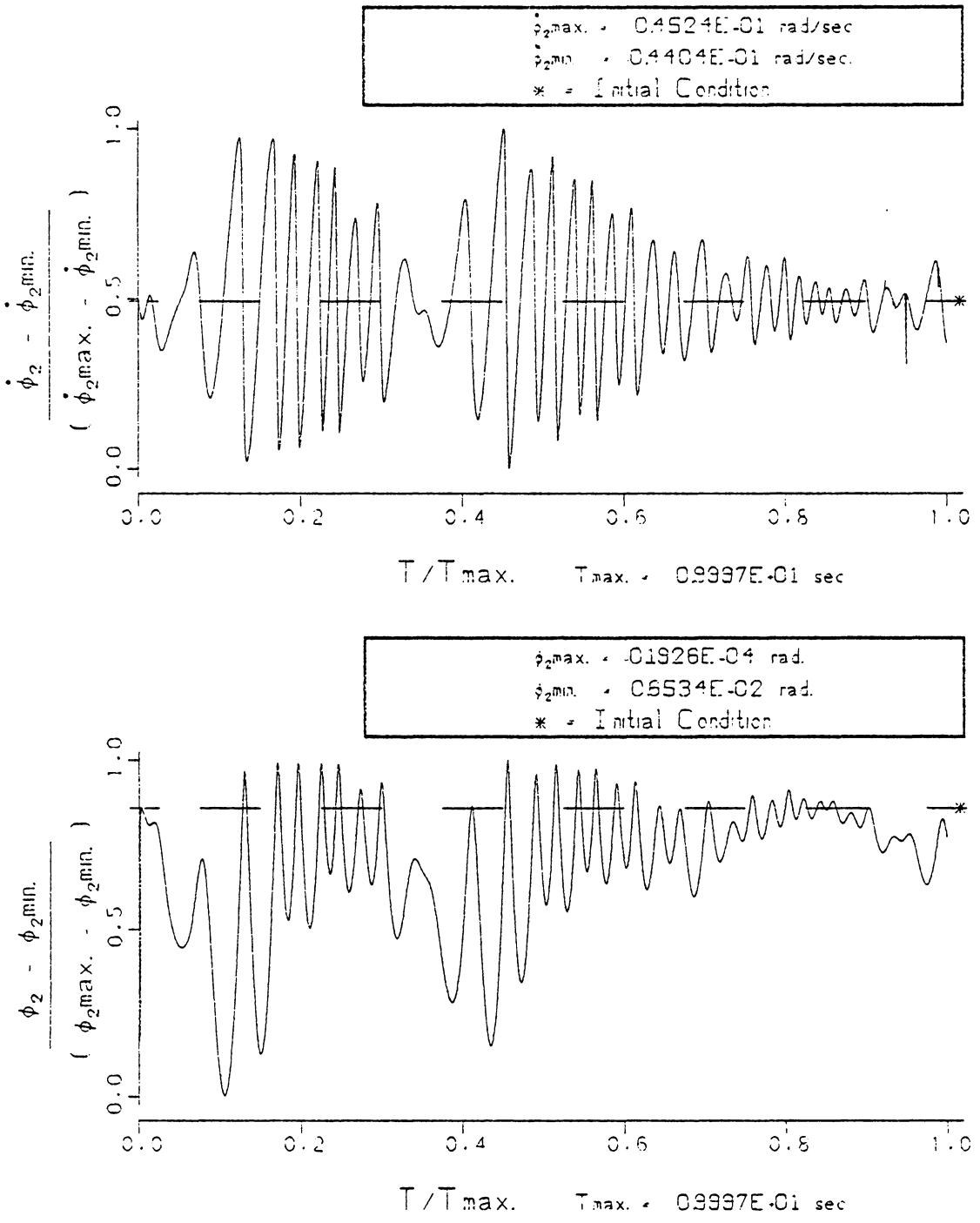

FIG. 49 ROTATIONAL RESPONSE OF THE TRACKS. (ϕ_2 , $\dot{\phi}_2$) FOR CONDITIONS OF CASE C WHEN THE CABLE DRUM BRAKE IS APPLIED DURING LOAD-LOWERING. (UNCOMPENSATED CRANE)

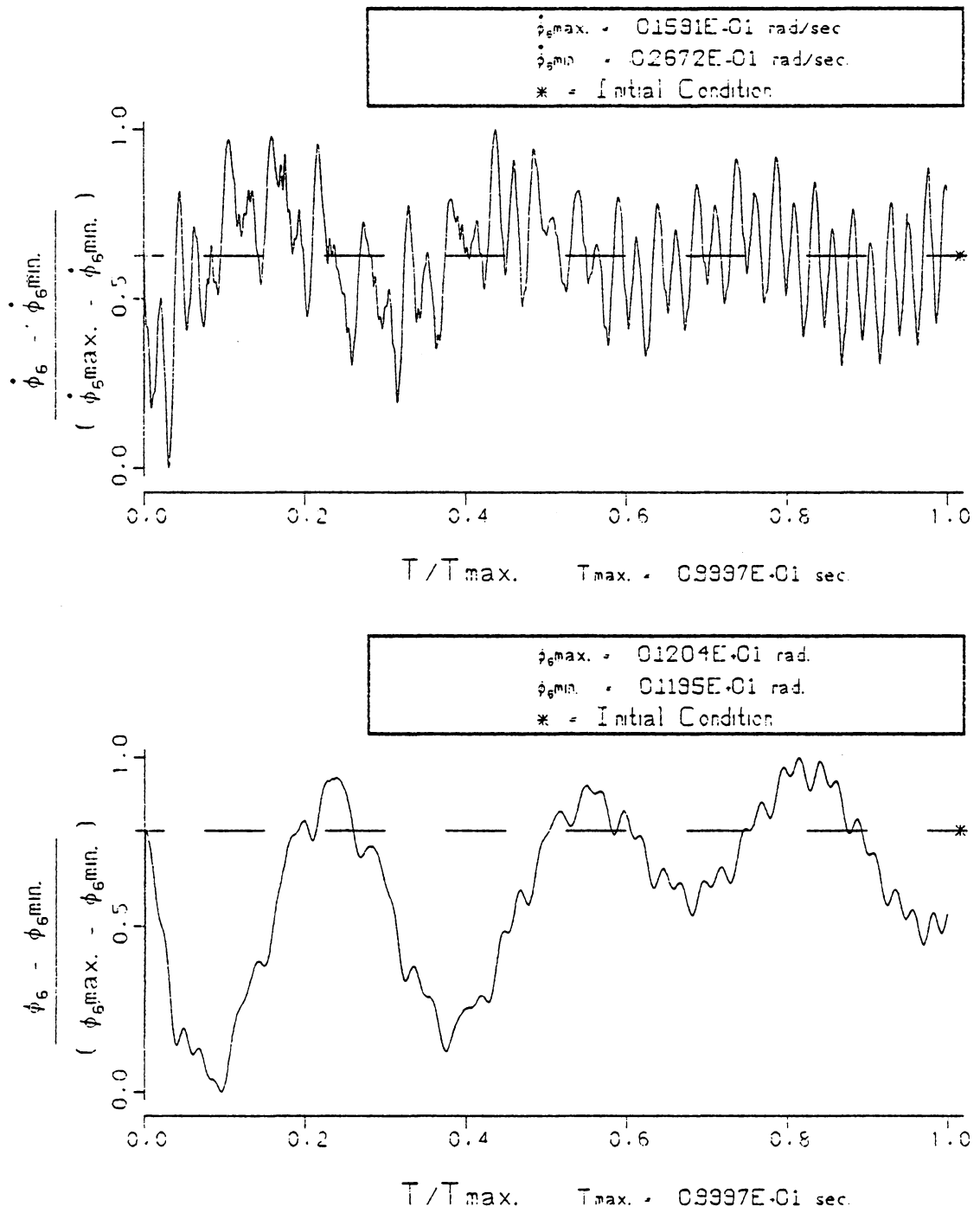

FIG. 50 ROTATIONAL RESPONSE OF THE BOOM CORD. (ϕ_5 , $\dot{\phi}_5$) FOR CONDITIONS OF CASE C WHEN THE CABLE DRUM BRAKE IS APPLIED DURING LOAD-LOWERING. (UNCOMPENSATED CRANE)

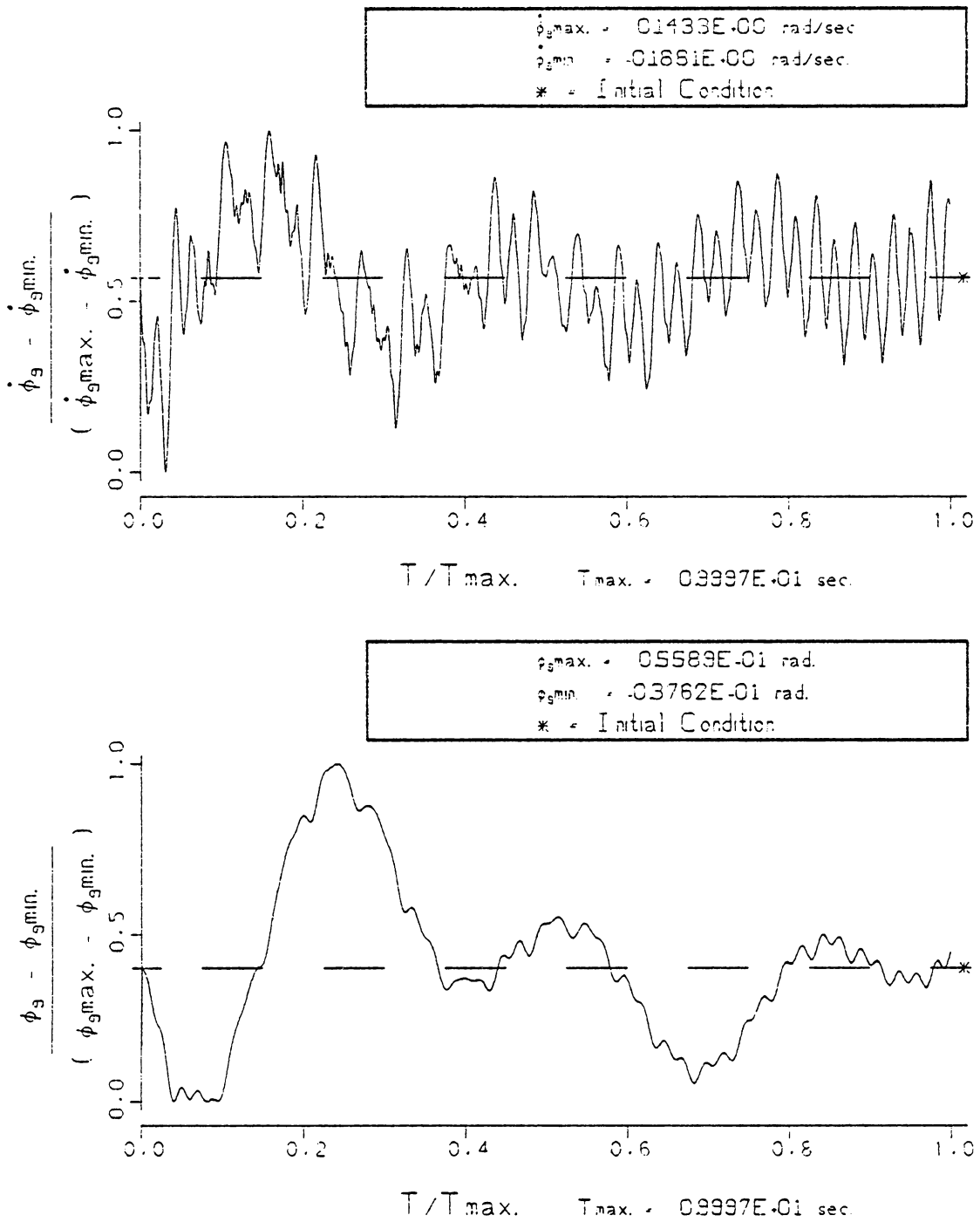

FIG. 51 PENDULATION OF THE LOAD. (ϕ_g , $\dot{\phi}_g$)
FOR CONDITIONS OF CASE C WHEN THE CABLE
DRUM BRAKE IS APPLIED DURING LOAD-LOWERING.
(UNCOMPENSATED CRANE)

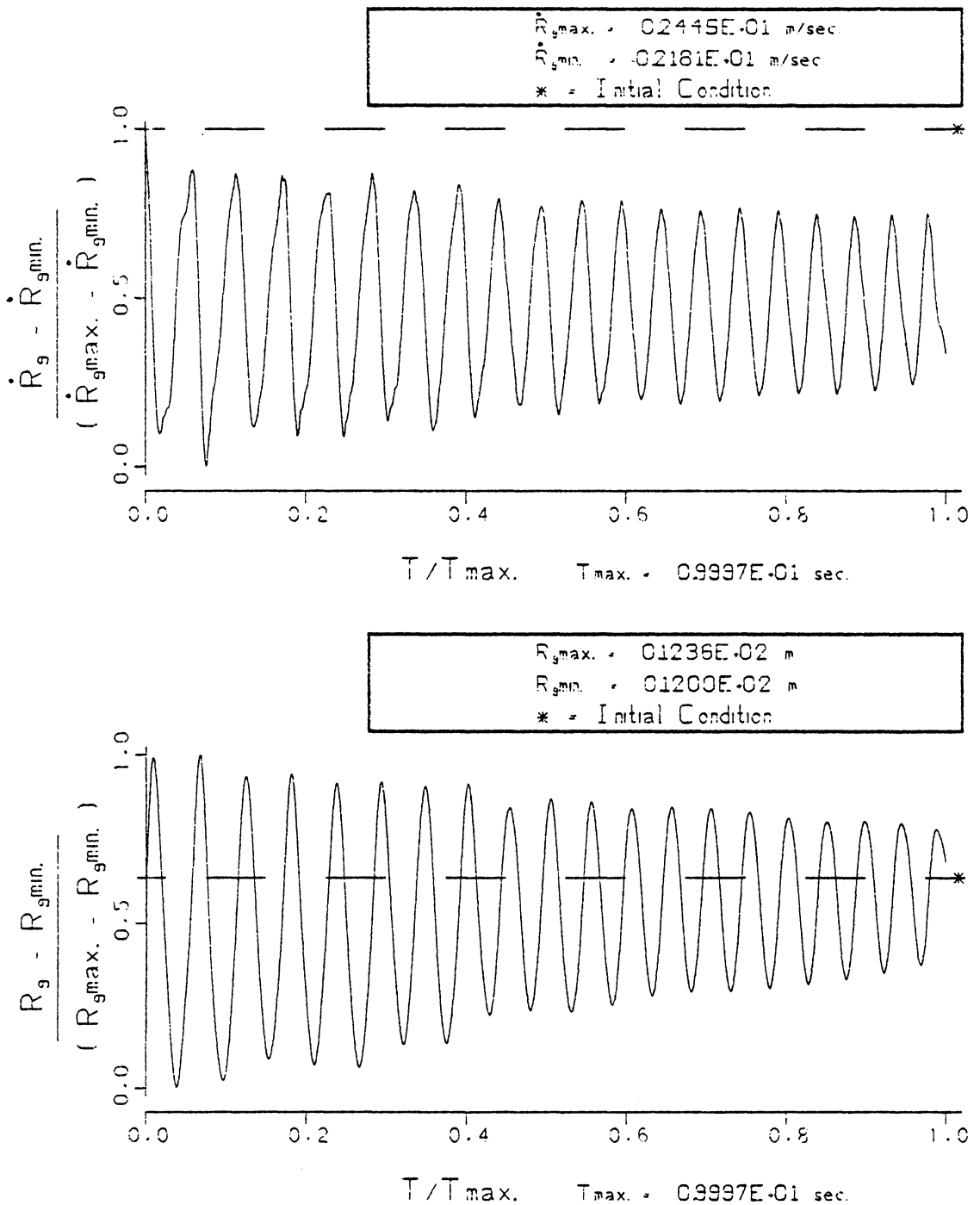

FIG. 52 STRETCH OF THE LOAD LINE CABLE. (R_g , $\dot{R}_g$) FOR CONDITIONS OF CASE C WHEN THE CABLE DRUM BRAKE IS APPLIED DURING LOAD-LOWERING. (UNCOMPENSATED CRANE)

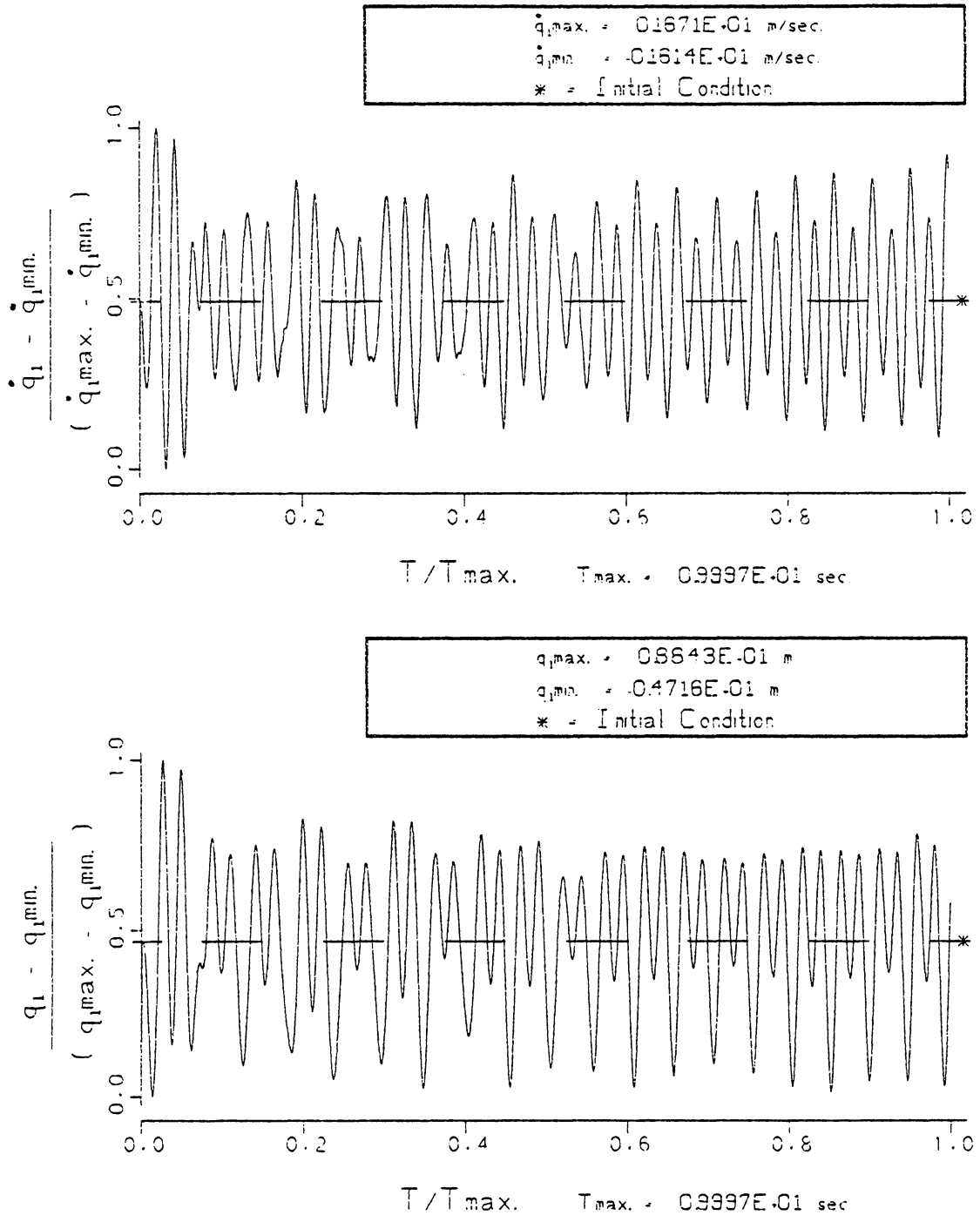

FIG. 53 LOWER BOOM JOINT RESPONSE. (q_1 , $\dot{q}_1$)
FOR CONDITIONS OF CASE C WHEN THE CABLE
DRUM BRAKE IS APPLIED DURING LOAD-LOWERING.
(UNCOMPENSATED CRANE)

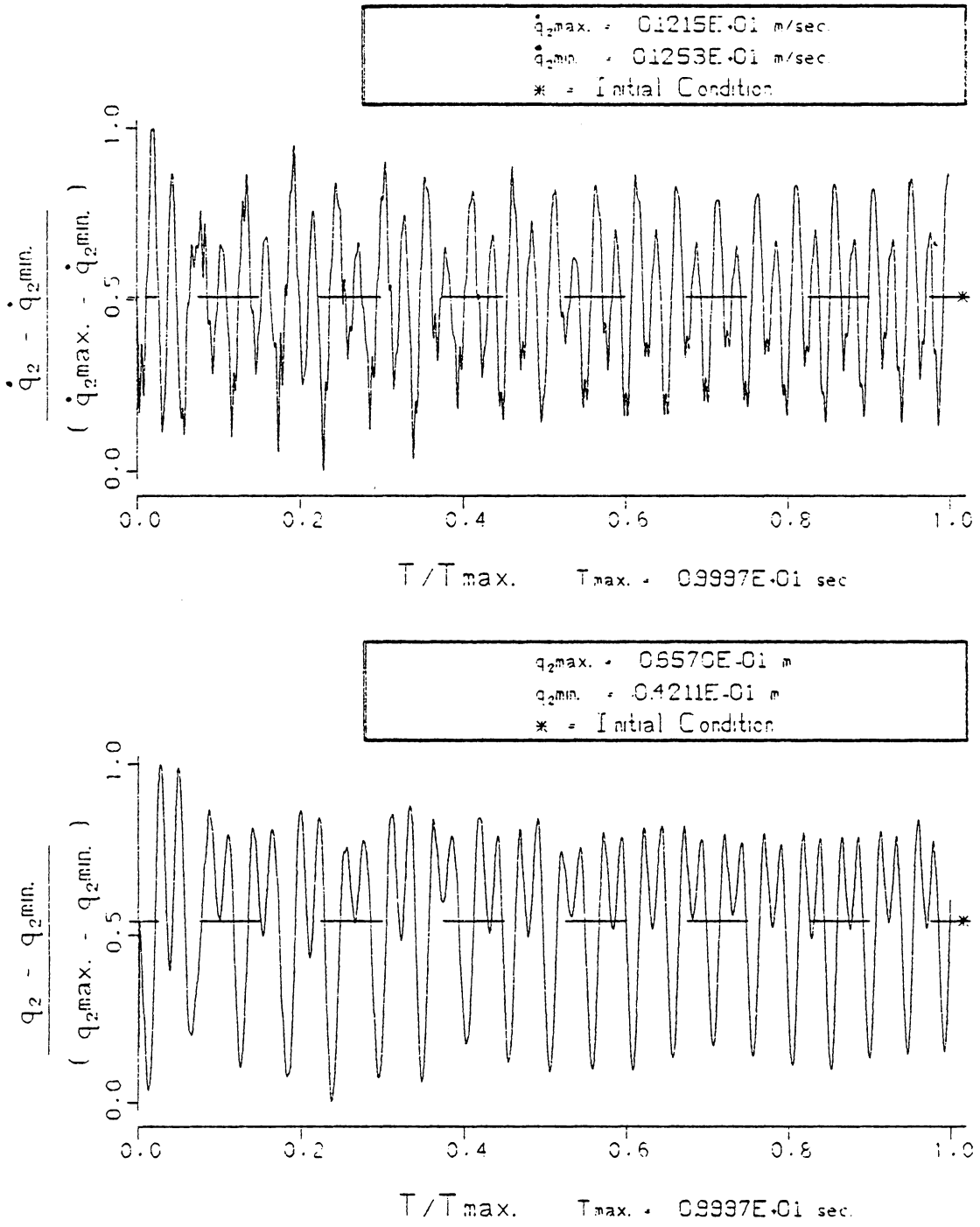

FIG. 54 UPPER BOOM JOINT RESPONSE. (q_2 , $\dot{q}_2$) FOR CONDITIONS OF CASE C WHEN THE CABLE DRUM BRAKE IS APPLIED DURING LOAD-LOWERING. (UNCOMPENSATED CRANE)

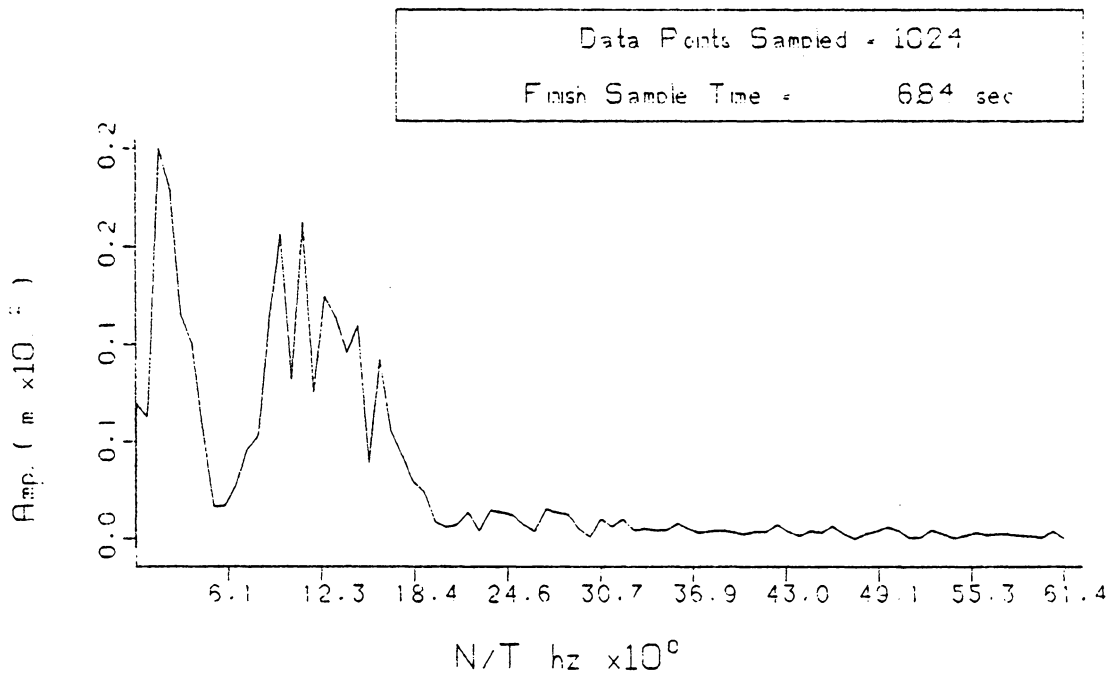

FIG. 55 FREQUENCY ANALYSIS OF COORDINATE R_1 FOR THE CONDITIONS OF CASE C WHILE BRAKING AT LOAD LOWERING. (UNCOMPENSATED)

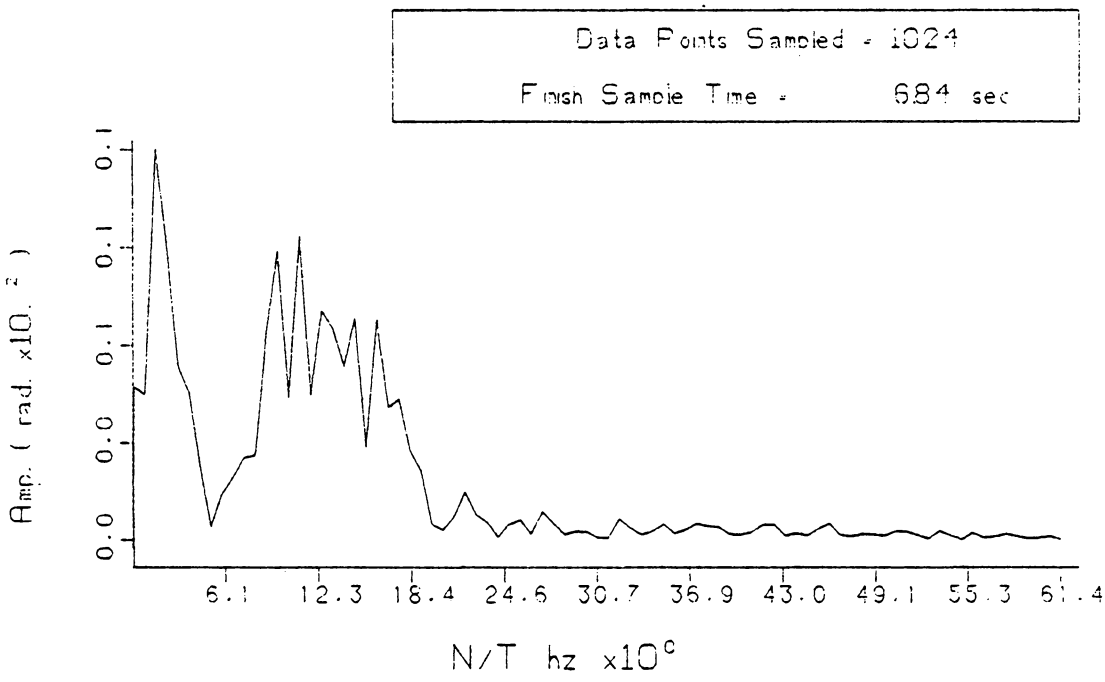

FIG. 56 FREQUENCY ANALYSIS OF COORDINATE ϕ_2 FOR THE CONDITIONS OF CASE C WHILE BRAKING AT LOAD LOWERING. (UNCOMPENSATED)

The boom chord rotation, ϕ_6 in Fig. 50, and the load pendulation, ϕ_9 in Fig. 51, in Case C look very different from both Case A and Case B since the motion of these coordinates is dominated by the single 2.0 Hz frequency as seen in Fig. 57.

The longer boom is responsible for the remaining peculiarities in this case. Notice that the initial vertical drop of the load does not produce the largest stretch in the load line, coordinate R_9 in Fig. 52, but subsequent coupled motion with the crane system does. The most curious effect of the longer boom is apparent in the boom displacements, q_1 and q_2, in Figs. 53 and 54. Although the load motion in Fig. 52 is significantly damped out at the end of the 10 second simulation; the boom motion shows no indication of damping. The frequency content of coordinate q_1, in Fig. 58, displays a very different nature than the frequency content of q_1 in Case A as seen in Fig. 36.

The lower damping effects in the longer boom are perhaps most obvious in Fig. 59 since the boom chord length continues to oscillate at 10 sec with similar amplitudes as at 4 sec. Notice that the low frequency which characterizes the boom rotation in Fig. 50 also characterizes the tension in the pendent lines. The pendent lines do not become slack during the simulation, in fact, the fluctuation in the pendent line tension in Case C is much smaller than either Case A in Fig. 29 or Case B in Fig. 47.

This simulation represents the response of a crane operating near its limits, and is offered primarily to test the compensating controls in Chapter 7.

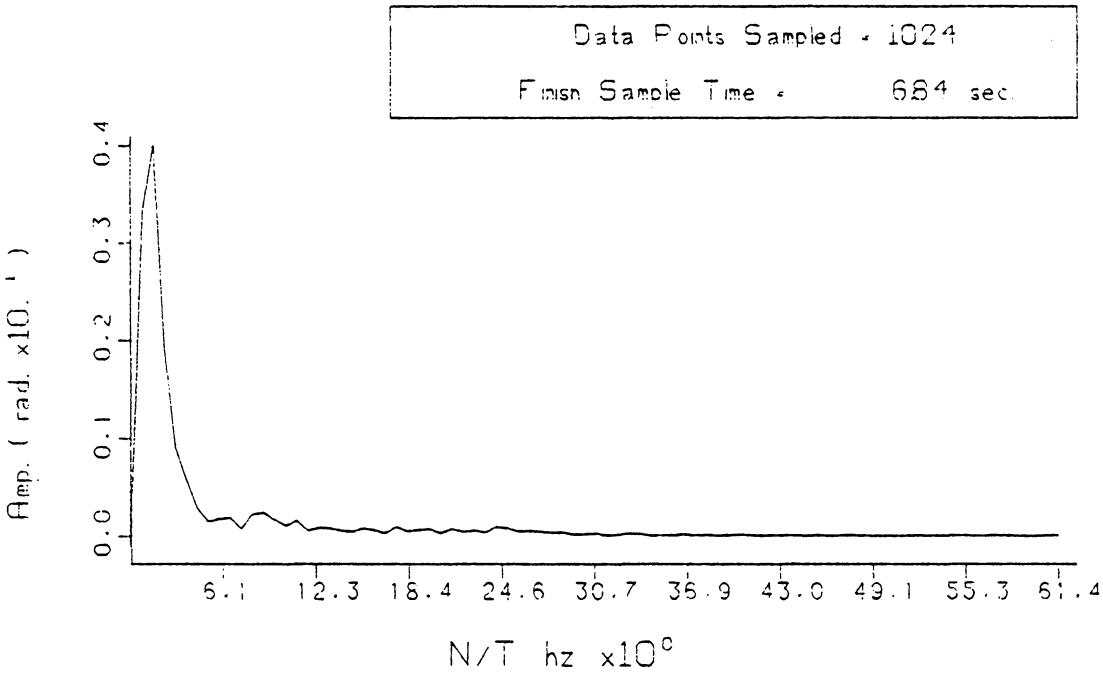

FIG. 57 FREQUENCY ANALYSIS OF COORDINATE ϕ_3 FOR THE CONDITIONS OF CASE C WHILE BRAKING AT LOAD LOWERING. (UNCOMPENSATED)

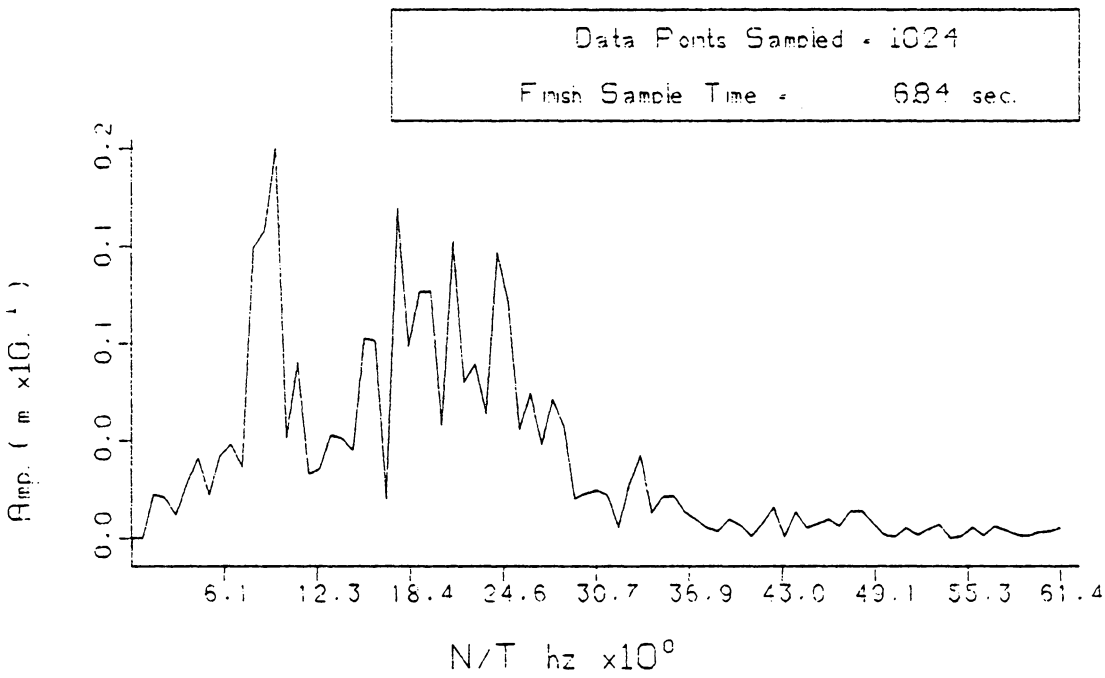

FIG. 58 FREQUENCY ANALYSIS OF COORDINATE q_1 FOR THE CONDITIONS OF CASE C WHILE BRAKING AT LOAD LOWERING. (UNCOMPENSATED)

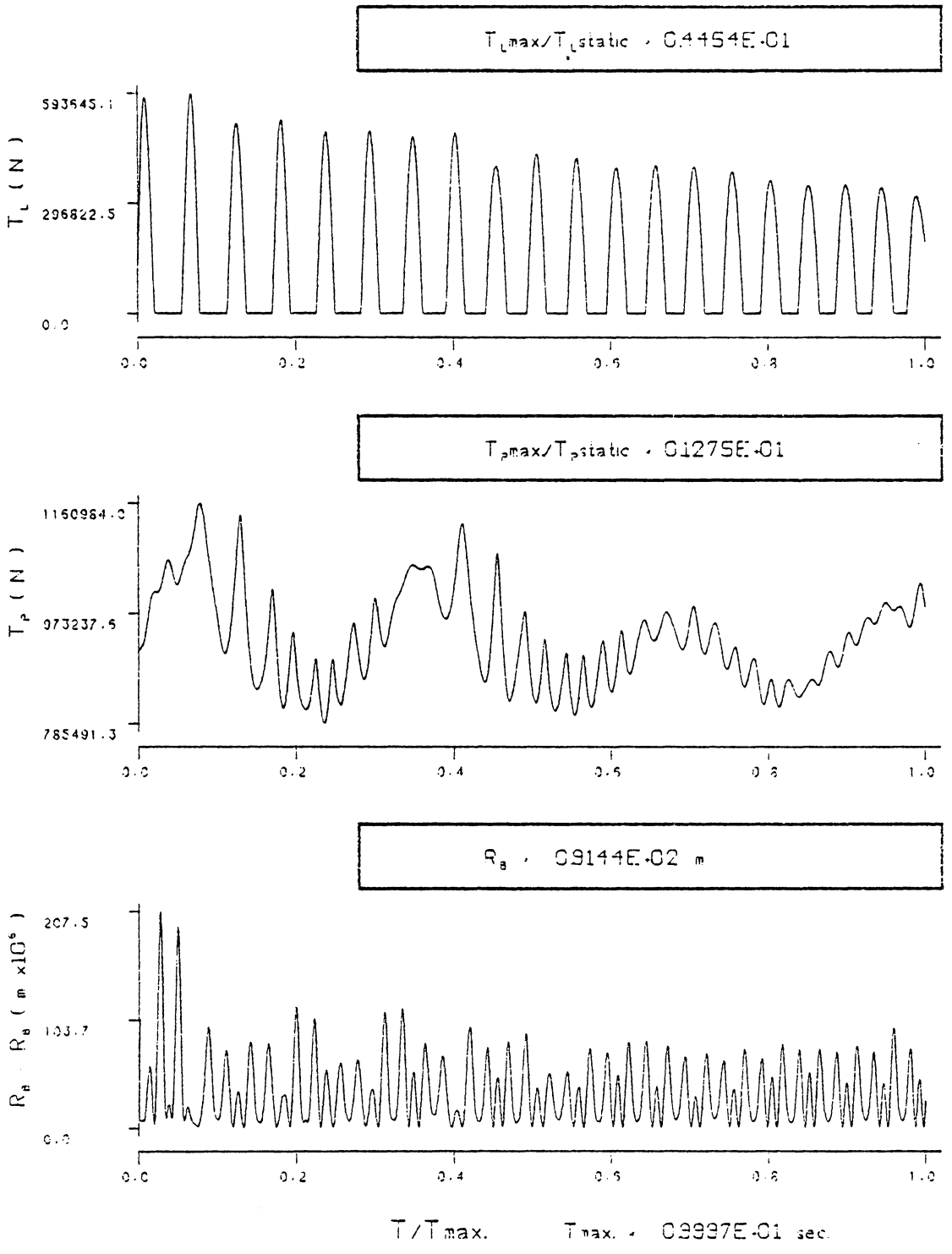

FIG. 59 THE TIME DEPENDENT BOOM CORD LENGTH. (R_B) AND THE TENSION IN THE PENDENT AND LOAD LINE ASSEMBLIES. (T_p AND T_L) FOR THE CONDITIONS OF CASE C (UNCOMPENSATED)

6. CONTROL SYSTEM DESIGN

The dynamic characteristics of a crane system are uniquely prescribed by its operating conditions. The response of the same crane, presented in Case A and Case B in Chapter 5, subjected to a different set of operating conditions varied significantly. This unique relationship is primarily responsible for causing crane operator errors which induce adverse dynamic loading conditions in the crane components.

A control system that is sensitive to the crane's dynamics and can compensate its response is developed in this chapter. The control system absorbs energy from the crane system which might otherwise induce large stresses in the crane components or even cause the crane to overturn. The large variety of operating conditions and the complexity of the crawler crane suggest that the control system should include an actuator with a feedback controller to insure stability and achieve maximum attenuation. The actuator dynamics which govern the control system's ability to respond to control inputs are developed first. The actuator control force is treated as a nonconservative external force, so the virtual work expression which describes the compensation effects on the crane dynamics are developed next. The chapter concludes with three simple compensation techniques used for feedback control.

The crawler crane and the suspended load can be viewed simply as two independent systems coupled at a single point, the boom tip. Previous studies by Patten (2), Dobeck (13), and Casler (15) suggest that these two systems transfer energy back and forth in such a fashion that the amplitudes of oscillation may potentially grow due to the nonlinear

inertial coupling between the two systems. If boom-tip excursions excite load pendulation, a control system which reduces boom-tip excursions could likely control the entire crane system. Casler (15) developed a boom-topping controller and attempted to reduce boom-tip motion induced by random base motion by actuating the boom-hoist winch; therefore, adjusting the length of the equalizing assembly. The crane operated on a ship deck at sea, and the controller was designed to compensate for boom-tip excursions caused by low frequency rocking motion of the ship. This controller does not suit a land-based crawler crane because the boom-hoist winch is not able to respond to the higher frequency base and structural motions present in land-based cranes. Although this controller successfully reduced boom-tip excursions at sea, Casler did not recommend the control technique because of its large power requirements.

The pendent controller chosen for this study controls boom-tip oscillations by adjusting the pendent line length. This controller is shown mounted between the equalizing assembly and the pendent cables in Fig. 60. The actuating device is a hydraulic valve-controlled piston, as shown schematically in Fig. 61. The actuator housing is securely mounted to the multiple-reeving block between the equalizing assembly and the pendent lines. The pendent lines are attached to the actuator piston, thus boom-tip control is effected by moving the actuator piston to adjust the functional length of the pendent line.

The equations of motion which describe the actuator dynamics are developed by first defining the equilibrium conditions for the actuator, as seen in Fig. 61. Hydraulic fluid occupies the chambers on both sides

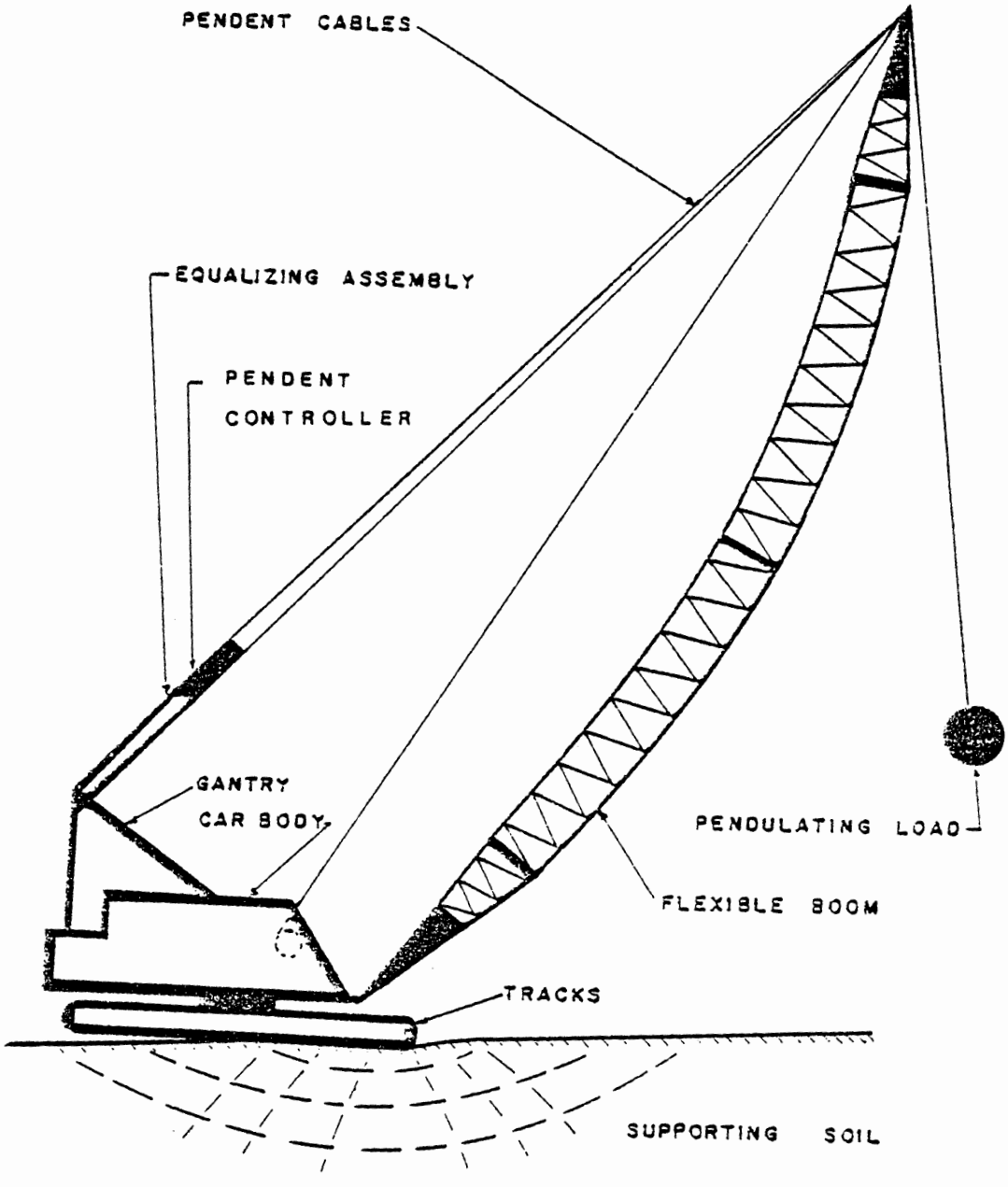

FIG. 60 PENDENT CONTROLLER MOUNTED ON A CRAWLER CRANE

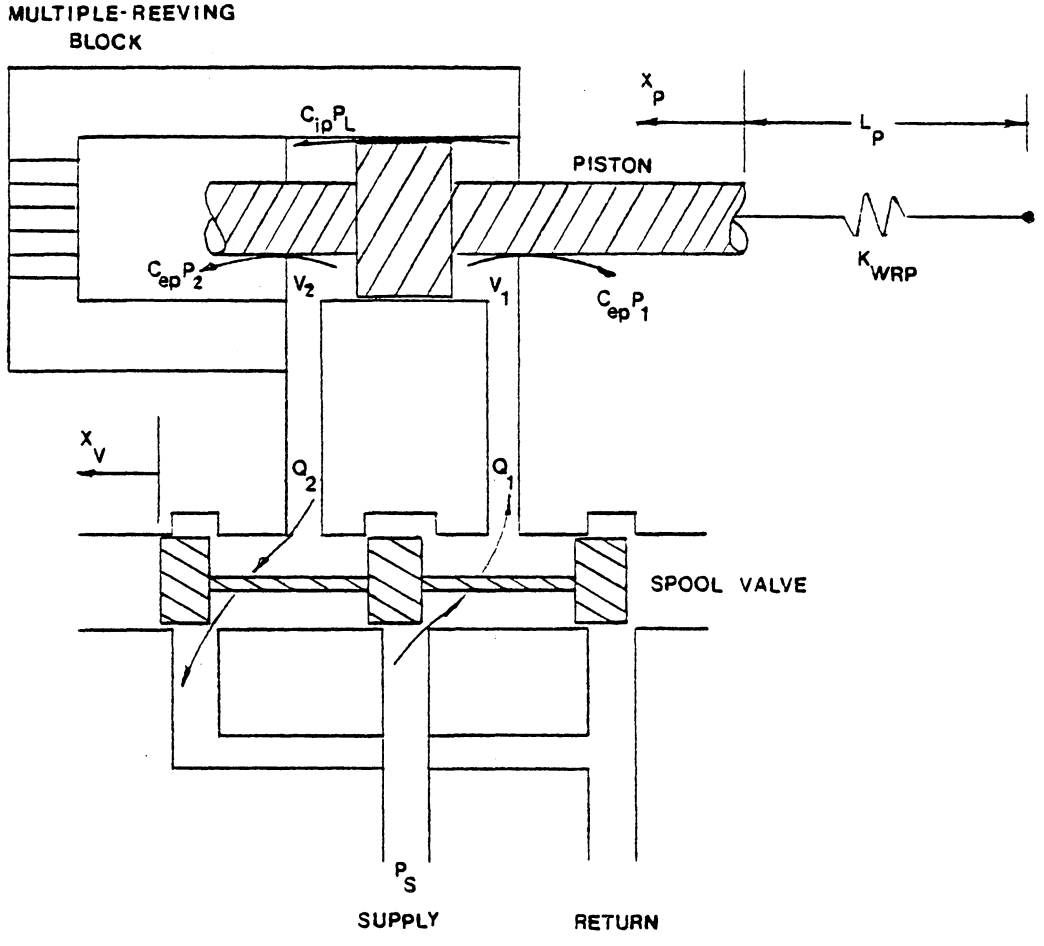

FIG. 61 HYDRAULIC SPOOL-VALVE PISTON ACTUATOR

of the actuator piston. The pressurized fluid applies a force on each side of the piston face. The net result of these two forces at equilibrium obviously must equal the initial force in the pendent lines. Using the notation from equation 3.1.2-3 the force in the pendent line is

$$F_{pendent} = K_{WRP} (L_{p_e} - L_p(t_0)) \tag{6-1}$$

where $L_p(t_0)$ is the unstressed pendent line length, and L_{p_e} is the pendent line length at equilibrium due to the static deflections. The net force on the actuator piston produced by the hydraulic fluid is

$$F_{piston} = A_p(P_{1_0} - P_{2_0}) \tag{6-2}$$

where:

A_p = area of a single piston face,

P_{1_0} = initial pressure in the right piston chamber, and

P_{2_0} = initial pressure in the left piston chamber.

Defining the initial load pressure as the pressure difference across the piston at equilibrium, or

$$P_{L_0} = (P_{1_0} - P_{2_0}) \tag{6-3}$$

and combining equations 6-1 and 6-2 the force balance in the controller at equilibrium becomes

$$K_{WRP} (L_{p_e} - L_p(t_0)) = A_p \cdot P_{L_0} \tag{6-4}$$

Increasing the load pressure above the equilibrium value so that the pressure in the right chamber, P_1, is greater than the pressure in the left chamber, P_2, displaces the actuator piston in the positive X_p direction. This also increases the force in the pendent lines; the force balance in the controller is, in general

$$K_{WRP}(L_p(t) - L_p(t_0) + X_p) = A_p(P_L + P_{L_0}) \tag{6-5}$$

where:

$$P_L = P_1 - P_2$$

represents the load pressure above the initial load pressure, P_{L_0}.

The hydraulic valve-controlled piston actuator has its own dynamic characteristics which govern its ability to respond to controller commands. The spool valve position is generally specified by a control input. When the spool valve is displaced in the positive X_v direction, as in Fig. 80, hydraulic fluid with a flowrate, Q_1, fills the right piston chamber of volume, V_1, and at the same time fluid with a flowrate, Q_2, empties out of the left piston chamber of volume, V_2. Since the pressure in the right chamber, $P_1 + P_{1_0}$ is greater than the pressure in the left chamber, $P_2 + P_{2_0}$, the actuator piston moves to left and increases the functional pendent line length.

The performance characteristics for a valve-controlled piston are developed by Merritt (24). It is convenient to define the load flow, Q_L, as the average flowrate in a piston chamber, or

$$Q_L = \tfrac{1}{2}(Q_1 + Q_2) \tag{6-6}$$

Let the spool valve be given a positive displacement, X_v, from its equilibrium position, which is arbitrarily defined as zero, that is, $X_{v_0} = 0$. The nonlinear steady-state equations which completely describe the pressure-flow characteristics of a spool valve can be solved simultaneously to yield a relationship for the load flow in the form

$$Q_L = Q_L(X_v, P_L) \tag{6-7}$$

A general linearized expression for the load flow is obtained by

expanding equation 6-7 in a Taylor's series about the operating point $Q_L = Q_{L_0}$, which yields

$$Q_L = Q_{L_0} + \frac{\partial Q_L}{\partial X_V}\bigg|_{Q_{L_0}} \Delta X_V + \frac{\partial Q_L}{\partial P_L}\bigg|_{Q_{L_0}} \Delta P_L + \ldots \tag{6-8}$$

The higher order terms in equation 6-8 can be neglected for small valve excursions with little loss of accuracy. Defining the flow gain as

$$K_q = \frac{\partial Q_L}{\partial X_V} \tag{6-9}$$

and the flow-pressure coefficient as

$$K_c = \frac{\partial Q_L}{\partial P_L} \tag{6-10}$$

the linearized expression for the load flow in equation 6-8 becomes

$$Q_L = Q_{L_0} + K_q X_V - K_c(P_L - P_{L_0}) \tag{6-11}$$

Equation 6-11 describes the spool valve's dynamic characteristics.

The motion of the actuator piston is governed by the flow of hydraulic fluid into and out of the piston chambers including small leakage flows. Applying the continuity equation to the right piston chamber yields (see Fig. 80)

$$Q_1 - C_{ip}[(P_1+P_{1_0}) - (P_2+P_{2_0})] - C_{ep}(P_1+P_{1_0}) = \frac{dV_1}{dt} + \frac{V_1}{\beta_e}\frac{d(P_1+P_{1_0})}{dt} \tag{6-12}$$

and for the left piston chamber

$$Q_2 - C_{ip}[(P_1+P_{1_0}) - (P_2+P_{2_0})] + C_{ep}(P_2+P_{2_0}) = \frac{dV_2}{dt} + \frac{V_2}{\beta_e}\frac{d(P_2+P_{2_0})}{dt} \tag{6-13}$$

where:

C_{ip} = internal cross-port leakage coefficient,

C_{ep} = external leakage coefficient, and

β_e = the effective hydraulic fluid bulk modulus.

The piston chamber volumes are written as

$$V_1 = V_0 + A_p X_p \tag{6-14}$$

and

$$V_2 = V_0 - A_p X_p \tag{6-14}$$

where V_0 represents the initial volume of either chamber since the piston is considered centered at equilibrium. The total volume of both piston chambers is then

$$V_t = V_1 + V_2 = 2V_0 \tag{6-16}$$

The time derivatives of equations 6-14 and 6-15 are given by

$$\frac{dV_1}{dt} = A_p \frac{dX_p}{dt} \tag{6-17}$$

and

$$\frac{dV_2}{dt} = -A_p \frac{dX_p}{dt} \tag{6-18}$$

Defining the total leakage coefficient as

$$C_{tp} = C_{ip} + \tfrac{1}{2}C_{ep} \tag{6-19}$$

further simplifies the addition of equations 6-12 and 6-13. Substituting equations 6-14 through 6-19 into equations 6-12 and 6-13 and adding the two continuity expressions yields

$$Q_L = C_{tp}(P_L + P_{L_0}) + A_p \frac{dX_p}{dt} + \frac{Vt}{4\beta} \frac{dP_L}{dt} \tag{6-20}$$

Equation 6-20 describes the dynamic characteristics of the actuator piston.

The differential equation describing the dynamic response of the

spool-valve controlled piston actuator is formed by substituting equation 6-5 into equations 6-11 and 6-20 and then equating 6-11 and 6-20. The differential equation of motion for the actuator, written in terms of the piston velocity becomes

$$\dot{X}_p = \left[\frac{-V_t K_{WRP}}{4A_p\beta_e}\dot{L}_p(t) - \frac{K_{WRP}}{A_p}(K_c+C_{tp})(L_p(t)-L_p(t_0)) + Q_{L_0} + K_q X_v + 2K_c P_{L_0} - \frac{K_{WRP}}{A_p}(K_c+C_{tp})X_p\right] \Big/ \left[\frac{V_t K_{WRP}}{4A_p\beta_e} + A_p\right] \tag{6-21}$$

where the dots indicate time derivatives. The equation of motion for the actuator is integrated in real-time with the equations of motion for the crane system during each simulation step.

The actuator specifications chosen for this simulation are consistent with those of currently manufactured valve-controlled pistons (25). The hydraulic source supplies a constant pressure, P_s, of 28MPa to the actuator. The actuator piston face is 645 cm^2, or twice the area required to maintain static equilibrium. A critical-center spool valve design was chosen with no overlap since this type produces faster responses than a closed-center design and a stiffer control mechanism with lower leakage flows than an open-center design (24). The spool valve is designed for maximum load flowrates of 0.0164 m^3/sec., which is capable of producing a 2.54 cm piston displacement in 0.1 seconds. The load flow for a critical-center spool valve is given by Merritt (24)

$$Q_L = C_d \pi D_v X_v \left[\frac{1}{\sigma}(P_s - \left|\frac{X_v}{X_v}\right| \cdot P_L)\right]^{0.5} \tag{6-22}$$

where:

C_d = 0.61 = discharge coefficient,

D_v = spool valve diameter, and

σ = the hydraulic fluid density.

The maximum spool valve travel allowed is 0.76 cm, and the maximum load pressure is constrained to 21MPa. Substituting these values into equation 6-22 yields a spool-valve diameter of 3.64 cm.

The valve coefficients which appear in equation 6-11 are evaluated at the operating condition $Q_L = Q_{L_0}$. The flow gain is given by (24).

$$K_{q_0} = C_d \pi D_v \left[\frac{1}{\sigma}(P_s - P_{L_0})\right]^{\frac{1}{2}} \tag{6-23}$$

and the flow-pressure coefficient is

$$K_{c_0} = \frac{C_d \pi D_v X_{v_0} \left[\frac{1}{\sigma}(P_s - P_{L_0})\right]}{2(P_s - P_{L_0})} \tag{6-24}$$

The initial load pressure required to sustain equilibrium for a 18,000 Kg suspended load is 1.6MPa. The flow gain, K_{q_0}, from equation 6-23, is 4.12 m^3/sec./m, and since the initial valve displacement is arbitrarily defined equal to zero the flow-pressure coefficient, K_{c_0}, likewise, becomes zero. The initial leakage flow, Q_{L_0}, is also assumed zero. Finally, choosing a maximum piston travel from center of 10 cm, specifies the total piston chamber volume, V_t, of 1.31 m^3. These specifications have not been optimized, but however, do reflect an understanding of the crane system dynamics and are within current valve-controlled piston design limits (25).

A positive actuator piston displacement, using the notation in Fig. 61, increases the total length of the pendent lines, and hence, increases the total potential energy stored in the pendent cables. The variations of the potential energy stored in the pendent cables were formulated for the Lagrange equations of motion for the uncompensated

crawler crane from equation 3.1.2-3. The total force developed in the pendent lines on the compensated crane due to the crane dynamics and the actuator piston displacement is treated as a nonconservative external force performing virtual work rather than as storing potential energy. The variations of the potential energy derived from equation 3.1.2-3 are therefore discarded from the Lagrange equations of motion for the compensated crane, and are replaced with generalized forces derived from the virtual work produced by the nonconservative pendent force.

Recall from the force balance in equation 6-5 that the force developed in the pendent lines equals the force produced by the hydraulic actuator. The virtual work produced by the nonconservative external pendent force due to the variations in the pendent length, δL_p, is

$$\delta W = F_{pendent} \cdot \delta L_p \tag{6-25}$$

where:

$$F_{pendent} = K_{WRP}(L_p(t) - L_p(t_0) + X_p) \tag{6-26}$$

and

$$\delta L_p = \sum_{K=1}^{n} \frac{\delta L_p}{\delta P_K} \cdot \delta P_K \tag{6-27}$$

Performing the indicated variations the virtual work produced by the pendent force becomes

$$\delta W = -F_{pendent}\left[\frac{1}{L_p}(R_8 - R_d\cos\phi_B)\left(\frac{1}{L_B}(q_2 - 2q_1)\right)\right]\delta q_1$$

$$+F_{pendent}\left[\frac{1}{L_p}(R_8 - R_d\cos\phi_B)\left(\frac{1}{L_B}(q_1 - 2q_2)\right)\right]\delta q_2$$

$$+F_{pendent}\left[\frac{1}{L_p}R_8R_d\sin\phi_B\right]\delta\phi_2$$

$$-F_{pendent}\left[\frac{1}{L_p}R_8R_d\sin\phi_B\right]\delta\phi_6 \qquad (6\text{-}28)$$

The boom-topping controller developed by Casler (15) utilizes a feedforward compensation technique, with first-order lag and an integrator, that senses the crane-base motion and describes a boom-hoist winch actuator extension. Casler uses a relatively complex compensation scheme to control a simple crane model. In this thesis three proportional feedback compensation techniques are used separately to control a relatively complex crane model. Casler is interested in controlling the motion of a crane-ship system driven by the motion of sea waves. Casler used a linearized crane model in his study that neglected boom structural motion and nonlinear coupling terms. The land-based crane model developed in this thesis includes a flexible boom and nonlinear equations of motion because these effects strongly influence the energy transfer between the crane and the suspended load.

A diagram of the control scheme used to reduce boom-tip excursions is shown in Fig. 62. The control scheme presumes that the necessary crane states are available in real-time during the simulation. The hydraulic actuator receives a prescribed spool-valve displacement from the controller. The actuator's dynamics produce a resultant piston displacement, and the piston displacement modifies the crane pendent force. Each proportional controller detects an error signal, or a deviation between the actual and desired crane state, and describes the

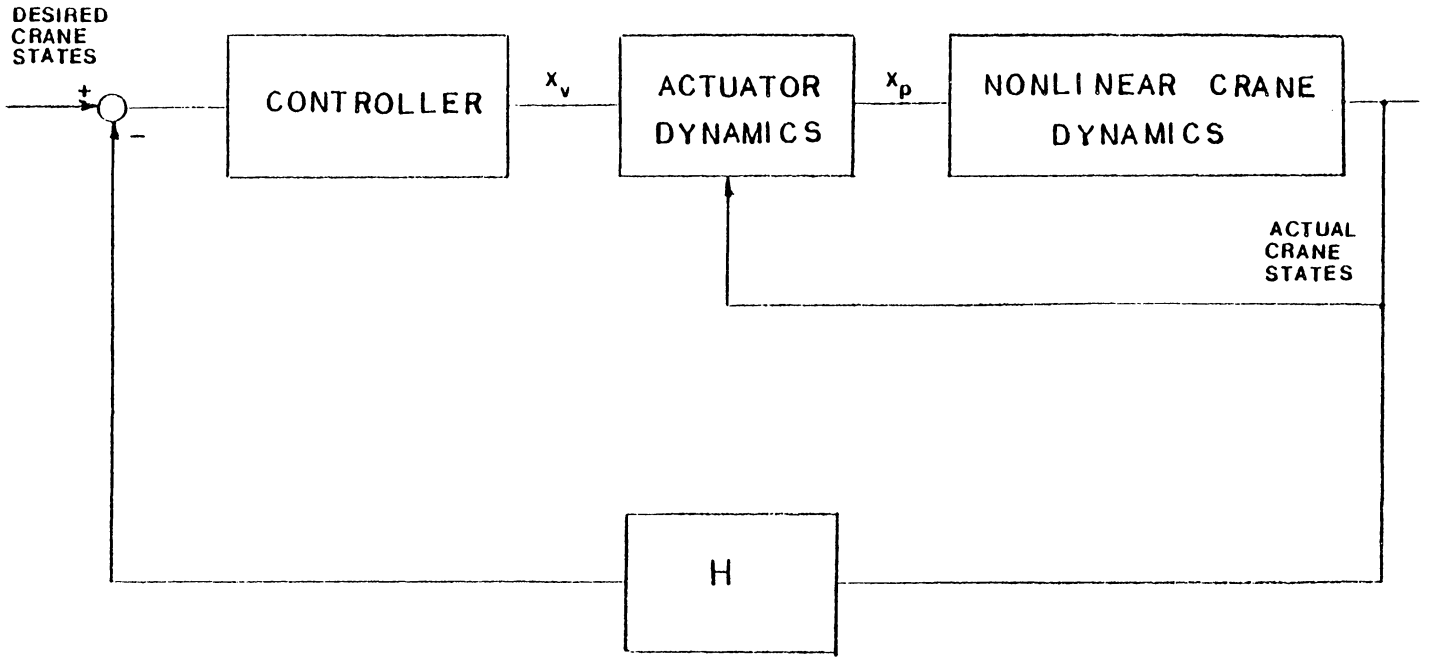

FIG. 62 CRANE CONTROL SCHEME

actuator's valve displacement. The three proportional selected state feedback techniques used in this simulation follow:

a. Controller 1

$$K_1(\phi_{6_D} - \phi_6) + K_2(\dot{\phi}_{6_D} - \dot{\phi}_6) = X_V \tag{6-29}$$

b. Controller 2

$$K_3(q_{1_D} - q_1) = X_V \tag{6-30}$$

c. Controller 3

$$K_4(\dot{\phi}_{9_D} - \dot{\phi}_9) = X_V \tag{6-31}$$

where the subscript, D, indicates the desired crane state. The value of the desired crane state corresponds to the initial value of the crane state at equilibrium.

The hydraulic power required by the piston actuator to adjust the effective pendent line length is given by Merritt (24) as

$$\text{Control Power} = \frac{P_L Q_L}{2298.0} \tag{6-32}$$

in units of Kilowatts where the load pressure, P_L is calculated from equation 6-5 and the load flow, Q_L, is calculated from equation 6-11. The time dependent values of the actuator control power, the piston displacement, X_p, and the spool-valve displacement, X_v, are plotted for each compensated crane simulation.

7. COMPENSATED CRANE RESPONSE

The results of the numerical solution of the crane system equations of motion incorporating the hydraulic pendent line controller developed in Chapter 6 are presented in this chapter for the same three sets of crane configurations and initial conditions simulated in Chapter 5.

The three compensation techniques presented in Chapter 6 are each used to control the motion of the crane subject to the conditions of Case A. The controller which most attenuates the response of the uncompensated crane in Case A is applied to the simulations of Case B and C.

The discussion of each simulation begins with a description of the compensation technique used to control the crane motion. The crane properties, initial conditions, and crane configuration particular to each case are not discussed in this chapter; the reader should consult Table 1 on page 63 and the case discussions in Chapter 5. The compensated crane response is compared to the uncompensated crane response, given in Chapter 5, for the same case to assess the controller's contribution. The controller gains used in each simulation were chosen by trial and error to yield the maximum attenuations in the crane response. Selected time histories of the generalized coordinates and plots of their frequency contents are offered when informative.

Case A (controller 1)

Controller 1 has two feedback loops. One to detect the error between the current angle of boom chord and the desired angle of the

boom chord, and the other to detect the error in the rotational velocity of the boom chord. The desired value of the boom chord angle is the angle of the boom chord at equilibrium due to the static deflections of the crane system. The desired rotational velocity of the boom chord is zero. Controller 1 prescribes the spool-valve displacement on the pendent actuator proportional to the error in the crane states, and is given by equation 6-29 as

$$X_v = K_1(\phi_{6_D} - \phi_6) + K_2(\dot{\phi}_{6_D} - \dot{\phi}_6)$$

The controller gains $K_1 = 0.05$ and $K_2 = 0.2$ are used in this simulation.

Recall from Chapter 6 that the crane and the suspended load transfer energy at the boom tip and that the boom-tip excursions excite the motion of the suspended load. Controller 1 is designed to fix the boom chord in the inertial plane, thus eliminating the rotations of the boom chord. The error signal of the boom-chord rotational velocity is included to improve the controller's speed of response.

The time histories of the response of the compensated crane with Controller 1 subject to the conditions of Case A are presented in Figs. 63 through 66. The ground coordinates R_1 and ϕ_2, given in Figs. 63 and 64, experience larger maximum displacements than the ground coordinates of the uncompensated crane in Figs. 24 and 24, but are attenuated dramatically within 3.0 sec after the initial shock of the dropped load. Controller 1 does slightly reduce the maximum amplitude of the boom chord oscillation in the compensated crane, as

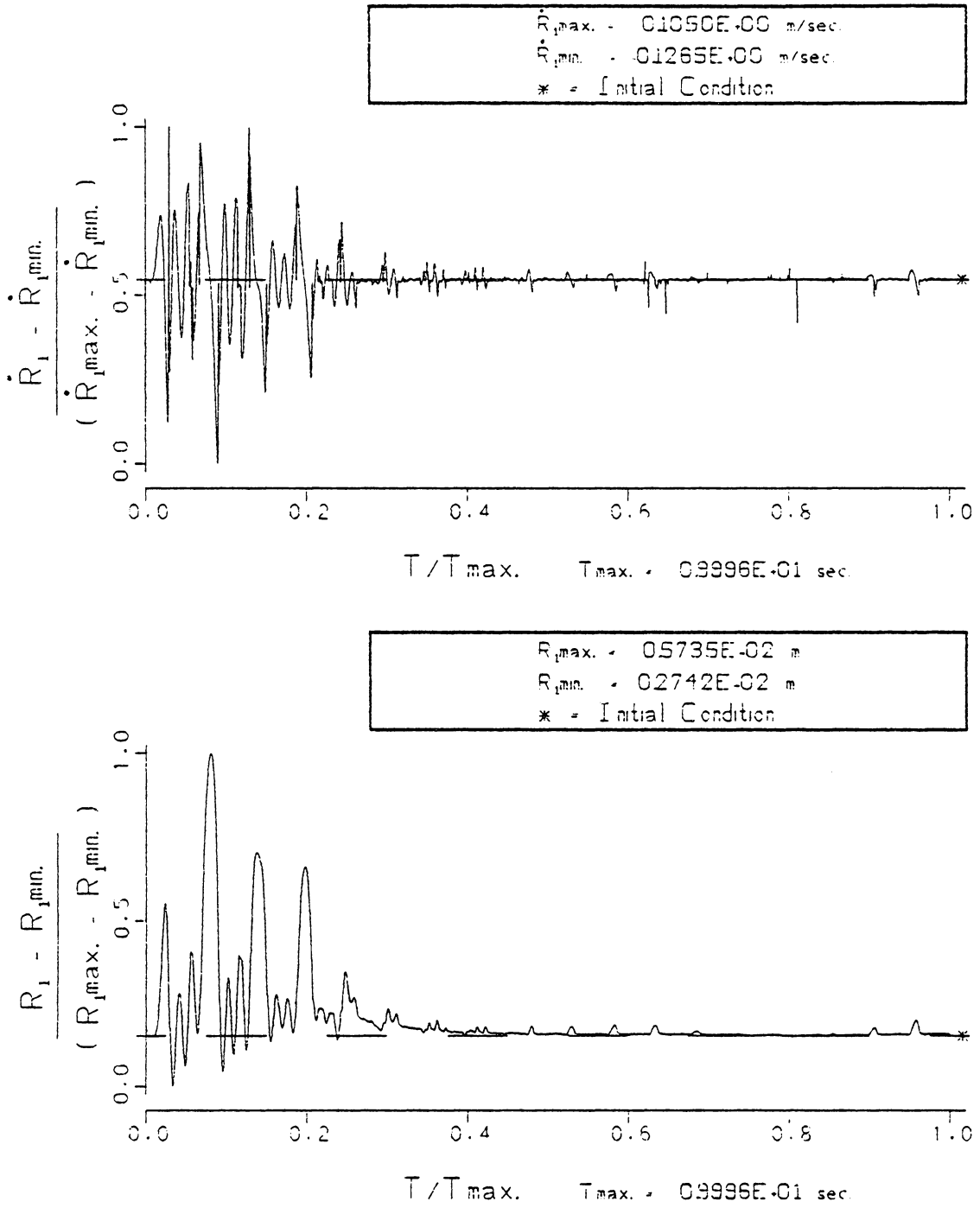

FIG. 63 VERTICAL RESPONSE OF THE TRACKS. (R_1 , $\dot{R}_1$) FOR CONDITIONS OF CASE A WHEN THE CABLE DRUM BRAKE IS APPLIED DURING LOAD-LOWERING. (COMPENSATED CRANE WITH CONTROLLER 1)

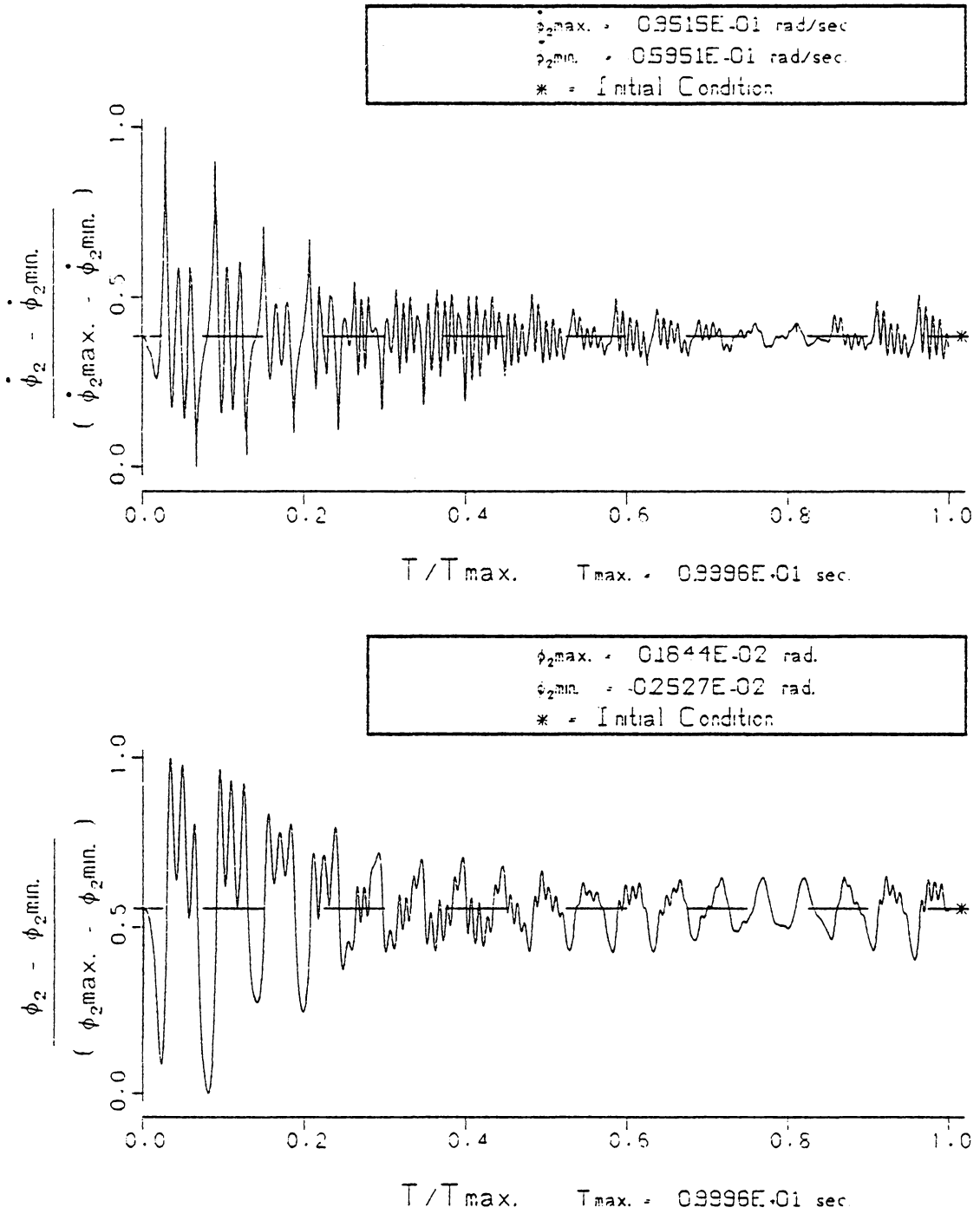

FIG. 64 ROTATIONAL RESPONSE OF THE TRACKS. (ϕ_2 , $\dot{\phi}_2$) FOR CONDITIONS OF CASE A WHEN THE CABLE DRUM BRAKE IS APPLIED DURING LOAD-LOWERING. (COMPENSATED CRANE WITH CONTROLLER 1)

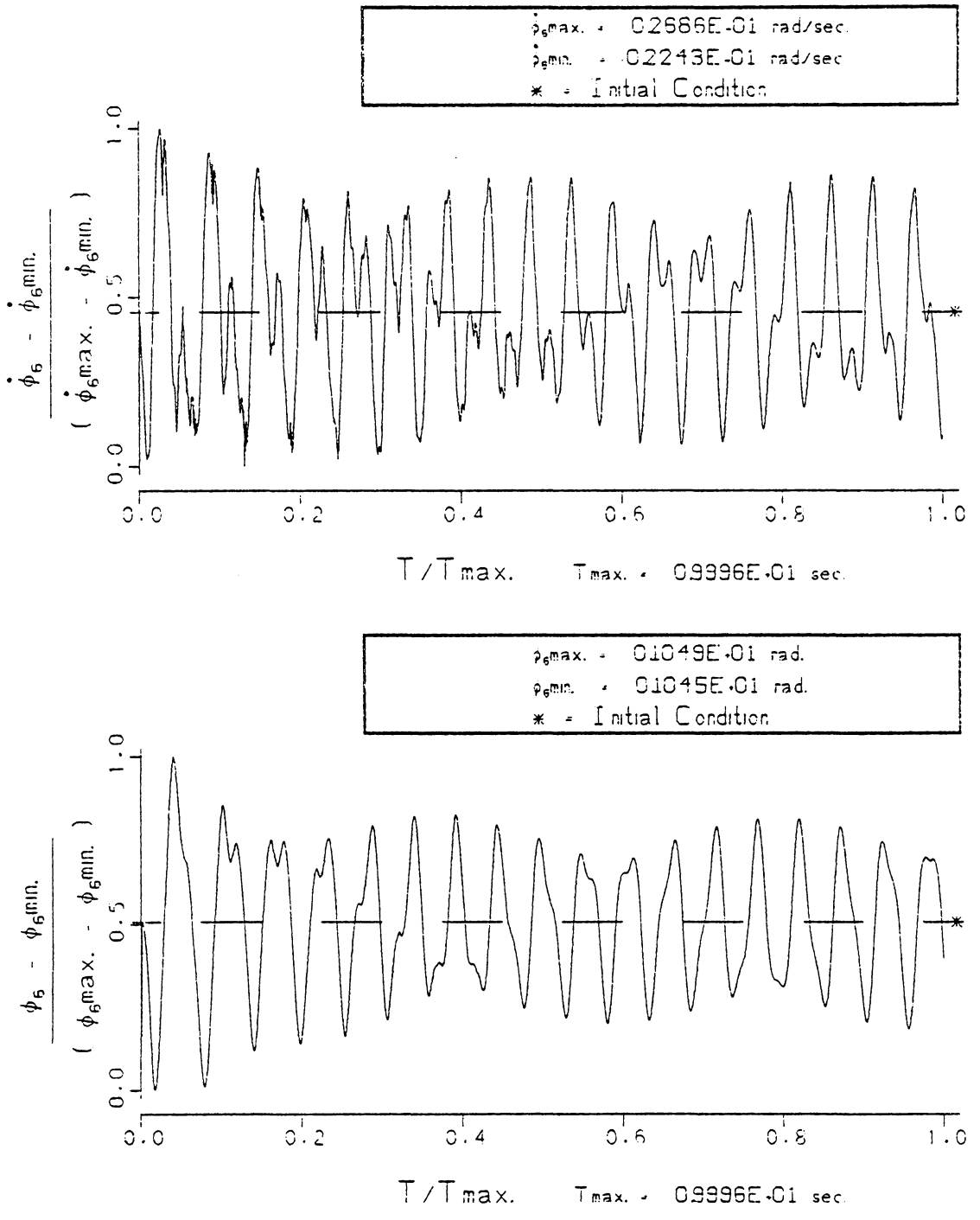

FIG. 65 ROTATIONAL RESPONSE OF THE BOOM CORD. (ϕ_6 , $\dot{\phi}_6$) FOR CONDITIONS OF CASE A WHEN THE CABLE DRUM BRAKE IS APPLIED DURING LOAD-LOWERING. (COMPENSATED CRANE WITH CONTROLLER 1)

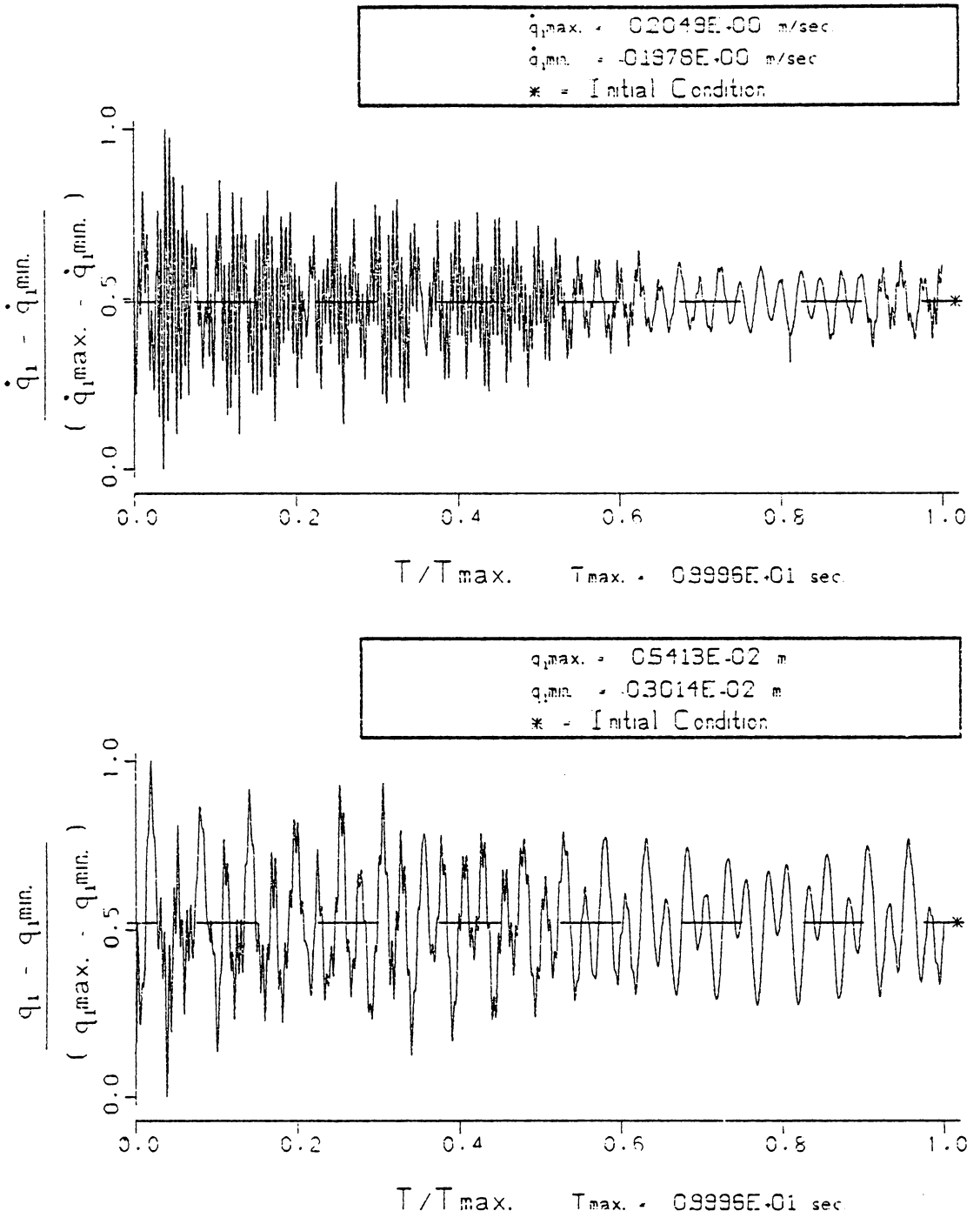

FIG. 66 LOWER BOOM JOINT RESPONSE. (q_1 , $\dot{q}_1$)
FOR CONDITIONS OF CASE A WHEN THE CABLE
DRUM BRAKE IS APPLIED DURING LOAD-LOWERING.
(COMPENSATED CRANE WITH CONTROLLER 1)

seen in Fig. 65, compared to the boom chord oscillation of the uncompensated crane in Fig. 26. The magnitude of the boom chord rotations in Fig. 65 are reduced initially, but continue to oscillate with significant amplitude to the end of the simulation without any further reductions. Notice the higher frequency which dominates the compensated response of coordinate ϕ_6, 9.0 Hz in Fig. 67 compared to 7.0 Hz in the uncompensated crane in Fig. 33.

The pendent controller has added some damping to the system as evidenced in response of the ground coordinates in Figs. 63 and 64. The added damping, which is not present in the uncompensated crane response, is most obvious in the boom response, coordinate q_1 in Fig. 66. The maximum response of all the crane states, excluding the ground coordinates, R_1 and ϕ_2, is attenuated by the controller.

Controller 1 does improve the response of the crane system, but the pendent actuator requires almost 96 Kw, as seen in Fig. 68, to accomplish the reduction. The controller works very hard to hold the boom chord in its initial position after a 7.6 cm drop of the 13,600 Kg load. The supporting soil of even an uncompensated crane dissipates energy from the vibrating crane system. Therefore, an effective controller could attenuate the response of the crane system by transferring energy advantageously to the dissipating soil. The soil damping as developed in Chapter 3 depends on the velocity of the ground coordinates R_1 and ϕ_2, and on the frequency at which they oscillate. Controller 1 does not dissipate the system energy advantageously to the soil, but rather works against the ground motion. This is

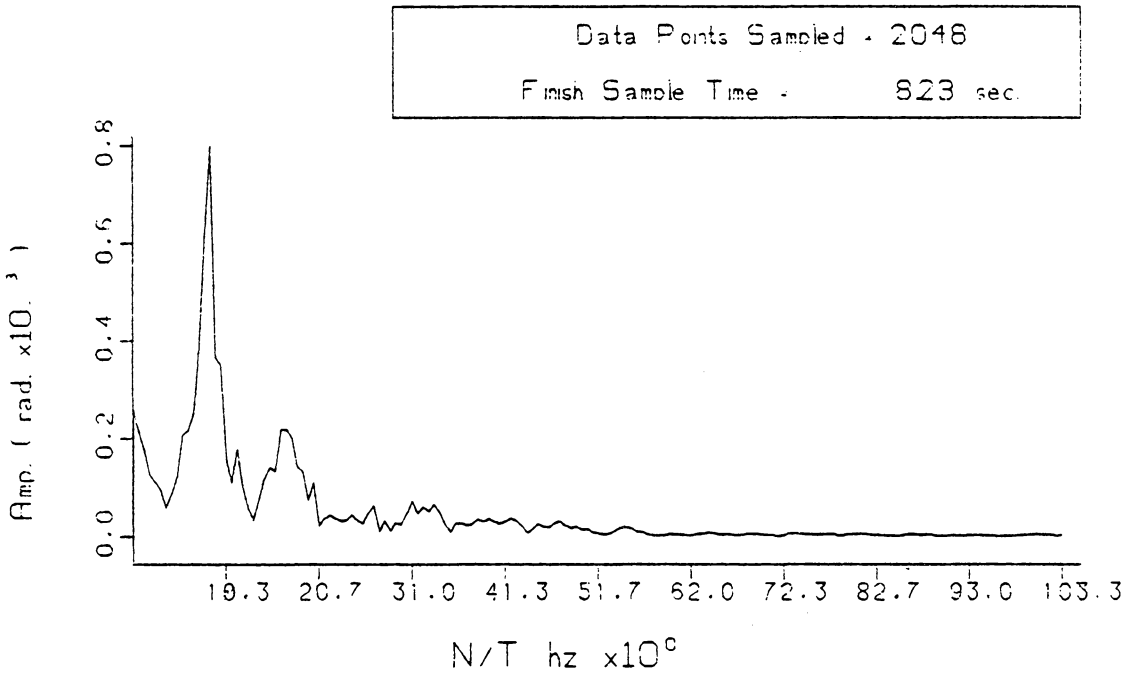

FIG. 67 FREQUENCY ANALYSIS OF COORDINATE ϕ_s FOR THE CONDITIONS OF CASE A WHILE BRAKING AT LOAD LOWERING (CONTROLLER 1)

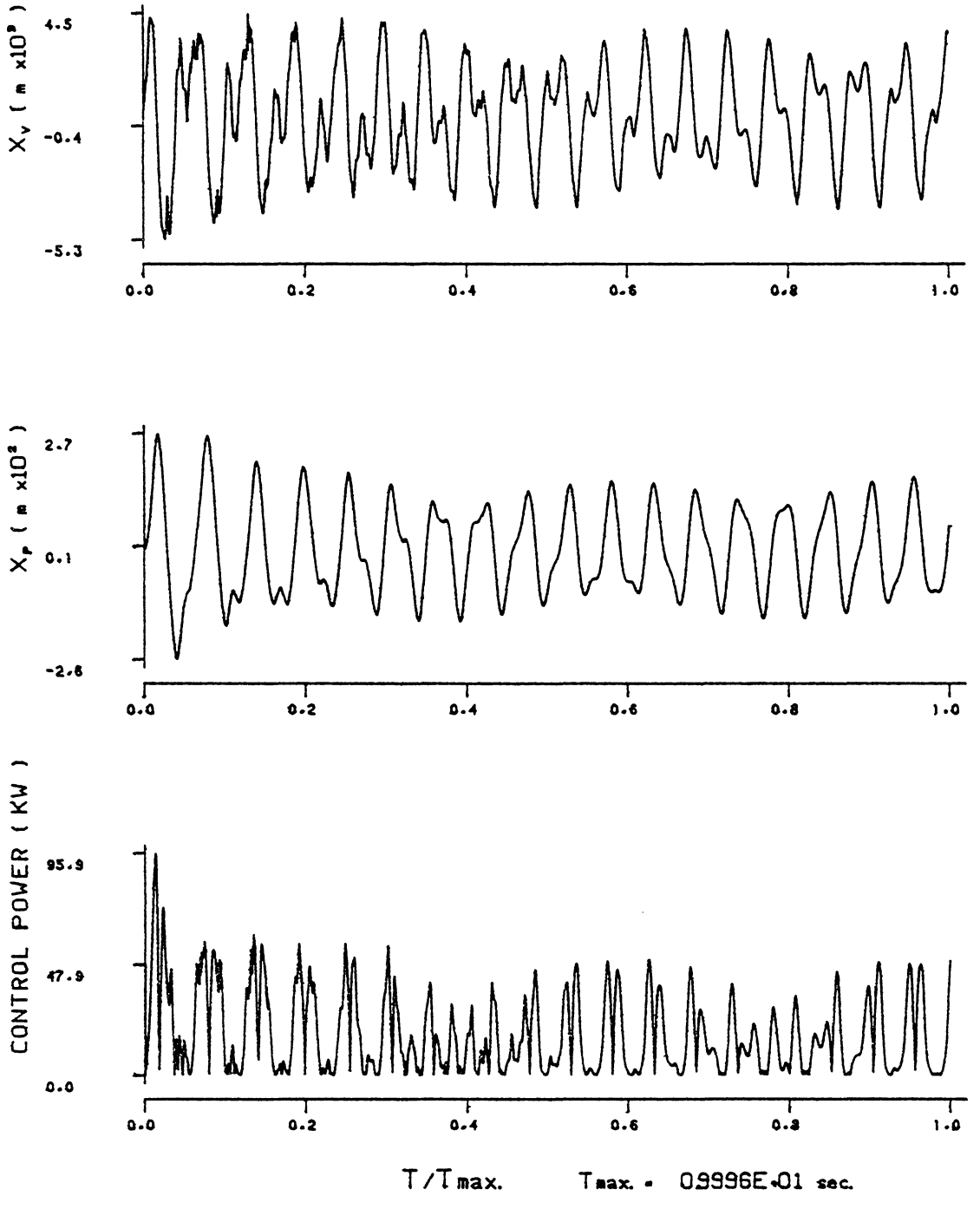

FIG. 68 THE TIME DEPENDENT ACTUATOR CONTROL POWER. AND THE DISPLACEMENT OF THE ACTUATOR PISTON AND SPOOL VALVE. (X_p AND X_v) FOR THE CONDITIONS OF CASE A. (CONTROLLER 1)

apparent in Figs. 69 and 70 since the frequency content of the amplitude responses of coordinates R_1 and R_9 change so from those describing the uncompensated response in Figs. 31 and 35.

Case A (controller 2)

Controller 2 detects the error between the desired lower boom joint displacement and the actual displacement, and specifies the spool-valve position proportional to the error. The desired lower boom joint displacement is the static equilibrium value corresponding to the initial boom deflection. The compensation technique is given in equation 6-30 as

$$X_v = K_3(q_{1_D} - q_1)$$

A gain of $K_3 = 0.15$ is used in this simulation.

Controller 2 is designed to reduce the boom-tip excursions, which potentially excite the motion of the suspended load, by reducing the deflections in the boom. Smaller lower boom joint deflections reduce the fluctuations in the boom chord length, which act as inputs to the motion of the suspended load. The lower and upper boom joints, coordinates q_1 and q_2, are strongly coupled; the compensation technique used in controller 2 works on the premise that the total boom motion can be reduced by only the deflection of a single boom joint.

The time histories of the coordinate responses, given in Figs. 71 through 76, show that Controller 2 very successfully attenuates

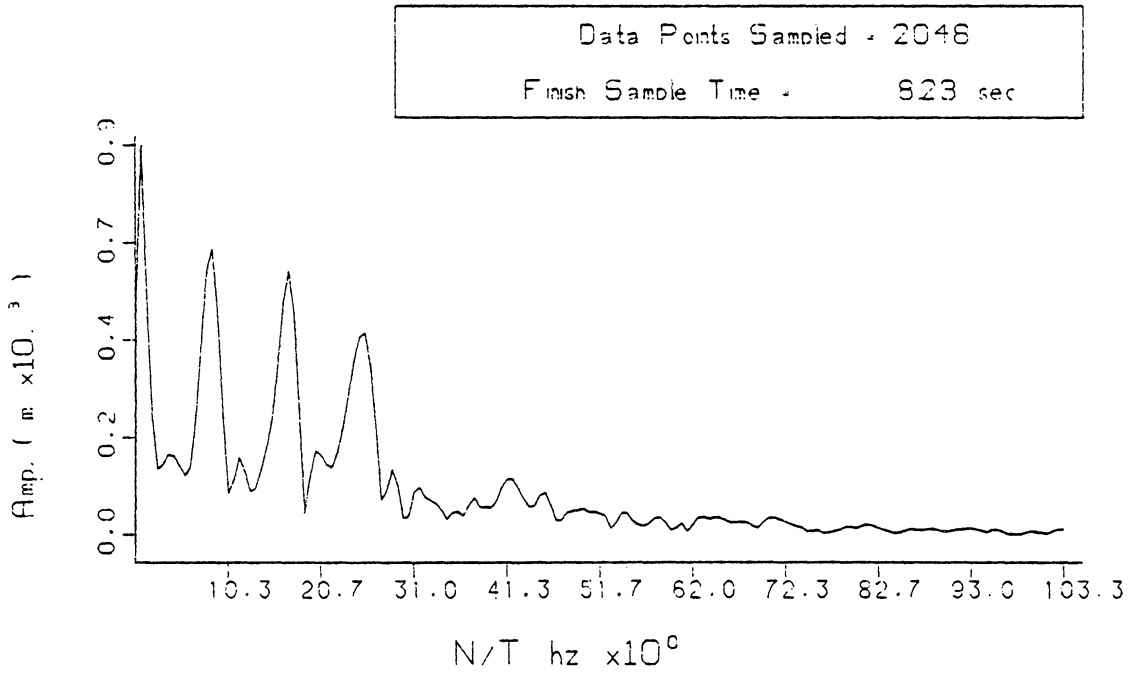

FIG. 69 FREQUENCY ANALYSIS OF COORDINATE R_1 FOR THE CONDITIONS OF CASE A WHILE BRAKING AT LOAD LOWERING (CONTROLLER 1)

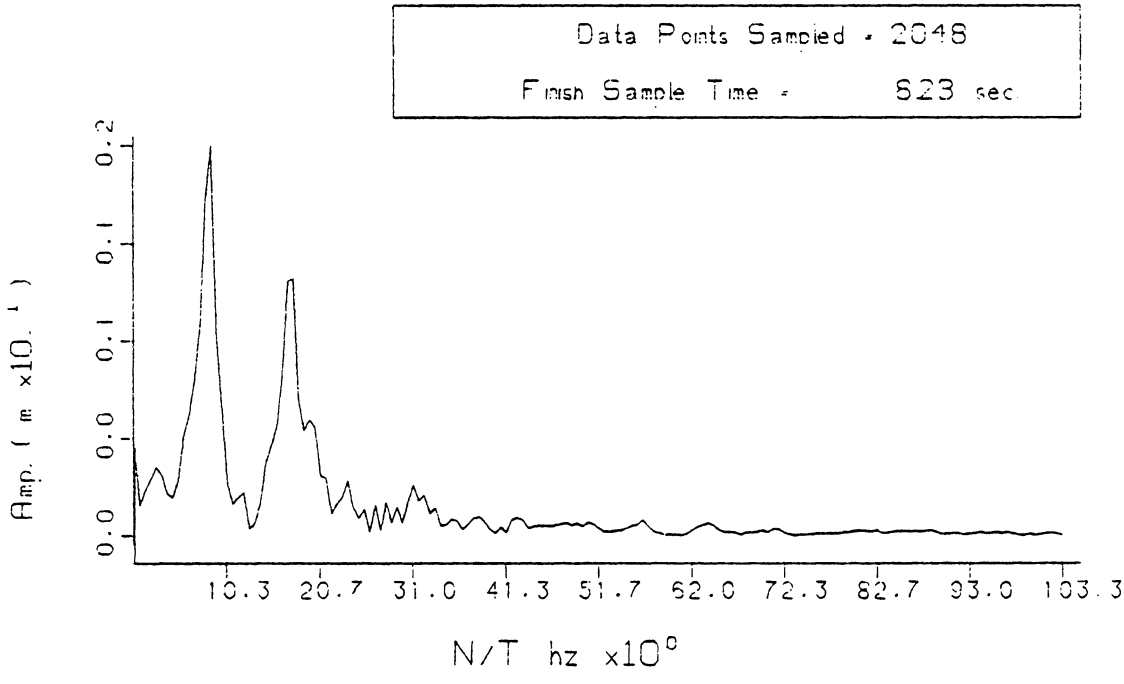

FIG. 70 FREQUENCY ANALYSIS OF COORDINATE R_3 FOR THE CONDITIONS OF CASE A WHILE BRAKING AT LOAD LOWERING (CONTROLLER 1)

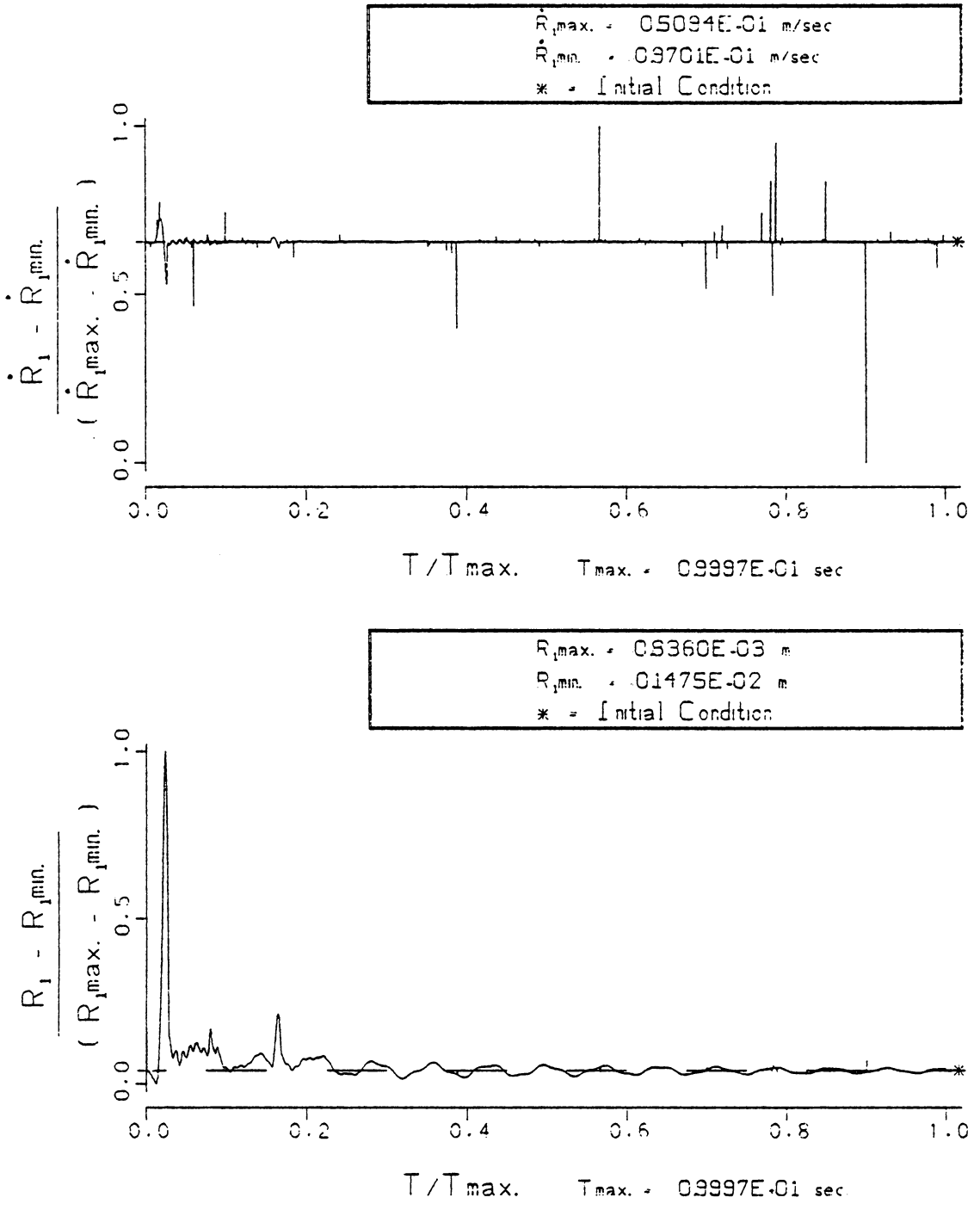

FIG. 71 VERTICAL RESPONSE OF THE TRACKS. (R_1 , $\dot{R}_1$) FOR CONDITIONS OF CASE A WHEN THE CABLE DRUM BRAKE IS APPLIED DURING LOAD-LOWERING. (COMPENSATED CRANE WITH CONTROLLER 2)

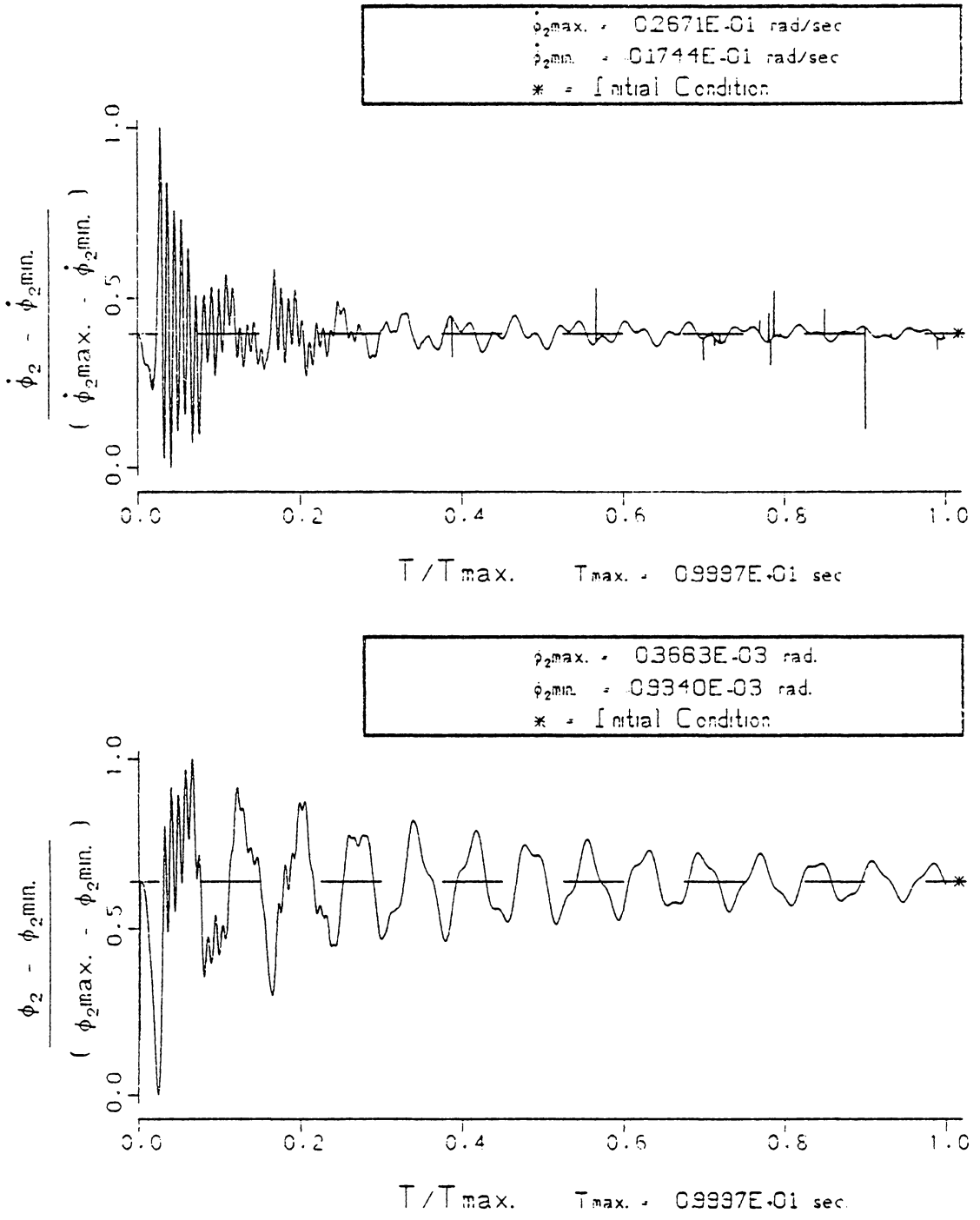

FIG. 72 ROTATIONAL RESPONSE OF THE TRACKS. (ϕ_2 , $\dot{\phi}_2$) FOR CONDITIONS OF CASE A WHEN THE CABLE DRUM SRAKE IS APPLIED DURING LOAD-LOWERING. (COMPENSATED CRANE WITH CONTROLLER 2)

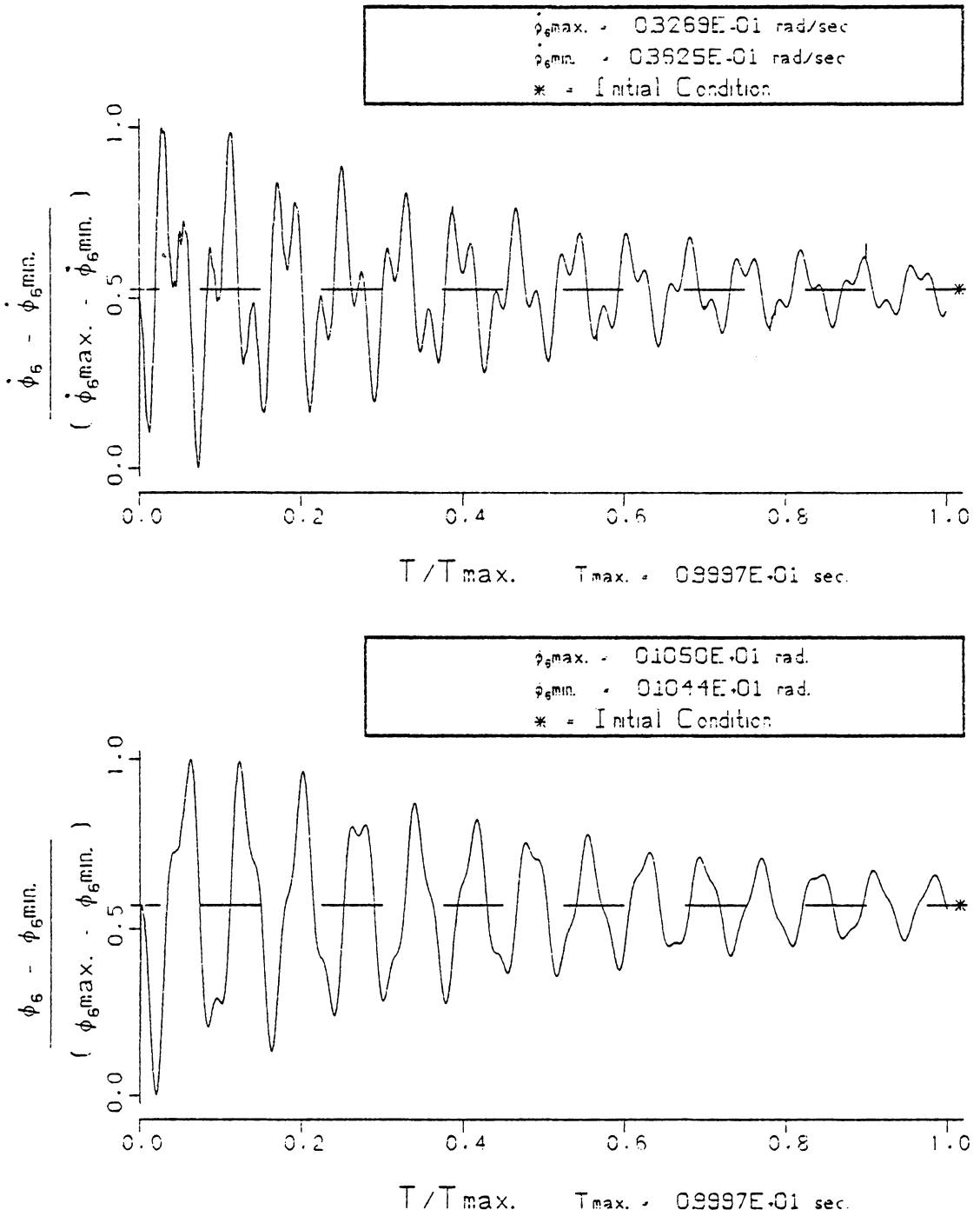

FIG. 73 ROTATIONAL RESPONSE OF THE BOOM CORD. (ϕ_6 , $\dot{\phi}_6$) FOR CONDITIONS OF CASE A WHEN THE CABLE DRUM BRAKE IS APPLIED DURING LOAD-LOWERING. (COMPENSATED CRANE WITH CONTROLLER 2)

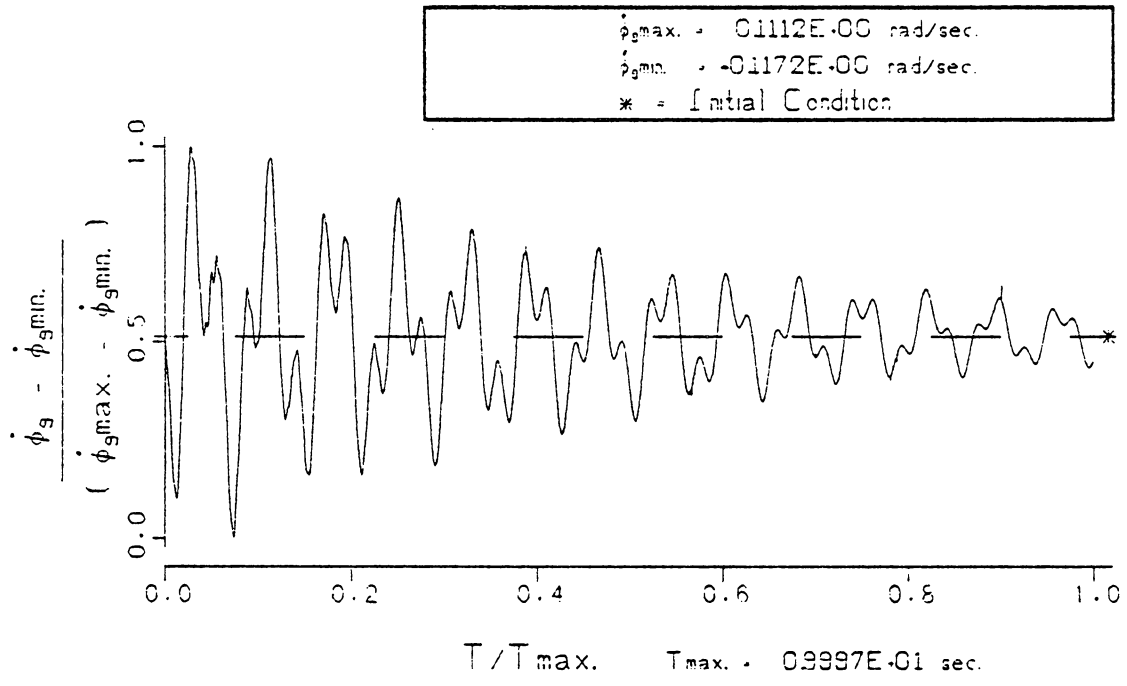

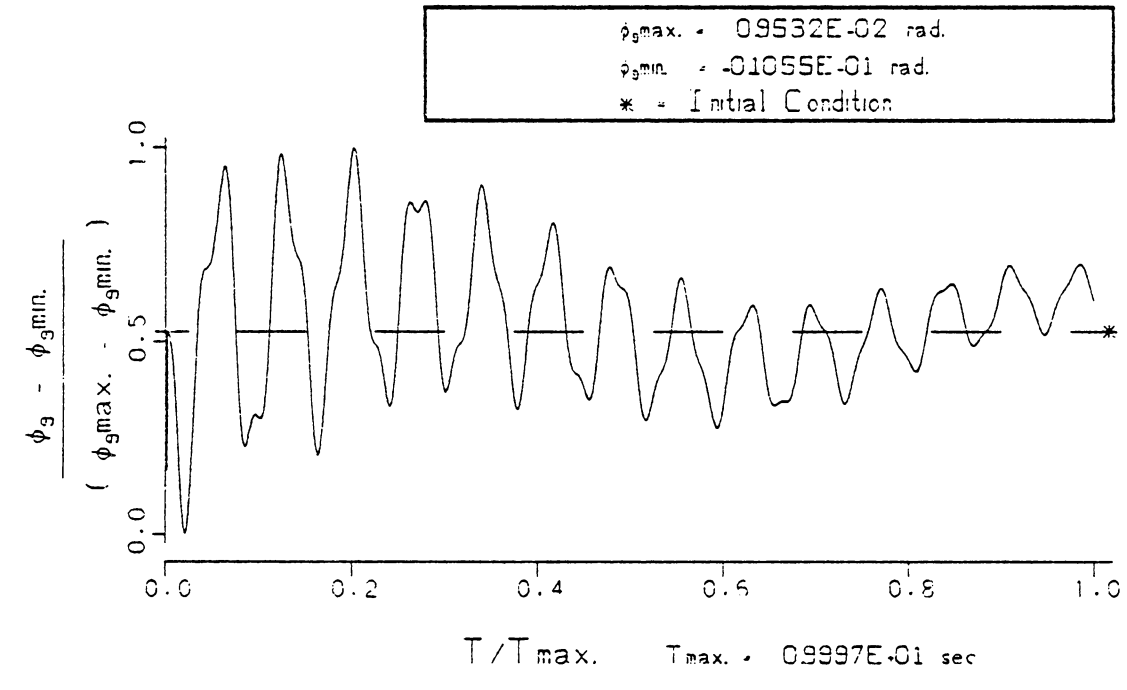

FIG. 74 PENDULATION OF THE LOAD. (ϕ_g , $\dot{\phi}_g$)
FOR CONDITIONS OF CASE A WHEN THE CABLE
DRUM BRAKE IS APPLIED DURING LOAD-LOWERING.
(COMPENSATED CRANE WITH CONTROLLER 2)

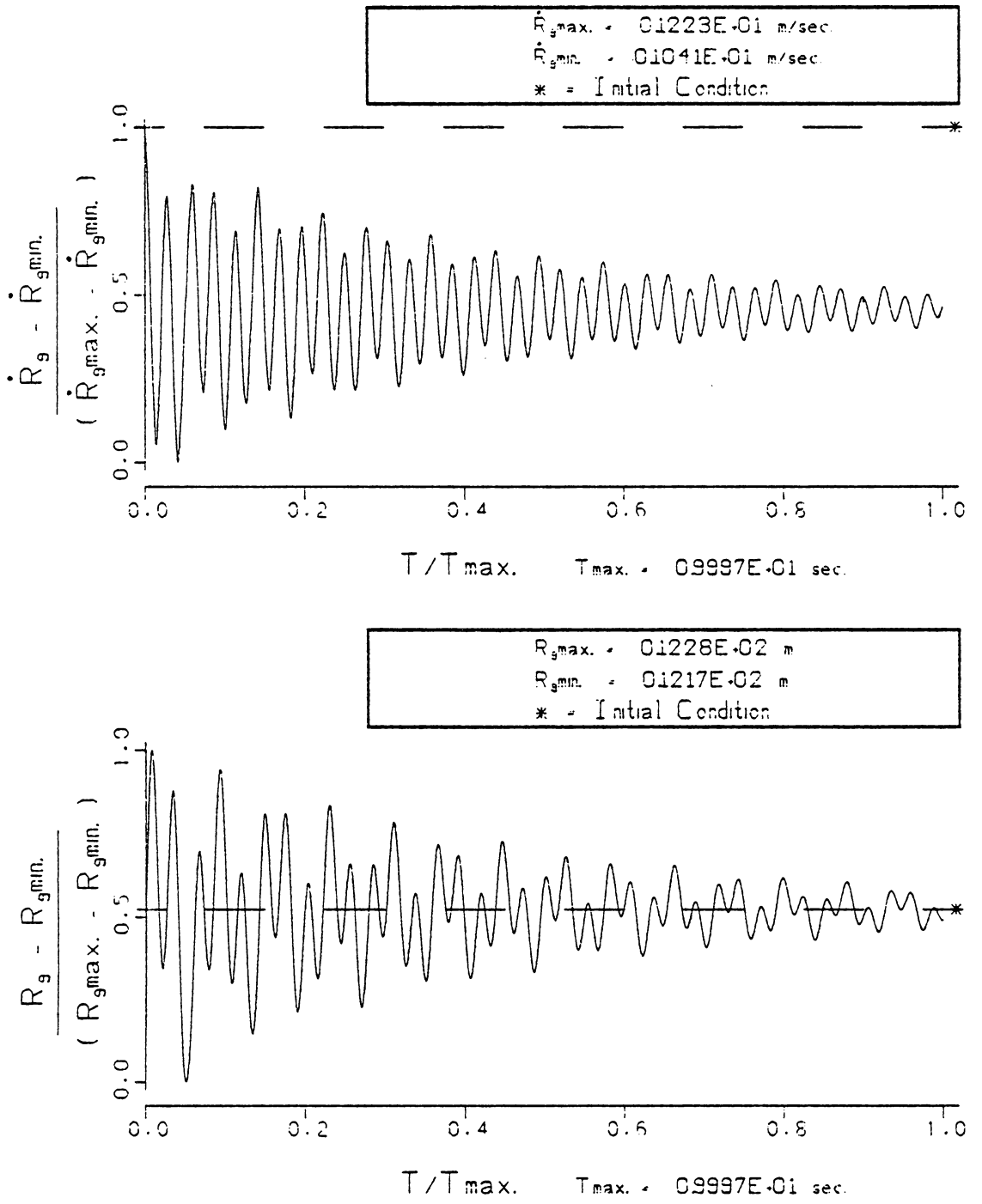

FIG. 75 STRETCH OF THE LOAD LINE CABLE. (R_g , $\dot{R}_g$) FOR CONDITIONS OF CASE A WHEN THE CABLE DRUM BRAKE IS APPLIED DURING LOAD-LOWERING. (COMPENSATED CRANE WITH CONTROLLER 2)

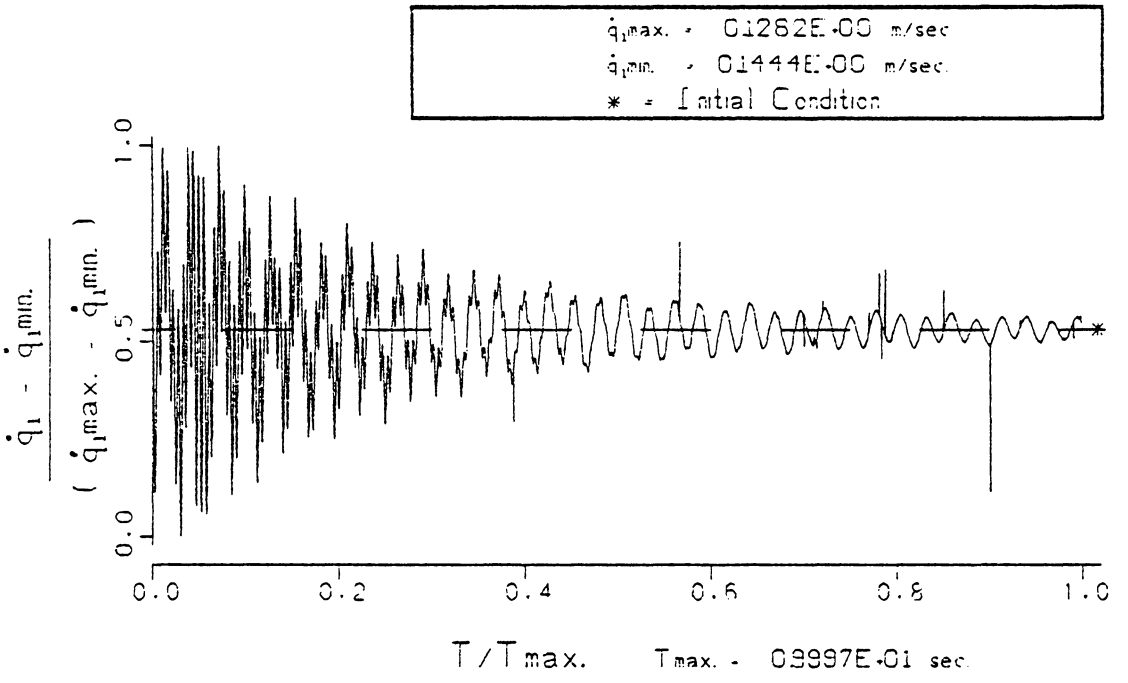

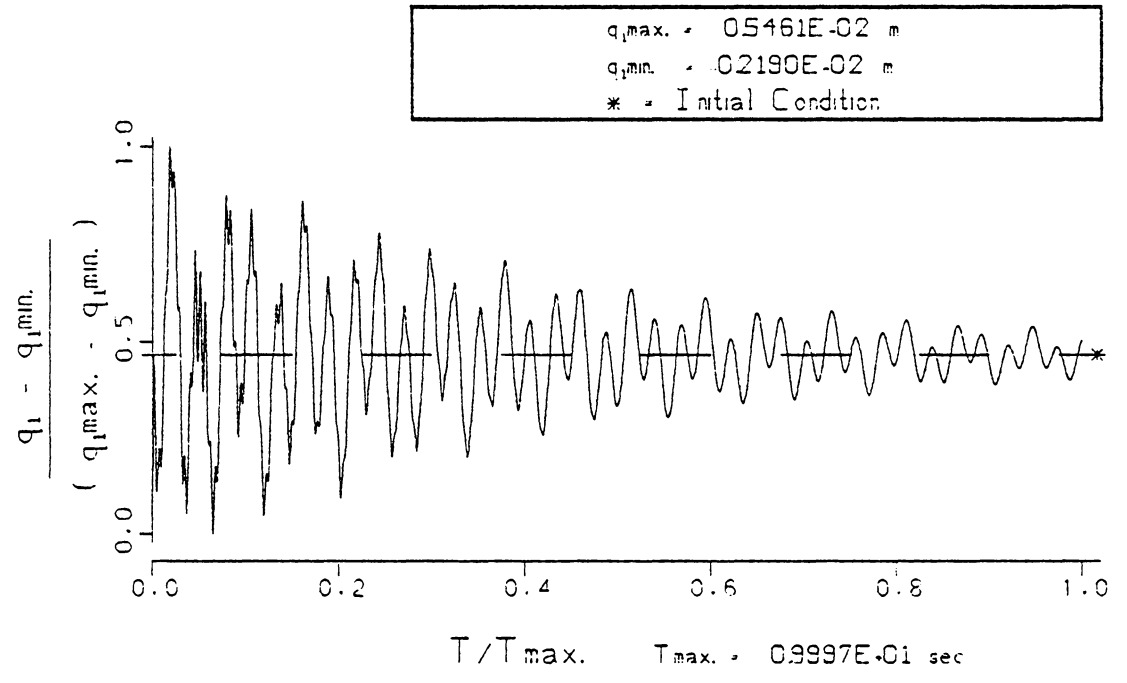

FIG. 76 LOWER BOOM JOINT RESPONSE. (q_1 , $\dot{q}_1$)
FOR CONDITIONS OF CASE A WHEN THE CABLE
DRUM BRAKE IS APPLIED DURING LOAD-LOWERING.
(COMPENSATED CRANE WITH CONTROLLER 2)

the crane system response subject to the conditions of Case A. The maximum vertical translation of the tracks, coordinate R_1 in Fig. 71, due to the initial shock of the dropped load is 20% greater than the uncompensated track response in Fig. 24; however, the remaining vertical response of the tracks is dramatically attenuated within 2.0 seconds. The rotational track response is smaller than the uncompensated track response in Fig. 25, and damps out significantly during the 10 second simulation. The boom chord rotation, ϕ_6 in Fig. 73, looks similar to the uncompensated response in Fig. 26, but also damps out significantly. The maximum load pendulation, ϕ_9 in Fig. 74, is smaller than the uncompensated load pendulation in Fig. 27. The amplitude of the response of ϕ_9 is attenuated significantly during the simulation, but the lower system frequency which dominates the ground motion, as seen in Fig. 77, is still present in the load pendulation. The time histories of coordinates R_9 and q_1 in Figs. 75 and 76 respectively are almost identical records, and both also are attenuated.

Figure 78 shows that the compensated pendent line tension experiences smaller fluctuations and that the pendent line does not become slack as the uncompensated pendent line in Fig. 29. The load line tension in Fig. 78 indicates that the load line experiences fewer periods of slackness and that the load motion damps out more quickly in the compensated response.

The characteristics of the compensated crane response with Controller 2, in Figs. 71 through 76, look very similar to those of

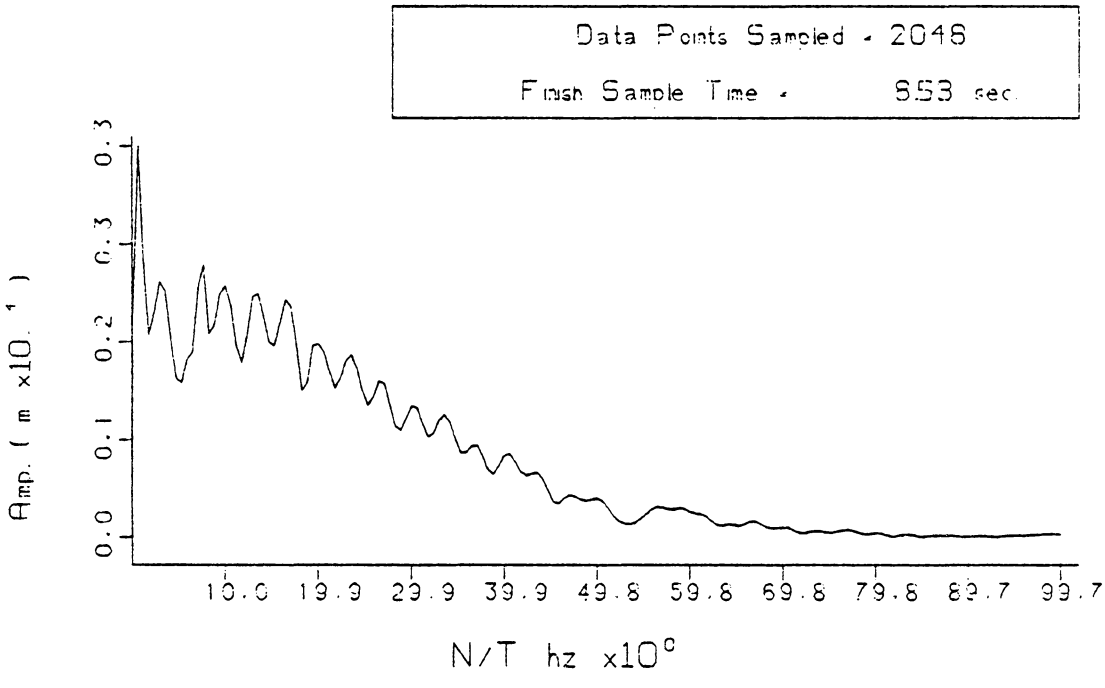

FIG. 77 FREQUENCY ANALYSIS OF COORDINATE R_1 FOR THE CONDITIONS OF CASE A WHILE BRAKING AT LOAD LOWERING (CONTROLLER 2)

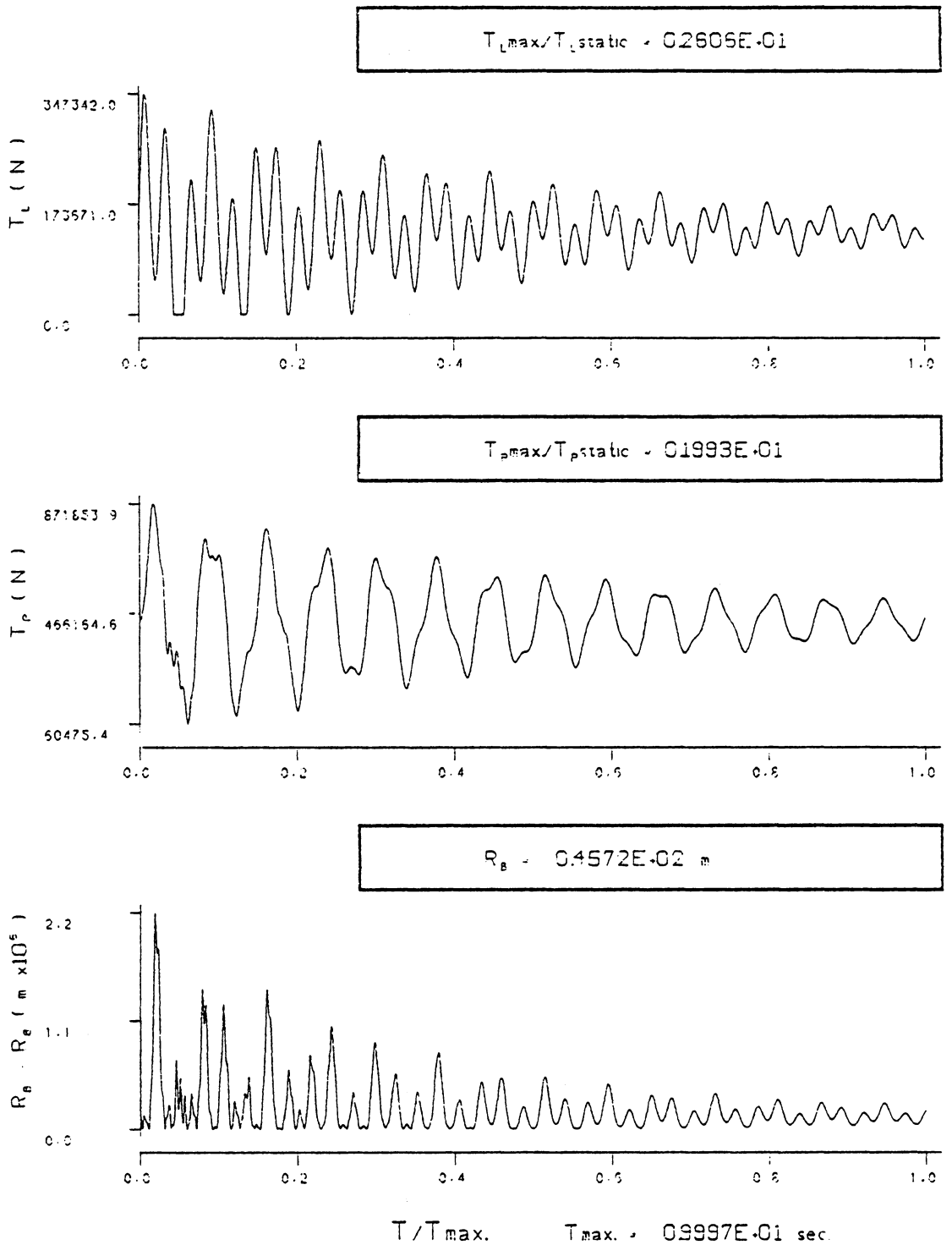

FIG. 78 THE TIME DEPENDENT BOOM CORD LENGTH. (R_B) AND THE TENSION IN THE PENDENT AND LOAD LINE ASSEMBLIES. (T_P AND T_L) FOR THE CONDITIONS OF CASE A. (CONTROLLER 2)

the uncompensated crane response, in Figs. 24 through 28. Recall that the characteristics of the crane response with Controller 1, in Figs. 63 through 66, looked very different from the characteristics of the uncompensated crane in Chapter 5. Controller 2 attenuates the response of the crane system by transferring energy advantageously to the supporting soil; the hydraulic actuator requires only 13.0 Kw to accomplish this reduction, as seen in Fig. 79. Controller 1 works against the ground motion and attenuates the response of the crane system by absorbing energy in the pendent actuator. Controller 1 requires 96 Kw, and attenuates the crane system response less than Controller 2.

The compensation technique used in Controller 2 detects the error in the lower boom joint displacement. The response of coordinate q_1 is characterized by higher frequencies, as seen in Fig. 80, than the response of coordinate ϕ_6 in Fig. 67 which is used by Controller 1. Detecting the error in a signal that changes more quickly enables Controller 2 to attenuate the crane system response with less power.

Case A (controller 3)

Controller 3 detects the error between the desired velocity of load pendulation and the actual velocity of load pendulation, and specifies the spool-valve position proportional to the error. The desired value of the load pendulation velocity, $\dot{\phi}_9$, is zero. The compensation technique is given in equation 6-31 as

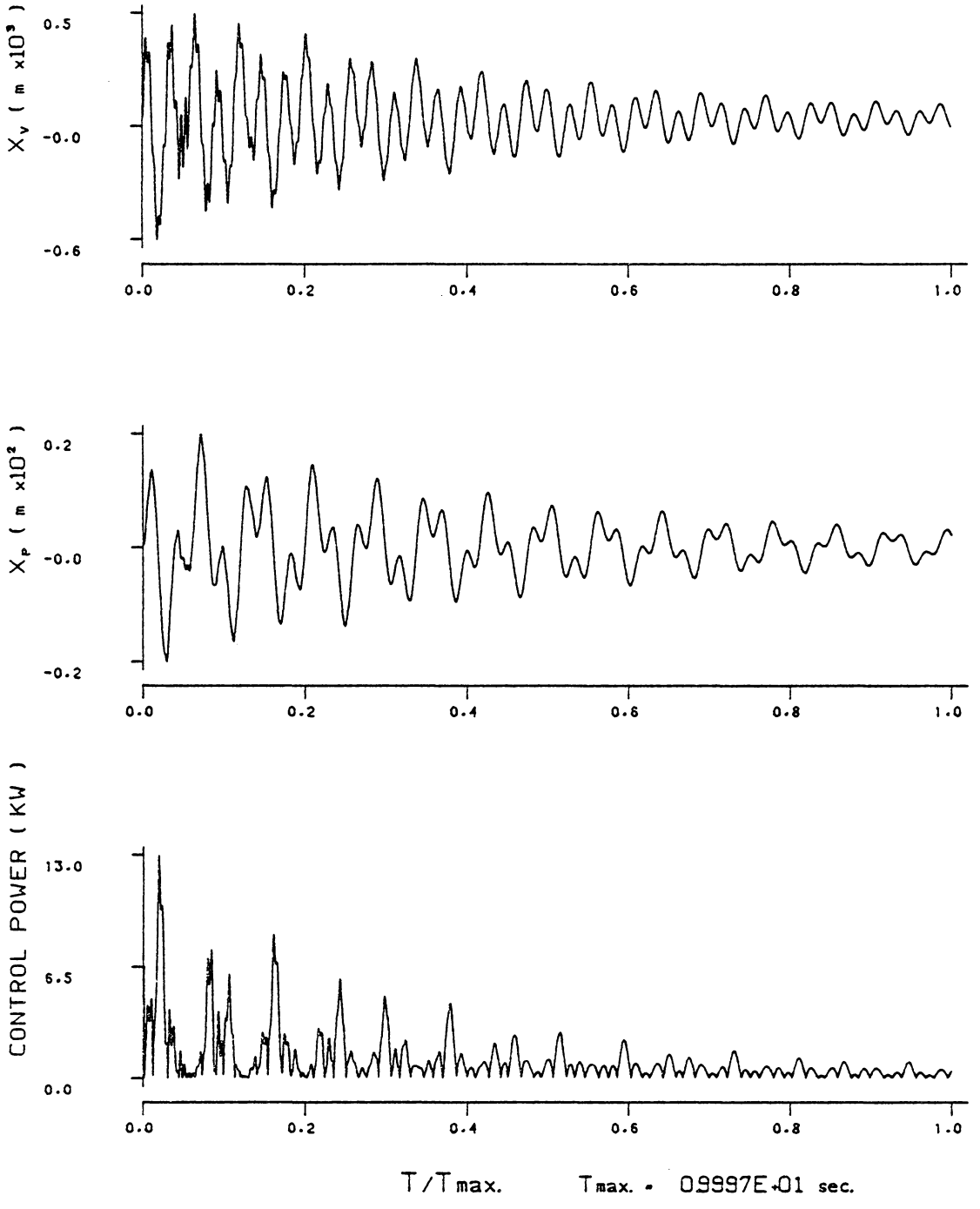

FIG. 79 THE TIME DEPENDENT ACTUATOR CONTROL POWER. AND THE DISPLACEMENT OF THE ACTUATOR PISTON AND SPOOL VALVE. (X_p AND X_v) FOR THE CONDITIONS OF CASE A. (CONTROLLER 2)

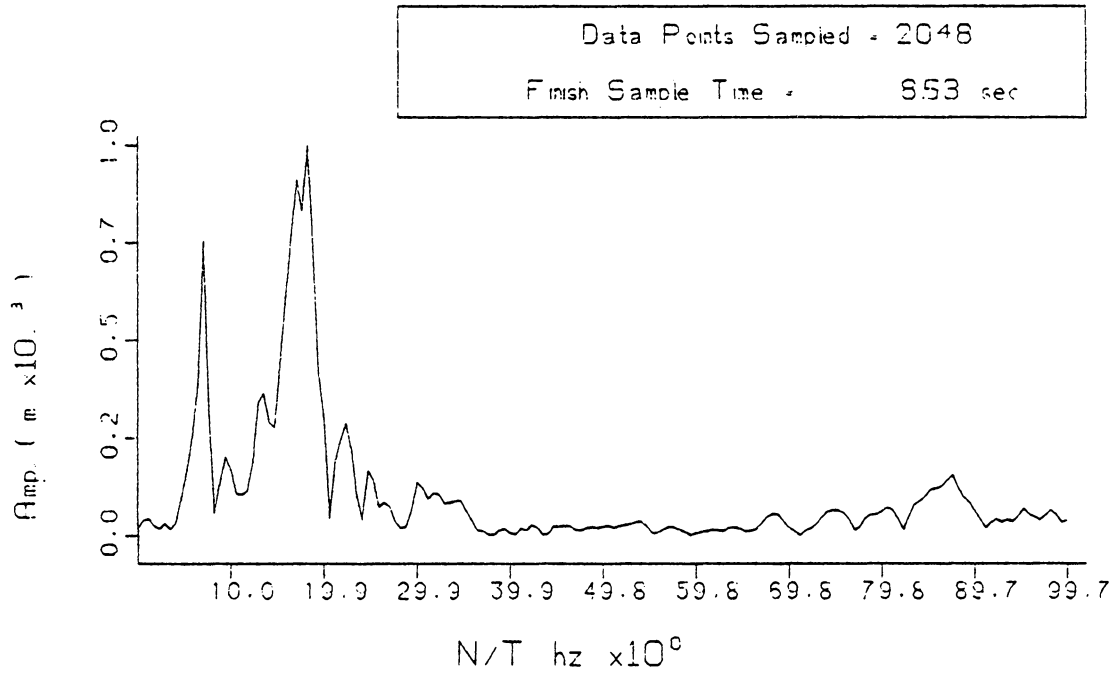

FIG. 80 FREQUENCY ANALYSIS OF COORDINATE q_1 FOR THE CONDITIONS OF CASE A WHILE BRAKING AT LOAD LOWERING (CONTROLLER 2)

$$x_v = K_4(\dot{\phi}_{9_D} - \dot{\phi}_9)$$

A gain of $K_4 = 0.20$ is used in this simulation.

The pendulations of the suspended load excite the crane system motion. Controller 3 is designed to reduce the load pendulations by allowing the boom tip to follow the motion of the suspended load. The controller monitors the load pendulation velocity because the centripetal and coriolis forces produced by the swinging load excite the crane system.

The time histories of the coordinate responses of the compensated crane with Controller 3 subject to the conditions of Case A are presented in Figs. 81 through 84. It is not surprising that the response records of the ground coordinates, R_1 and ϕ_2 in Figs. 81 and 82 respectively, look very similar to the response records of R_1 and ϕ_2 with Controller 1 in Figs. 63 and 64 since the boom chord rotation, ϕ_6 used in Controller 1, is strongly coupled to the load pendulation, ϕ_9 used in Controller 3. Notice that the maximum displacements of R_1 and ϕ_2 with Controller 3, in Figs. 81 and 82, are larger than the maximum displacements of R_1 and ϕ_2 with Controller 1, but Controller 3 attenuates the ground motion more during the 10 seconds of simulation than Controller 1.

The maximum amplitude of the pendulations of the suspended load with Controller 3, as seen in Fig. 83, are smaller than the pendulations in the uncompensated crane of Case A, given in Fig. 27. In addition, Controller 3 attenuates the pendulations dramatically within three

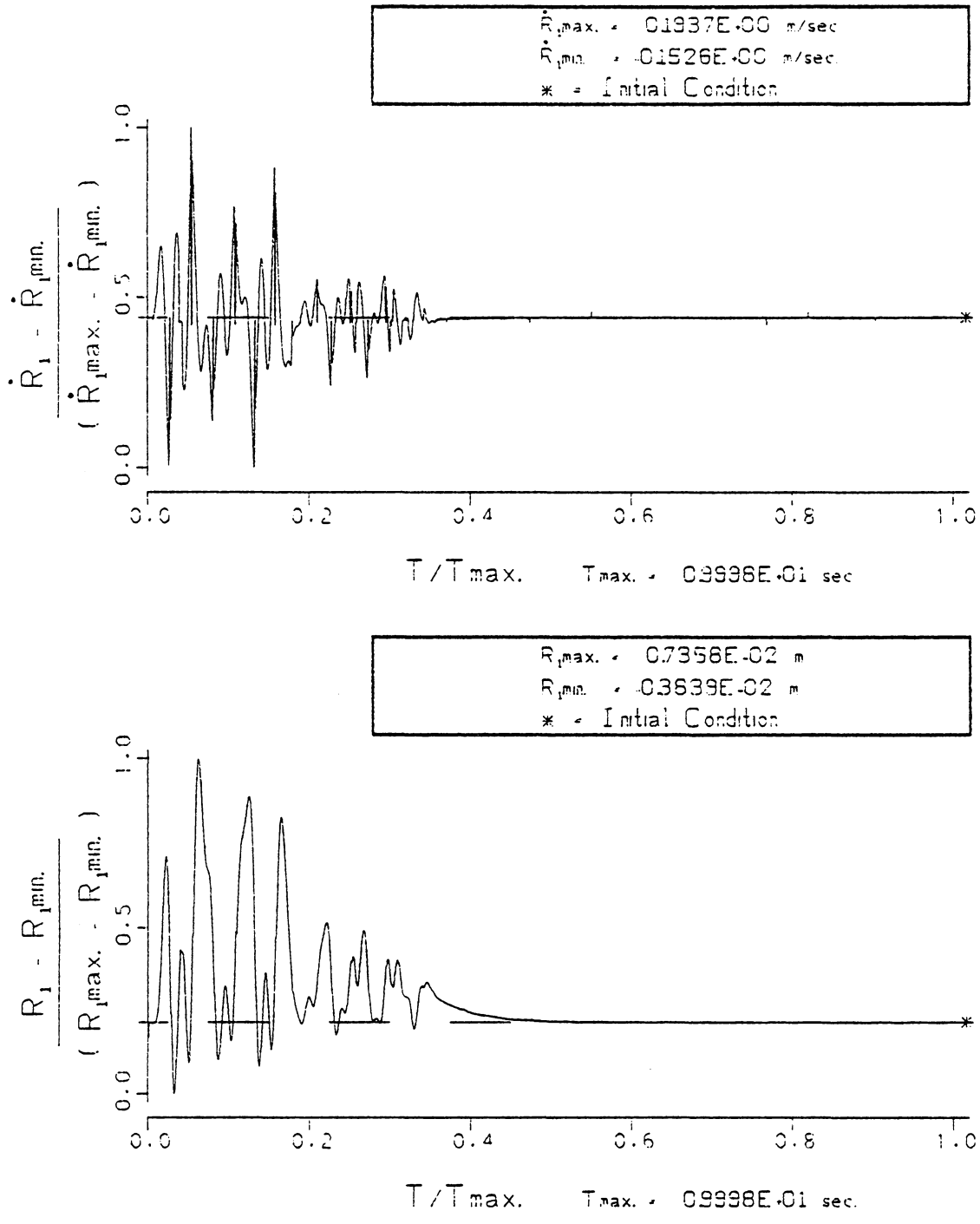

FIG. 81 VERTICAL RESPONSE OF THE TRACKS. (R_1 , $\dot{R}_1$) FOR CONDITIONS OF CASE A WHEN THE CABLE DRUM BRAKE IS APPLIED DURING LOAD-LOWERING. (COMPENSATED CRANE WITH CONTROLLER 3)

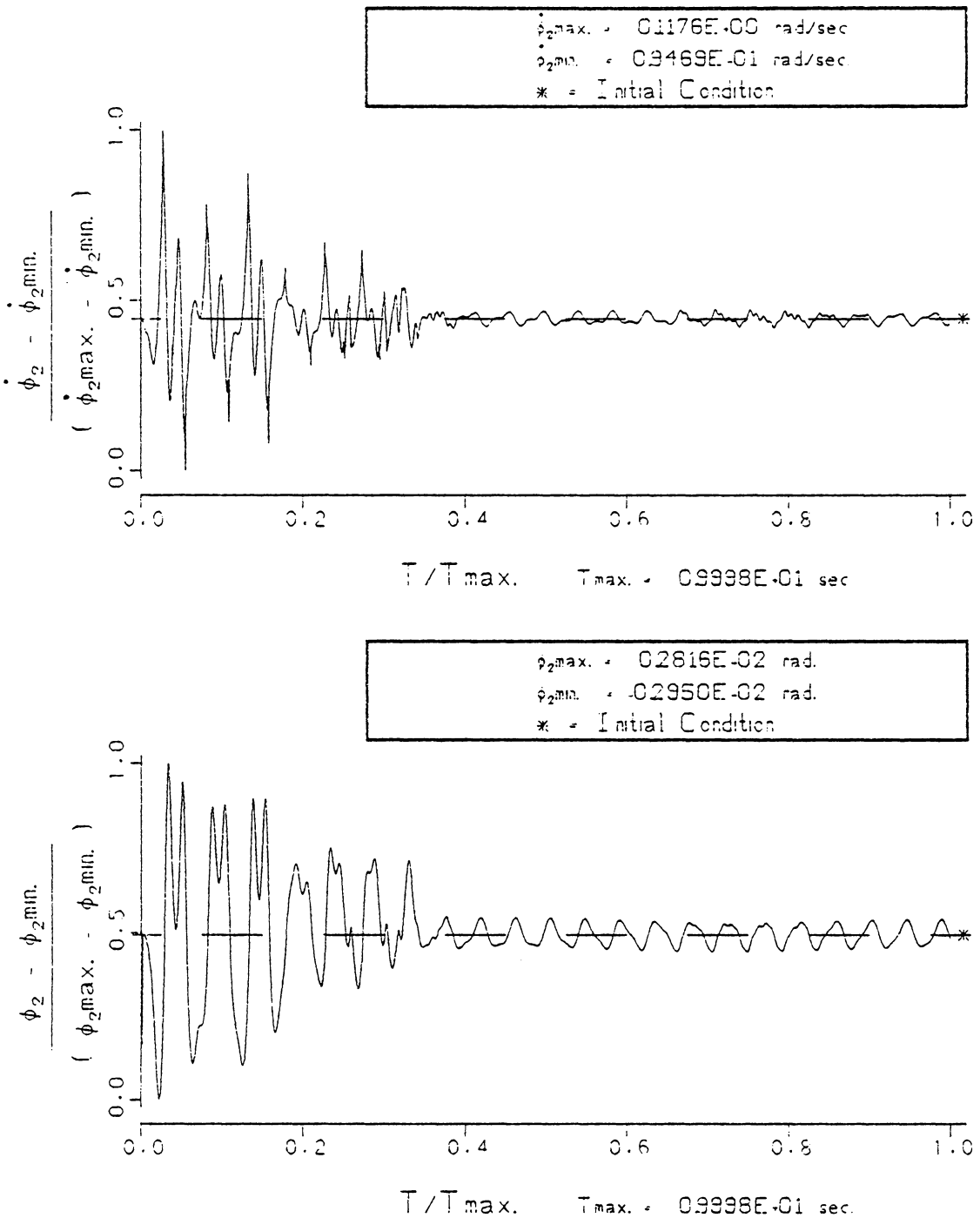

FIG. 82 ROTATIONAL RESPONSE OF THE TRACKS. (ϕ_2 , $\dot{\phi}_2$) FOR CONDITIONS OF CASE A WHEN THE CABLE DRUM BRAKE IS APPLIED DURING LOAD-LOWERING. (COMPENSATED CRANE WITH CONTROLLER 3)

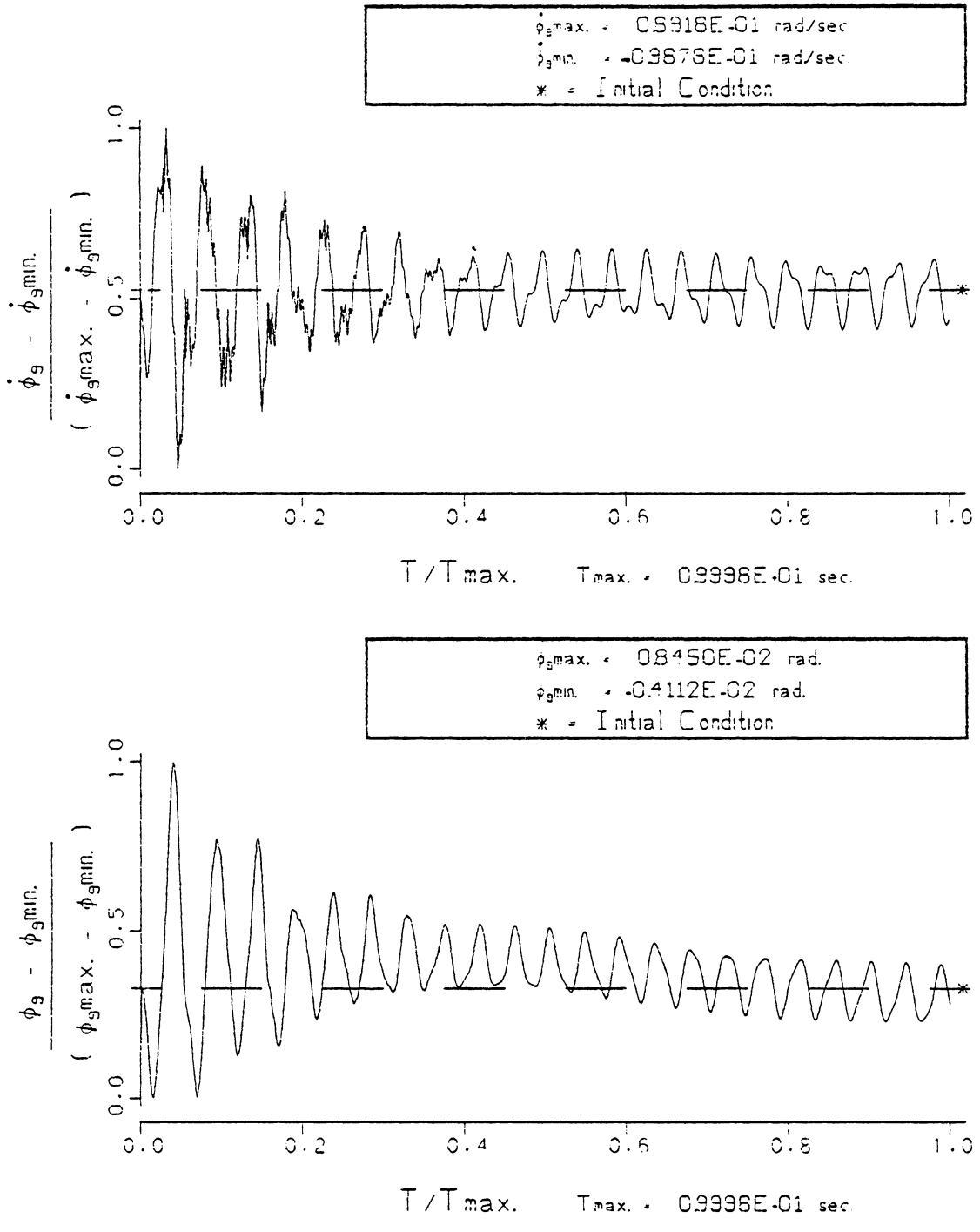

FIG. 83 PENDULATION OF THE LOAD, (ϕ_g , $\dot{\phi}_g$) FOR CONDITIONS OF CASE A WHEN THE CABLE DRUM BRAKE IS APPLIED DURING LOAD-LOWERING. (COMPENSATED CRANE WITH CONTROLLER 3)

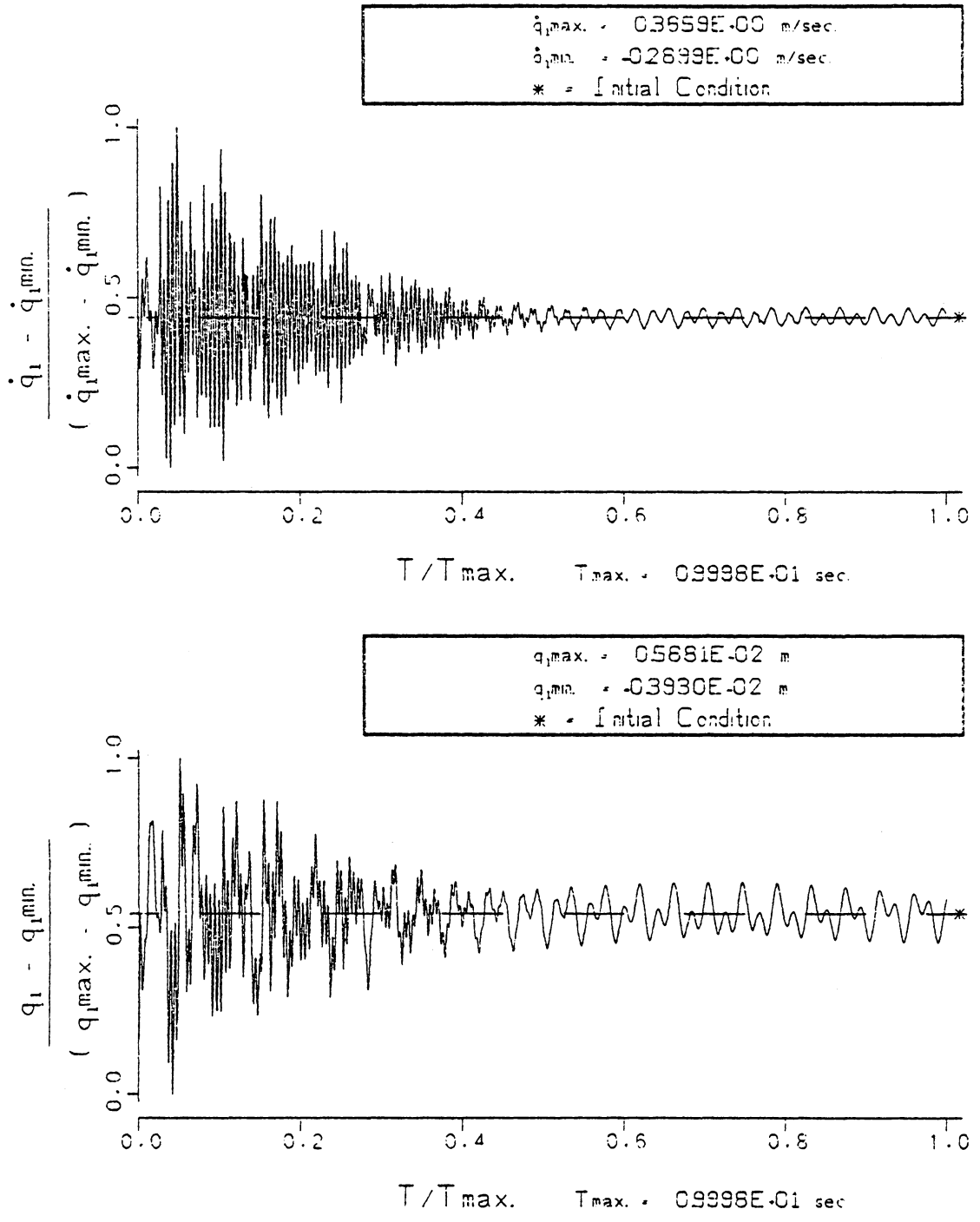

FIG. 84 LOWER BOOM JOINT RESPONSE. (q_1 , $\dot{q}_1$)
FOR CONDITIONS OF CASE A WHEN THE CABLE
DRUM BRAKE IS APPLIED DURING LOAD-LOWERING.
(COMPENSATED CRANE WITH CONTROLLER 3)

seconds. Reducing the load pendulation also reduces the boom motion, as seen in the response of coordinate q_1 in Fig. 84. Controller 3 attenuates the load pendulation and the boom motion more than either Controller 1 or Controller 2.

Controller 3 does attenuate the response of the crane at the sacrifice of the motion of the ground coordinates. Unfortunately the hydraulic actuator requires an extraordinary amount of power to reduce the crane motion, over 200 Kw as seen in Fig. 85. Notice that the spool-valve displacement, X_v, has reached its limit on both sides of the center position. Controller 3, like Controller 1, seems to work against the ground motion and does not transfer the crane system energy advantageously to the dissipating soil. The frequency content describing the ground motion, coordinates R_1 and ϕ_2 in Figs. 86 and 87, is very different from the frequency content describing the uncompensated ground motion, as seen in Figs. 31 and 32. The dominate frequency in the uncompensated ground motion, 7.0 Hz, is increased to 10.5 Hz by Controller 3.

Case B (controller 2)

Controller 2, which detects the error between the desired lower boom joint displacement and the actual displacement, is applied to a crane subject to the conditions of Case B. Recall that Case B models essentially the same crane as Case A, but subject to a different set of operating conditions. The crane in Case B is supported by a softer foundation than Case A, the boom operates at a steeper angle

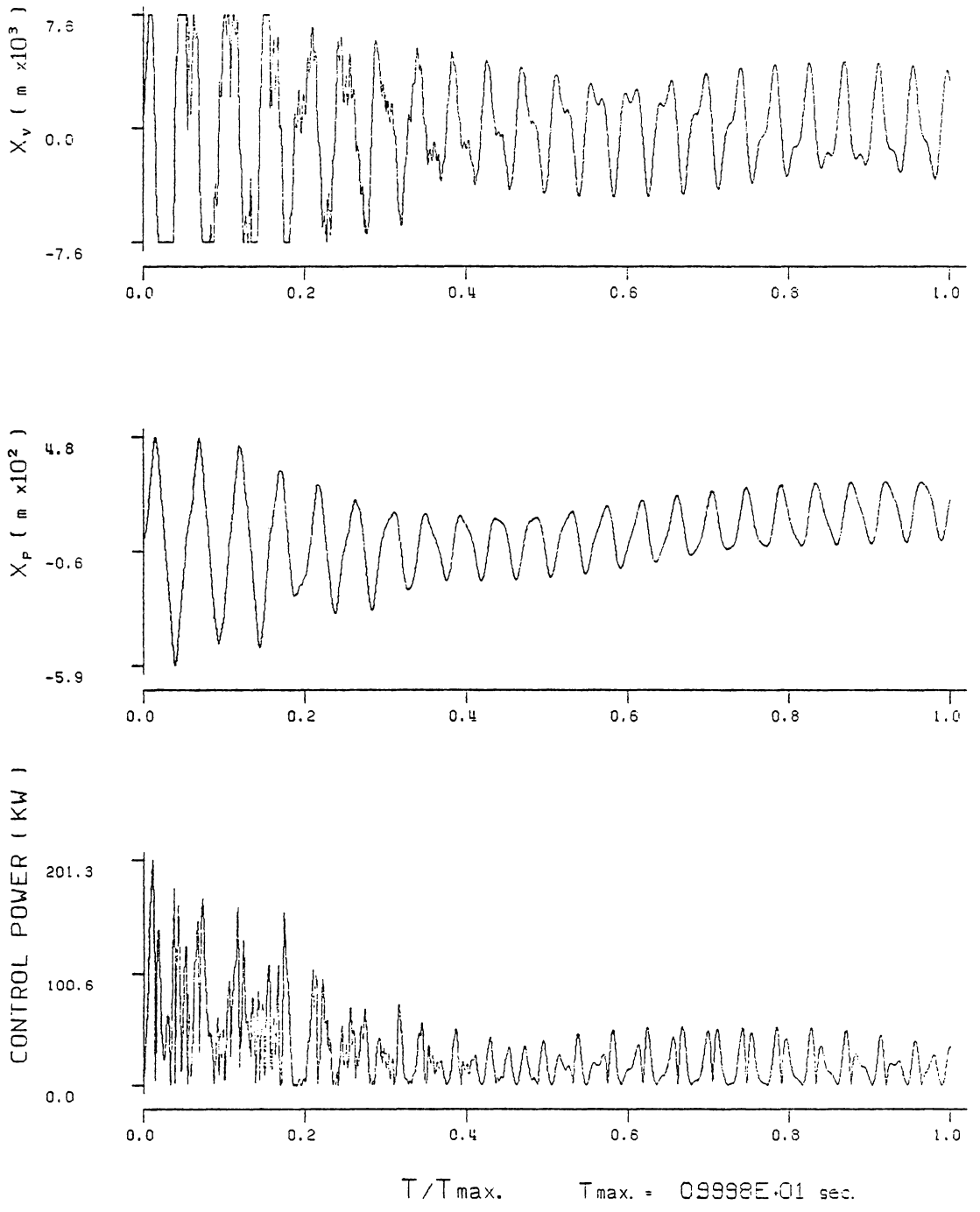

FIG. 85 THE TIME DEPENDENT ACTUATOR CONTROL POWER, AND THE DISPLACEMENT OF THE ACTUATOR PISTON AND SPOOL VALVE, (X_p AND X_v) FOR THE CONDITIONS OF CASE A (CONTROLLER 3).

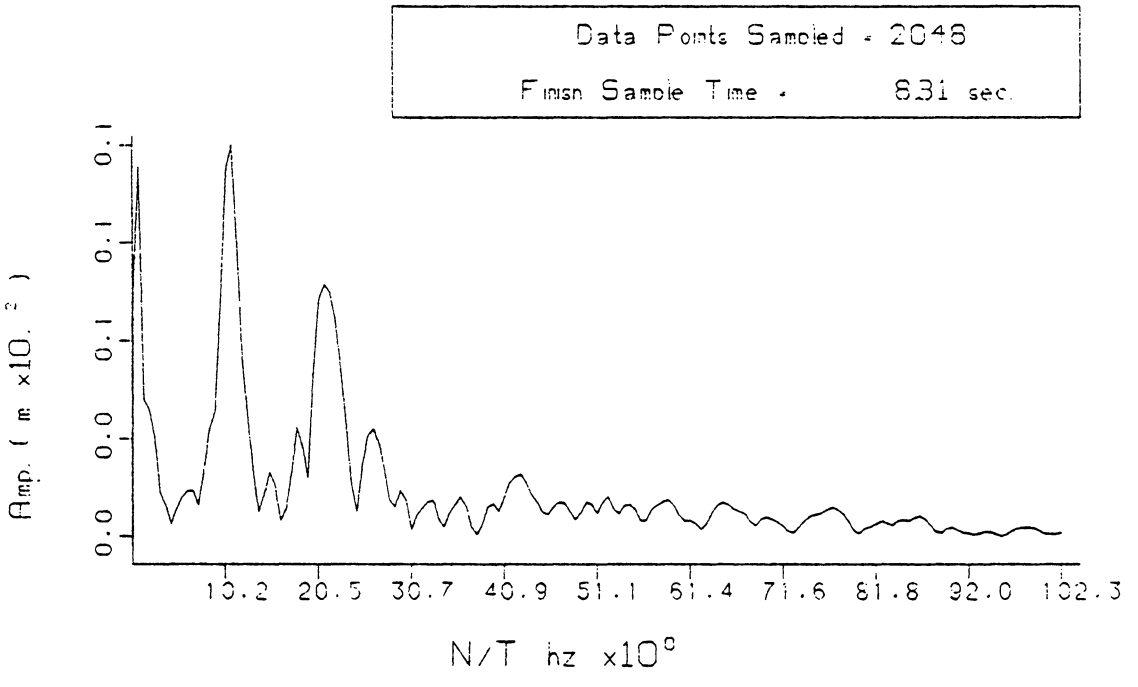

FIG. 86 FREQUENCY ANALYSIS OF COORDINATE R_1 FOR THE CONDITIONS OF CASE A WHILE BRAKING AT LOAD LOWERING (CONTROLLER 3)

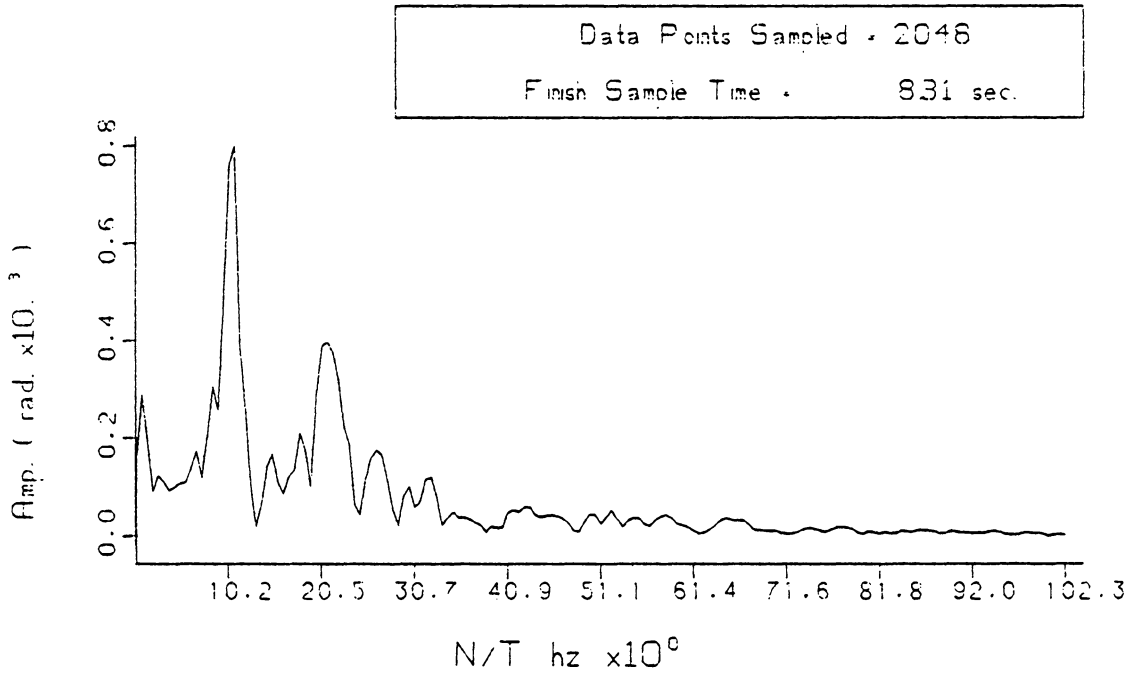

FIG. 87 FREQUENCY ANALYSIS OF COORDINATE φ_2 FOR THE CONDITIONS OF CASE A WHILE BRAKING AT LOAD LOWERING (CONTROLLER 3)

and the initial velocity of the dropped load in Case B is twice Case A. Controller 2 was chosen for Case B because it attenuated the crane response in Case A so well with the least power requirements of the three controllers developed in Chapter 6. A controller gain $K_3 = 0.15$ is used in this simulation.

The time histories of the coordinate responses for a crane subjected to the conditions of Case B compensated by Controller 2 are presented in Figs. 88 through 90. The ground motion, coordinates R_1 and ϕ_2 in Figs. 88 and 89 respectively, looks similar to the uncompensated ground motion in Figs. 37 and 38. The maximum amplitude of the compensated vertical translation is 43% less than the uncompensated track response in Fig. 37, and the compensated response damps out 2 sec sooner than the uncompensated response. The maximum amplitude of the compensated track rotation, in Fig. 89, is only 7% less than the uncompensated track rotation in Fig. 38, but the compensated motion damps out 2 sec sooner than the uncompensated motion. The maximum amplitude of the compensated boom displacement, coordinate q_1 in Fig. 90, is essentially the same as the uncompensated response in Fig. 42; however, the compensated boom response exhibits slightly more damping than the uncompensated response. The lower boom joint velocity, $\dot{q}_1$ also in Fig. 90, is 46% less than the uncompensated boom joint velocity in Fig. 42, and does not display the pronounced beat phenomenon that the uncompensated response does.

The pendent controller does add some damping to the crane system, as seen in Fig. 91. The boom deflections in the compensated crane are slightly smaller and do damp out more quickly, since the

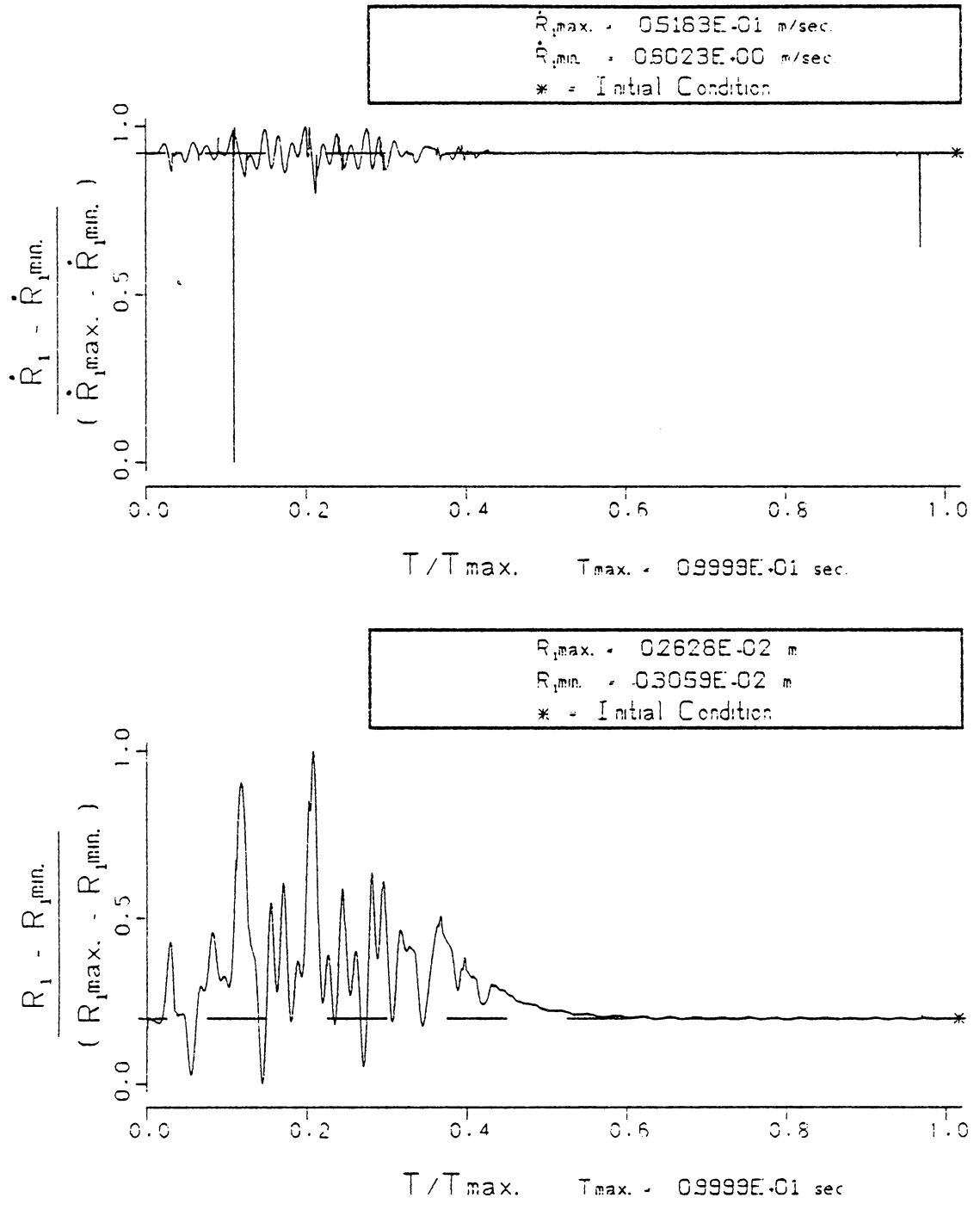

FIG. 88 VERTICAL RESPONSE OF THE TRACKS. (R_1 , $\dot{R}_1$) FOR CONDITIONS OF CASE B WHEN THE CABLE DRUM BRAKE IS APPLIED DURING LOAD-LOWERING. (COMPENSATED CRANE WITH CONTROLLER 2)

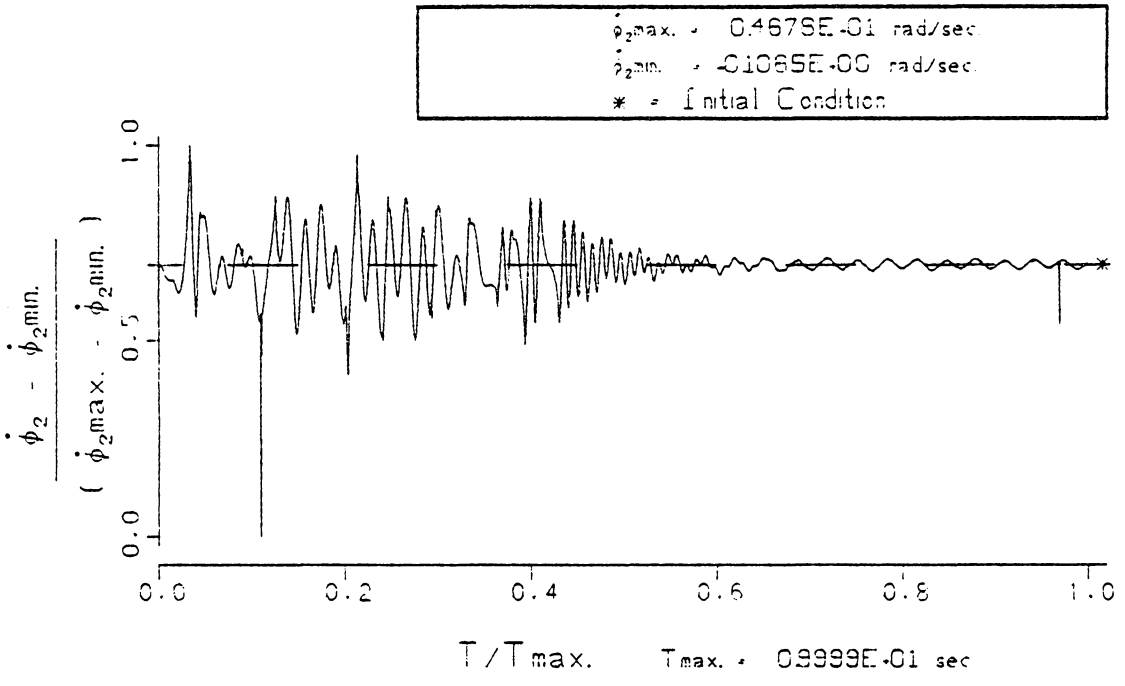

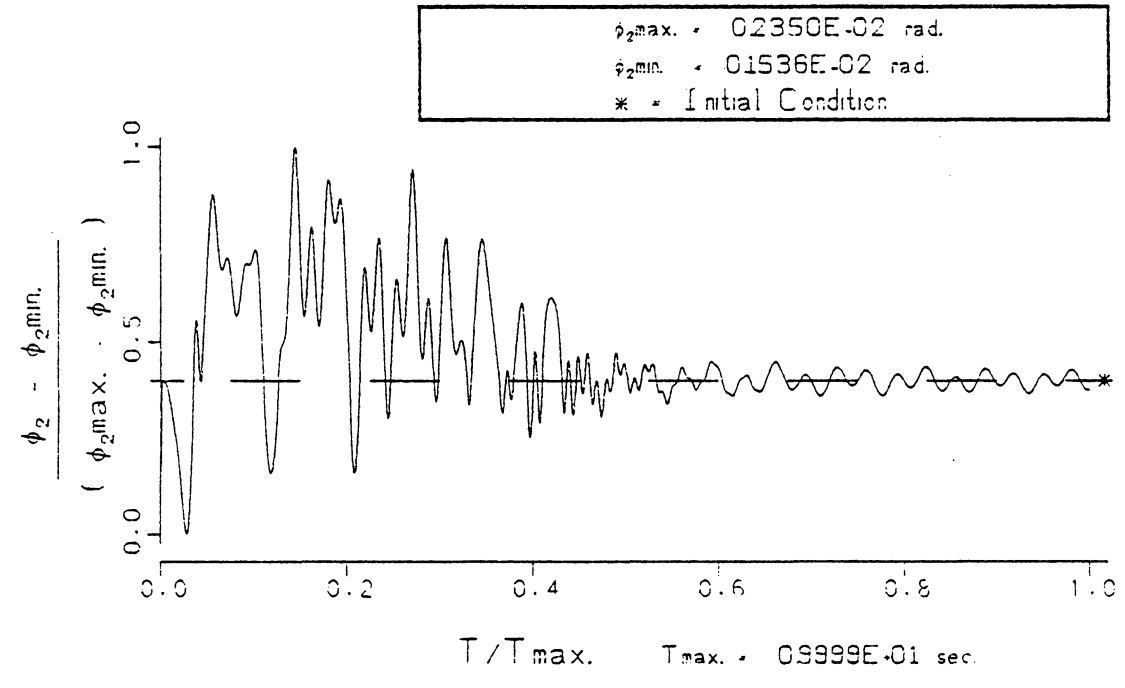

FIG. 89 ROTATIONAL RESPONSE OF THE TRACKS. (ϕ_2 , $\dot{\phi}_2$) FOR CONDITIONS OF CASE B WHEN THE CABLE DRUM BRAKE IS APPLIED DURING LOAD-LOWERING. (COMPENSATED CRANE WITH CONTROLLER 2)

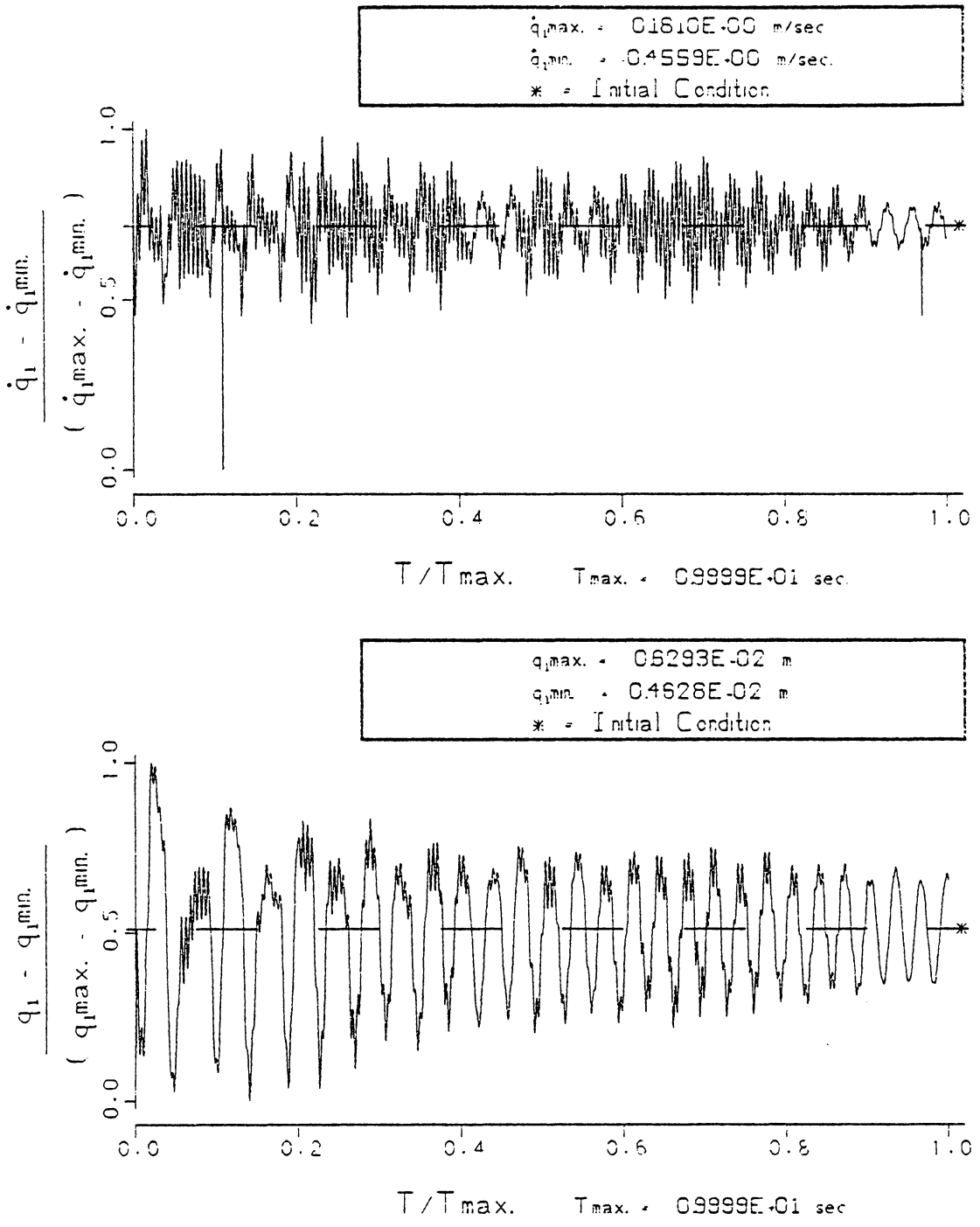

FIG. 90 LOWER BOOM JOINT RESPONSE. (q_1 , $\dot{q}_1$)
FOR CONDITIONS OF CASE B WHEN THE CABLE
DRUM BRAKE IS APPLIED DURING LOAD-LOWERING.
(COMPENSATED CRANE WITH CONTROLLER 2)

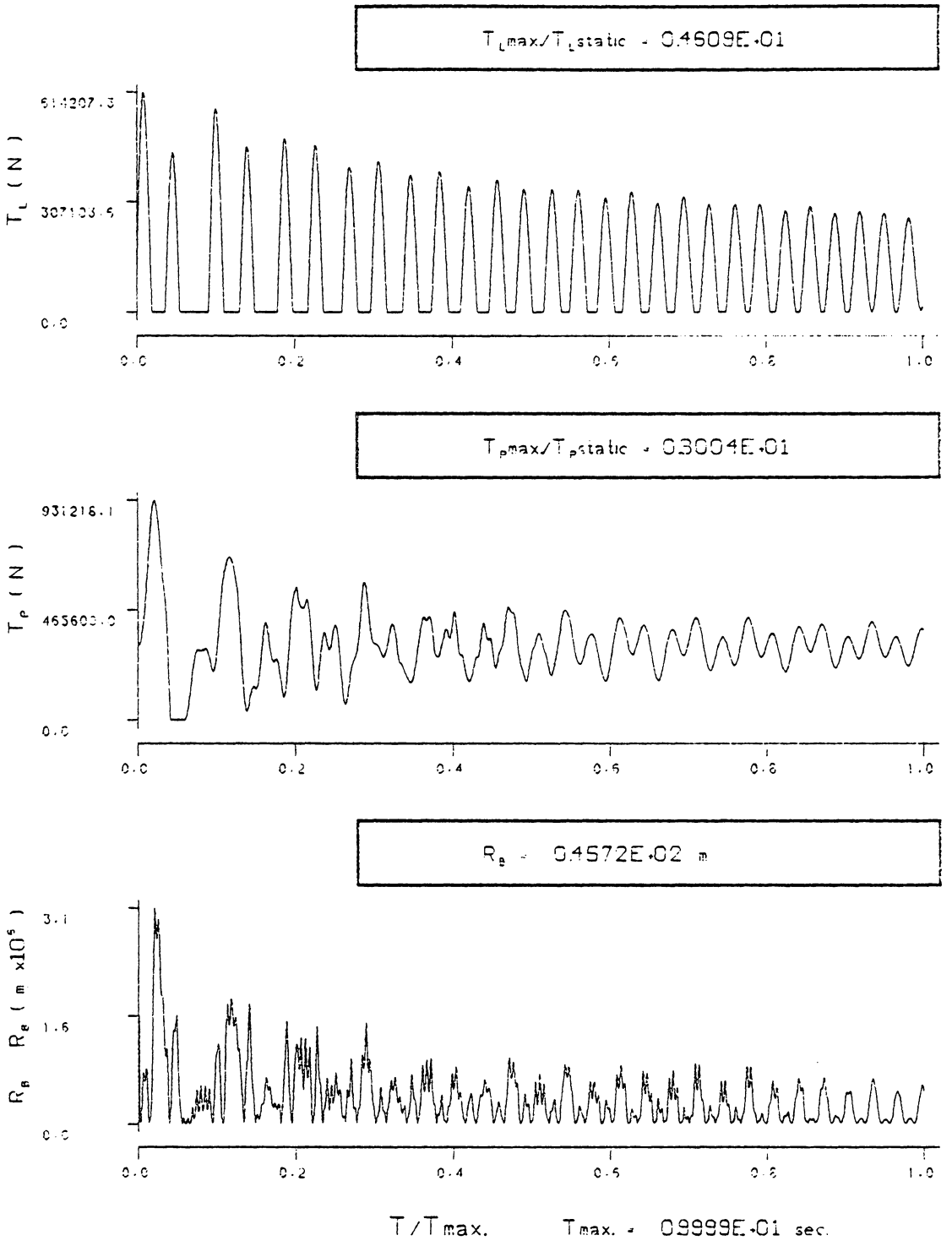

FIG. 91 THE TIME DEPENDENT BOOM CORD LENGTH. (R_B) AND THE TENSION IN THE PENDENT AND LOAD LINE ASSEMBLIES. (T_p AND T_L) FOR THE CONDITIONS OF CASE B. (CONTROLLER 2).

amplitude of the boom chord length oscillations is smaller than the uncompensated oscillations in Fig. 47 and damps out more quickly. The maximum compensated pendent line tension is also slightly smaller than the uncompensated pendent line tension, but more importantly the fluctuations in the compensated pendent line are attenuated more during the simulation. Likewise, the fluctuations in the load line tension are also attenuated.

Controller 2 requires a maximum of 18 Kw during the simulation, as seen in Fig. 92, but only modestly attenuates the response of the crane system subject to the conditions of Case B. Earlier, Controller 2, with the same gain $K_3 = 0.15$, dramatically attenuated the response of essentially the same crane operating under the conditions of Case A and required only 13 Kw. Is it feasible that a controller could attenuate the response of a crane system dramatically under one set of operating conditions, and then only modestly attenuate the response of the same crane for another set of operating conditions?

Recall that Controller 2 in Case A efficiently attenuated the crane system response by transferring or dumping energy to the dissipating soil. Controller 1 and Controller 3 worked against the ground motion, but Controller 2 dumps energy to the ground at the same frequencies that the ground motion occurs. The frequency content of coordinate R_1, in Fig. 77, is populated by many frequencies, and the frequency content of coordinate q_1, given in Fig. 80, is dominated by three frequencies which fall within the range of the major frequencies in the motion of coordinate R_1. It is no surprise then,

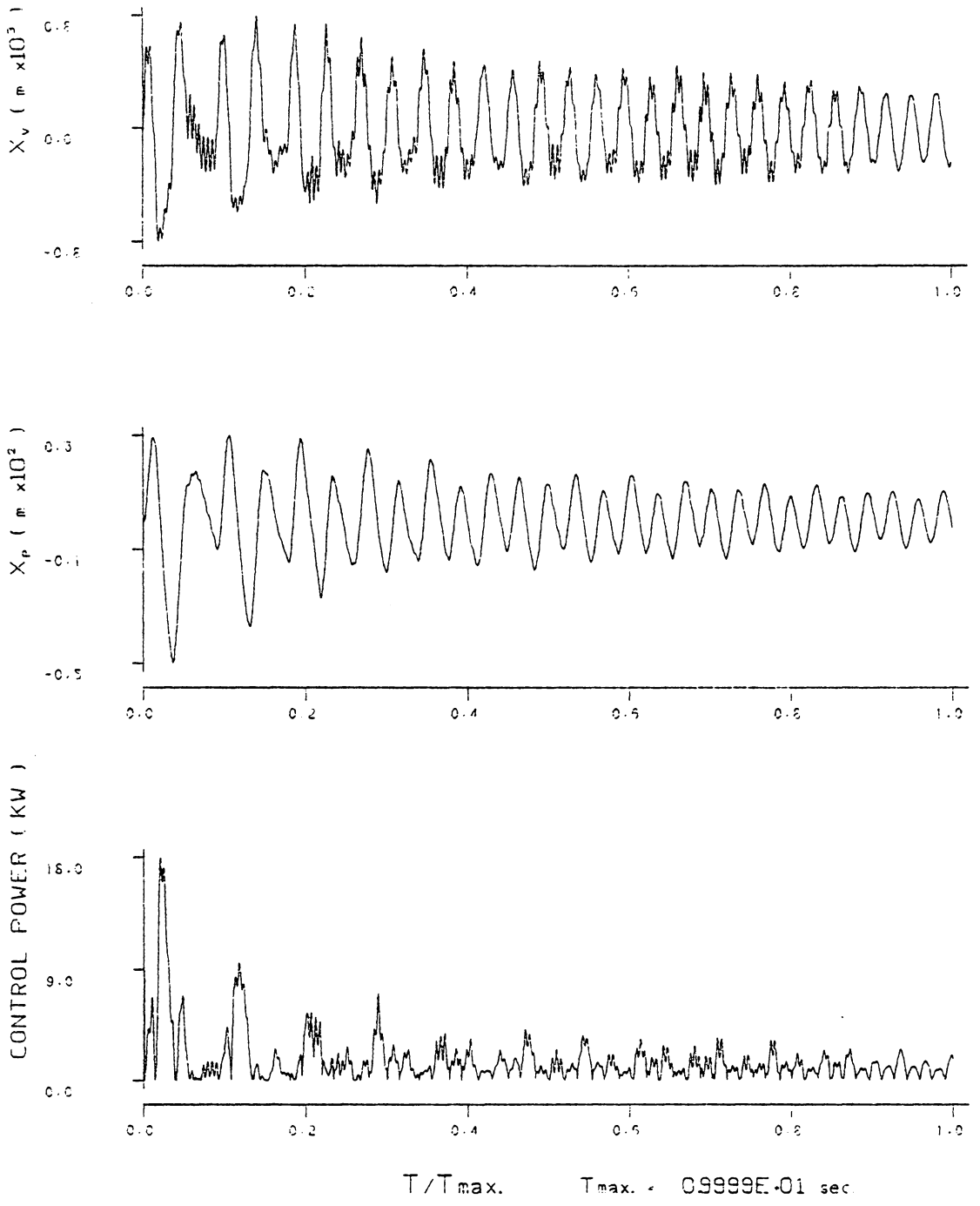

FIG. 92 THE TIME DEPENDENT ACTUATOR CONTROL POWER. AND THE DISPLACEMENT OF THE ACTUATOR PISTON AND SPOOL VALVE. (X_p AND X_v). FOR THE CONDITIONS OF CASE 5. (CONTROLLER 2).

that Controller 2 in Case A which monitors the error in coordinate q_1, is able to dump energy to the soil at a frequency that is compatible with the ground motion.

Controller 2 in Case B dumps energy to the dissipating soil advantageously because it works with the ground motion. This is apparent because the frequency content of the compensated motion of coordinate R_1, given in Fig. 93, is practically unchanged from the frequency content of the uncompensated ground motion in Fig. 44. The frequency content of the compensated motion of coordinate R_1, in Fig. 93 of Case B, looks very different from the frequency content of the compensated ground motion of Case A in Fig. 77 because the soil modulus in Case B is three-quarters the value used in Case A. Notice that many frequency components describe the ground motion in Case A, and that only a few major frequencies describe the ground motion in Case B. The motion of coordinate q_1 in Case B is dominated by a single frequency, as seen in Fig. 94, and this frequency coincides with the dominate frequency in the motion of coordinate R_1 in Fig. 93. Then, the frequencies at which Controller 2 tries to dump energy to the ground do not have the same opportunities to coincide with frequencies in the ground motion as they did in Case A. The controller frequencies that do coincide with frequencies in the ground motion do not describe a large portion of the crane system energy, so the crane system response is only attenuated modestly.

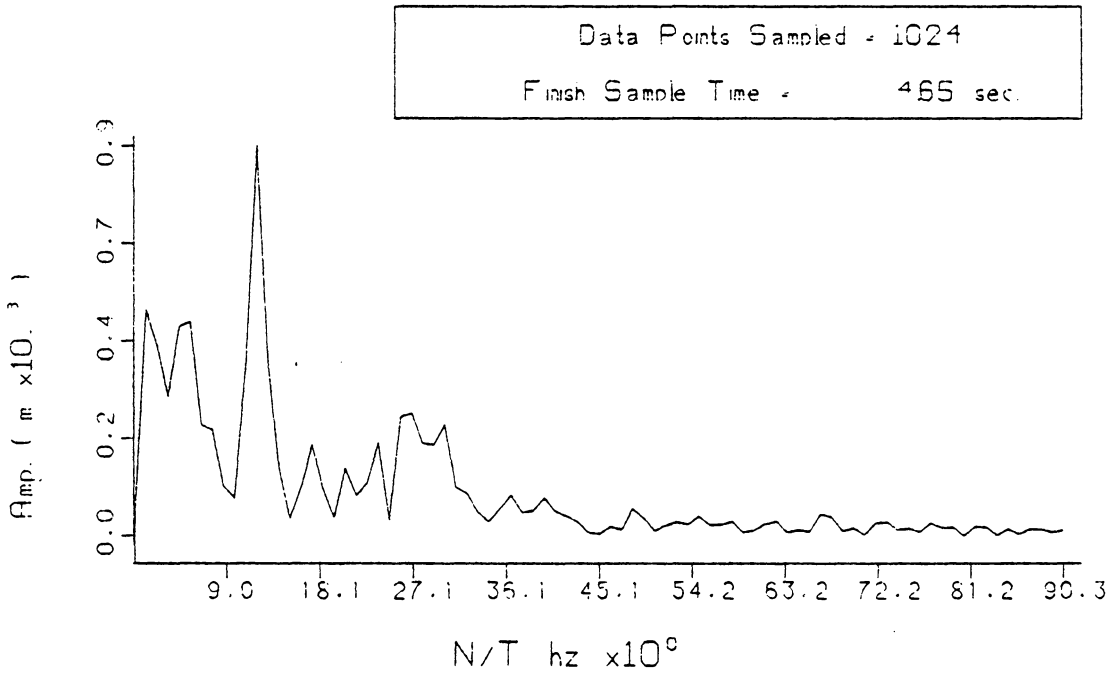

FIG. 93 FREQUENCY ANALYSIS OF COORDINATE R_1 FOR THE CONDITIONS OF CASE 5 WHILE BRAKING AT LOAD LOWERING (CONTROLLER 2)

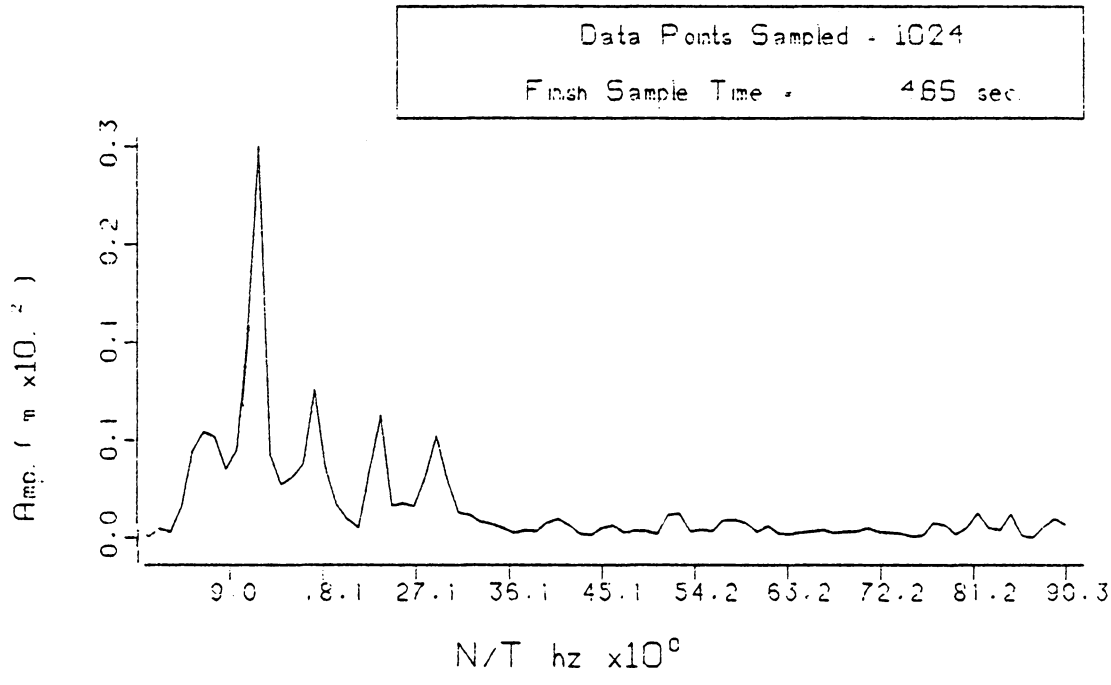

FIG. 94 FREQUENCY ANALYSIS OF COORDINATE q_1 FOR THE CONDITIONS OF CASE B WHILE BRAKING AT LOAD LOWERING (CONTROLLER 2)

Case C (controller 2)

Controller 2, which detects the error between the desired lower boom joint displacement and the actual displacement, is applied to the crane modelled in Case C. Recall that Case C represents an extreme set of operating conditions. The crane boom is twice as long as the boom used in Cases A and B and operates at a steeper angle than used in Case A. The soil modulus in Case C represents the softest soil of all three cases, one-half the value used in Case A. Controller 2 was chosen to reduce the boom-tip excursions in the longer boom. A controller gain $K_3 = 0.02$ is used in this simulation.

The time histories of the ground response, coordinates R_1 and ϕ_2, are given in Figs. 95 and 96. The maximum compensated vertical translation of the tracks, in Fig. 95, is 9% smaller than the uncompensated response. Notice that the tracks are still displaced above the initial position for the entire 10 second simulation in the compensated model. The compensated vertical track response, in Fig. 95, is almost an identical record of the uncompensated track response, in Fig. 48, besides the slight reduction in amplitudes. The amplitude of the rotational track response, given in Fig. 96, is only 5% smaller than the uncompensated rotational track response in Fig. 49. Again the two records are almost identical, the pendent controller has not added any damping to the crane system.

The compensated boom deflections, as seen in Fig. 97, are actually slightly larger than the uncompensated boom deflections, in Fig. 59, since the amplitude of the boom chord length fluctuations are larger

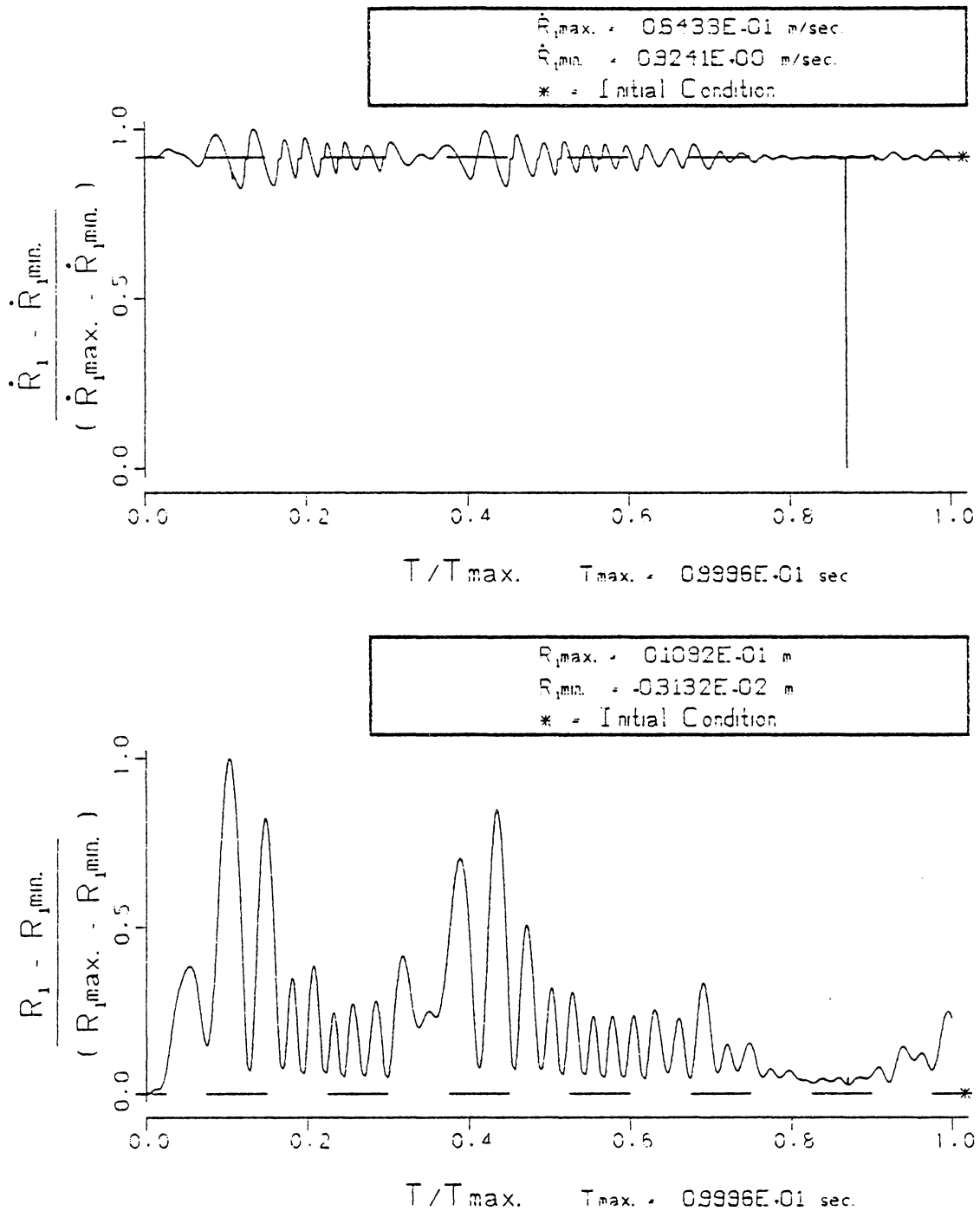

FIG. 95 VERTICAL RESPONSE OF THE TRACKS. (R_1 , $\dot{R}_1$) FOR CONDITIONS OF CASE C WHEN THE CABLE DRUM BRAKE IS APPLIED DURING LOAD-LOWERING. (COMPENSATED CRANE WITH CONTROLLER 2)

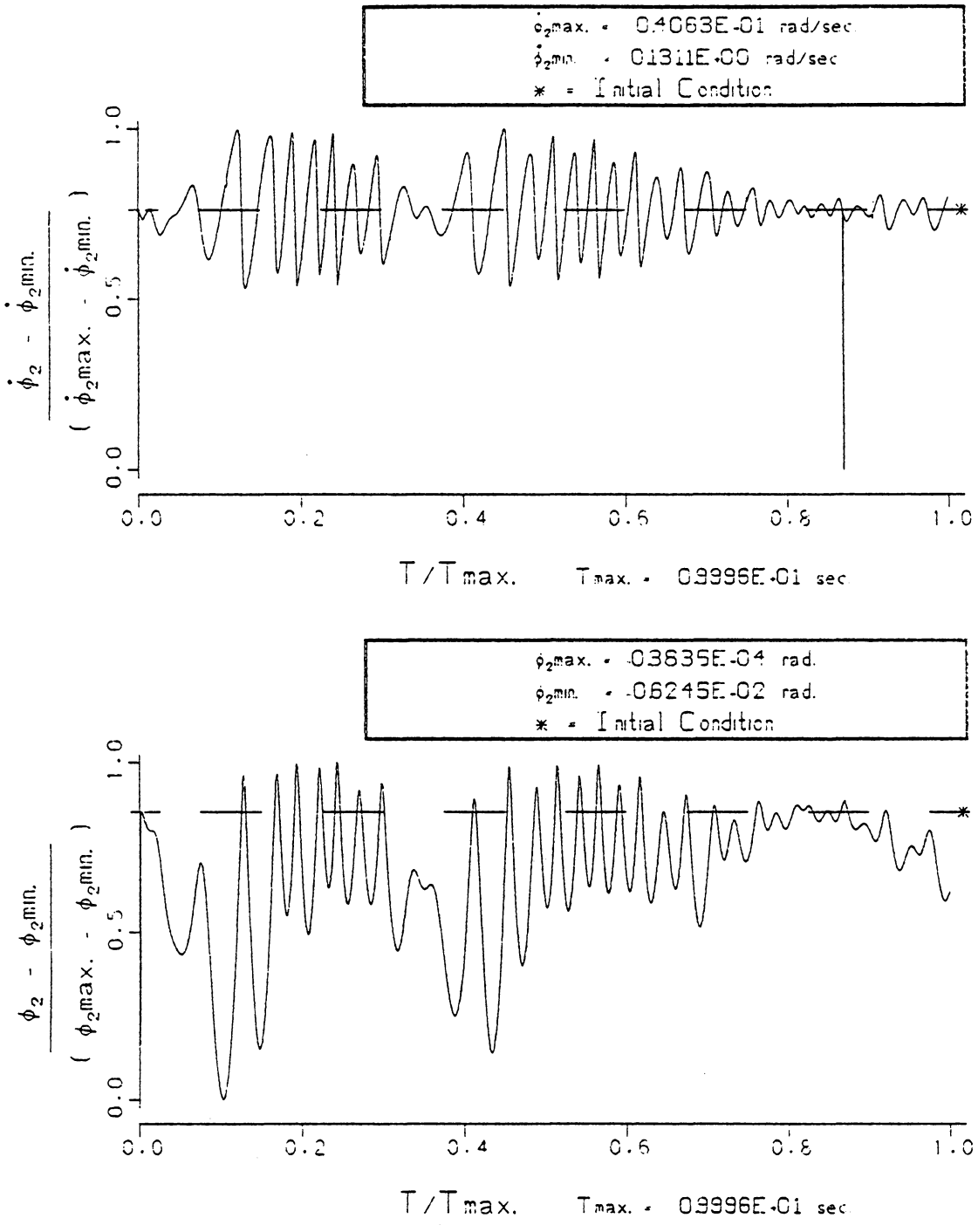

FIG. 96 ROTATIONAL RESPONSE OF THE TRACKS. (ϕ_2 , $\dot{\phi}_2$) FOR CONDITIONS OF CASE C WHEN THE CABLE DRUM BRAKE IS APPLIED DURING LOAD-LOWERING. (COMPENSATED CRANE WITH CONTROLLER 2)

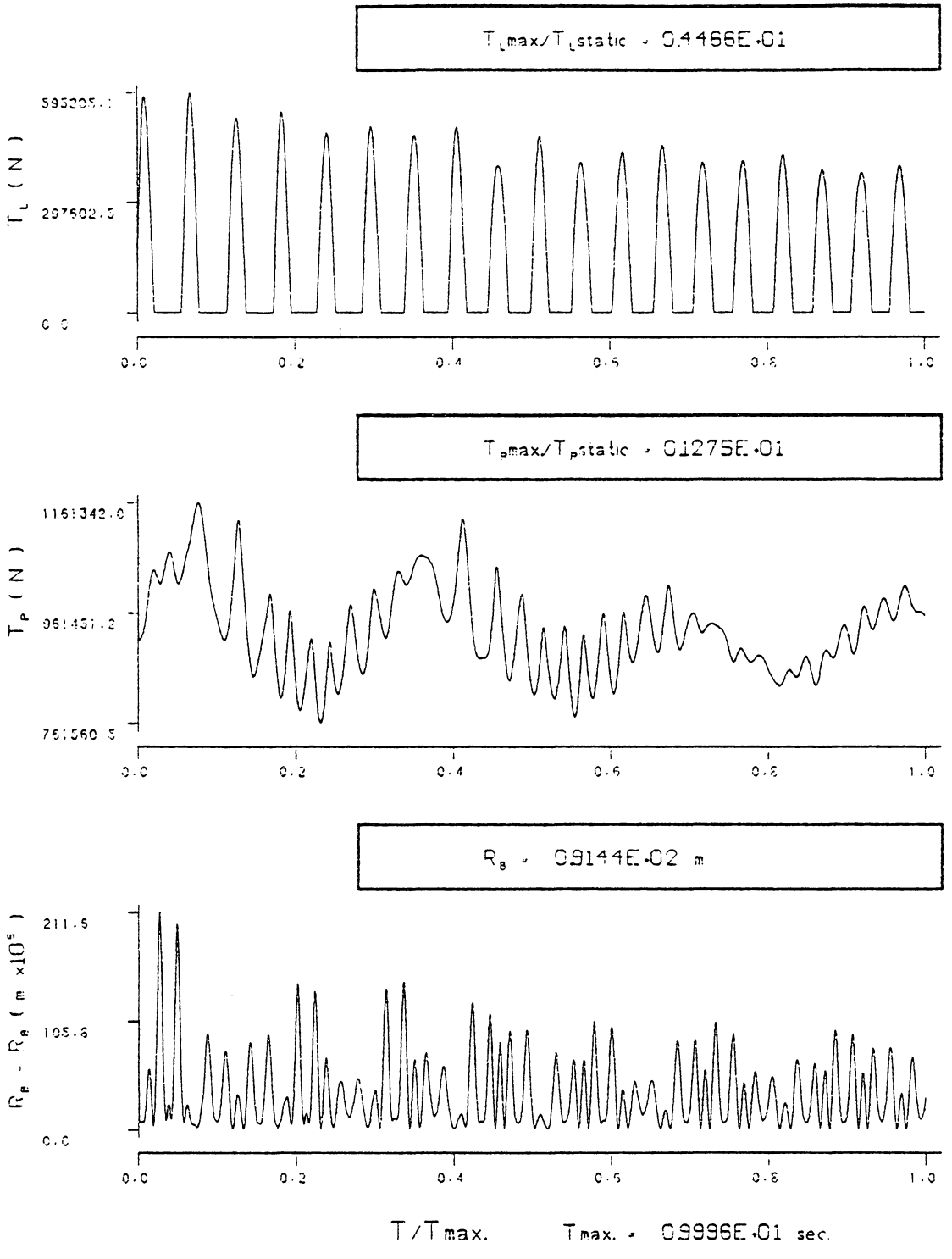

FIG. 97 THE TIME DEPENDENT BOOM CORD LENGTH. (R_B) AND THE TENSION IN THE PENDENT AND LOAD LINE ASSEMBLIES. (T_P AND T_L) FOR THE CONDITIONS OF CASE C. (CONTROLLER 2).

in the compensated model. The pendent controller drives the boom motion since the boom deflections increase in the compensated model. The boom motion, although larger in the compensated model, does not diverge from equilibrium, but damps out during the simulation as seen in Fig. 97. Doubling the controller gain produces larger boom deflections, but does not drive the crane away from equilibrium.

Controller 2 only marginally attenuates the crane response since the boom coordinates experience larger deflections. The hydraulic actuator requires a maximum of 37.1 Kw to accomplish the attenuations, as seen in Fig. 98. Notice that both the frequency content of coordinate R_1 in Fig. 99 and the frequency content of coordinate q_1 in Fig. 100 are populated with many major frequencies; however, only one of their major frequencies coincide. The pendent controller, therefore, is not able to dump much energy at a frequency that the ground motion can accept the energy.

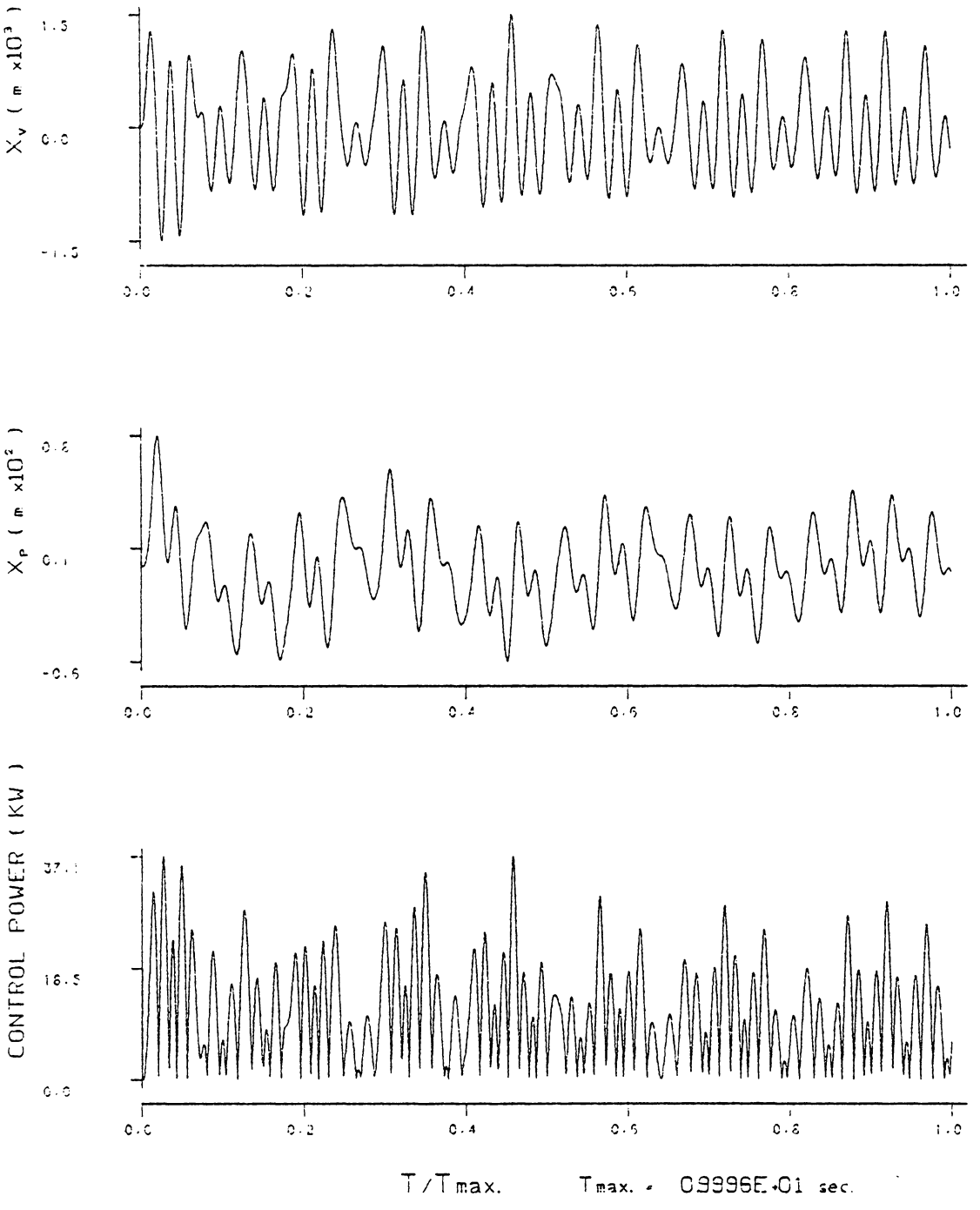

FIG. 98 THE TIME DEPENDENT ACTUATOR CONTROL POWER. AND THE DISPLACEMENT OF THE ACTUATOR PISTON AND SPOOL VALVE. (X_p AND X_v) FOR THE CONDITIONS OF CASE C. (CONTROLLER 2)

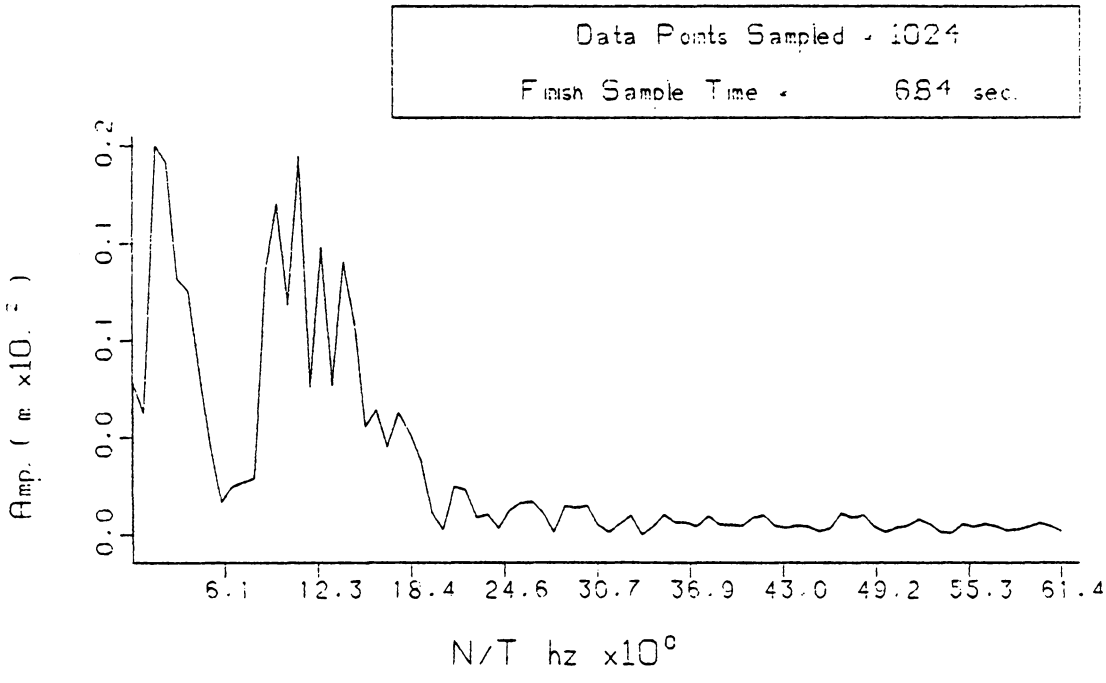

FIG.99 FREQUENCY ANALYSIS OF COORDINATE R_1 FOR THE CONDITIONS OF CASE C WHILE BRAKING AT LOAD LOWERING (CONTROLLER 2)

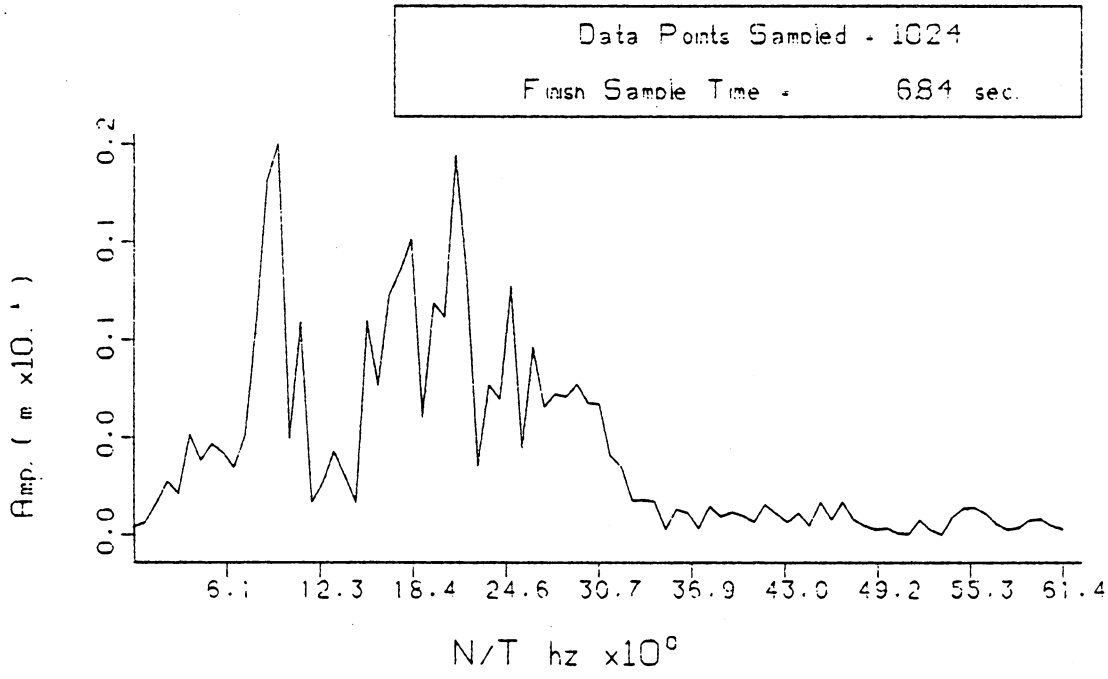

FIG. 100 FREQUENCY ANALYSIS OF COORDINATE q_1 FOR THE CONDITIONS OF CASE C WHILE BRAKING AT LOAD LOWERING (CONTROLLER 2)

8. CONCLUSIONS AND RECOMMENDATIONS

The purpose of this thesis was to develop a reduced-order analytical model to describe the transient response characteristics of a crawler crane and to apply a feedback control system and actuator to the crane to attenuate transient vibrations.

The simulations have shown that the reduced-order model is able to predict the following conditions:

1. Tilting of the crane tracks and car-body system where a portion of the tracks leaves the supporting soil surface.

2. Loss of tension or periods of slackness in both the pendent cables and the load line cable.

3. Finite deflections in the elastic crane boom.

4. Nonlinear coupled motion between the crane system generalized coordinates where the motion of a coordinate is seen to decrease and then grow again quickly.

The reduced-order crane model produced response characteristics similar to a higher-order crane model developed by Patten (2). The plots of the transient response of the same generalized coordinate predicted by both models had similar shapes. The three-link discretized boom approximation used in the reduced-order model replaces the continuum boom approximation used in the Patten model. The response of the same point in the discretized boom is characterized

by similar deflections and similar frequencies, but the boom chord in the discretized boom approximation shortens less than the continuum boom approximation.

The dynamic response characteristics of the crawler crane system are shown to be uniquely related to the crane's operating conditions. The shear modulus of the supporting soil greatly effects this description. The translational coordinates, which includes the vertical displacement of the tracks, the stretch of the load line, and both boom joint deflections, oscillate with the same dominate frequencies. Likewise, the rotational motion of the crane system, which includes the rotation of the tracks, the rotation of the boom chord, and the pendulation of the suspended load, is also characterized by common frequencies.

The reduced-order crane model was developed to serve as a tool to further the study of the crawler crane's dynamic characteristics. The model is able to predict many of the conditions that have been shown to influence the crane's response, yet has also retained enough simplicity, primarily due to the Lagrangian formulation of the equations of motion, to allow a researcher to adapt auxiliary control systems to the crane with relative ease. A pendent line controller is added to the reduced-order model in this thesis.

The hydraulic pendent actuator with proportional feedback control is able to attenuate the transient response of the crane system operating under conservative conditions. Three compensation techniques, which detect the error between the desired crane state

and the actual crane state, were each used to describe the pendent actuator input. Two of the compensation techniques, Controller 1 and Controller 3, detect the error in the lower frequency crane rotations. Controllers 1 and 3 attenuate the crane system response by absorbing energy in the pendent actuator. Neither controller is able to efficiently transfer energy to the dissipating soil foundation, but rather works against the ground motion. The resulting compensated translation and rotation of the crane tracks is larger than the uncompensated motion.

Controller 2 detects the error between the desired boom deflection and the actual boom deflection and describes the pendent actuator input to reduce the boom-tip excursions. This higher frequency translational motion enables Controller 2 to dump the crane system energy to the dissipating soil foundation at frequencies that coincide with the motion of the crane tracks.

The character of the rotational and translational motion of the crane tracks largely depends on the ground's stiffness or the shear modulus of the soil. Controller 2 attenuates the crane system response quite well when the supporting soil is stiff, as in Case A, but is not able to attenuate the crane system response as significantly for softer soil conditions, as in Cases B and C. Figure 101 presents both the uncompensated vertical response of the tracks for Cases A, B and C from Figs. 24, 37 and 48; and the compensated vertical response of the tracks with Controller 2 for Cases A, B and C from Figs. 71, 88 and 95.

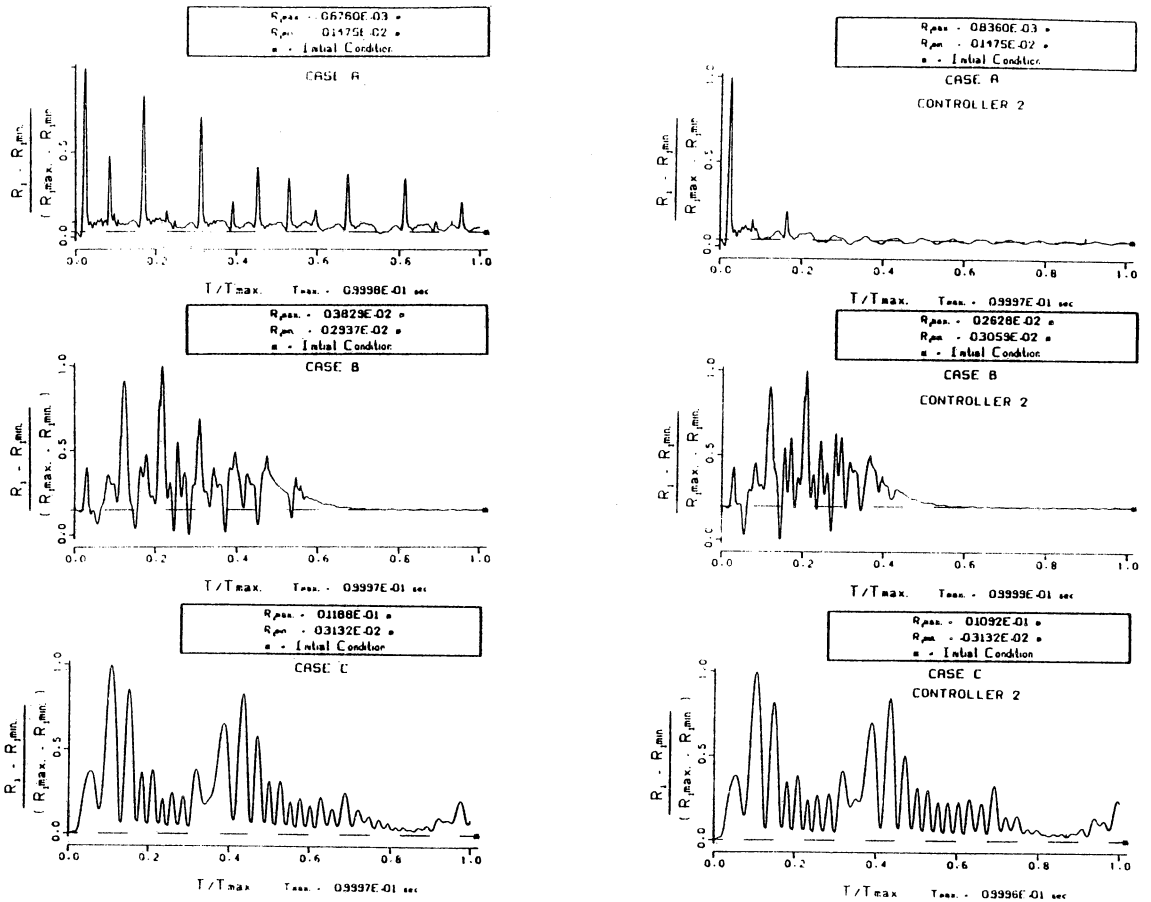

FIG. 101 VERTICAL RESPONSE OF THE TRACKS, (R_1) FOR CONDITIONS OF CASES A, B AND C (UNCOMPENSATED AND COMPENSATED WITH CONTROLLER 2)

The efficient transfer of energy to the dissipating soil foundation seems to be frequency dependent, and the frequencies which characterize the motion of the supporting soil change with the shear modulus of the soil. The crawler crane is a complex system, but the simple proportional pendent controller presented in this thesis is able to attenuate the crane motion under a particular set of operating conditions. Future work to develop a control system to attenuate the crane motion under more varied operating conditions should consider the hydraulic pendent actuator and a more sophisticated compensation technique. A compensation technique that continues to monitor the error between the desired crane states and the actual crane states, and in addition, is sensitive to the vertical translation and rotation of the crane tracks. The controller, sensing a need to correct the crane response, would dump energy from the crane system to the supporting soil when the ground motion provides the maximum damping and at frequencies which represent major components in the ground motion.

REFERENCES

1. Shapiro, H. I., Cranes and Derricks, McGraw-Hill, New York, 1980.

2. Patten, W. N., Transient Response Characteristics of a Construction Crawler Crane, Master's Thesis in Mechanical Engineering, Virginia Polytechnic Institute and State University, 1980.

3. Johnson, F. R., Jr., Procedures for Determining Load Ratings for Truck Cranes Supported on a Floating Platform Moored in the Open Sea, U. S. Naval Civil Engineering Laboratory, T. M. No. 51-76-1, Port Hueneme, California, February 1976.

4. Johnson, F. R., Jr., Dynamic Analysis of the P&H 6250 Truck Crane Employing the 150 Foot Boom Stick Model, U. S. Naval Civil Engineering Laboratory, T. M. No. M-51-76-16, Port Hueneme, California, September 1976.

5. Ward, C. C., and Johnson, F. R., Jr., Dynamic Loads on a Shipboard Crane Boom Due to Ship Motion, U. S. Naval Civil Engineering Laboratory, T. M. No. 51-78-12, Port Hueneme, CA, March 1978.

6. Saul, W. E., and Asavanich, S., "Variable Configuration Structures with Base Motion," ASCE Conference, San Francisco, CA, 17-19 October 1977 (Preprint No. 293).

7. Saul, W. E., and Peyrot, A. H., "Analysis of Crane Boom in a Random Sea," Unpublished Report, University of Wisconsin, June 1976.

8. Ito, H., Senda, Y., and Fujimoto, H., "Dynamic Behavior of a Load Lifted by a Mobile Construction-type Crane, 4th Report, The Study on Boom Hoist Motion, etc. . . .," Bulletin of the JSME, Vol. 21, No. 154, April 1978, pp. 600-608.

9. Ito, H., Senda, Y., and Fujimoto, H., "Dynamic Behavior of a Load Lifted by a Mobile Construction-type Crane, 5th Report, The Investigation of Dynamic Load Factors," Bulletin of the JSME, Vol. 21, No. 154, April, 1978, pp. 609-617.

10. Smith, N. S., A Comparison of Dynamic Crane Structures Models for the Container Offloading and Transfer System, U. S. Naval Coastal Systems Laboratory, Panama City, Florida, October 1978.

11. Podgorski, W., Crane Simulation Manual, The Charles Stark Draper Laboratory, Inc., Report C-4799, Cambridge, Massachusetts, December 1976.

12. Vyzral, F. J., and Welch, R. E., Development of Ratings and Dynamic Simulation Procedures for Shipboard Mobile Cranes, Final Technical Report, Illinois Institute of Technology Research Institute, March 1977.

13. Dobeck, G. J., A Control System Analysis for COTS Crane-On-Deck Configuration, U. S. Naval Coastal Systems Laboratory, Panama City, Florida, August 1977.

14. Summey, D. C., and Dobeck, G. J., Control Systems Model User's Manual for the Container Offloading and Transfer System, U. S. Naval Coastal Systems Laboratory, Technical Note TN-413, Panama City, Florida, August 1977.

15. Casler, R., Browne, F., Foster, E., Eterno, J., and Podgorski, W., The Design of Control Systems to Aid Cargo Transfer Operations in Moderate Seas, The Charles Stark Draper Laboratory, Inc., Report R-1018, Cambridge, Massachusetts, December 1976.

16. Clough, R. W., and Penzien, J., Dynamics of Structures, McGraw-Hill, New York, 1975.

17. Goldstein, H., Classical Mechanics, Addison-Wesley Publishing Co., Inc., Reading, Massachusetts, 1950.

18. Harris, C. M., and Crede, C. E., Shock and Vibration Handbook, 2nd ed., McGraw-Hill, New York, 1976.

19. Costello, G. A., and Phillips, J. W., "Effective Modulus of Twisted Wire Cables," Journal of the Engineering Mechanics Division, ASCE, 102, No. EM1, February 1976, pp. 171-181.

20. Richart, F. E., Woods, R. D., and Hall, J. R., Jr., Vibrations of Soils and Foundations, Prentice-Hall, Inc., Englewood Cliffs, New Jersey, 1970.

21. Parmelee, R. A., and Wronkieniez, J. H., "Dynamic Coefficients for Evaluating the Seismic Response of Soil-Structure Interaction Systems," Proceedings, 5th World Conference on Earthquake Engineering, 2, 1974, pp. 2606-2609.

22. Langhaar, H. L., Energy Methods in Applied Mechanics, John Wiley and Sons, Inc., New York, 1962.

23. Johnson, L. W., and Riess, R. D., Numerical Analysis, Addison-Wesley Publishing Co., Reading, Massachusetts, 1977.

24. Merritt, H. E., Hydraulic Control Systems, John Wiley and Sons, Inc., New York, 1967.

25. Sperry-Vickers, Inc., Power and Motion Control Systems Industrial Products Catalog, Troy, Michigan, 1974.

The vita has been removed from the scanned document

A REDUCED-ORDER CRAWLER CRANE MODEL WITH ACTIVE CONTROL TO ATTENUATE THE TRANSIENT VIBRATIONS

by

Kellen Matthew Finn

(ABSTRACT)

The nonlinear differential equations describing the motion of a crawler crane in a plane are formulated by applying Lagrange's equation to the system kinetic energy, potential energy and virtual work. The transient response of the crane system due to the vertical drop of the suspended load is simulated by numerically integrating the equations of motion.

The crane model includes the vertical translation and rotation of the crane body, the rotation of the boom, the stretch and pendulation of the load line, and two discrete boom displacements. The model includes the effects of tilting of the crane tracks, shortening of the boom length, and loss of tension in the elastic cables.

Tne model has been carefully developed to include the important effects which influence the crane system motion without loosing the simplicity which allows auxiliary control systems to be added with relative ease. A hydraulic valve-controlled piston actuator is adapted to the crawler crane pendent line to reduce the boom-tip excursions which excite the motion of the suspended load. Three proportional feedback compensation techniques, which detect the

error between the desired crane state and the actual crane state, are used to describe the pendent actuator's valve position.

The transient response of the system generalized coordinates for both the uncompensated crane and the compensated crane is presented subject to three sets of initial conditions and crane configurations. One controller which measures the deflection at a single point in the crane boom is able to attenuate the entire crane system response due to a 7.6 cm vertical drop of the 13,600 Kg load with only 13 Kw of hydraulic source power.